INFORMATION TO USERS

This reproduction was made from a copy of a document sent to us for microfilming. While the most advanced technology has been used to photograph and reproduce this document, the quality of the reproduction is heavily dependent upon the quality of the material submitted.

The following explanation of techniques is provided to help clarify markings or notations which may appear on this reproduction.

1. The sign or "target" for pages apparently lacking from the document photographed is "Missing Page(s)". If it was possible to obtain the missing page(s) or section, they are spliced into the film along with adjacent pages. This may have necessitated cutting through an image and duplicating adjacent pages to assure complete continuity.
2. When an image on the film is obliterated with a round black mark, it is an indication of either blurred copy because of movement during exposure, duplicate copy, or copyrighted materials that should not have been filmed. For blurred pages, a good image of the page can be found in the adjacent frame. If copyrighted materials were deleted, a target note will appear listing the pages in the adjacent frame.
3. When a map, drawing or chart, etc., is part of the material being photographed, a definite method of "sectioning" the material has been followed. It is customary to begin filming at the upper left hand corner of a large sheet and to continue from left to right in equal sections with small overlaps. If necessary, sectioning is continued again—beginning below the first row and continuing on until complete.
4. For illustrations that cannot be satisfactorily reproduced by xerographic means, photographic prints can be purchased at additional cost and inserted into your xerographic copy. These prints are available upon request from the Dissertations Customer Services Department.
5. Some pages in any document may have indistinct print. In all cases the best available copy has been filmed.

University
Microfilms
International

300 N. Zeeb Road
Ann Arbor, MI 48106

Chan, Chang Sing

SEARCH FOR GLUEBALL PRODUCTION IN NEGATIVE PION PROTON → PHI PHI N

City University of New York Ph.D. 1985

University
Microfilms
International 300 N. Zeeb Road, Ann Arbor, MI 48106

SEARCH FOR GLUEBALL PRODUCTION IN $\pi^- p \rightarrow \phi\phi n$

by

Chan, Chang-Sing

A dissertation submitted to the Graduate Faculty in Physics in partial fulfillment of the requirements for the degree of Doctor of Philosophy, the City University of New York.

1985

This manuscript has been read and accepted for the Graduate Faculty in Physics in satisfaction of the dissertation requirement for the degree of Doctor of Philosophy.

May 3, 1985
date

Chairman of Examining Committee

May 2, 1985
date

Executive Officer

B. Sakita

M. KRAMER

WON YONG LEE

CARL SHAKIN

Supervisory Committee

MANUSCRIPT WAS
READ AND ACCEPTED
THESE
COMMITTEE
MEMBERS
ALL SIGNED
APPROVAL
IN MY PRESENCE
ON DOCUMENT
SUBMITTED TO
REGISTRAR

S.J. LINDENBAUM

The City University of New York

SEARCH FOR GLUEBALL PRODUCTION IN $\pi^-p \to \phi\phi n$

by

Chang Sing Chan

Advisor: Prof. S.J. Lindenbaum

ABSTRACT

The present dissertation describes an investigation of the reaction:

$$\begin{array}{llll} \pi^- p \to & \phi & \phi & n \\ & & \to K^+K^- & \\ & \to K^+K^- & & \end{array} \qquad (A.1)$$

at 22 GeV/c. The experiment was performed by the BNL/CCNY collaboration in an unseparated negative pion beam from the Brookhaven Alternating Gradient Synchrotron using the BNL Multiparticle Spectrometer II. A collection of about 4000 $\phi\phi n$ events has been observed during two spring runs in 1982 and 1983. The $\phi\phi$ system has $I^G = 0^+$ and $C = +$. Statistically, this quantity of data samples is sufficient to allow for a meaningful partial wave analysis on the $\phi\phi$ system.

In order to determine the partial waves playing a major role in the $\phi\phi$ spectrum the isobar model was used, the events in the mass region 2.04 and 2.64 GeV were fitted with both coherent and incoherent backgrounds plus additional partial waves of specific J^P, L, S, M and exchange naturality η (see Table 2.1 of main text). All possible partial waves with permitted values of quantum numbers for up to $J = 4$ and $L = 3$ were tried. Our result shows that a good fit was obtained with three waves, apart from backgrounds, all characterized by the same quantum numbers $I^G = 0^+$ and $J^{PC} = 2^{++}$, each well described by a coupled set of Breit-Wigner

resonances. The three partial waves include one S-wave with S = 2, two D-waves with S = 0 and S = 2 respectively. The resonance parameters for each state were extracted from a 3-pole K-matrix fit. The coherent background with $J^{PC} = 1^{--}$ is needed to account for the $\cos\alpha$ distribution where α is the kaon's azimuthal angle measured in the ϕ rest frame (see Fig. 2.3).

An unexpected observation in the reaction A.1 is that this is an OZI (Okubo-Zweig-Iizuka) suppressed channel in which OZI suppression is found to be absent. This distinctive feature is clearly seen by an excess of $\phi\phi$ events above the number expected for uncorrelated production of two ϕ mesons. If the mechanism for OZI violation involves gluon exchange the gluonium states (or glueballs) may manifest themselves in the $\phi\phi$ mass spectrum. Assuming both QCD is the correct strong interaction theory and OZI rule is universal in the absence of glueballs, one is led to interpret the breakdown of the OZI suppression is due to the intervention of glueballs. It turns out that one or more primary glueballs with $I^G J^{PC} = 0^+ 2^{++}$ are responsible for the observed three states. Therefore, $\pi^- p \rightarrow \phi\phi n$ provides direct evidence for the existence of glueballs.

ACKNOWLEDGEMENTS

I wish to express my gratitude to my advisor, Prof. S.J. Lindenbaum, for his continuous advice and assistance in this experiment.

Special thanks go to Dr. R.S. Longacre who instructed me in the techniques of partial-wave analysis.

Warmest thanks are due to Drs. A. Etkin, K.J. Foley, M.A. Kramer, W.A. Love, T.W. Morris, E.D. Platner, A.C. Saulys and Y. Teramoto for their physics insights and valuable help.

For technical support I would like to thank S.E. Eiseman, C.L. Jacobs and the MPS group technicians: H. Arnesen, D. Brady, T. Cannizzo, R. Chmiel, D. David, W. Dieffenbach, L. Hawkins, T. Mogavero, L. Toler and R. Wheeler. I would also like to thank the staff of the Brookhaven On-Line Data Facility, D. Bartolomeo, L. Davis, J. Gould, R. Imossi, P. Popken, T. Savage and C. Zein for their contribution to this experiment.

The efforts of Miss S. Smith, Mrs. E. Mogavero and Mrs. M. Kassner in typing and preparing the manuscript are thankfully acknowledged.

I wish to express my gratitude and appreciation to my parents and my brothers, Edward and Mike, whose moral and financial support helped me during my years as a graduate student.

Finally, I wish to thank my wife, Mitzi, for her patience and encouragement during my graduate career.

This research was supported in part by the United States Department of Energy under contract DE-AC02-83ER40107 and the Research Foundation of the City University of New York.

TABLE OF CONTENTS

Page No.

Abstract iii

Acknowledgements iv

List of Tables x

List of Figures xiii

Chapter 1: Introduction 1

1.1 Motivation for Glueball Search 1

1.2 Identification of Glueballs 2

1.3 OZI Rule 4

1.4 Failure of the OZI Rule in the $\pi^- p \rightarrow \phi\phi n$ Reaction 6

1.5 Glueball Interpretation for the Breakdown of OZI Suppression 9

1.6 Description of $\phi\phi$ System 10

Chapter 2: Methods and Formulae of the Partial Wave Analysis 18

2.1 Introduction 18

2.2 The Isobar Model Formalism 18

2.2.1 Historical Review 18

2.2.2 The Generalized Isobar Model 19

2.2.3 Labeling Scheme 20

2.2.4 Definition of Decay Angles and Reference Systems 21

2.2.5 Basis Vectors and the Differential Cross Section 22

2.2.6 Maximum Likelihood Method 23

Page No.

Chapter 2: Methods and Formulae of the Partial Wave Analysis (cont.)

2.3 K-Matrix Fits and Breit-Wigner Parameters 24

2.3.1 General Description 24

2.3.2 K-Matrix Formalism 25

Chapter 3: Experimental Apparatus 32

3.1 Incident Pion Beam 32

3.2 Main Spectrometer (MPS II) 34

3.2.1 MPS I Improvement (MPS II) 34

3.2.2 Experimental Setup 35

3.3 Experimental Trigger 39

3.4 Data Handling and Monitoring 41

Chapter 4: Event Selection 48

Chapter 5: Monte Carlo Studies of the $\phi\phi$ System 52

5.1 Introduction 52

5.2 Characteristics of $\phi\phi$ Pure Waves 53

5.3 Interference Between 0^{++} and 2^{++} Waves 56

5.4 Test of Analysis Program Uniqueness 57

Chapter 6: Data Fitting and Results 81

6.1 Introduction 81

6.2 Mass Spectrum 81

6.3 Data Folding and Symmetry 82

6.3.1 Double Entries for α and $\cos\theta$ 83

6.3.2 Discussion of Symmetry 83

6.3.3 Reduced Ranges and Data Folding 84

6.3.4 Unnatural Parity Exchange 91

Page No.

Chapter 6: Data Fitting and Results (continued)

6.4 t-Dependence and Peripheral Production 91

6.4.1 Exchange Mechanism 91

6.4.2 t'-Plot and Peripheral Production 94

6.4.3 A_1 and A_2 Exchanges 95

6.4.4 One-Pion-Exchange in Relation to Glueballs 96

6.5 Fitting Procedure 97

6.5.1 Preparation of Decay Amplitudes and Acceptance Normalization Integrals 98

6.5.2 Fitting with OPTIME 100

6.6 Backgrounds 102

6.6.1 Determination of the Backgrounds by Extrapolation 102

6.6.2 Incoherent Background 103

6.6.3 Coherent Background 104

6.6.4 Determinations of Coherent and Incoherent Backgrounds 108

6.6.5 Real and Imaginary Parts of Coherent Background ($J^{PC} = 1^{--}$) 110

6.7 Wave Fitting 112

6.7.1 Preliminary Fits 114

6.7.2 Fitting with Two-Wave Without Background Subtraction 115

TABLE OF CONTENTS (continued)

Page No.

Chapter 6: Data Fitting and Results (continued)

6.7 Wave Fitting (continued)

6.7.3 Fitting with Three-Wave Without Background Subtraction 119

6.7.4 Detailed Fitting in Narrow Bins with Backgrounds 121

6.7.5 Final Solution 124

6.8 K-Matrix Fit 128

6.8.1 Production Amplitudes for Final Solution .. 128

6.8.2 K-Matrix Parameterization 129

6.8.3 Resonance Parameters and Argand Plot 138

6.9 χ^2-Calculation 140

6.9.1 Monte Carlo Simulation of Acceptance 140

6.9.2 Comparison Between Monte Carlo Solution and Data 141

Chapter 7: Discussion of Results and Conclusion 173

7.1 Summary of Results 173

7.2 Axioms 174

7.3 Results Compared with Theory 174

7.4 Other Comments 178

7.5 Conclusion 179

Appendix A: Observed Cross Section 180

Appendix B: The Relationship Between Loglikelihood (L) and $\Delta\chi^2$ ... 181

Appendix C: Conversion Between the Loglikelihood Change and σ 183

LIST OF TABLES

Page No.

Table 4.1 Definition of quantities for the partial wave labeling scheme and of the isobar model for the process $\pi^- p \rightarrow \phi\phi n$ in the $\phi\phi$ rest frame 49

Table 5.1(a) Solution found by loglikelihood method for file MCDATAA 60

Table 5.1(b) Solution found by loglikelihood method for file MCDATAB 61

Table 5.1(c) Solution found by loglikelihood method for file MCDATAC 62

Table 5.1(d) Solution found by loglikelihood method for file MCDATAD 63

Table 5.1(e) Solution found by loglikelihood method for file MCDATAE 64

Table 5.1(f) Solution found by loglikelihood method for file MCDATAF 65

Table 5.1(g) Solution found by loglikelihood method for file MCDATAG 66

Table 6.1 Ranges and the corresponding sizes of data in ten mass bins 83

Table 6.2(a) Foldings of the eight angular distributions which preserve the Bose and charge symmetries 92

Table 6.2(b) Folding of an angular distribution which violates the charge symmetry 92

Table 6.2(c) Special binning with cuts on $\cos\theta_1$ and $\cos\theta_2$ 92

LIST OF TABLES (continued)

Page No.

Table 6.3 The quantum numbers and the naturalities of the allowed exchange particles for $\pi^- p \to \phi\phi n$ along with the J^{PC} values of the associated $\phi\phi$ states 93

Table 6.4 List of partial waves tried in the PWA 99

Table 6.5 Loglikelihood values calculated by OPTIME fitting program for each combination of incoherent background plus one ϕK^+K^- partial wave 106

Table 6.6(a) Incoherent and total coherent ($J^{PC} = 1^{--}$) backgrounds determined by the same momentum extrapolation method and also the smoothes values 111

Table 6.6(b) Interfering background (Re1^{--}) and the non-interfering background (incoherent background + Im1^{--}) determined from the smoothed values 111

Table 6.7 Comparison of loglikelihood values between the 2^{++} S-wave of the $\phi\phi$ data which interferes with only the real part of the 1^{--} and without 1^{--}. In the former case the imaginary part of 1^{--} is combined with the incoherent background 112

Table 6.8(a) Loglikelihood values for one partial wave and background fits in the mass range $M_{\phi\phi} = 2.20 \pm 0.10$ GeV 116

Table 6.8(b) Loglikelihood values for two-wave fits (2^+S20^+ background + one selected partial wave) in the mass range = 2.20 ± 0.10 GeV 117

Page No.

Table 6.8(c) Loglikelihood values for three-wave fits (2^+S20^- and 2^+D20^- + background + one selected partial wave) in the mass range = 2.20 ± 0.10 GeV 117

Table 6.9 List of the top ten coupled two-waves with the highest loglikelihood values in 400 MeV bins 120

Table 6.10 Loglikelihood values for twenty-seven sets of three-wave fit calculated in each of the ten mass bins with (upper) and without (lower) backgrounds .. 125

Table 6.11(a) Amplitudes for three dominant partial waves and two backgrounds calculated for production by isobar model 130

Table 6.11(b) Amplitudes for three dominant partial waves and two backgrounds calculated for production by isobar model 131

Table 6.12 Resonance parameters of the three-pole K-matrix fit 139

Table 6.13 χ^2 values for nine projected angular distributions obtained by comparing the three-pole K-matrix solution and the observed events 143

LIST OF FIGURES

Page No.

Fig. 1.1 The dominant diagram in radiative J/ψ decay where the multigluon state is possible to form a glueball 12

Fig. 1.2(a) Zweig connected diagram for $\omega \to \pi^+\pi^-\pi^0$ 12

Fig. 1.2(b) Zweig connected diagram for $\phi \to K^+K^-$ 12

Fig. 1.2(c) Zweig disconnected diagram for $\phi \to \pi^+\pi^-\pi^0$ 12

Fig. 1.3(a) Zweig disconnected diagram for $\phi \to \pi^-p^+$ 13

Fig. 1.3(b) Two-step process for $\phi \to K^+K^- \to p^+\pi^-$ 13

Fig. 1.4(a) Zweig disconnected diagram for $\pi^-p \to \phi n$ 13

Fig. 1.4(b) Two-step process for $\pi^-p \to K^+K^-n \to \phi n$ 13

Fig. 1.5(a) The Zweig quark line diagram for the reaction $\pi^-p \to \phi K^+K^-n$, which is connected and Zweig allowed . 14

Fig. 1.5(b) The Zweig quark line diagram for the reaction $\pi^-p \to K^+K^-K^+K^-n$, which is connected and OZI allowed 14

Fig. 1.5(c) The Zweig quark line diagram for the reaction $\pi^-p \to \phi\phi n$ which is disconnected (i.e. a double hairpin diagram) and is OZI forbidden 14

Fig. 1.6 A scatter plot of K^+K^- effective mass. Two randomly chosen mass combinations are plotted for each event. Clear bands of ϕ (1.020 GeV) are seen with an enormous enhancement (black spot) where they overlap ... 15

Fig. 1.7 The effective mass of each K^+K^- pair for which the other pair was in the ϕ mass band 16

LIST OF FIGURES (continued)

Page No.

Fig. 1.8 The Zweig quark line diagram for the reaction $\pi^- p \rightarrow \phi\phi n$ which is disconnected (i.e. a double hairpin diagram) and is OZI forbidden. Two or three gluons are shown connecting the disconnected pars of the diagram depending upon the quantum numbers of the $\phi\phi$ system 17

Fig. 2.1 Schematic diagram describing the isobar model for $\pi^- p \rightarrow \phi\phi n$. The variables are described in the text. 29

Fig. 2.2 The Gottfried-Jackson frame with polar angle β and azimuthal angle γ 30

Fig. 2.3 The ϕ_1 rest frame with the polar angle θ_1 of the decay K_1^+ (relative to ϕ direction) and the azimuthal angle α_1 of the decay K_1^+ 31

Fig. 3.1 Beam transport system 43

Fig. 3.2 The MPS II Spectrometer layout for the reaction $\pi^- p \rightarrow \phi\phi n$ 44

Fig. 3.3 Isometric view of the MPS magnet 45

Fig. 3.4 The construction of a drift chamber module 46

Fig. 3.5 The experimental arrangement of the target, veto box, drift chambers and trigger PWC's 47

Fig. 4.1 The missing mass squared for the neutral system recoiling from the $\phi\phi$ 50

Page No.

Fig. 4.2 A typical 4K ($K^+K^-K^+K^-$) event projected on different planes and reconstructed by MPS pattern recognition program. An X-view or Y-view means a projection of the reconstructed tracks on X-Z or Y-Z plane 51

Fig. 5.1(a) Angular distributions expected for decay of individual spin states 67

Fig. 5.1(b) Angular distributions expected for decay of individual spin states 68

Fig. 5.1(c) Angular distributions expected for decay of individual spin states 69

Fig. 5.1(d) Angular distributions expected for decay of individual spin states 70

Fig. 5.1(e) Angular distributions expected for decay of individual spin states 71

Fig. 5.1(f) Angular distributions expected for decay of individual spin states 72

Fig. 5.1(g) Angular distributions expected for decay of individual spin states 73

Fig. 5.1(h) Angular distributions expected for decay of individual spin states 74

Fig. 5.2(a) χ^2 separation of 0^{++} from 2^{++} partial waves for α projection as a function of R at θ = 0°, 90° and 180° where R is the ratio of 0^{++} in the mixture of 0^{++} and 2^{++}, and θ is the phase difference between these two partial waves 75

LIST OF FIGURES (continued)

Page No.

Fig. 5.2(b) χ^2 separation of 0^{++} from 2^{++} partial waves for eight projections (α, $\alpha_1 \pm \alpha_2$, $\cos\beta$, α, $\cos\theta$, $\cos\theta_1 \pm \cos\theta_2$) as a function of R at $\theta = 0°$, $90°$ and $180°$ when R is the ratio of 0^{++} in the mixture of 0^{++} and 2^{++}, and θ is the phase difference between these two partial waves 76

Fig. 5.2(c) Monte Carlo study of α distribution for $\theta = 0°$, $90°$ and $180°$ at two fixed values of R 77

Fig. 5.2(d) Monte Carlo study of α distributions for $\theta = 0°$, $90°$ and $180°$ at two fixed values of R. R = 0.6 and 0.8. 78

Fig. 5.3(a) A three-pole K-matrix fit (smooth curves) of the searched solution compared to the Monte Carlo generated $\phi\phi$ solution (file MCDATAB). The generated solution has background put in whereas the K-matrix fit did not consider the background contribution ... 79

Fig. 5.3(b) A K-matrix fit of the D-S phase difference (obtained from the searched solution) compared to the generated $\phi\phi$ solution (file MCDATAB). The generated solution has background put in whereas the K-matrix fit did not consider this 80

Fig. 6.1 The observed $\phi\phi$ effective mass spectrum (1982 data). 147

Fig. 6.2 The observed $\phi\phi$ effective mass spectrum (1983 data). 147

Fig. 6.3 The observed $\phi\phi$ effective mass spectrum for a combined 1982 and 1983 data 148

Page No.

Fig. 6.4 The $\phi\phi$ mass spectrum corrected for acceptance. The solid line is the fit to the data with the three resonant states to be described later. The points at the bottom of the diagram are the acceptance for each mass bin to be read with the scale at the right 149

Fig. 6.5 The diagram to illustrate the maping of a point A in α_1 vs α_2 scatter plot which satisfies charge symmetry, $A(\alpha_1,\alpha_2) \to B(\alpha_1 + \pi, \alpha_2 + \pi)$, and Bose symmetry, $A(\alpha_1,\alpha_2) \to A'(\alpha_2,\alpha_1)$ and $B(\alpha_1 + \pi, \alpha_2 + \pi) \to B'(\theta_2 + \pi, \alpha_1 + \pi)$ 150

Fig. 6.6 The signs associated with $\cos\chi$ or $\sin\chi$ term ($\chi = \alpha_1 + \alpha_2$) for different values of θ_1 ($0 \to \pi$) and θ_2 ($0 \to \pi$) 150

Fig. 6.7 Mappings of the $\alpha_1 - \alpha_2$ and $\alpha_1 + \alpha_2$ projections in α_1 vs α_2 scatter plot which satisfy both Bose symmetry and charge symmetry. The natural ranges for both projections are reduced to $\pi/2$ 151

Fig. 6.8 Diagram for the charge exchange (CEX) process $\pi^- p \to Gn$ where G represents an intermediate state (glueball) for the reaction $\pi^- p \to \phi\phi n$ 152

Fig. 6.9 The process $\pi^- p \to Gn$ in the center-of-mass frame. θ_s is the S-channel scattering angle 152

Fig. 6.10 Four momentum transfer squared distribution of the $\phi\phi$ system 153

LIST OF FIGURES (continued)

Page No.

Fig. 6.11 The extraction of the ϕK^+K^- background events (rectangular block) from the K^+K^- effective mass scatter plot 154

Fig. 6.13 Fitting the three ϕK^+K^- backgrounds (1^{--}, 2^{++} S-wave and flat background) in four 100-MeV-wide bins 155

Fig. 6.14(a) The effective mass spectrum for the ϕK^+K^- background (1004 events) 156

Fig. 6.14(b) The γ-distribution for the ϕK^+K^- background 156

Fig. 6.14(c) The $\cos\beta$-distribution for the ϕK^+K^- background 156

Fig. 6.14(d)(e) The α-distributions for α_1 and α_2 of the ϕK^+K^- background where α_1 is the azimuthal angle of K^+ in the CMS frame and α_2 is the corresponding angle due to the decay of ϕ 157

Fig. 6.14(f)(g) The $\cos\theta$-distributions for $\cos\theta_1$ and $\cos\theta_2$ of the ϕK^+K^- background where θ_1 is the polar angle of K^+ in CMS frame and θ_2 is the corresponding angle due to the decay of ϕ 158

Fig. 6.15 Fitting the real part of 1^{--} (interfering) background and non-interfering background. The non-interfering consists of the incoherent background and imaginary part of 1^{--} 159

Fig. 6.16 D-S phase difference from the partial wave analysis vs. $\phi\phi$ mass. The smooth curves are derived from a K-matrix fit 160

Page No.

Fig. 6.17 The three $\phi\phi$, $J^{PC} = 2^{++}$ partial waves at production in 50 MeV mass bins (except ends). The smooth curves are derived from a K-matrix fit 161

Fig. 6.18 Argand plot from K-matrix 162

Fig. 6.19(a) Comparison of Monte Carlo generated events to the observed angular variable α 163

Fig. 6.19(b) Comparison of Monte Carlo generated events to the observed angular variable $\alpha_1 + \alpha_2$ 164

Fig. 6.19(c) Comparison of Monte Carlo generated events to the observed angular variable $\alpha_1 - \alpha_2$ 165

Fig. 6.19(d) Comparison of Monte Carlo generated events to the observed angular variable $\alpha_1 + \alpha_2$ 166

Fig. 6.19(e) Comparison of Monte Carlo generated events to the observed angular variable $\cos\beta$ 167

Fig. 6.19(f) Comparison of Monte Carlo generated events to the observed angular variable γ 168

Fig. 6.19(g) Comparison of Monte Carlo generated events to the observed angular variable $\cos\theta$ 169

Fig. 6.19(h) Comparison of Monte Carlo generated events to the observed angular variable $\cos\theta_1' + \cos\theta_2'$ 170

Fig. 6.19(i) Comparison of Monte Carlo generated events to the observed angular variable $\cos\theta_1' - \cos\theta_2'$ 171

Page No.

Fig. 6.20 Comparison of the generated K-matrix fit with $J^{PC} = 1^{--}$ partial wave and the data for the α projection in $0 \rightarrow \pi$ range. The asymmetrical structure for α distribution in low and high mass bins are clearly shown 172

CHAPTER 1: INTRODUCTION

1.1 Motivation for Glueball Search

In the past two decades there has been a remarkable progress in the search of understanding of hadronic physics. Our present notion of the basic constituents of hadronic matter is pointlike quarks.[1] The prime candidate for a fundamental theory of hadronic forces is a model of quarks interacting through the exchange of a non-Abelian gauge fields.[2] Quarks, in addition to their electric and weak charges, carry a color charge that may take one of three values. The interquark interactions are assumed to be invariant under color interchange, thus quarks are described by symmetry group $SU(3)_{color}$[3] and belong to the triplet representation. Gluons, the quanta of the color field, are color octet states coupled to the color triplet charges of quarks. The strong color interactions between quarks via the gluonic fields are described by a formal gauge theory, Quantum Chromodynamics (QCD).[4-5]

Gluons are massless vector particles. Since there is no evidence for a long-range interaction associated with color it has led to the wide speculation that color is permanently confined.[6] Thus hadronic states that are not color singlets are unobservable. Color confinement is believed to be a consequence of the $SU(3)_{color}$ gauge theory. Support for this comes from lattice gauge theory models[7] in which space-time is replaced by a lattice of points on which an analog of a gauge theory can be defined. Such models do lead to confinement.[8]

Due to its non-Abelian nature, QCD also predicts the gluon-gluon and multigluon interactions which occur with the same coupling constant as the quark-gluon interaction; these couplings become stronger as the energy decreases and weaken as the energy increases. This is described as the asymptotic freedom of the theory.[9]

It turns out that the self-interaction of gauge bosons which occurs in non-Abelian gauge theory (gluons in QCD) but not in Abelian gauge theory such as Quantum Electrodynamics (photons in QED) is a most characteristic feature of QCD. The combination of asymptotic freedom and the requirement of color confinement has led to the prediction of existence of multi-gluon resonances or glueballs. In fact the bag model,[10–15] lattice gauge theory,[16–18] the quark potential model and simple confinement arguments[19] all predict glueball resonances. Therefore the discovery of glueballs has fundamental importance in establishing the validity of QCD. However, if glueballs can never be found it would be difficult to conclude that QCD is not a questionable theory despite its other successes.

Therefore, it is left as a great challenge to the experimental establishment of the glueball states. Motivated by this demand, the BNL/CCNY group has initiated to study the $\pi^- p \rightarrow \phi\phi n$ reaction, results of which have a natural glueball interpretation within the context of QCD.

1.2 Identification of Glueballs

From the success of the quark model it is clear that the hadronic sector is dominated by $q\bar{q}$ and qqq states; in particular, these states cover the mass range 1-3 GeV where glueballs are most likely to be produced. Evidently, if glueballs exist they are masked in the quark-built meson nonets (B = 0 for glueballs) which always make the unambiguous identification of glueballs difficult.

Nevertheless, some prominent features of glueball characteristics have been observed in certain channels which provide useful clues in relation to finding glueballs.

a. Observation of a state in a channel in which an intermediate state consists of two or more gluons is the first indication that a state could be a glueball state. Glueball candidates produced in this gluon enriched channel can be seen in the process $\psi \rightarrow \gamma + X$.[20–21] The leading order diagram for this process is shown in Fig. 1.1. The enhanced production of glueballs is described as due to the variation of γ energy so that the effective mass of the two gluons could sweep over a range of masses and if there is a gg resonance corresponding to a glueball it can manifest in the resonance. Glueball candidates of this type are iota(1440), $J^{PC} = 0^{-+}$, and $\theta(1640)$ with $J^{PC} = 2^{++}$. A discussion of these glueball candidates will be given later.

b. Another signal of glueballs comes by way of pattern recognition of a decuplet. Since the glueball states are color singlets with I = 0, B = 0 (u, d, s, c, b = 0), they could appear as additional singlets resembling I = 0 singlet of an SU(3) nonet. If the J^{PC} of the nonet and the glueball are the same, mixing of the isoscalar in the nonet and the glueball singlet is expected to take place.[12] In other words, after observation of a new state the difficulty in accommodating the state as a member of the standard $q\bar{q}$ SU(3) nonet is an important clue that this could be a glueball state. A glueball candidate of this type is the BNL/CCNY $J^{PC} - 0^{++}$, $g_s(1240)$.[22] Of course, one could also argue that this assignment difficulty may arise from mixing of basic nonet with those of a radial excitation.

c. Finally, it is the purpose of this thesis to describe the study of the reaction $\pi^- p \rightarrow \phi\phi n$ performed by the BNL/CCNY group, the failure of the OZI rule observed in this process can be satisfactorily explained by the intervention of glueball resonance. The remainder of this report is to present a full account of this experiment and its' associated glueball interpretation.

1.3 OZI Rule

The OZI rule,[23-25] also known as the quark line rule,[26] has been of considerable value in understanding certain aspects of particle phenomena. In fact, this rule has successfully explained some important decay mechanism such as ϕ,f',J/ψ,ψ' and Υ resonances.

The quark line diagram, originally proposed by Zweig, depicted hadronic reactions by the behaviour of the individual quarks that make them up. Following his idea a reaction which proceeds by a continuous flow of quark lines carrying color from the initial state to a final state hadron or hadrons is considered an OZI allowed process. Whereas for reactions in which the quark lines are disjointed and give rise to the so-called disconnected or hairpin diagram is considered forbidden (or the process is subject to a substantial suppression factor). In this connection, the quark line diagram rule is phenomenlogically very useful in visualizing processes.

Experimental evidence which demonstrates the operation of the quark line rule (QLR) can be seen in the allowed process $\omega \rightarrow \pi^+\pi^-\pi^o$, Fig. 1.2(a), and $\phi \rightarrow K^+K^-$ (Fig. 1.2(b)) as well as the forbidden process $\phi \rightarrow \pi^+\pi^-\pi^o$ (Fig. 1.2(c)). In an illustration to show the magnitude of suppression associated with the forbidden process, a quantitative measure of the suppression factor for a disconnected diagram was determined from the ratio of the forbidden process $\phi \rightarrow \pi^+\pi^-\pi^o$ to the allowed process $\omega \rightarrow \pi^+\pi^-\pi^o$.[27] The result of such measurement was found to be $\approx$ 100. On the other hand, the diagram for $\phi\to K\bar{K}$ (Fig. 1.2(b)) which is allowed by QLR representing about ≈ 80% of the ϕ decays. A qualitative treatment based on estimated deviation from an ideal mixing of a nonet is useful for us to get some idea about the OZI suppression factor.

If the nonet differs from ideal mixing by an angle θ, then the ratio of the square of the couplings g_S and g_{U+D} for the strangeonium state of OZI allowed divided by OZI forbidden is given by

$$f_{OZI} = \frac{g_S^2 \cos^2\theta}{g^2_{U+D} \sin^2\theta} \tag{1.1}$$

where g_{U+D} and g_S are the couplings of the isosinglet $(u\bar{u} + d\bar{d})\sqrt{2}$ of the singlet state and isosinglet $s\bar{s}$ of octet state. Eq. 1.1 follows from the knowledge that the ratio of partial widths for decays with strange quarks in the final state and decays without strange quarks dividing out phase space barrier suppression.

Assuming $g_S \approx g_{U+D}$, the angle θ of Eq. 1.1 for the mesons on the leading Regge trajectory 1^{--}, 2^{++} and 3^{--} can be calculated. From the mass rule, θ for each nonet is derived (see 1984 Particle Data Tables) we get $\theta = 3.7°$ for the 1^{--}, $\theta = 7.3°$ for the 2^{++} and $\theta = 6.3°$ for the 3^{--}. Thus for the three strangeonium state ϕ,f' and ϕ' in these nonets

$$f^{\phi}_{OZI} = \cot^2 3.7° = 240 \tag{1.2}$$

$$f^{f'}_{OZI} = \cot^2 7.3° = 61 \tag{1.3}$$

$$f^{\phi'}_{OZI} = \cot^2 6.3° = 82 \tag{1.4}$$

Even though one should not take these numbers too literally, indeed, they show the order of large OZI suppression.

Another interesting point about the OZI rule was raised by Okubo[26] who demonstrated that the large suppression associated with the disconnected diagram could disappear, at least topologically, by a replacement of a two-step process. This can be illustrated by referring to the channel $\phi \to \pi^- \rho^+$ [Fig. 1.3(a)] which is supposed to be OZI suppressed. However, the combination of two allowed processes $\phi \to K^+K^-$ and $K^+K^- \to \pi^-\rho^+$ [Fig. 1.3(b)] may convert an originally forbidden process to proceed like an allowed one. A similar situation can be found in the reaction $\pi^-p \to \phi n$ [Fig. 1.4(a)] via another two-step process $\pi^-p \to K^+K^-n \to \phi n$ [Fig. 1.4(b)].

In order that the quark line diagram be compatible with the established experimental observations, a quark line rule[28] was proposed to prevent the use of two-step processes. Otherwise one could always turn a disconnected quark line diagram into a topologically equivalent connected diagram with the subsequent disappearance of the substantial suppression.

1.4 Failure of the OZI Rule in the $\pi^-p \to \phi\phi n$ Reaction

While the OZI rule has remarkable agreement with the experimental observations it is discovered that this rule is patently violated in an exceptional channel $\pi^-p \to \phi\phi n$[29] which becomes the main subject of the present study.

The basic reactions studied by the BNL/CCNY group essentially select the four kaon ($K^+K^-K^+K^-$) events with a recoiled neutron in the pion-proton interaction. In this case any such event should belong to one of the following three channels:

$$\pi^- p \rightarrow K^+ K^- K^+ K^- n \qquad (1.5)$$

$$\pi^- p \rightarrow \phi K^+ K^- n \qquad (1.6)$$

$$\pi^- p \rightarrow \phi\phi n \qquad (1.7)$$

Figs. 1.5(a) and 1.5(b) are the quark line diagrams for reactions 1.5 and 1.6 respectively in which one clearly sees these diagrams are connected and thus OZI allowed. Whereas the quark line diagram (Fig. 1.5(c)) for Reaction 1.7 shows the complete isolation of the final state $\phi\phi$ system from rest of the diagram, and as a consequence, should be OZI forbidden. Following the previous discussion, an immediate OZI prediction would certainly favor a huge suppression of the double ϕ production relative to the other two allowed processes. In fact, the cross section for the reaction 1.6 measured in our prior experiment was in good agreement with the CERN measurement which studied the $\pi^- p \rightarrow K^+ K^- \phi \pi^- p$ reaction at comparable energies.[30] However, contrary to what one would expect from Reaction 1.7 $\phi\phi$ production was much more intense than the corresponding uncorrelated kaon or ϕ production which provided an undoubted evidence for the complete absence of the OZI suppression in that channel.

To see how this unexpected conclusion comes about here we present a scatter plot of the effective mass of one K^+K^- pair of an event against the second K^+K^- pair of the same event (Fig. 1.6). All available data have been used in making up this plot. Moreover, since there are two possible ways to form these kaon pairs, consequently each event is plotted twice. Two interesting phenomena are related to this plot:

a. An enhancement over background is seen in two ϕ bands.

b. An enormous enhancement over background is seen where the two ϕ mass bands cross.

Quantitatively, an enhancement factor ≈ 20 is obtained for the ϕK^+K^- events over the four-kaon events and this factor is increased to more than 50 for $\phi\phi$ over the ϕK^+K^- events. We thus see that the peak intensity of the overlap region is more than 1000 times that of the adjoining $K^+K^-K^+K^-$ event intensity. The enhancement seen in (a) can be understood as the result of ϕ resonance and also the process is allowed by the OZI rule, but the second enhancement is mysterious since the enriched $\phi\phi$ production contradicts the OZI suppression.

An alternative approach to demonstrate the $\phi\phi$ enhancement is to plot the effective mass of K^+K^- pair for the ϕK^+K^- events. Such a plot is displayed in Fig. 1.7 in which a huge signal is clearly seen at the ϕ mass.

Independent evidence of the breakdown of the OZI suppression is given[31] by a study of the reaction $K^-p \rightarrow \phi\phi\Lambda$ or $\phi\phi\Sigma^o$. The cross section obtained from this allowed process is about a factor 4 larger than that obtained from $\pi^-p \rightarrow \phi\phi n$. Assuming that the productions of $\phi\phi\Sigma^o$ and $\phi\phi\Lambda$ are equally probable in this channel then this factor should be reduced to 2 in consideration of these two contributions. The net result of this comparison implies that the cross sections for the OZI allowed and forbidden processes are comparable within a factor of 2.

However, similar comparison for other reactions[32] still show the typical OZI suppression:

$$\frac{\sigma(K^-p \rightarrow \phi\Lambda)}{\sigma(\pi^-p \rightarrow \phi n)} \approx 60 \tag{1.8}$$

$$\frac{\sigma(\pi^-p \rightarrow \omega n)}{\sigma(\pi^-p \rightarrow \phi n)} \approx 100 \tag{1.9}$$

We thus conclude based on the established experimental facts that the OZI suppression is completely absent in the supposedly suppressed channel $\pi^-p \rightarrow \phi\phi n$.

1.5 Glueball Interpretation for the Breakdown of OZI Suppression

In recent development, quark line diagram finds a natural interpretation in the context of QCD. In accordance with the present concepts of QCD, a reaction which can be depicted by a connected quark line diagram should proceed by a continuous series of exchange of single gluon without violating color confinement. However, the disconnected diagram where there is an interruption of the flow of quark lines carrying color from the initial state to a final state hadron or hadrons should proceed by two or more (to conserve color) hard gluons bridging the gap. The resultant multiple relatively low coupling constant of the hard multi-gluon exchange leads to a suppression which to a large factor forbids the processes depicted by these diagrams.

As noted in the proceeding section, the BNL/CCNY collaboration has shown that the Zweig suppression was essentially absent in the forbidden reaction $\pi^- p \rightarrow \phi\phi n$. A logical explanation[29-30,33] for this observed fact is that the multi-gluon intermediate state, which connects the two disconnected parts of the diagram, has a variable mass and all glueball quantum numbers with $C = +$. Thus if some part of the mass region covers existing glueball resonances, these resonances may lead to effectively strong coupling and the OZI rule may be defeated (Fig. 1.6). In this view, the breakdown of the OZI rule has a natural glueball explanation in the context of QCD and, as a result $\pi^- p \rightarrow \phi\phi n$ reaction is a good place to look for glueballs.

It has been shown in Section 1.3 that two OZI allowed processes can be used to eliminate the OZI forbidden diagram and appears to be a general phenomenon occurring in production as well as decay. This apparently violates crossing symmetry and unitarity. From the QCD point of view this is equivalent to converting the nature of the multi-gluon exchange needed in the one-step diagrams to a series of the ordinary OZI allowed one gluon exchanges. Thus a topologically equivalent two-step process, which is in serious disagreement with QCD, cannot be justified. It follows that Zweig's diagrams are to be taken literally as one-step processes.

1.6 Description of $\phi\phi$ System

The $\phi\phi$ system is a four-body system in which the ϕ is a vector system and its helicity structure is transmitted to the decay produces K^+K^- and another K^+K^- for the other ϕ. Unlike the general four-body problem the $\phi\phi$ system has good analyzing power due to the vector nature of ϕ and the exact identity of its two constituent ϕ's. As will be presented in later discussions, the helicity structure can be untangled through the decay angles of $\phi\phi$.

The $\phi\phi$ system has isospin $I = 0$ and also the spin coupling of two ϕ's gives the spin of $\phi\phi$ $S = 0,1,2$.

An important property associated with the $\phi\phi$ system is its intrinsic symmetry. There are two types of symmetry possessed by this system:

a. Since the ϕ's form a pair of identical bosons they must obey Bose symmetry. It turns out that in order to satisfy the Bose symmetry the wavefunctions of the orbital angular momentum part (L) and the spin part (S) must be either both symmetric or both antisymmetric. This leads to the following rules for the $\phi\phi$ system:

$$L + S = \text{even} \qquad S = 0,1,2 \qquad (1.10)$$

$$L = 0,1,2,3,\ldots\ldots$$

and

$$C = (-1)^{L+S} = + \qquad (1.11)$$

It should be noted that Rule 1.10 reduces the number of possibilities for L and S. The even charge conjugation implies that if reaction A.1

involves gluon exchange, both two-gluon or three-gluon exchanges are permitted.

b. The fact that the $\phi\phi$ system has even charge conjugation and each ϕ decays into a pair of oppositely charged kaons also requires the charge symmetry.

The nature of these symmetries implies that in the process of interchanging ϕ_1 and ϕ_2 (Bose symmetry), K^+ and K^- (charge symmetry) the physics of the $\phi\phi$ system remains unchanged. To actually satisfy these symmetry requirements in our analysis we have "folded" our data in accordance with these interchange procedures. In Chapter 6 we shall describe in detail how we performed the folding of a wider data region into a more condensed range by ways of mapping.

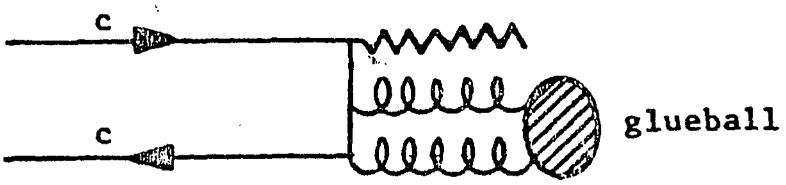

Fig. 1.1 The dominant diagram in radiative J/ψ decay where the multigluon state is possible to form a glueball

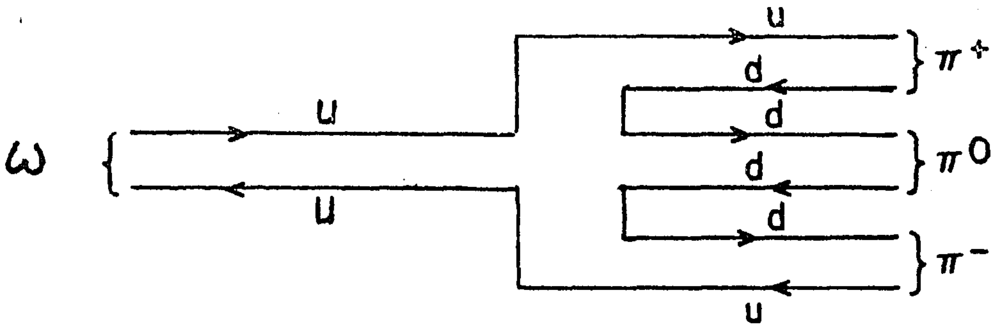

Fig. 1.2(a) Zweig connected diagram for $\omega \rightarrow \pi^+\pi^-\pi^0$

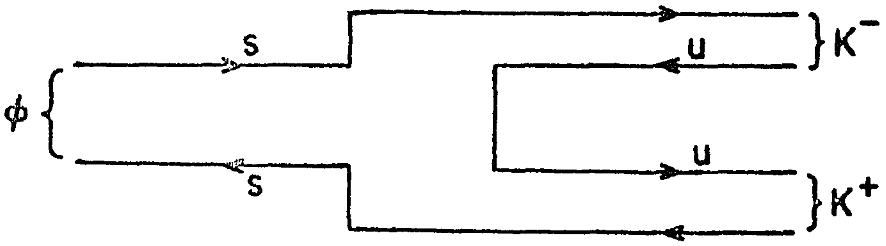

Fig. 1.2(b) Zweig connected diagram for $\phi \rightarrow K^+K^-$

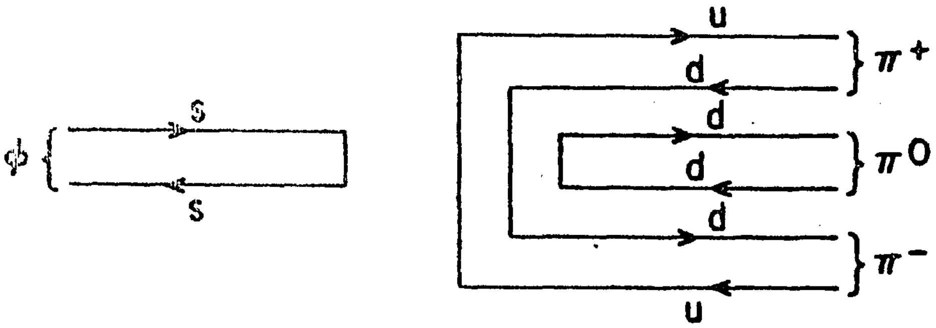

Fig. 1.2(c) Zweig disconnected diagram for $\phi \rightarrow \pi^+\pi^-\pi^0$

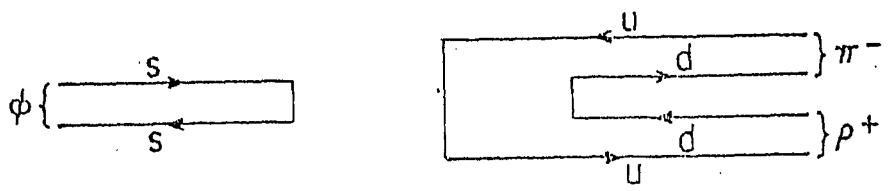

Fig. 1.3(a) Zweig disconnected diagram for $\phi \to \pi^- p^+$

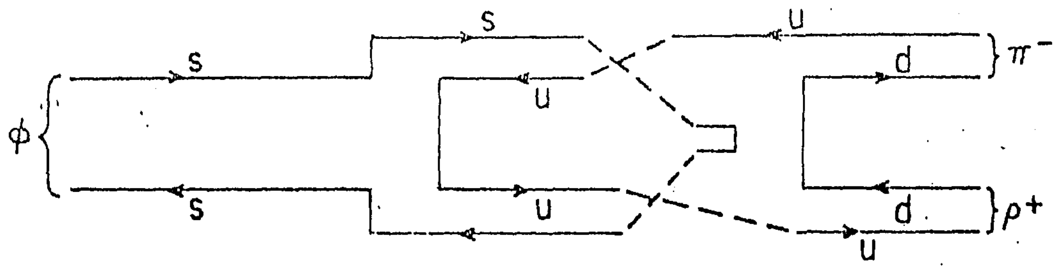

Fig. 1.3(b) Two-step process for $\phi \to K^+K^- \to p^+\pi^-$

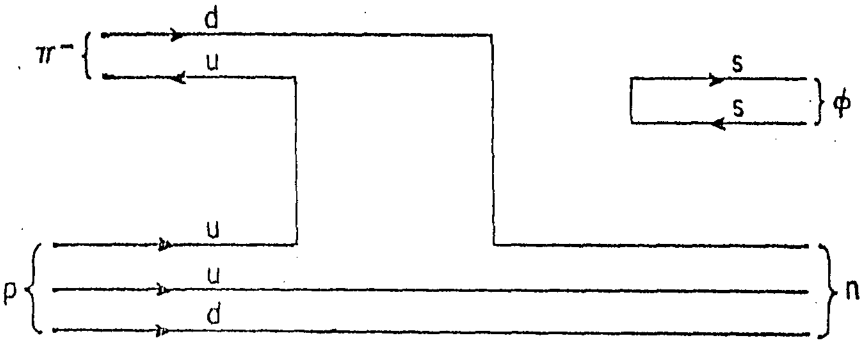

Fig. 1.4(a) Zweig disconnected diagram for $\pi^- p \to \phi n$

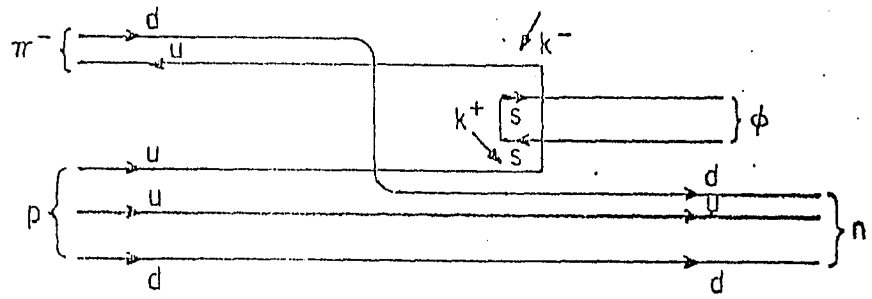

Fig. 1.4(b) Two-step process for $\pi^- p \to K^+K^- n \to \phi n$

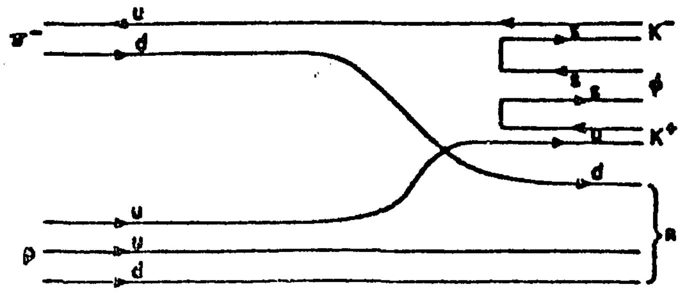

Fig. 1.5(a) The Zweig quark line diagram for the reaction $\pi^- p \rightarrow \phi K^+ K^- n$, which is connected and Zweig allowed

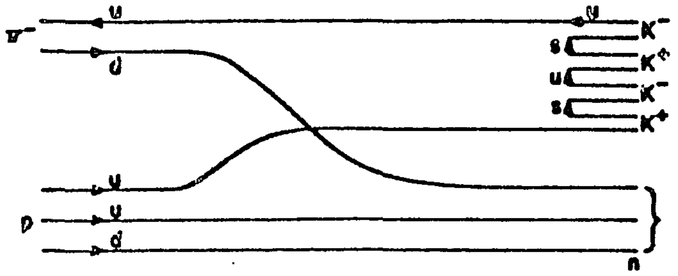

Fig. 1.5(b) The Zweig quark line diagram for the reaction $\pi^- p \rightarrow K^+ K^- K^+ K^- n$, which is connected and OZI allowed

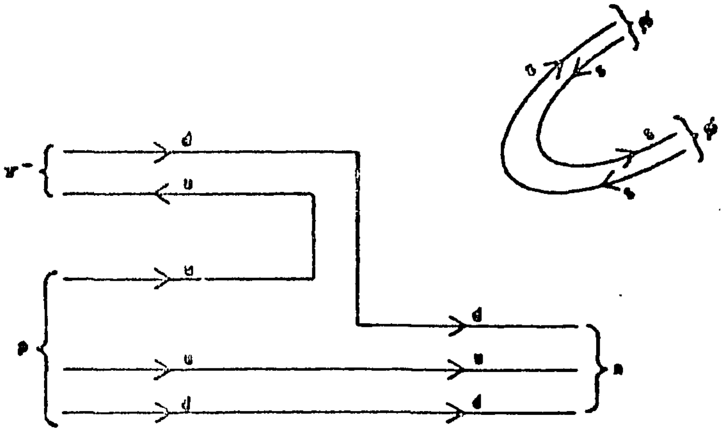

$\pi^- p \longrightarrow \phi \phi n$

Fig. 1.5(c) The Zweig quark line diagram for the reaction $\pi^- p \rightarrow \phi\phi n$ which is disconnected (i.e. a double hair-pin diagram) and is OZI forbidden

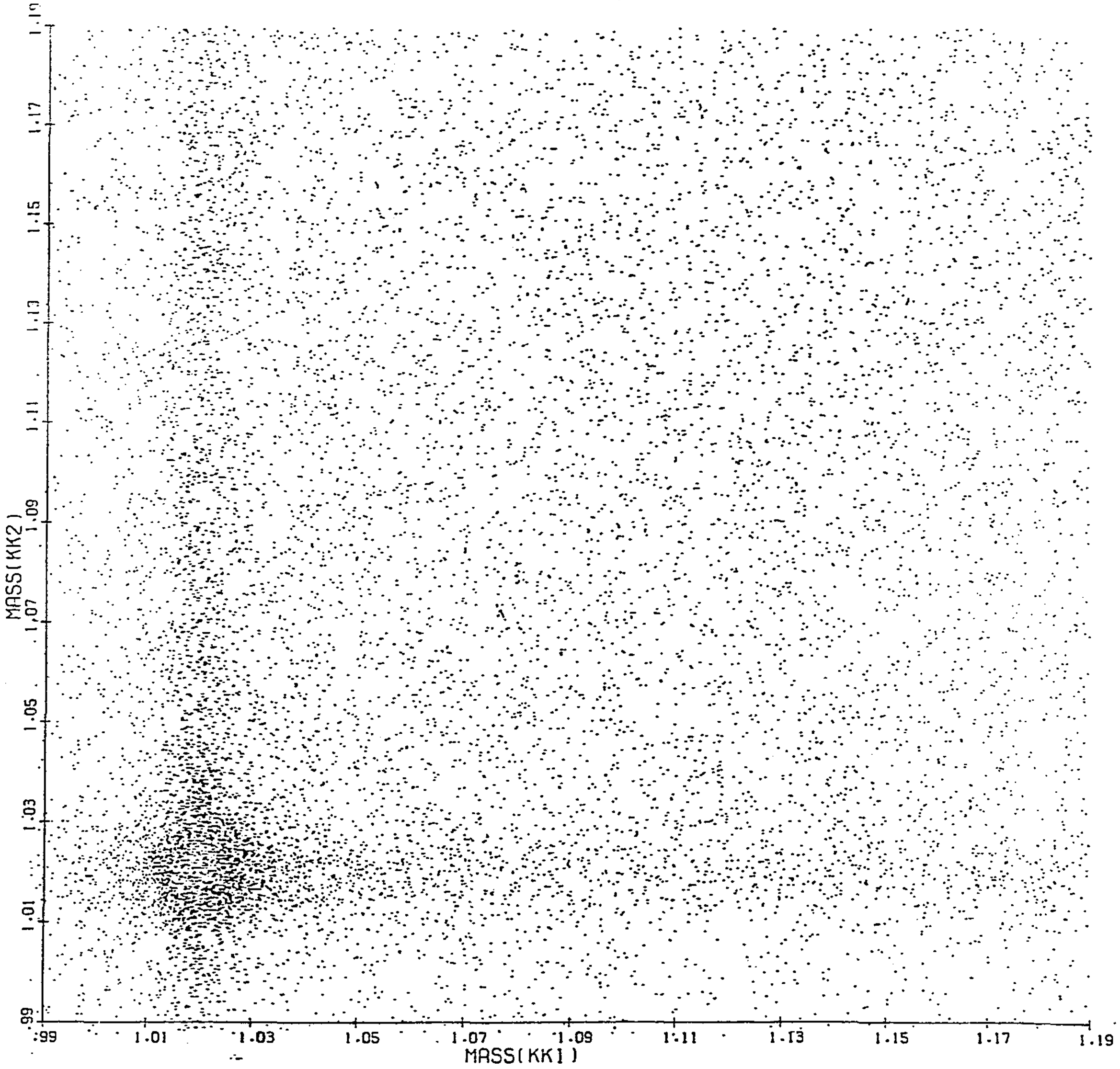

Fig. 1.6 A scatter plot of K^+K^- effective mass. Two randomly chosen mass combinations are plotted for each event. Clear bands of ϕ (1.020 GeV) are seen with an enormous enhancement (black spot) where they overlap

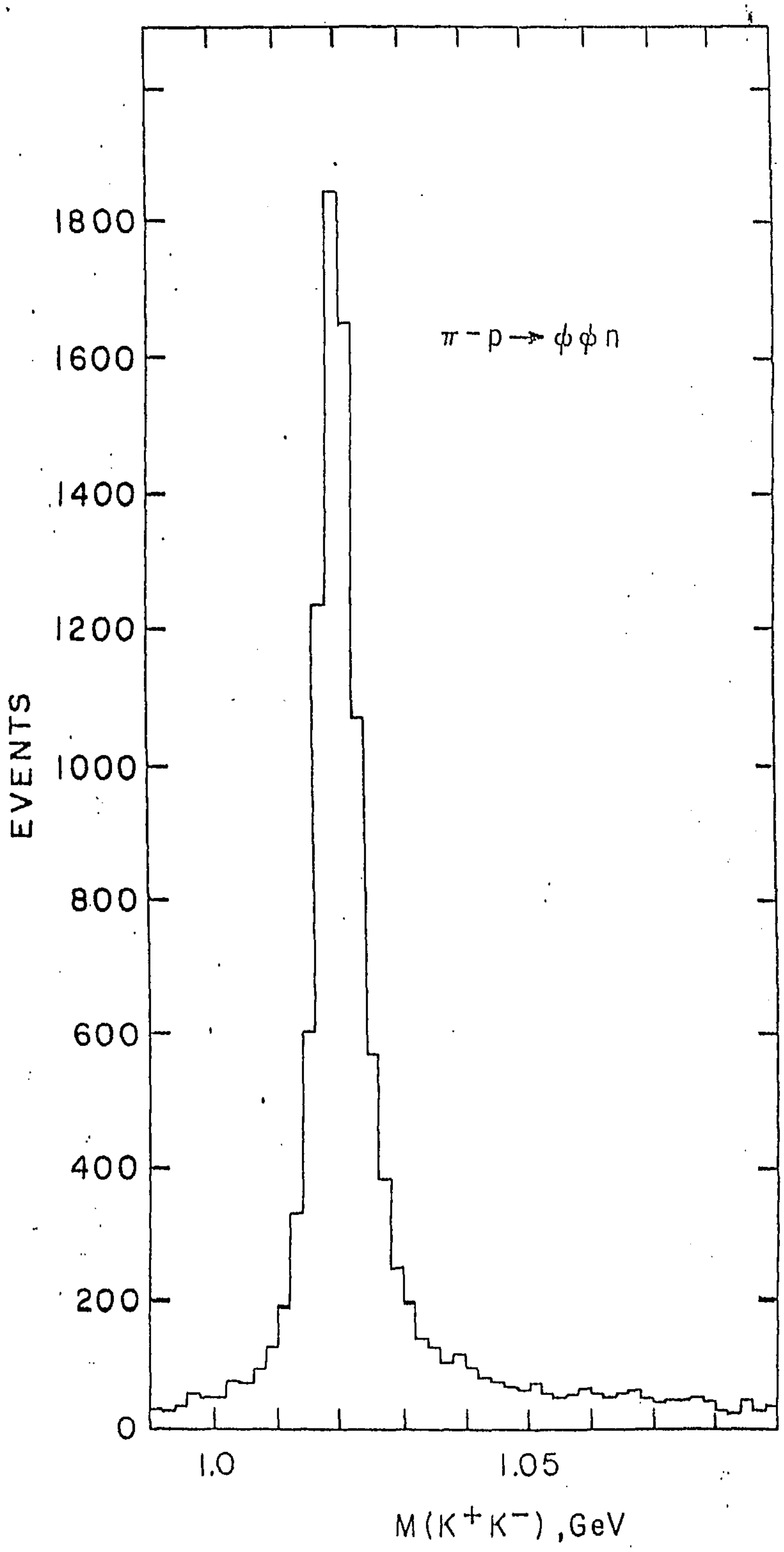

Fig. 1.7 The effective mass of each K^+K^- pair for which the other pair was in the ϕ mass band

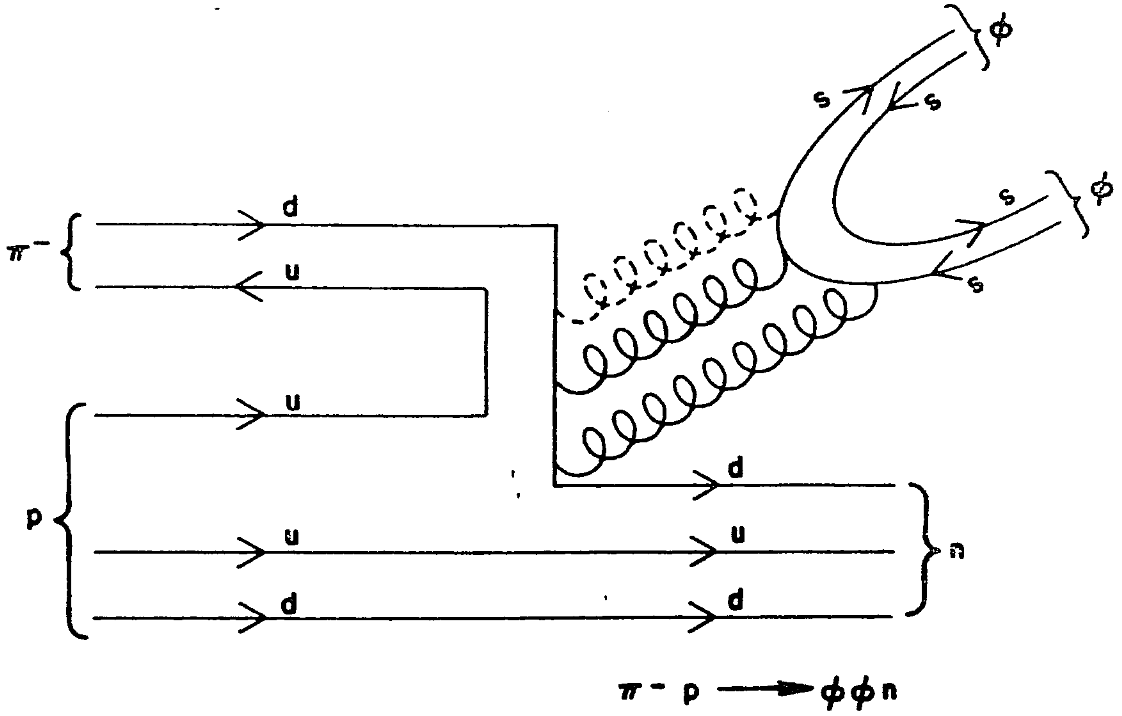

Fig. 1.8 The Zweig quark line diagram for the reaction $\pi^- p \rightarrow \phi\phi n$ which is disconnected (i.e. a double hairpin diagram) and is OZI forbidden. Two or three gluons are shown connecting the disconnected parts of the diagram depending upon the quantum numbers of the $\phi\phi$ system.

CHAPTER 2: METHODS AND FORMULAE OF THE PARTIAL WAVE ANALYSIS

2.1 Introduction

In this chapter we present an outline of the methods and the formulae related to the partial wave analysis. Since the underlying theory of the partial wave analysis is a well-developed subject,[34] it is beyond the interest of the present work to elaborate the mathematical formulations and the complexities of the various models being used here, such as the isobar model[35] and the K-matrix formalism.[36]

To extract the useful information out of the data, the analyzing program proceeds in two steps.

a. The initial step consists of the use of the isobar model formalism together with the maximum likelihood method which enable us to search for the dominant waves associated with the $\phi\phi$ data. In addition, the isobar model also makes measurements of the production amplitudes of the partial waves found by this method.

b. The next step is a fitting procedure which applies the K-matrix formalism to fit the production amplitudes with Breit-Wigner type of resonances. To achieve a good fit it is necessary to make a series of trials beginning with just one-pole K-matrix fit and the fitting procedure is terminated when the χ^2 calculation is not significantly improved with further addition of poles. The resonance parameters can be readily derived as a result of this fitting process.

The remainder of the chapter deals with each formalism in turn.

2.2 The Isobar Model Formalism

2.2.1 Historical Review

The isobar model was originally proposed by Lindenbaum and Sternheimer[37] to describe the pion-nucleon elastic scattering $\pi N \rightarrow \pi N$.

Phenomenologically, it assumes that single pion production takes place via production and subsequent decay of I = J = 3/2 nucleon isobar. According to this model the isobar is produced due to the incoming pion scatters off the incoming nucleon and the isobar later decays into a nucleon and a pion. Such a description successfully accounts for the above observed process.

2.2.2 The Generalized Isobar Model

The present version of the isobar model[35] is generalized to include several resonances with interference effects such as the spins and polarization. It considers specific three-body final state as a superposition of two-body states, each involving an isobar and a spectator particle. The amplitude for the reaction of interest is written as a product of two parts: the first part is an amplitude to form from a particular incoming partial wave an intermediate state consisting of a stable particle and a resonance, and the second part is the amplitude for propagation and decay of the resonance into the other two particles. In this framework it assumes the decay amplitudes of the resonance as fixed quantities but the production amplitudes for the intermediate state are the variable quantities to be determined by the fitting procedure.

In actual practice, in order to make our four-body ($K^+K^-K^+K^-$) final state fits with this three-body formalism, it was necessary for us to modify the original isobar model program. Initially we treated one of the two ϕ's as a stable particle and the other ϕ as a resonance which decayed into K^+K^-, after that we considered the decay of the stable ϕ to complete the process.

2.2.3 Labeling Scheme

To facilitate the partial wave analysis we have adopted a labeling scheme to our isobar model so that each partial wave associated with the $\phi\phi$ system is characterized by a set of quantum numbers. The complete notation for any partial wave is consistently represented by J^PLSM^η with $I = 0$ and $C = +$ identically. The meanings of these variables are explained in Table 2.1.

In addition, a schematic diagram of the isobar model which describes the reaction $\pi^-p \to \phi\phi n$ via an intermediate resonance state and decays to three-body ϕK^+K^- state is depicted in Fig. 2.1. In a separate drawing of this diagram the decay of the stable ϕ is also indicated.

TABLE 2.1

Definition of quantities for the partial wave labeling scheme and of the isobar model for the process $\pi^-p \to \phi\phi n$ in the $\phi\phi$ rest frame.

$W_{\phi\phi}$ = effective mass of $\phi\phi$ system

J = total angular momentum

P = parity

L = relative orbital angular momentum between the spectator ϕ and the isobar ϕ.

S = total intrinsic spin

M = z-component of J

η = reflection parity which corresponds to exchange naturality at high energy.

I = isospin of $\phi\phi$

ω = isobar or diparticle mass.

2.2.4 Definition of Decay Angles and Reference Systems

In our experiment we have measured the four momenta, $\vec{P}_{K_1^+}$, $\vec{P}_{K_1^-}$, $\vec{P}_{K_2^+}$, $\vec{P}_{K_2^-}$ of the four final state kaons in reaction A.1 at 22.6 GeV/c in the laboratory frame. In order to describe the sequential decay amplitude assumed in the isobar formalism, a full description of the $\phi\phi$ decay amplitudes and production cross section requires the use of two reference frames in which a set of six independent angles (γ, β, α_1, α_2, θ_1, θ_2) are defined.

To specify the orientations of the incident pion, proton and the recoiled neutron, the usual Gottfried-Jackson frame (t-channel) is employed. This frame (unprimed system) is defined in the rest frame of the $\phi\phi$ system (Fig. 2.2) in which γ and β are specified as the azimuthal and polar angles for each ϕ. The axis of the G-J frame are chosen such that the z-axis is given by the direction of the incoming π^-, the Y-axis defined by the proton momentum ($\vec{P}$) cross the neutron momentum ($\vec{N}$).

Another frame of reference (primed system) is defined in the rest frame of each ϕ (ϕ_1 or ϕ_2). Figure 2.3 shows the case for the rest frame of ϕ_1. In this ϕ_1 stationary frame, the momentum vector of the other $\phi(\vec{P}_{\phi_2})$ is fixed in the negative direction of the z'-axis while the x'-axis lies in the (z, z') plane. To account for the decay of ϕ_1 the decay angles of the daughter particle K_1^+ are used. In this case α_1 and θ_1 represent the usual azimuthal and polar angles measured in this frame. There is a similar rest frame (not shown) for the second ϕ (ϕ_2) with corresponding polar angle θ_2. Since the azimuthal angles are the same in either rest frame, α_2 is also shown in Fig. 2.3.

These frames are related by some rotations which preserve J but mixes M, and in addition, the helicity formalism developed by Jacob and

Wick[38] can be conveniently incorporated into the present isobar model with this choice of coordinates.

2.2.5 Basis Vectors and the Differential Cross Section

The angular dependences of the various physical quantities of interest, such as the differential cross section and loglikelihood function used for the fitting purpose, can be conveniently expressed in terms of an expression defined as basis vector. Each basis vector $G^{J^PLSM^\eta}$ (γ, β, α_1, α_2, θ_1, θ_2) is designated by a set of six quantum numbers J^PLSM^η (=j) as defined in Table 2.1.

Within the framework of the isobar model and the helicity formalism, the explicit form of the basis vector[29d] corresponding to a particular set of j is given by

$$G^{J^PLSM^\eta}(\gamma,\beta,\alpha_1,\alpha_2,\theta_1,\theta_2) = \text{Real}\;\Big[\frac{(1-i)-\eta(1+i)}{2}$$

$$\sum_{\mu,\lambda} C(1,1,S/\mu,-\lambda)\;\; C(L,S,J/0,\mu-\lambda)\;\; e^{iM\gamma}\;\; e^{i\mu\alpha_1}\;\; e^{i\lambda\alpha_2}$$

$$d^J_{M,\mu-\lambda}\,(\beta)\;\, d^1_{\mu,0}\,(\theta_1)\;\, d^1_{\lambda,0}\,(\theta_2)\Big] \tag{2.1}$$

where μ,λ = helicities of the ϕ's which have three values, 1, 0 or −1;

C = Clebsch-Gordon coefficients.

The real and imaginary parts of the basis vector obtained by substituting η = −1 or +1 into Expression 2.1 correspond to the unnatural or natural waves.

The complete set of the basis vectors provides a means to determine the relative amounts of the partial waves associated with these vectors in describing the experimentally measured angular distributions. To accomplish this goal, the differential cross section is expressed as an absolute square of the sum of all available basis vectors, each weighed by a parameter $A_{J^PLSM^\eta}$ to be determined by a fitting procedure using maximum likelihood techniques. Hence the differential cross section is given by

$$\frac{dI(\Omega)}{d\Omega} = \left|\sum_{J^PLSM^+} A_{J^PLSM^+} G^{J^PLSM^+}(\Omega)\right|^2 + \left|\sum_{J^PLSM^-} A_{J^PLSM^-} G^{J^PLSM^-}(\Omega)\right|^2 + \left|A_B\right|^2 \qquad (2.2)$$

where $\Omega = (\gamma, \beta, \alpha_1, \alpha_2, \theta_1, \theta_2)$. Since different natural exchanges do not interfere so Eq. 2.2 is expressed as a sum of two absolute squares contributed independently by natural and unnatural waves. The last term in Eq. 2.2 is responsible for background which is consistent with no structure.

2.2.6 Maximum Likelihood Method

In order to determine quantitatively the fitting parameters $A_{J^PLSM^\eta}$ a standard maximization procedure[39] is followed. In our case, this maximization is done by maximizing a loglikelihood function (log L) defined by Eq. 2.4.

To include the acceptance bias of the apparatus into the probability calculation an acceptance normalization integral (M_{jk}) is introduced:

$$M_{jk} = \int G_j\, G_k\, a(\Omega)\, d\Omega \qquad (2.3)$$

where $a(\Omega)$ is the acceptance of the apparatus given by the program. These matrix elements (M_{jk}) are determined by integrating over the phase space generated $\phi\phi n$ events, produced and detected in the Monte Cárlo simulation of our MPS apparatus. This matrix is an essential ingredient in determining the fitting parameters A_j.

The loglikelihood function is defined as

$$\log L = \sum_{i=1}^{\text{events}} \log I(\Omega_i) - \sum_{j,k} A_j M_{jk} A_k \qquad (2.4)$$

where j and k represent the six quantum numbers J^PLSM^η. Since log L is related to the cross section $[I(\Omega_i)]$ by a summation over all events, the loglikelihood value obtained from Eq. 2.4 in general increases with the increasing statistics. Furthermore, the way that log L is defined permits the loglikelihood values corresponding to a set of coupled waves calculated in different mass regions to be combined by simple addition. Thus for a mass spectrum which is divided up into a number of small bins, the log L value for a continuous solution corresponding to this spectrum can be obtained as a sum due to the individual bins.

2.3 K-Matrix Fits and Breit-Wigner Parameters

2.3.1 General Description

The present study considers a situation in which there are several overlapping resonance states. The T-matrix approach to this problem has encountered the difficulty in solving the constraints imposed by unitarity on the resonance parameters because the constraints are complicated non-linear conditions. In this connection, the use of the K-matrix is a simple way to satisfy the constraints of unitarity, and the existence and properties of the K-matrix can be established on rather general grounds.

In our analysis we adopt a K-matrix formalism proposed by Aitchison[36b] which combines a more general production mechanism with resonance propagation. This K-matrix approach which is a natural generalization of the Watson theorem, suitably parameterized with real poles and complex production vector, can be used to fit the previous isobar model amplitudes. As a result of this fit, the desired resonance parameters such as widths, masses and coupling signs for the resonances can be subsequently determined.

2.3.2 K-Matrix Formalism

At the outset, we present a brief description of the Watson theorem which is later generalized by Aitchison in his K-matrix formalism. According to this theorem the production amplitudes for the two-particle system can be described by a phase shift parameterization ($e^{i\delta}\sin\delta$) due to the propagation and decay of the intermediate state. In this approach, the production amplitude is made up by a product of two factors: one describes the production process and the other is a phase shift δ resulting from the scattering of the two-body intermediate state. The formation amplitude (W_f) is described by the two-body T-matrix

$$W_f = \frac{e^{i\delta}\sin\delta}{q^{\ell + 1}} \tag{2.5}$$

In the standard K-matrix theory, the unitary two-body formation T-matrix is related to the intermediate resonance states described by the K-matrix

$$T = (1 - iK)^{-1} K. \tag{2.6}$$

An elegant interpretation of this expression is that the first factor of Eq. 2.6 describes the propagation of the intermediate states while the K term governs the formation and decay of these states.

Even the K-matrix poles developed in the above formulation could satisfactorily account for the normal resonance phenomenon, Eq. 2.6 is incapable of describing effects such as Deck mechanism[40] which involves double particle exchange. In this respect, Aitchison was able to achieve a more general formulation of the production amplitudes which combines production mechanism like the Deck effect with resonance propagation. To this end, a P vector is introduced to replace the K term in Eq. 2.6 so that other participations in the production mechanism are also included. Thus Eq. 2.6 is generalized by the expression

$$T = (1 - iK)^{-1}\,P \tag{2.7}$$

The explicit forms of the K-matrix and the P vector are as follows:[41]

(a) For a K-matrix, for n-poles formed in channel α and decaying into channel β, is given by

$$K_{\alpha\beta} = \sum_{j=1}^{n} \pm \frac{(m_j\Gamma_{j\alpha})^{1/2}\,(m_j\Gamma_{j\beta})^{1/2}}{m_j^2 - S} \tag{2.8}$$

where the ± signs depend on the signs of the couplings.

(b) The P vector is defined by

$$P_\beta = \sum_{j=1}^{n} \frac{C_j(m_j\Gamma_{j\beta})^{1/2}}{m_j^2 - S} \tag{2.9}$$

where C_j is a complex number which characterizes the production strength and phase of the intermediate state.

Each pole in the K-matrix has decay probabilities into a 2^{++} channel. The partial width of each decay channel is given by

$$\Gamma_{ja} = q_{\phi\phi}\,B_a(q_{\phi\phi}^2)\,\gamma_{ja}^2 \tag{2.10}$$

where $q_{\phi\phi}$ is the CMS momentum of ϕ, γ_{ja} is the coupling constant and $B_a(q_{\phi\phi}^2)$ is the Blatt-Weiskopf barrier factor using one Fermi length of interaction.

To obtain the relationship between the K-matrix poles and Breit-Wigner resonance parameters, the following symbols are defined:

$$U_{ja} = \sqrt{q_{\phi\phi}\, B_a(q^2_{\phi\phi})}\ \gamma_{ja} \tag{2.11}$$

$$\Gamma_{ja} = U^2_{ja} \tag{2.12}$$

$$\Gamma_j = \sum_a \Gamma_{ja} \tag{2.13}$$

$$D_j = m_j^2 - s - i\Gamma_j \tag{2.14}$$

$$D_{jK} = i \sum_a U_{ja} U_{Ka} \tag{2.15}$$

Following the approach pursued by Goebel and McVoy,[42] the multichannel resonance is given in the form

$$T^R_{ab} = \frac{m\Gamma_a^{1/2}\ \Gamma_b^{1/2}\ e^{i\theta a}\ e^{i\theta b}}{m^2 - s - im\Gamma} \tag{2.16}$$

where $\Gamma = \sum_a \Gamma_a$, θ_a and θ_b are functions of energy and depend on background parameterization.

The corresponding partial widths and phase information for two and three K-matrix poles have been worked out in detail and reproduced below.

For two K-matrix poles, parameters for the second poles is given by

$$m^2 - s - im\Gamma = D_2 - \frac{D_{12}^2}{D_1} \tag{2.17}$$

$$\Gamma_a = \left| U_{2a} + \frac{D_{12} U_{1a}}{D_1} \right|^2 \tag{2.18}$$

$$e^{i\theta a} = \frac{(U_{2a} + D_{12}U_{1a}/D_1)}{U_2 + D_{12}U_{1a}/D_1} \tag{2.19}$$

and for three K-matrix poles parameters for the third pole is given by

$$m^2 - s - im\Gamma = D_3 - \frac{D_1D_{23}^2 + D_2D_{13}^2 + 2D_{12}D_{23}D_{13}}{D_1D_2 - D_{12}^2} \qquad (2.20)$$

$$\Gamma_a = \left|U_{3a} + \left\{\frac{D_1D_{23} + D_{12}D_{13}}{D_1D_2 - D_{12}^2}\right\} U_{2a} + \left\{\frac{D_2D_{13} + D_{12}D_{23}}{D_1D_2 - D_{12}^2}\right\} U_{1a}\right|^2 \qquad (2.21)$$

$$e^{i\theta_a} = \frac{U_{3a} + \left\{\frac{D_1D_{23} + D_{12}D_{13}}{D_1D_2 - D_{12}^2}\right\}U_{2a} + \left\{\frac{D_2D_{13} + D_{12}D_{23}}{D_1D_2 - D_{12}^2}\right\}U_{1a}}{\left|U_{3a} + \left\{\frac{D_1D_{23} + D_{12}D_{13}}{D_1D_2 - D_{12}^2}\right\}U_{2a} + \left\{\frac{D_2D_{13} + D_{12}D_{23}}{D_1D_2 - D_{12}^2}\right\}U_{1a}\right|} \qquad (2.22)$$

To obtain parameters for other poles cycle through change 1 → 2, 2 → 3, 3 → 1.

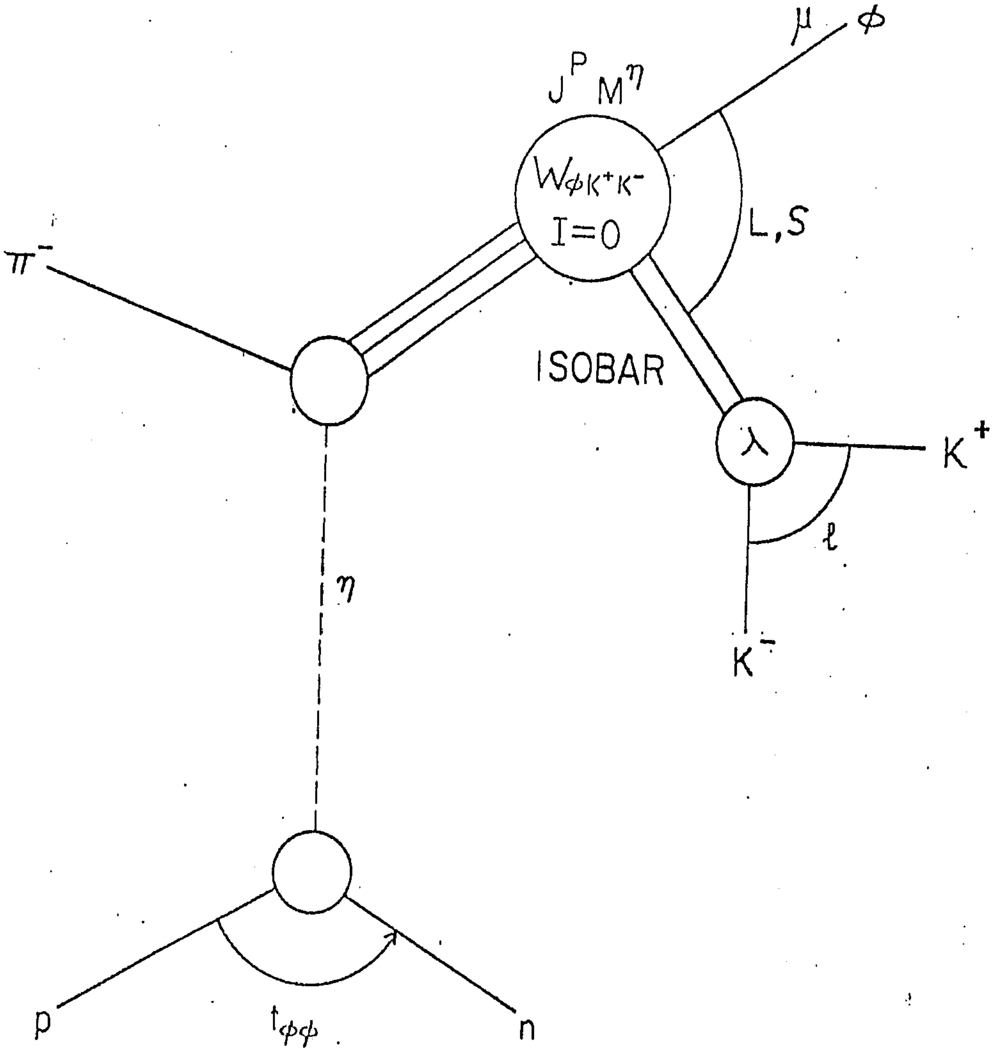

Fig. 2.1 Schematic diagram describing the Isobar model for ¶$^-$p$\rightarrow$ØØn. The variables are described in the text.

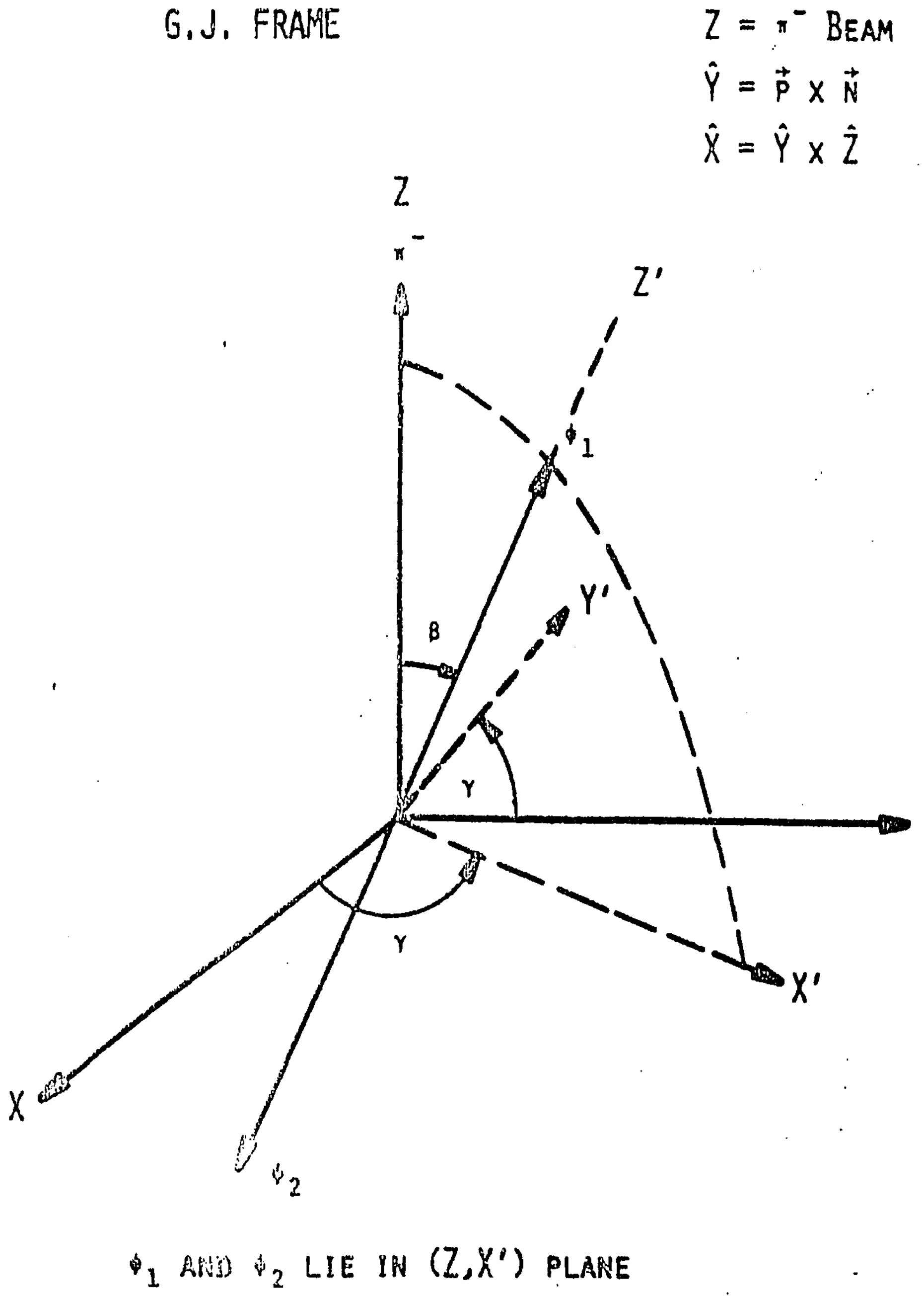

Fig. 2.2 The Gottfried-Jackson frame with polar angle β and azimuthal angle γ.

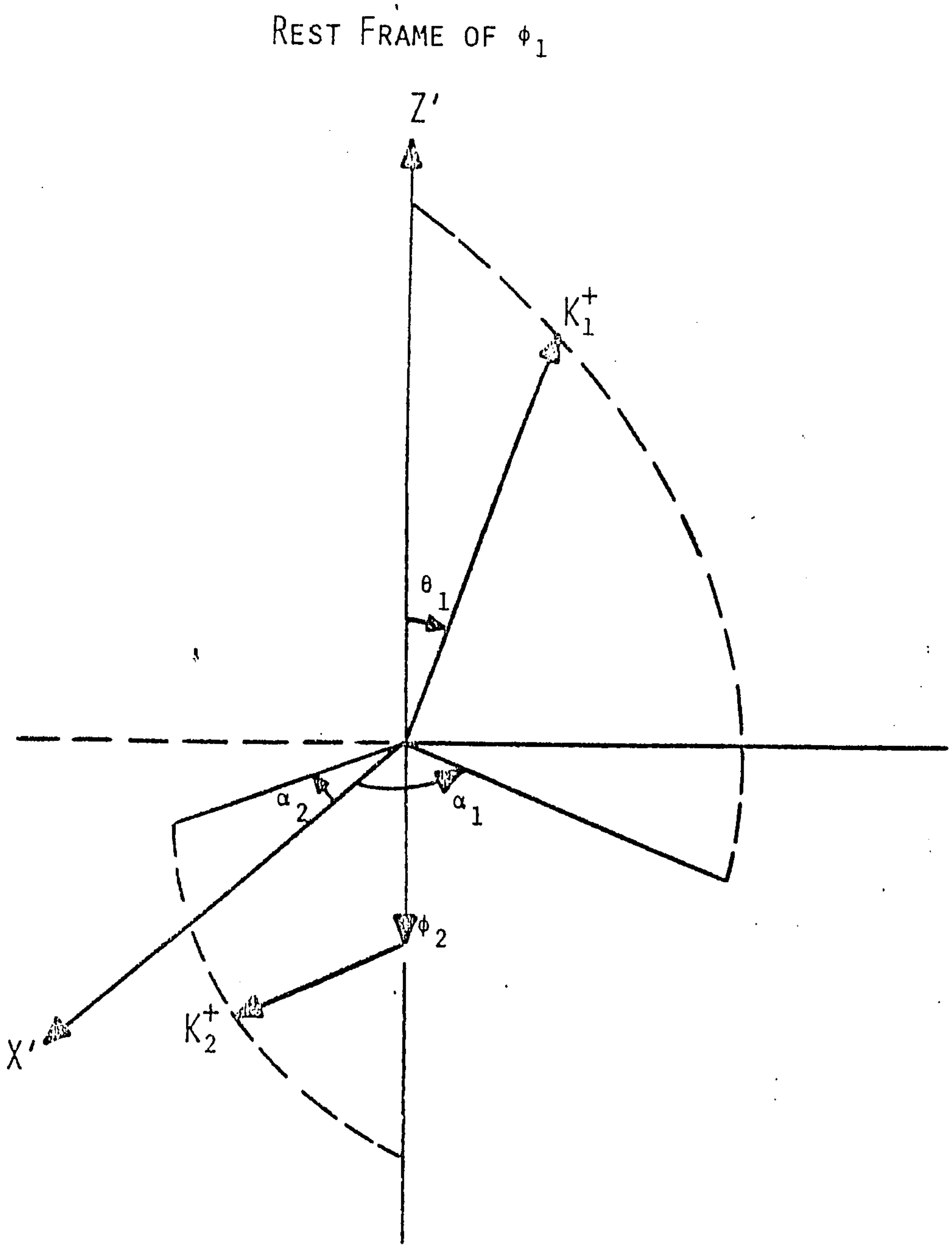

Fig. 2.3 The ϕ_1 rest frame with the polar angle θ_1 of the decay K_1^+ (relative to ϕ direction) and the azimuthal angle α_1 of the decay K_1^+.

CHAPTER 3: EXPERIMENTAL APPARATUS

In this chapter we present the essential features of the experimental apparatus which are relevant to the present study of the experiment. This includes a general description of the incident beam transport system, the main spectrometer with the associated trigger devices, the data handling system and on-line computer monitoring of the experiment.

3.1 Incident Pion Beam

The experiment was performed in the Multiparticle Spectrometer Facility using the A1 secondary beam produced by the Alternating Gradient Synchrotron. At the AGS, protons were accelerated up to 28.5 GeV with a circulating beam intensity of ~ 10^{13} protons per pulse. Each accelerating cycle required 2.2 seconds with a beam spill 0.8 seconds in duration. Protons from the AGS were focused at the A line platinum target which produced secondary particles and were transported to the experimental areas such as MPS. The negative beam consisted of 99.8% of pions and 0.2% of kaons and antiprotons.

The main objective of the beam transport system, shown in Fig. 3.1, was to select negative particles of 22.6 Gev/c momenta and to focus and steer the beam onto the liquid hydrogen target at the MPS. To this end, the various components of the beam system performed the following functions:

(a) The secondary beam produced at 0° of the A station target of the AGS slow-extracted beam was focused by quadrupole magnets Q_1 through Q_4 onto the horizontal and vertical collimators.

(b) The horizontal collimator of C was an adjustable slit which determined the acceptance of the beam intensity.

(c) The dipoles D_1 and D_2 which formed a pair of bending magnets were used to select particles with the desired beam momentum, since the momentum was inversely proportional to deflection.

(d) Quadrupoles Q_5 and Q_6 acted as two field lenses which refocused the beam while it emerged from the collimator as well as after it was deflected through a successive bending of three dipoles D_3 - D_5.

(e) Q_7 and Q_8 formed a pair of quadrupole doublets which focussed the beam both horizontally and vertically before it was momentum analyzed.

(f) The aligned proportional wire chambers A_1 through A_4 together with the measured deflection of the particles in the known field of six bending dipoles D_6 through D_{11} served as a spectrometer which provided a precise measurement of the beam momentum.

(g) Q_9, Q_{10}, Q_{11} focussed the beam onto the liquid hydrogen target at the MPS. The spot size of the beam at the center of the target was 2 cm x 4 cm.

(h) The tracks of the beam particles were identified by four scintillation counters S_1, S_2, S_3, S_4 in coincidence and two ring veto counters S_5 and S_6 rejected the beam from the beam halo.

(i) Two beam PWC's, A_5 and A_6 determined the position and direction of each particle as it entered the MPS magnet.

(j) Two threshold Cerenkov counters C_1 and C_2 in coincidence were used to select pions and eliminated kaons and antiprotons. Separation efficiency for π^-'s from K^- and $\bar{p}$'s was better than 99.9%.

A good beam particle was defined as $SH\overline{A}\pi$, where:

$$S = S_1 \cdot S_2 \cdot S_3 \cdot S_4$$

$$H = A_1 \cdot A_2 \cdot A_3 \cdot A_4 \cdot A_5 \cdot A_6$$

$$\overline{A} = \overline{S_5} + \overline{S_6} + (\overline{A_{1x} \geq 2}) + (\overline{A_{2x} \geq 2}) + (\overline{A_{3x} \geq 2}) + (\overline{A_{4x} \geq 2}) + (\overline{A_{5x} \geq 2}) + (\overline{A_{5y} \geq 2}) + (\overline{A_{6x} \geq 2}) + (\overline{A_{6y} \geq 2})$$

$$\pi = C_1 \cdot C_2$$

in which $A \cdot B$ stands for a coincidence between A and B, and $A + B$ stands for "OR" between A and B. Here S's stand for the signals from the corresponding scintillation counters. A's for those of the beam PWC's (A_1 through A_4 each consisted of two x planes, whereas A_5 and A_6 each consisted of two x planes and two y planes), and C's for the Cerenkov counters. $\overline{A_{nx} \geq 2}$ stands for vetoing events with two or more hits detected by the x plane of the n'th beam PWC.

The beam momentum resolution was 0.75%.

3.2 Main Spectrometer (MPS II)

The Multiparticle Spectrometer is the laboratory's major spectrometer facility which provides BNL's user community with a large aperture spectrometer suitable for handling high energy interactions with multiparticle final states. This detector system has demonstrated to possess good momentum and angular resolutions as well as high data rate capability.

3.2.1 MPS I Improvement (MPSII)

The present experiment made use of the MPS II detector which represented an improved experimental setup as compared to those used in the MPS I experiment.

The spectrometer was upgraded in two areas: the major change was the replacement of all the MPS I spark chamber detectors by narrow-cell drift chambers.[43] The chambers have ten times more data-gathering rate capability than the MPS I detector and with better resolution than the spark chambers. The second change was the use of an improved veto box to detect large-angle charged particles or photons from the target.

With these improvements MPS II could eliminate the pathological effects caused by the spark chambers: E x B effect, spurious sparking and refiring, old event tracks. In addition, the efficiency of these new chambers was greater than 98%.

Moreover, the event reconstruction time was substantially reduced by providing point-plus-slope information on tracks in each detector module. In Table 3.1 we compare the performance between MPS I and MPS II.

Table 3.1

Comparison of performance between MPS I and MPS II

	MPS I	MPS II
Resolving time	3 μs	< 70 ns
Position resolution	700 μm	200 μm
Trigger event deadtime	30 ms	< 1 ms
Typical event size (tracking detector)	550 bytes	280 bytes

3.2.2 Experimental Setup

A schematic layout of the MPS II is shown in Fig. 3.2. The major part of the spectrometer is a magnet with a very open structure (Fig. 3.3). Inside the large field volume, a liquid H_2 target surrounded by the veto counter was placed near the upstream magnet entrance. This was followed by a set of modular drift chambers which effectively gave a good multiparticle handling capability for particle trajectory detection. These chambers were capable of handling beam rates of several million particles per pulse and with a spatial resolution of the order of 200 μm. Cathode readout could provide unique three-dimensional points for each track. In addition, several proportional chambers (TPX's) and scintillation counter hodoscopes were connected with a programmable combinational logic system RAM for trigger purposes. A threshold gas Cerenkov counter was used for particle identification, i.e. mainly to distinguish between the π's and K's. Beyond the magnet a pair of hodoscopes (H5) completed the downstream system.

In addition to the basic detectors, the MPS is outfitted with special electronics like the detector readout electronics, data acquisition and recording devices and the on-line computer PDP10.

(a) MPS magnet

The main feature of the spectrometer was a large momentum analyzing magnet with an active magnetic volume 1.2m × 1.8m × 4.6m. All of the magnetic return yoke was one side, leading to a very open C-shaped aperture. During the course of the experiment the central field of the magnet was set at 5 KG which was half the value of the full field. An accurate measurement of the track momentum considered the nonuniformity of the magnetic field. The corrections for the approximate momentum assuming a uniform magnetic field was done by evaluating a polynomial with 216 coefficients as a function of the positions and angles. The resultant momentum accuracy was better than 0.2%.

(b) Target and Target Veto Counter

The fixed target liquid H_2 in use was encapsuled in a cylindrical cell 61 cm long and 7.6 cm in diameter. The entire unit was placed in a cylindrically shaped vacuum jacket with mylar windows at each end and surrounded by 40 layers of aluminized mylar for superinsulation of the cell. During each AGS spill about 6% of the incident beam produced interactions in the target.

To identify a recoil neutral which was produced in an interaction, use was made by a veto counter surrounding the target. For an improved acceptance, the present veto counter was reconstructed to detect the large recoil angle. Its basic structure consisted of sheets of scintillator interleaved with lead sheets to detect recoil charged particles and convert neutral. There were four such multilayer counters surrounding the target with each one connected with a photomultiplier. A scintillator layer was placed on each inner-most surface to detect low energy charged particles. Events with the recoil particles (charged and γ's) were vetoed by this lead-scintillator sandwiched counter.

(c) Drift Chambers

There were seven drift chamber modules with cathode readout placed in the MPS magnet. Each module contained 15 wire planes and one window frame all of which were stacked up on a 3/4" thick aluminum base to form a detector. The compact drift cell (~ 3 mm) had a linear drift time vs. distance even in a maximum field of the MPS magnet (10 KG). The spatial resolution was 200 μm.

The construction of main drift chamber modules is shown in Fig. 3.4. A complete module had 3 X-measuring planes and 2 Y-measuring planes. One of the X-planes was displaced in half gap from the other two.

This arrangement permitted us to resolve the left-right ambiguity inherent in multi-wire drift chambers. These modules also had U-V planes with anode wires ± 30° to Y. Therefore locally within a module it was possible to reconstruct three-dimensional vectors of the particle track. The point-slope vectors greatly reduced the combinational problem that was encountered in high track multiplicity pattern recognition. Among a number of possible vectors formed in a module, the correct vectors were selected by matching with the vectors in adjacent modules. The gas used in the chambers was a mixture of 78% A, 15% CO_2, 5% C_4H_{10} and 2% dimethoxymethane. Tests made on these gases gave good efficiency characteristics and linearity in drift velocity.

In order to handle signals from as many as 20,000 sense wires and cathode readout strips, the MPS had developed three integrated circuits, i.e. an amplifier, a discriminator and a digital-time encoder. These circuits provided us with a threshold of approximately 2.5 μamp, ~ 1 μsec delay for trigger information, and time digitization with 4 ns time quantization. The digital delay and time encoder was made from a static 256-bit shift register which could be clocked at an effective speed of 250 MHz. In this system the clock kept running, shifting the input from the discriminator continually down the register. When a desired event occurred, the clock stopped 256 clock cycles after a time $t = 0$; the data in a higher segment of the register was read out which contained the time information and then the clock was restarted to shift in new data.

(d) Proportional Wire Chambers (PWC)

Two multiwire proportional chambers were used in the main spectrometer and had vertical sense wires only, spaced 10 per inch. The output from each chamber was proportional to the number of hits for any one event. This determined the track multiplicity at each chamber and thus could be used for the trigger purpose.

(e) C6 Gas Threshold Cerenkov Counter

The C6 Cerenkov counter was used as an overall veto and had a 95% measured efficiency for rejecting any pion of momentum greater than 3.1 GeV/c. C6 was divided into 18 optically isolated cells. Each cell has an elliptical mirror and 6 phototubes attached to cone light collectors. Cerenkov light was reflected by the optical mirror into the photomultiplier tubes, and the signals were then amplified and discriminated. The counter was filled with Freon 114 and had a pion threshold momentum of 2.8 GeV/c.

(f) H5 Scintillation Hodoscope

Scintillation counter hodoscope H5, which was placed downstream of MPS, enabled us to trigger on charged multiparticle final states. H5 consisted of 112 plastic scintillation counters 6.5 cm wide and 214 cm in length. The counter was V-shaped and divided into two equal sections of 56 counters each at an angle of 172°.

3.3 Experimental Trigger

Our trigger design considered the topology of the events of interest which consisted of production vertex in the target with two pairs of outgoing charged kaons flying down the MPS. Under normal running conditions we confined the event triggers to 25 or less per pulse.

The trigger was basically to select events with three, four or five kaons produced in the liquid hydrogen target with at least one of each charge. In addition, it also required that only recoil neutral be detected at the production. To actually implement these selection criteria the set of central trigger devices installed at the MPS were made up by two multiplicity-counting proportional wire chambers (TPX2, TPX3), Freon 114 Cerenkov hodoscope with a threshold momentum 2.8 GeV/c (C6), scintillation counter hodoscope (H5) and a scintillation veto counter box (V). The kaon signature was a track emerging from the target and measured by two PWC's (TPX2 and TPX3) and H5 counter hodoscope with no signal from the corresponding cell in C6. A recoil neutral at the production vertex was identified by no signal coming from the target veto counter.

The above selection criteria were achieved using a special trigger system developed by the MPS group. This system used a fast random-access memory (RAM)[44] with two million bits in a 128 x 128 x 128 array. RAM represented a programmable logic system arranged as a three-dimensional lookup table. With the Monte Carlo simulated correlations, a set of three detector planes with momentum patterns stored in RAM memory could be used to select events with charged particles in a given range of angle and momentum, even in the presence of other particles. Thus each dimension represented one of the three trigger elements (TPX2, TPX3 and H5) with the memory preloaded to contain "ones" at all three-dimensional points satisfying chosen criteria. The detector outputs were strobed into a fast register which served to address the RAM's to see if any of the addressed combination contained logical "ones". Moreover, the RAM memory was divided into two sections to account for the positive and negative charge of kaons. In this way, we were able to determine the number of particles of each charge.

In terms of the conventional logic symbol, the above three-kaon exclusive trigger (3KE) can be described by

$$3\mathrm{KE} = \mathrm{S} \cdot \mathrm{H} \cdot \overline{\mathrm{A}} \cdot \overline{\mathrm{C6}} \cdot \overline{\mathrm{V}} \cdot (3 \leq \mathrm{TPX2} \leq 5) \cdot (3 \leq \mathrm{TPX3} \leq 5) \cdot$$

$$[(\mathrm{RAM}^{+} \geq 1) \cdot (\mathrm{RAM}^{-} \geq 2)\ \Lambda\ (\mathrm{RAM}^{+} \geq 2) \cdot (\mathrm{RAM}^{-} \geq 1)]$$

The significance of this notation for trigger system is as follows:

(a) An identified π^- incident upon the target and no signal from the beam veto counter ($S \cdot H \cdot \overline{A}$).

(b) At least one hit on both sides of the hodoscope H5 (H5E and H5W).

(c) For every hodoscope (H5) hit, an absence of light in the appropriate cells of the threshold Cerenkov counter C6 placed between the downstream magnet exit and the hodoscope, and filled with freon at one atmosphere pressure (in this way the trigger selected events producing a forward-going kaon with a momentum between 2.8 and 12.0 GeV/c or a forward-going proton or antiproton with momentum > 2.8 GeV/c).

(d) The absence of a signal from a system of scintillator-lead-scintillator sandwich counters (V) placed around the target on four sides to identify a recoil neutral.

(e) Three or four or five charged particles detected by two trigger PWC's (TPX2 and TPX3).

(f) The particles detected by trigger PWC's, with at least one of each charge, satisfied the pre-determined three-dimensional correlation matrix between TPX2, TPX3 and H5 stored in RAM memory.

During the expeirmental runs, this trigger system generally produced trigger rates on the order of one in approximately 200K pions. We recorded all together 2 million triggers in the two running periods.

3.4 Data Handling and Monitoring

The data handler consisted of the data acquisition electronics and a 16K-byte buffer memory of 18-bit bytes. During each AGS pulse this buffer memory was used to collect, format and store the information of each triggered event from the devices into the buffer by interrogating the corresponding device controller. The data were organized into groups, and these groups were separated from each other by special bytes called group words. The data handler communicated with each device through a device port. The group numbers represented the address of the device controllers connected with the device port. The group words were generated by the data handler to address the corresponding device controller. For each triggered event, the data from the different devices arrived into the buffer memory in an ordered sequence. These included the data from scintillation counter hodoscopes, proportional wire chambers, drift chambers, etc.

At the end of the AGS pulse, the data handling system accepted data from a buffer containing DVM readings taken immediately after the previous AGS spill, scalar readings and time information. The contents of the data handler memory were then recorded on magnetic tape and simultaneously transmitted to the PDP-10 (KL) of the Brookhaven On-Line Data Facility (OLDF). Only a sample of the events (~ 10%) could reach the computer which were then completely reconstructed on-line. In addition to analyzing events, the on-line program also executed its monitoring of the apparatus. This provided a comprehensive picture of the overall system performance and a powerful mechanism for detecting system malfunctions, should they occur.

All events, including those analyzed on-line, were later analyzed off-line by the CDC 7600 of the Brookhaven Central Scientific Computing Facility (CSCF).

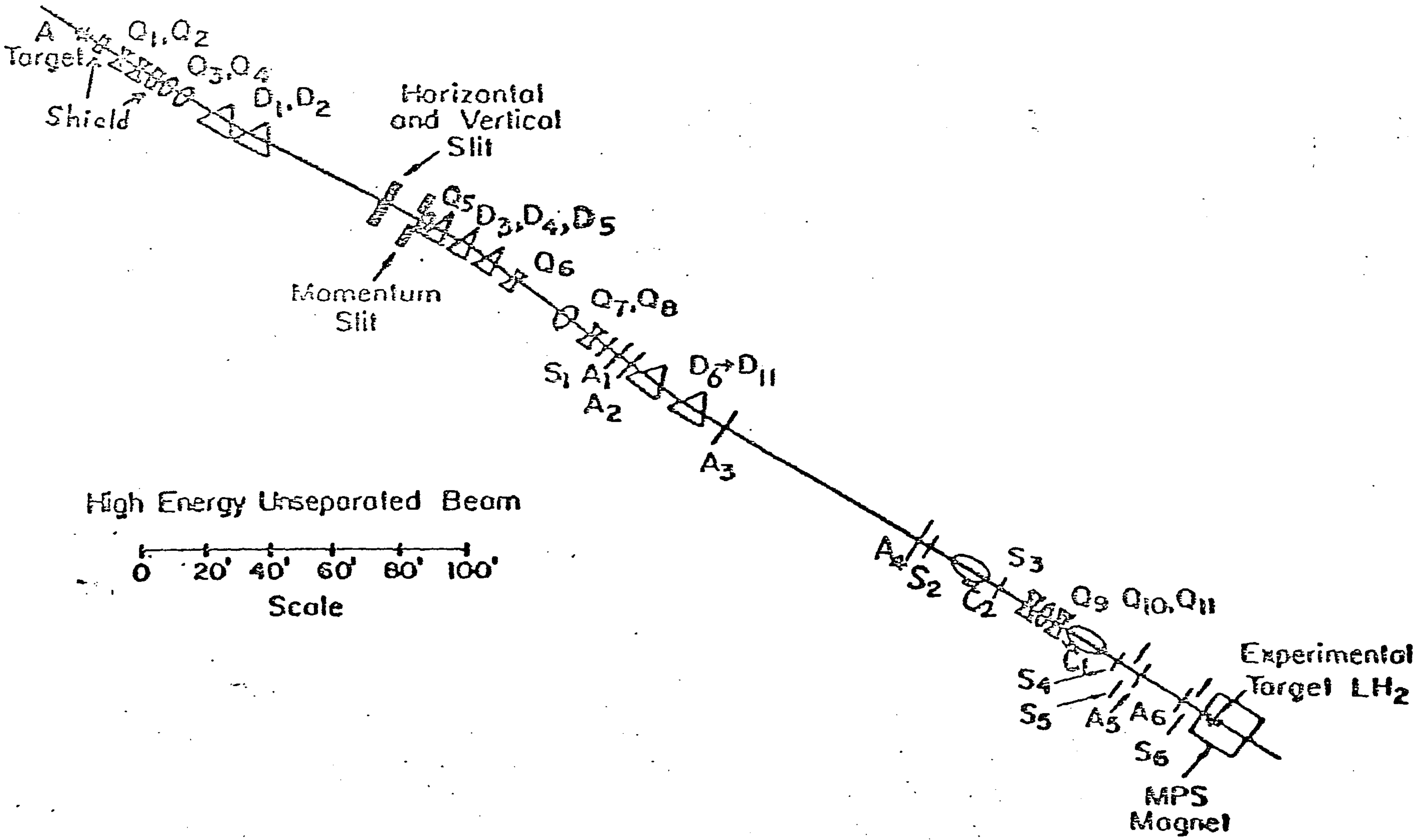

Fig. 3.1 Beam transport system.

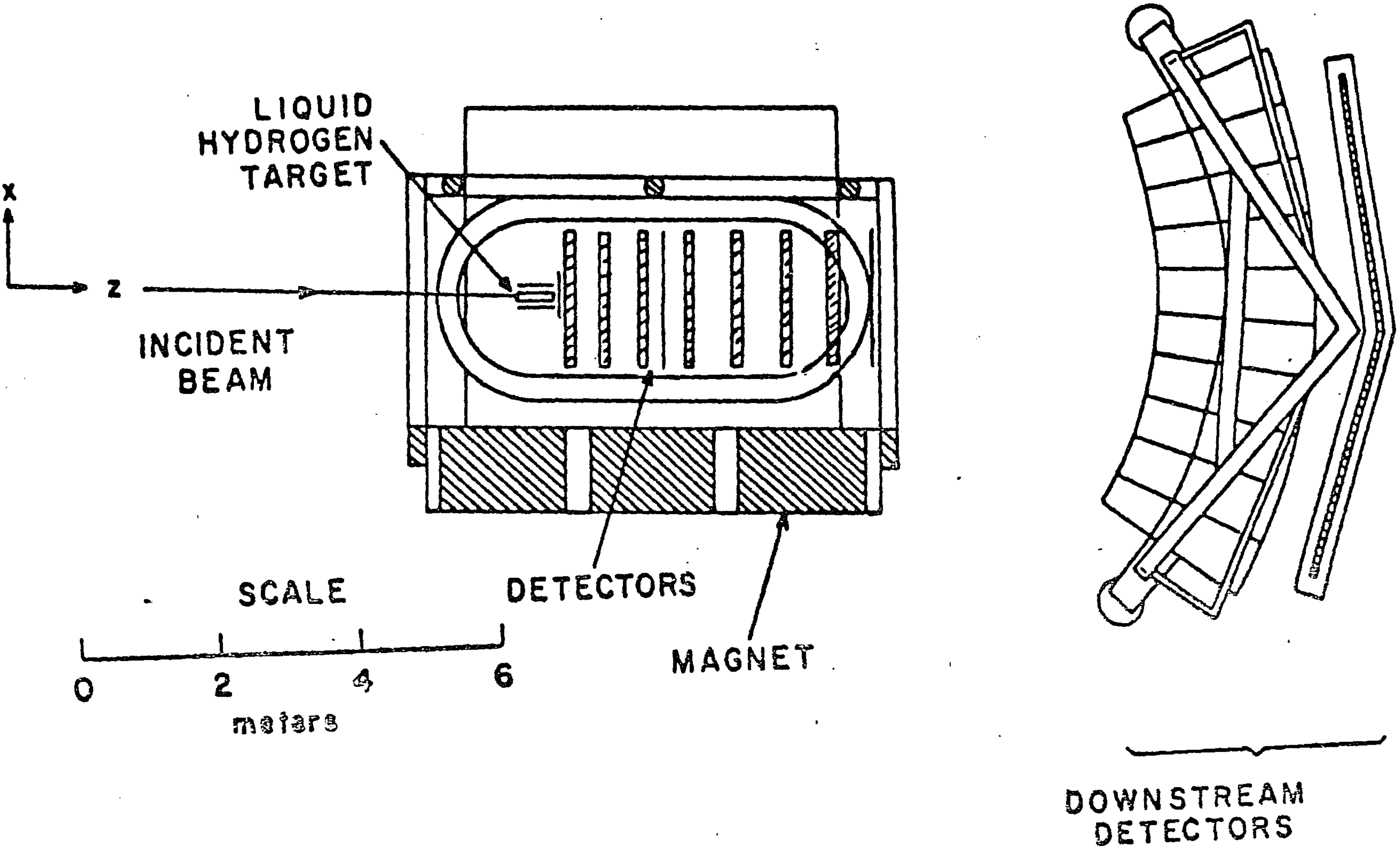

Fig. 3.2 The MPS II Spectrometer layout for the reaction $\pi^- p \to \phi\phi n$.

MPS MAGNET

Weight	650 tons
Gap	6' wide x 4' high x 15' long
Central Field	10kG
Coils	14 pancakes, 11 turns ea.
Power	10,000 A @ 240V
Cooling Water	400 GPM @ 20°C rise
Downward Force at Midplane	550 tons (magnet powered)
Support	4 hydrostatic bearings, 30" dia. on steel plates
Rotation	± 15°, pivot 18" inside upstream end

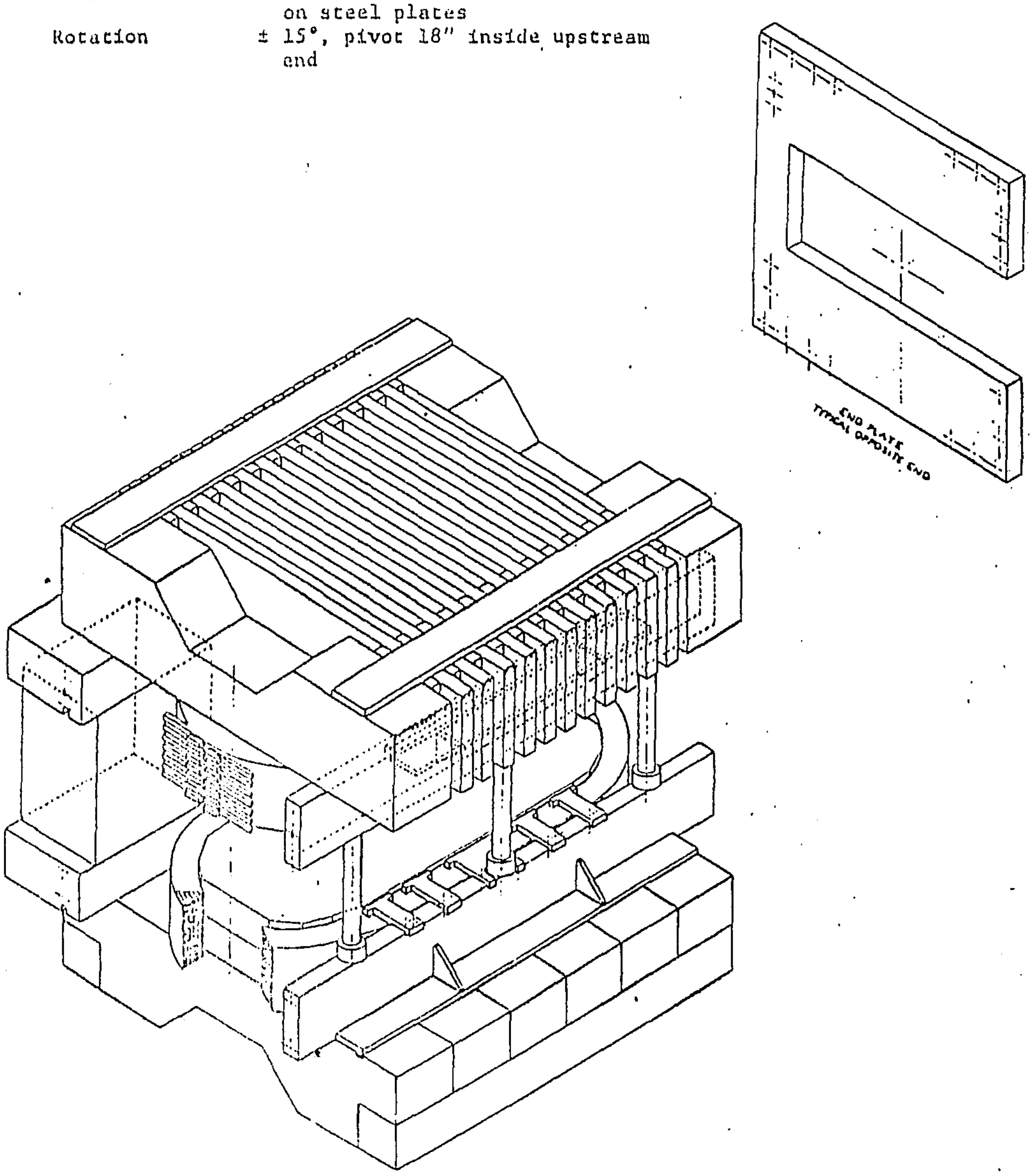

Fig. 3.3 Isometric view of the MPS magnet.

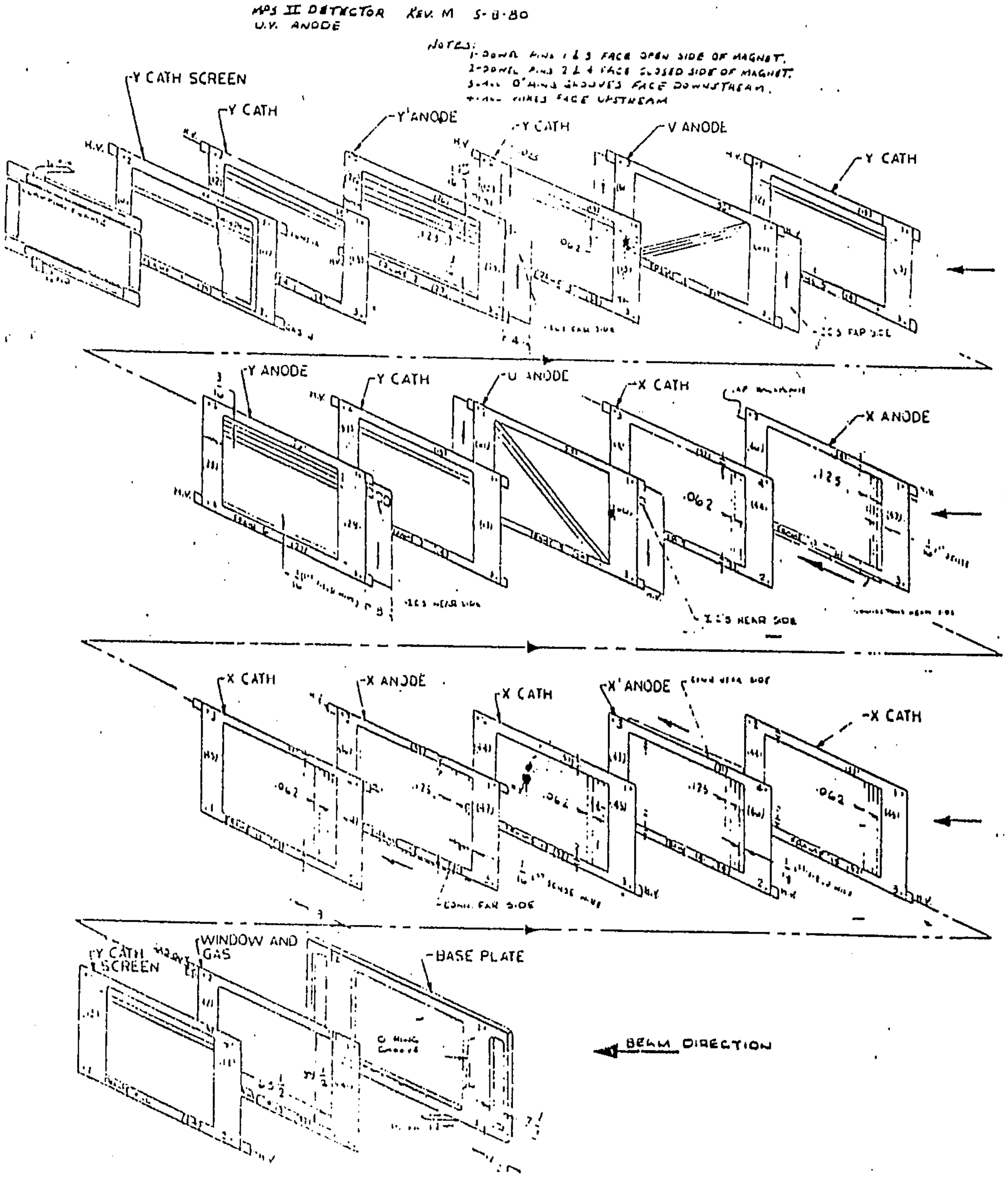

Fig. 3.4 The construction of a drift chamber module.

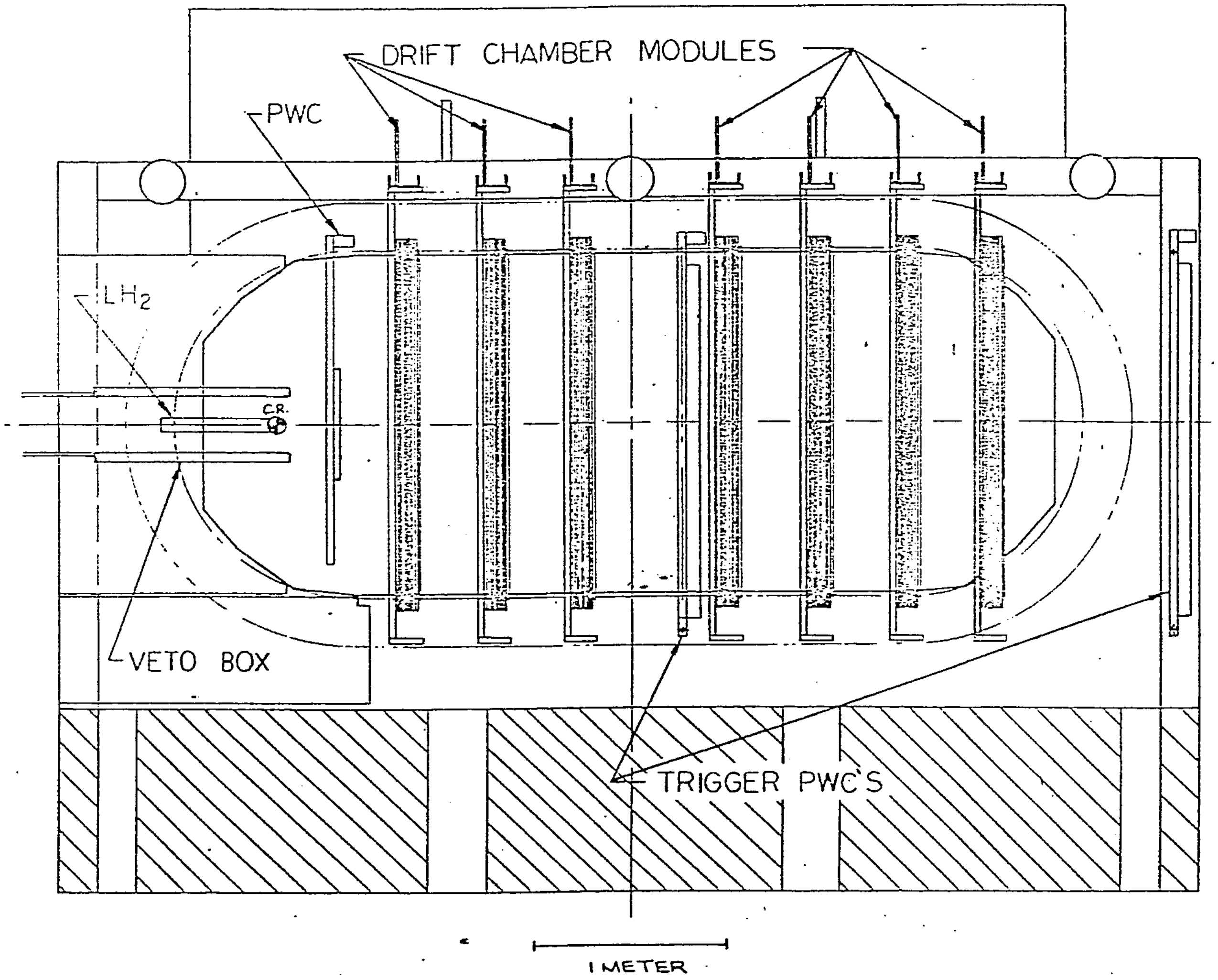

Fig. 3.5 The experimental arrangement of the target,veto box, drift chambers and trigger PWC's.

CHAPTER 4: EVENT SELECTION

Once the tapes were processed by the off-line program, those events corresponding to a particular trigger and satisfying certain topological and kinematic cuts were found. The relevant information corresponding to each of these events were written sequentially onto a summary tape. In the case of our four-kaon selection criteria, an event was recorded on the data summary tape if this event fitted the topology of four prongs with two positive tracks and two negative tracks plus a recoil neutral in the target. Of course, the intersecting four-prong vertex must be located within the target region. In addition, those events corresponding to the kaon-induced reaction were identified and rejected from our data tape.

To facilitate our subsequent analysis, much of the useful information was recorded on the summary tape. This included the important kinematic quantities such as the target interaction point, energy-momentum and momentum components of each particle involved in the reaction (π^-, p, K_1^+, K_1^-, K_2^+, K_2^-, n), the direction cosine at a point for a particular track, etc. Once the data were reduced to summary tape form, the subsequent analysis was performed by another program called SUMARY written to analyze these summary tapes.

All the topological and kinematic cuts were applied in this SUMARY program in order to make the final $\phi\phi$ event selections. The relevant cuts made here for the event of interest included the ϕ mass cut for each pair of kaons to form a ϕ, an effective $\phi\phi$ mass cut to form an accepted $\phi\phi$ system, the neutron missing-mass squared cut to the neutral system to identify a recoil neutron, kaon momentum cut, the ambiguous assignment of four kaons to two double ϕ's, etc. In Table 5.1 we summarize the topological criteria and the various cuts applied to each selected event used in our partial wave analysis.

Figure 4.1 shows a very clean neutron recoil from the $\phi\phi$ system after a neutron missing-mass squared cut. A typical 4K event ($K^+K^-K^+K^-$) is shown in Fig. 4.2. The estimated contamination of non-neutron events in our data sample is ≈ 3% which has a negligible effect on our analysis. These non-neutron events were estimated from the asymmetrical structure of the recoil neutrals after the neutron missing-mass squared cut.

Table 4.1

Summary of cuts applied to data

TOPOLOGY:	Select events with two positive charged and two negative charged particles plus a recoil neutral. The production vertex of the four outgoing tracks must be located inside the target region.
AMBIGUITY:	Events with the ambiguous assignment of four kaons to two double ϕ's were removed from the analysis. This assignment uncertainty has caused about 15% of the events discarded from the threshold bin.
MOMENTUM:	Kaon momentum > 3.2 GeV/c (1982 data) Kaon momentum > 2.8 GeV/c (1983 data)
MASS:	$1.005 \text{ GeV} \leq \phi \text{ mass} \leq 1.033 \text{ GeV}$ $2.040 \text{ GeV} \leq \phi\phi \text{ effective mass} \leq 2.640 \text{ GeV}$ $0.0 \text{ GeV}^2 \leq \text{neutron missing-mass squared} \leq 1.6 \text{ GeV}^2$

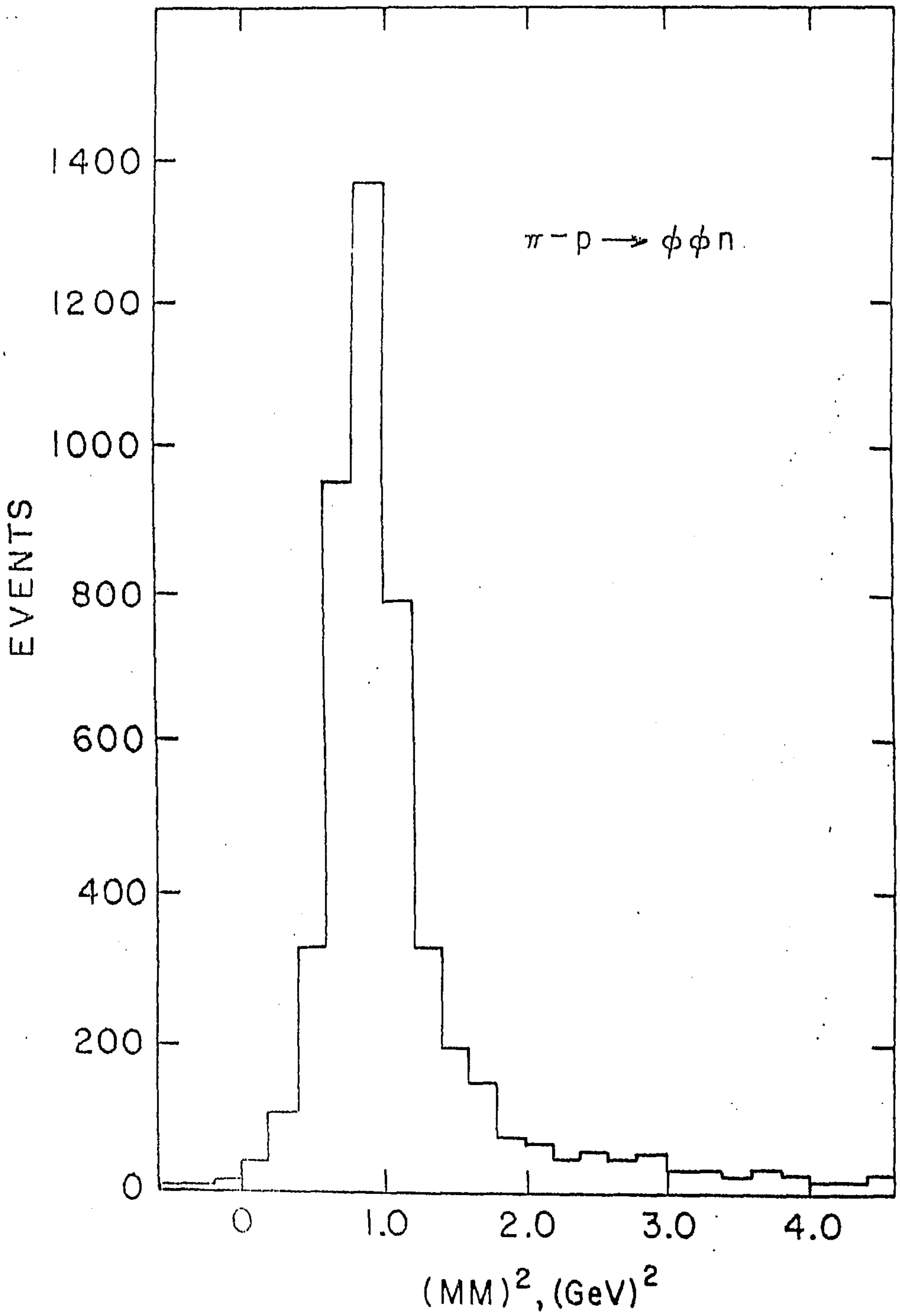

Fig. 4.1 The missing mass squared for the neutral system recoiling from the $\phi\phi$.

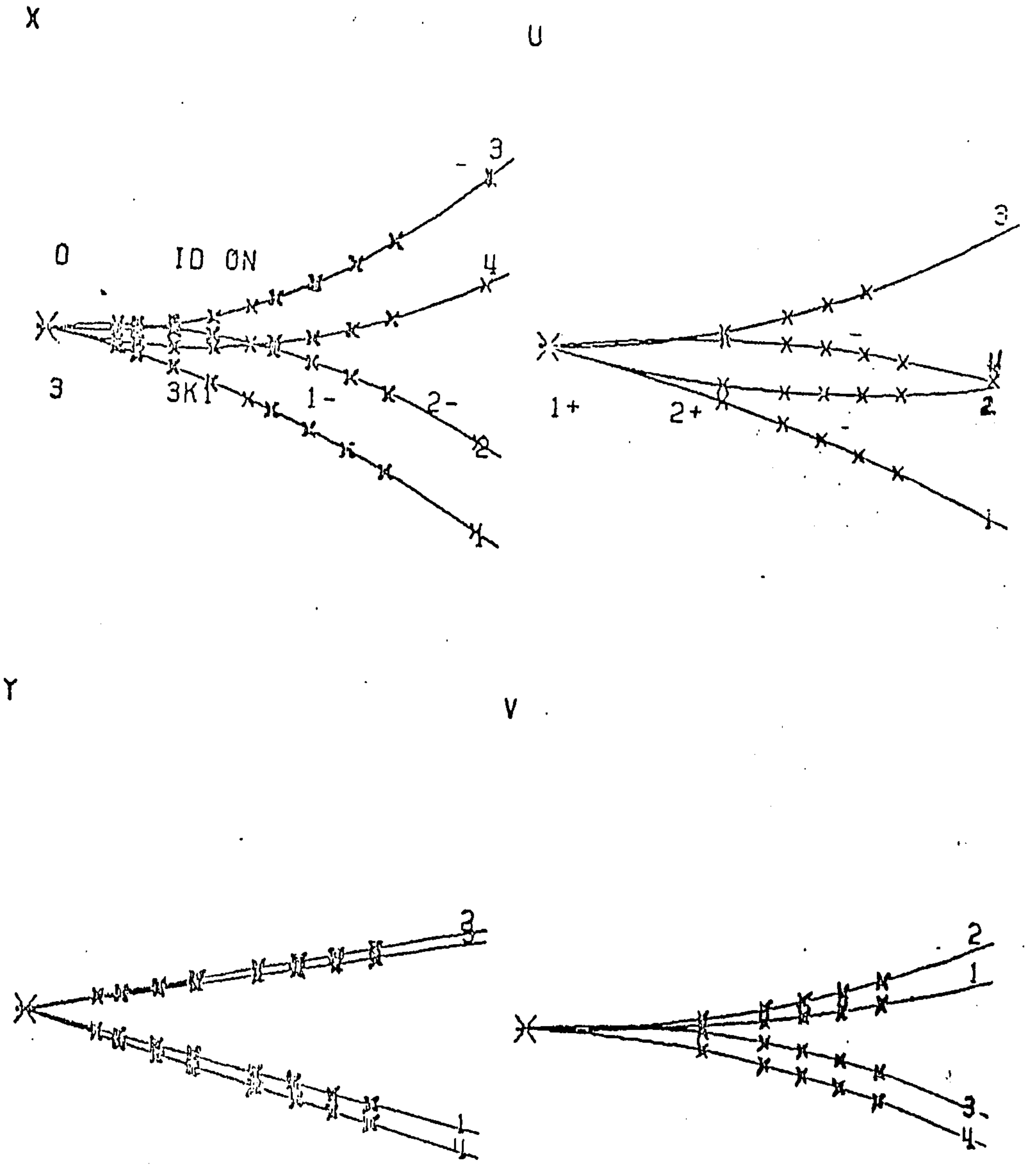

Fig. 4.2 A typical 4K($K^+K^-K^+K^-$) event projected on different planes and reconstructed by MPS pattern recognition program. A X-view or Y-view means a projection of the reconstructed tracks on X-Z or Y-Z plane.

CHAPTER 5: MONTE CARLO STUDIES OF $\phi\phi$ SYSTEM

5.1 Introduction

In the pursuit of understanding of the observed $\phi\phi$ spectrum, our preferred partial wave analysis method has made a substantial use of the Monte Carlo software package. The significance of this package in the present study can be briefly described by its two basic functions: generation of events in accordance with some well-defined specifications and a detailed description of event losses resulting from the failure of a simulated MPS detector test.

In the course of the analysis, the Monte Carlo simulation program was directly involved in the following studies:

(a) The characteristics of each projected distribution can be generated for any $\phi\phi$ partial wave. We shall see shortly that each partial wave is characterized by an unique set of angular distributions.

(b) Either the mass independent solution or the K-matrix solution can be generated by feeding the associated production amplitudes of either solution into the Monte Carlo program.

(c) Experimental acceptance can be determined for each partial wave by generating events according to the accepted solution and then detected at the simulated detector. Those survived events can be used to make direct comparison with the generated events and with the observation.

(d) The Monte Carlo program enables us to study the interference phenomenon due to a set of coherently coupled waves. By varying the phase and the relative amounts of the constituent waves in steps, a systematic change of the characteristic structures can be shown.

(e) Under different simulated conditions, an optimization of the experimental setup for the best possible acceptance and efficiency can be achieved.

In the next two sections only the situations corresponding to (a) and (d) are relevant; the situations related to the other three cases can be found in Chapters 3 and 6.

5.2 Characteristics of $\phi\phi$ Pure Waves

As will be shown in Chapter 6, our final solution to the observed $\phi\phi$ spectrum turns out to be one unique set of waves. This uniqueness of solution clearly demonstrates the selectivity of the analyzing program. In fact, the success of the wave searching is closely related to the $\phi\phi$ system being a very pwoerful analysis system for determining particular partial waves. To establish the last point the best approach is to display the characteristic structures for each $\phi\phi$ partial wave considered in the partial wave analysis.

The mathematical function, which fully governs the relationship between the six decay angles (γ, β, α_1, α_2, θ_1, θ_2) is defined by the basis vector of Eq. 2.1. A basis vector corresponding to a particular partial wave is specified by its associated quantum numbers. In order to generate the desired angular distributions for a selected $\phi\phi$ partial wave, it is only necessary to substitute the set of quantum numbers into Eq. 2.1. The functional form of Eq. 2.1 hints that among the possible combinations which can be formed out of the six angles, only eight projections are physically relevant (α, $\alpha_1 \pm \alpha_2$, $\cos\beta$, γ, $\cos\theta$, $\cos\theta_1 \pm \cos\theta_2$). In particular, the characteristic structures of the α and $\alpha_1 \pm \alpha_2$ projections are crucial in discriminating the $\phi\phi$ solution waves from the other partial waves.

To well determine the detailed structures of the various projected distributions as predicted by a basis vector, a generation of 100,000 $\phi\phi$ events for this pure wave was completed by the Monte Carlo program TRIA2. These events were subsequently binned by the histogram package TRIDAT to give the desired distributions.

In Figs. 5.1(a) through 5.1(b) we present the results of the eight generated characteristic distributions for each of the forty-one different pure waves. Only waves with both J and L up to 4 are shown. Moreover, we anticipate from Eq. 2.1 that the γ-distribution is flat everywhere for M = 0 waves, hence the γ-projection is omitted from Figs. 5.1(a) and 5.1(b). Also note that he three α, $\alpha_1 + \alpha_2$, $\alpha_1 - \alpha_2$ projections are not properly folded to their natural ranges (see Table 6.2).

A detailed comparison of these pure waves indicates that each pure wave is characterized by an unique set of characteristics unparalleled to other waves. In particular, the following points are noticeable:

(a) Except for L = 0, all pure waves with non-vanishing M show very prominent γ-structures. Consequently, the complete absence of the γ-structure in our observation greatly reduces the number of possible waves.

(b) In the event of $M^{\eta} = 0^-$ [Figs. 5.1(a) and 5.1(b)], the characteristic structures of the two important projections $\alpha_1 + \alpha_2$, $\alpha_1 - \alpha_2$, are opposite in phase for odd L (L = 1) and even L (L = 0, 2). The observed distributions are in favor of the S- and D-waves which agree with the final solution.

(c) For M = 0 waves, a very pronounced $\alpha_1 - \alpha_2$ central peak and dip can be seen only in two 2^{++} waves with spin S = 2; one is an S-wave and the other one is a D-wave. The observed $\alpha_1 - \alpha_2$ distribution is analogous to this structure.

(d) The pure wave with quantum numbers $J^{PC} = 2^{++}$, $L = 0$, $S = 2$ and $M^{\eta} = 0^{-}$, which is later identified as the most significant wave, has very similar α, $\alpha_1 + \alpha_2$, $\alpha_1 - \alpha_2$ behaviors to the $J^{PC} = 4^{++}$, $L = 2$, $S = 2$ and $M^{\eta} = 0^{-}$ wave. In regard to our data, this similarity has created certain ambiguity in obtaining a definitive solution in the threshold region (a competitive loglikelihood value). To resolve this ambiguity, the accepted solution relies on the flat $\cos\beta$ and $\cos\theta$ distributions of the 2^{++} wave together with an independent requirement, i.e. continuity of solution.

(e) In general, the $\cos\theta$ and $\cos\theta_1' \pm \cos\theta_2'$ projections are less definitive than the α, $\alpha_1 + \alpha_2$, $\alpha_1 - \alpha_2$ structures. In particular, the $\cos\theta_1' + \cos\theta_2'$ and $\cos\theta_1' - \cos\theta_2'$ vary in the same manner in most of the pure waves.

(f) After the completion of our analysis, Ono predicted that a $J^{PC} = 2^{++}$, $L = 4$ wave should be present at the high $\phi\phi$ mass. Since waves with high orbital angular momentum (L) were expected to be suppressed by the barrier factor, the $L = 4$ waves were not considered in the present study. However, for the sake of completeness we generated the characteristics of the $L = 4$ pure waves up to $J = 4$ and looked into this possibility.

Fig. 5.1(h) shows that the characteristics of the almost flat $\alpha_1 - \alpha_2$ distribution for the $J^{PC} = 2^{++}$, $L = 4$, $S = 2$ and $M^{\eta} = 0^{-}$ wave is in serious disagreement with the pronounced $\alpha_1 - \alpha_2$ structure observed in the entire $\phi\phi$ spectrum. Therefore, even in the absence of a detailed analysis our data do not seem to support a H-wave at high mass. In our next analysis which will follow shortly after the 1985 spring run of the same $\phi\phi$ experiment, the $L = 4$ wave will be considered.

5.3 Interference Between 0^{++} and 2^{++} Waves

The existence of 0^{++} state in the glueball spectrum is predicted by theory. This state is also permitted by the $\phi\phi$ system but not observed in our $\phi\phi$ data. It is conceivable that if 0^{++} state genuinely existed in the $\phi\phi$ spectrum its contribution to the solution should be a significant one. Of course, a logical explanation for the absence of this state can be related to a prediction which shows that the mass of the 0^{++} glueball is well below the $\phi\phi$ threshold. However, our present knowledge of the glueball mass spectrum is very model-dependent and often inconsistent. It is worth to take a phenomenological approach to determine how well the 0^{++} wave can be separated from the 2^{++} wave in the event of their co-existence. In addition, the characteristics of their interference is also useful to compare with the real data.

Our choice of these two waves is $J^{PC} = 0^{++}$, L = 0, S = 0 and $J^{PC} = 2^{++}$, L = 0, S = 2. The latter represents the dominant wave. The rejection of 0^{++} from 2^{++} is measured by χ^2 as a function of two parameters: the relative amount of 0^{++} in the presence of both partial waves (R) and the phase difference between them (θ). The same Monte Carlo program TRIA2 was used to generate both pure 2^{++} wave as well as the two coupled waves at 2.1 GeV $\phi\phi$ effective mass. The acceptance effect due to $\cos\beta$ was also considered. The variations of the χ^2 with R were studied at three different phases, i.e. $\theta = 0°$, 90° and 180°. Figs. 5.2(a) and 5.2(b) indicate such variations due to α projection alone and the combination of all eight projections. It is easy to see that the rejection of 0^{++} from the coupled waves is primarily due to α. Other projections made little contributions to this effect. The χ^2 for each point shown in these figures is obtained by comparing the randomly generated 4000 events of pure 2^{++} wave with ten sets of 400 events all generated at fixed R and θ. This allows us to estimate the statistical error associated with each comparison.

It is clear that 0^{++} and 2^{++} waves are most distinguishable when they are in phase and χ^2 reaches the maximum at R = 0.6. This ability becomes substantially reduced while they are orthogonal and 180° out of phase. At these two phases (θ = 0° and 180°), the discrimination between these two waves in small R (< 0.4) is contributed mainly by α. Beyond this range other projections also make some contribution, however, this is independent of the phase.

Those events used to plot Fig. 5.2(a) is rearranged to plot Figs. 5.2(c) and 5.2(d) which show the characteristics of the α-distribution as a result of the interference at discrete values of R (0.2, 0.4, 0.6, 0.8) and θ (0°, 90°, 180°). The variations of α structure with R and θ are clear and distinctive.

5.4 Test of Analysis Program Uniqueness

One of the key questions central to our analysis which has been raised on a number of occasions is that: to what extent can one trust the correctness and uniqueness of the solution claimed by the present program of analysis?

The best way to answer this question is to go through a comprehensive test of the analysis program with the aid of the Monte Carlo package. Such a test began with the Monte Carlo generation of events based on a pre-determined K-matrix solution. The size of these events was comparable to that of the real events in use. These events were then analyzed by the usual analysis program. To avoid possible preoccupied bias, this test was deliberately conducted with the help of two members of the group working independent of each other. One of them was solely responsible for generating a solution while the other one was totally committed to the search for this solution using the events created by the first one. In this way the uniqueness of the analysis program could be determined by comparing the solution obtained from the usual fitting procedure with the original solution.

In order that the results of the test be conclusive, the K-matrix solutions corresponding to seven different sets of coupled waves were created. The method of searching for the solution is described in detail in Section 6.7. In principle, the search of waves depends on the fitting program. The fitting procedure begins with only one wave at a time and cycling through all partial waves. The same fitting procedure is then repeated for all possible combinations of two waves. An addition of more waves to the fitting program for trials is terminated when the loglikelihood value is not significantly improved by this addition.

Tables 5.1(a) through 5.1(g) show the results of the solutions found by the method described above. These waves were searched in two separate 200 MeV wide bins (2.19 - 2.39 GeV, 2.39 - 2.59 GeV). The loglikelihood value (logL) for the entire 400 MeV wide bin (2.19 - 2.59 GeV) was obtained by adding the two individual loglikelihood values and listed in decreasing order. Note that in order to convert the change in loglikelihood (ΔlogL) into the equivalent number of standard deviations (σ), we use the result of Appendix C which states

$$\Delta\log L = 4.3 \longrightarrow 1\sigma$$

In interpreting the results one should realize that the background was included in the generated solution whereas the search for this solution did not consider its contribution. The reason for ignoring the background effect in present search will be explained in Section 6.6. But, as a consequence of this, the resulting number of standard deviations (σ) is relatively higher than one would normally expect.

Just as an illustration, we present the production and phase of the K-matrix fit (generated) to the mass-independent solution (searched) for the file MCDATAB in Figs. 5.3(a) and 5.3(b).

The result of this test is remarkable. The solutions found (output) by the usual analysis program are in complete agreement with the originally generated solutions (input) in all seven cases. This unambiguously demonstrates the selectivity of the analysis program and thus reaffirms our previous claim that the solution found by the present analysis is genuine and unique.

Table 5.1(a)
Solution found by loglikelihood method for file MCDATAA

TWO-WAVE FIT

Waves $J^P LSM^\eta$	Loglikelihood values (logL)			Compared to highest logL (ΔlogL)	σ
	M = 2.19-2.39	M = 2.39-2.59	M = 2.19-2.59		
2^+S20^- 2^+D20^-	19900	4709	24609		
2^+S20^- 0^+D20^-	19550	4630	24180	429	100
2^+S20^- 0^-P10^+	19540	4603	24143	466	108
0^+S00^- 2^+S20^-	19500	4611	24111	498	116

THREE-WAVE FIT

2^-P10^+ 2^+D20^- 2^+S20^-	19910	4716	24626		
2^+D20^- 4^+D20^- 2^+S20^-	19900	4712	24612	14	3
0^-P10^+ 2^+D20^- 2^+S20^-	19900	4712	24612	14	3
1^+D20^+ 2^+D20^- 2^+S20^-	19900	4711	24611	15	3

FOUR-WAVE FIT

2^-P10^+ 1^+D20^+ 2^+S20^- 2^+D20^-	19920	4719	24639		
2^-P10^+ 0^+D20^- 2^+S20^- 2^+D20^-	19920	4719	24639	0	0
2^-P10^+ 1^-P10^- 2^+S20^- 2^+D20^-	19920	4715	24635	4	1
2^-P10^+ 4^+D20^- 2^+S20^- 2^+D20^-	19910	4720	24630	9	2

ΔlogL (from two-wave fit to three-wave fit) = 24626 - 24609 = 17 (4σ)
ΔlogL (from three-wave fit to four-wave fit) = 24639 - 24626 = 13 (3σ)

INPUT (generated)	OUTPUT (searched)
2^+S20^-	2^+S20^-
2^+D20^-	2^+D20^-

Table 5.1(b)
Solution found by loglikelihood method for file MCDATAB

TWO-WAVE FIT

Waves $J^{P}LSM^{\eta}$	Loglikelihood values (logL)			Compared to highest logL (ΔlogL)	σ
	M = 2.19-2.39	M = 2.39-2.59	M = 2.19-2.59		
$2^{+}S20^{-}$ $2^{+}D20^{-}$	17750	5768	23518		
$0^{+}S00^{-}$ $2^{+}S20^{-}$	17680	5751	23431	87	20
$2^{+}S20^{-}$ $2^{+}D00^{-}$	17640	5760	23400	118	27
$2^{+}S20^{-}$ $0^{+}D20^{-}$	17590	5723	23313	205	48

THREE-WAVE FIT

$2^{+}D00^{-}$ $2^{+}D20^{-}$ $2^{+}S20^{-}$	17870	5851	23721		
$0^{+}S00^{-}$ $0^{+}D20^{-}$ $2^{+}S20^{-}$	17770	5802	23572	149	35
$3^{+}D20^{+}$ $2^{+}D20^{-}$ $2^{+}S20^{-}$	17790	5780	23570	151	35
$1^{+}D20^{+}$ $2^{+}D20^{-}$ $2^{+}S20^{-}$	17790	5773	23560	158	37

FOUR-WAVE FIT

$2^{+}D20^{+}$ $2^{+}D00^{-}$ $2^{+}S20^{-}$ $2^{+}D20^{-}$	17890	5862	23752		
$1^{+}D20^{+}$ $2^{+}D00^{-}$ $2^{+}S20^{-}$ $2^{+}D20^{-}$	17890	5861	23751	1	0
$0^{-}P10^{+}$ $2^{+}D00^{-}$ $2^{+}S20^{-}$ $2^{+}D20^{-}$	17890	5857	23747	5	1
$2^{-}P10^{+}$ $2^{+}D00^{-}$ $2^{+}S20^{-}$ $2^{+}D20^{-}$	17890	5855	23745	7	1.6

ΔlogL (from two-wave fit to three-wave fit) = 23721 - 23518 = 203 (47σ)
ΔlogL (from three-wave fit to four-wave fit) = 23752 - 23721 = 31 (7σ)

INPUT (generated)	OUTPUT (searched)
$2^{+}D00^{-}$	$2^{+}D00^{-}$
$2^{+}D20^{-}$	$2^{+}D20^{-}$
$2^{+}S20^{-}$	$2^{+}S20^{-}$

Table 5.1(c)

Solution found by loglikelihood method for file MCDATAC

TWO-WAVE FIT

Waves $J^{P}LSM^{\eta}$	Loglikelihood values (logL)			Compared to highest logL (ΔlogL)	σ
	M = 2.19-2.39	M = 2.39-2.59	M = 2.19-2.59		
$2^{+}S20^{-}$ $0^{+}D20^{-}$	17510	5887	23397		
$2^{+}S20^{-}$ $2^{+}D20^{-}$	17430	5867	23297	100	23
$0^{+}S00^{-}$ $2^{+}S20^{-}$	17450	5815	23265	132	31
$2^{+}S20^{-}$ $2^{+}D00^{-}$	17350	5824	23174	223	52

THREE-WAVE FIT

$0^{+}D20^{-}$ $2^{+}D00^{-}$ $2^{+}S20^{-}$	17570	5960	23530		
$0^{+}D20^{-}$ $2^{+}D20^{-}$ $2^{+}S20^{-}$	17610	5899	23509	21	5
$0^{+}S00^{-}$ $0^{+}D20^{-}$ $2^{+}S20^{-}$	17580	5919	23499	31	7

FOUR-WAVE FIT

$0^{+}D20^{-}$ $2^{+}D00^{-}$ $2^{+}S20^{-}$ $2^{+}D20^{-}$	17730	6000	23730		
$1^{+}D20^{+}$ $0^{+}D20^{-}$ $2^{+}S20^{-}$ $2^{+}D20^{-}$	17670	5911	23581	149	35
$0^{+}S00^{-}$ $0^{+}D20^{-}$ $2^{+}S20^{-}$ $2^{+}D20^{-}$	17620	5956	23576	154	36

ΔlogL (from two-wave fit to three-wave fit) = 23530 - 23397 = 133 (31σ)
ΔlogL (from three-wave fit to four-wave fit) = 23730 - 23530 = 200 (47σ)

INPUT (generated)	OUTPUT (searched)
$0^{+}D20^{-}$	$0^{+}D20^{-}$
$2^{+}D00^{-}$	$2^{+}D00^{-}$
$2^{+}S20^{-}$	$2^{+}S20^{-}$
$2^{+}D20^{-}$	$2^{+}D20^{-}$

Table 5.1(d)
Solution found by loglikelihood method for file MCDATAD

TWO-WAVE FIT

Waves J^PLSM^η	Loglikelihood values (logL) M = 2.19-2.39	 M = 2.39-2.59	 M = 2.19-2.59	Compared to highest logL (ΔlogL)	σ
2^+S20^- 2^+D20^-	17520	6544	24064		
2^+S20^- 2^+D00^-	17440	6537	23977	87	20
2^+S20^- 0^+S00^-	17470	6505	23975	89	21

THREE-WAVE FIT

2^+D00^- 2^+D20^- 2^+S20^-	17640	6681	24321		
0^+S00^- 2^+D20^- 2^+S20^-	17580	6597	24177	144	33
1^+D20^+ 2^+D20^- 2^+S20^-	17580	6551	24131	190	44
3^+D20^+ 2^+D20^- 2^+S20^-	17560	6550	24110	211	49

FOUR-WAVE FIT

1^+D20^+ 2^+D00^- 2^+S20^- 2^+D20^-	17660	6683	24343		
2^-P10^+ 2^+D00^- 2^+S20^- 2^+D20^-	17660	6683	24343	0	0
3^+D20^+ 2^+D00^- 2^+S20^- 2^+D20^-	17660	6683	24343	0	0
0^-P10^+ 2^+D00^- 2^+S20^- 2^+D20^-	17650	6681	24331	2	0.5

ΔlogL (from two-wave fit to three-wave fit) = 24321 - 24064 = 257 (60σ)

ΔlogL (from three-wave fit to four-wave fit) = 24343 - 24321 = 22 (5σ)

INPUT (generated)	OUTPUT (searched)
2^+D00^-	2^+D00^-
2^+D20^-	2^+D20^-
2^+S20^-	2^+S20^-

Table 5.1(e)
Solution found by loglikelihood method for file MCDATAE

TWO-WAVE FIT

Waves	Loglikelihood values (logL)			Compared to highest logL (ΔlogL)	σ
$J^{P}LSM^{\eta}$	M = 2.19-2.39	M = 2.39-2.59	M = 2.19-2.59		
$2^{+}S20^{-}$ $2^{+}D20^{-}$	18870	6879	25749		
$2^{+}S20^{-}$ $1^{-}P10^{-}$	18800	6883	25683	66	15
$0^{+}S00^{-}$ $2^{+}S20^{-}$	18780	6872	25652	97	23
$2^{+}S20^{-}$ $2^{+}D00^{-}$	18730	6893	25623	126	29

THREE-WAVE FIT

$1^{-}P10^{-}$ $2^{+}D20^{-}$ $2^{+}S20^{-}$	19080	6951	26031		
$0^{+}S00^{-}$ $1^{-}P10^{-}$ $2^{+}S20^{-}$	18960	6972	25932	99	23
$2^{+}D00^{-}$ $2^{+}D20^{-}$ $2^{+}S20^{-}$	18980	6927	25907	124	29
$1^{-}P10^{-}$ $2^{+}D00^{-}$ $2^{+}S20^{-}$	18840	7004	25844	187	43

FOUR-WAVE FIT

$1^{-}P10^{-}$ $2^{+}D00^{-}$ $2^{+}S20^{-}$ $2^{+}D20^{-}$	19230	7089	26319		
$0^{+}S00^{-}$ $1^{-}P10^{-}$ $2^{+}S20^{-}$ $2^{+}D20^{-}$	19120	7010	26130	189	44
$3^{+}D20^{+}$ $1^{-}P10^{-}$ $2^{+}S20^{-}$ $2^{+}D20^{-}$	19110	6988	26098	221	51

ΔlogL (from two-wave fit to three-wave fit) = 26031 - 25749 = 282 (66σ)
ΔlogL (from three-wave fit to four-wave fit) = 26319 - 26031 = 288 (67σ)

INPUT (generated)	OUTPUT (searched)
$1^{-}P10^{-}$	$1^{-}P10^{-}$
$2^{+}D00^{-}$	$2^{+}D00^{-}$
$2^{+}S20^{-}$	$2^{+}S20^{-}$
$2^{+}D20^{-}$	$2^{+}D20^{-}$

Table 5.1(f)

Solution found by loglikelihood method for file MCDATAF

TWO-WAVE FIT

Waves	Loglikelihood values (logL)			Compared to highest logL (ΔlogL)	σ
$J^P LSM^\eta$	M = 2.19-2.39	M = 2.39-2.59	M = 2.19-2.59		
2^+S20^- 2^+D20^-	14900	5327	20227		
2^+S20^- 2^+D00^-	14900	5313	20213	14	3
0^+S00^- 2^+S20^-	14880	5328	20208	19	4
2^+S20^- 4^+D20^-	14860	5327	20187	40	9

THREE-WAVE FIT

2^+D00^- 4^+D20^- 2^+S20^-	15080	5421	20501		
2^+D20^- 4^+D20^- 2^+S20^-	15080	5374	20454	47	11
0^+S00^- 4^+D20^- 2^+S20^-	15050	5390	20440	61	14
2^+D00^- 2^+D20^- 2^+S20^-	15030	5385	20415	86	20

FOUR-WAVE FIT

2^+D00^- 2^+D20^- 2^+S20^- 4^+D20^-	15230	5466	20696		
0^+S00^- 4^+D20^- 2^+S20^- 2^+D20^-	15140	5447	20587	109	25
3^+D20^+ 4^+D20^- 2^+S20^- 2^+D20^-	15140	5409	20549	147	34
1^+D20^+ 4^+D20^- 2^+S20^- 2^+D20^-	15150	5397	20547	149	35

ΔlogL (from two-wave fit to three-wave fit) = 20501 - 20227 = 274 (64σ)

ΔlogL (from three-wave fit to four-wave fit) = 20696 - 20501 = 195 (45σ)

INPUT (generated)	OUTPUT (searched)
2^+D00^-	2^+D00^-
2^+D20^-	2^+D20^-
2^+S20^-	2^+S20^-
4^+D20^-	4^+D20^-

Table 5.1(g)

Solution found by loglikelihood method for file MCDATAG

TWO-WAVE FIT

Waves	Loglikelihood values (logL)			Compared to highest logL (ΔlogL)	σ
J^PLSM^η	M = 2.19-2.39	M = 2.39-2.59	M = 2.19-2.59		
2^+S20^- 2^+D20^-	16710	5129	21839		
2^+S20^- 2^+D00^-	16700	5072	21772	67	16
0^+S00^- 2^+S20^-	16690	5077	21767	72	17

THREE-WAVE FIT

2^+D00^- 2^+D20^- 2^+S20^-	16860	5182	22042		
2^+D20^- 4^+D20^- 2^+S20^-	16840	5177	22017	25	6
2^+D00^- 4^+D20^- 2^+S20^-	16830	5170	22000	42	10

FOUR-WAVE FIT

2^+D00^- 4^+D20^- 2^+S20^- 2^+D20^-	16990	5248	22238		
0^+S00^- 4^+D20^- 2^+S20^- 2^+D20^-	16900	5223	22123	115	27
2^-P10^+ 2^+D00^- 2^+S20^- 2^+D20^-	16890	5191	22081	157	36

ΔlogL (from two-wave fit to three-wave fit) = 22042 - 21839 = 203 (47σ)

ΔlogL (from three-wave fit to four-wave fit) = 22238 - 22042 = 196 (46σ)

INPUT (generated)	OUTPUT (searched)
2^+D00^-	2^+D00^-
4^+D20^-	4^+D20^-
2^+S20^-	2^+S20^-
2^+D20^-	2^+D20^-

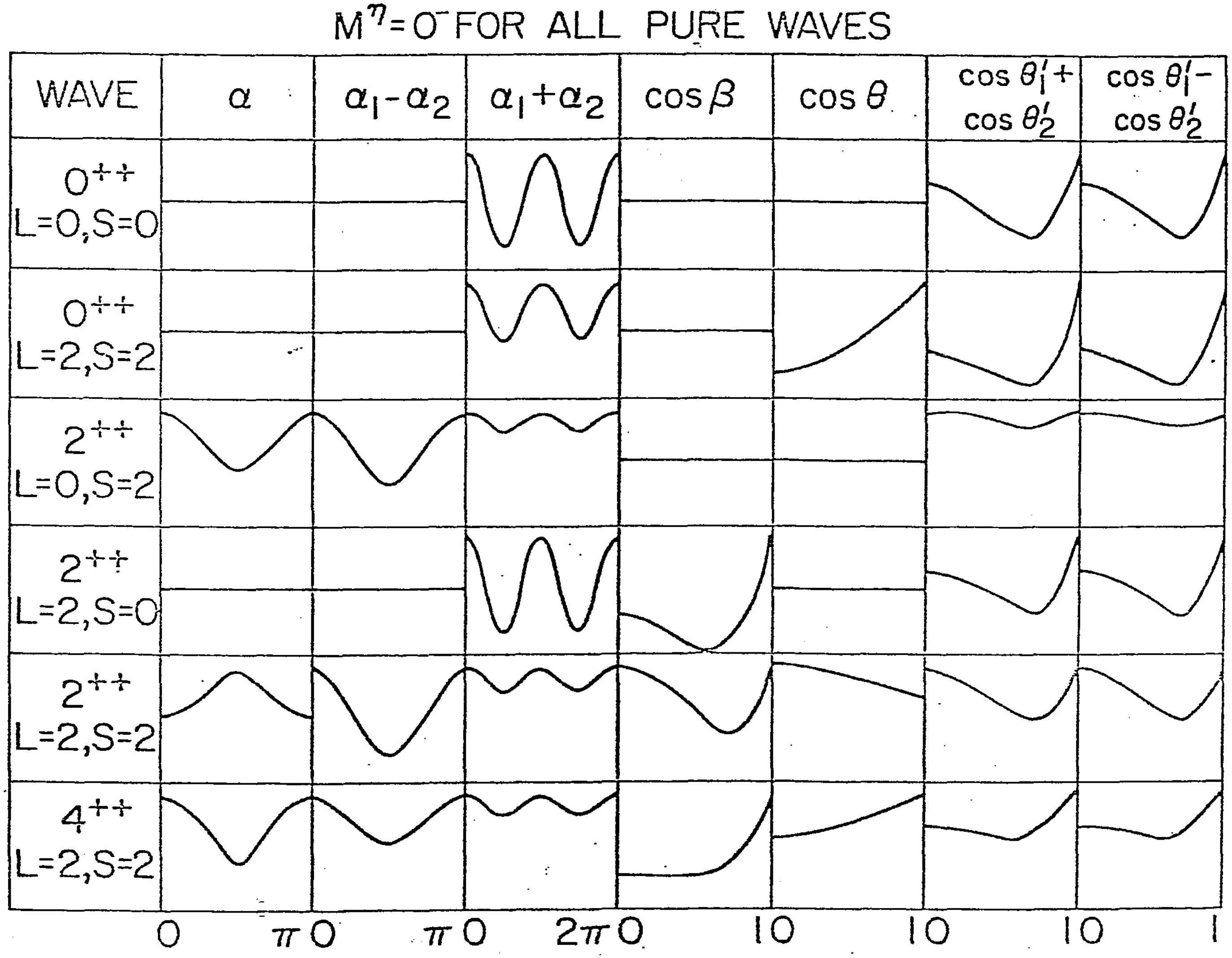

Fig. 5.1a Angular distributions expected for decay of individual spin states.

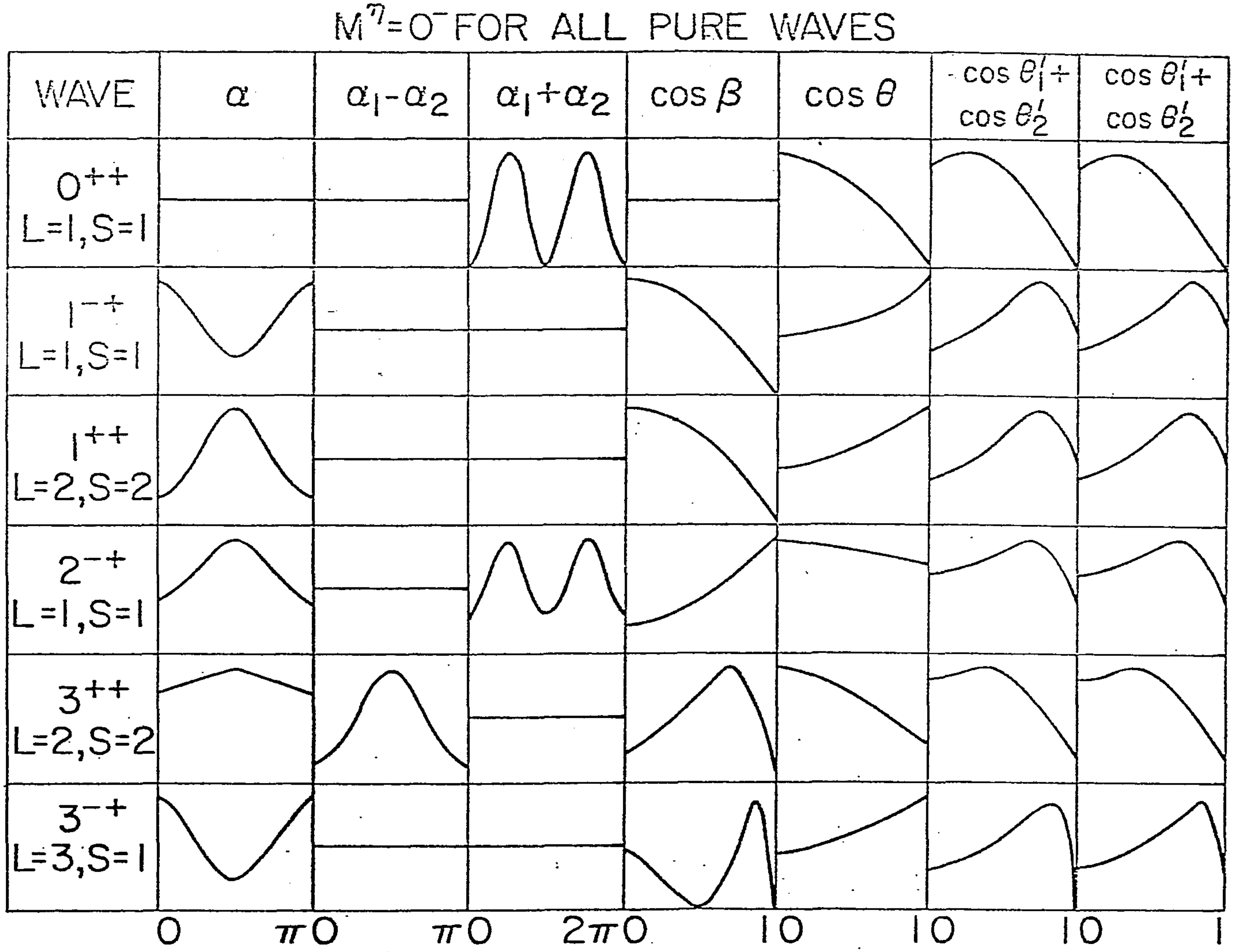

Fig. 5.1b Angular distributions expected for decay of individual spin states.

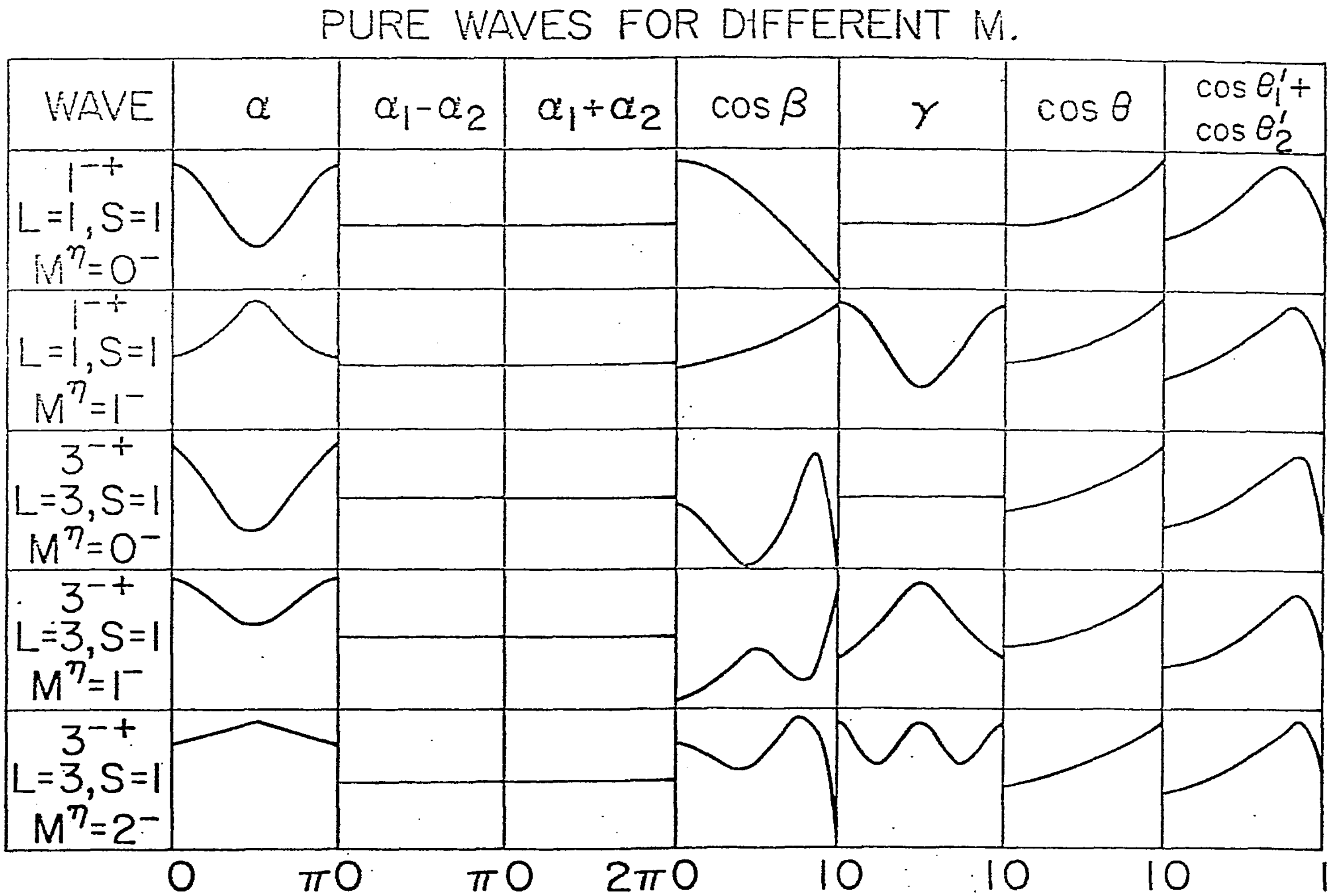

Fig. 5.1c Angular distributions expected for decay of individual spin states.

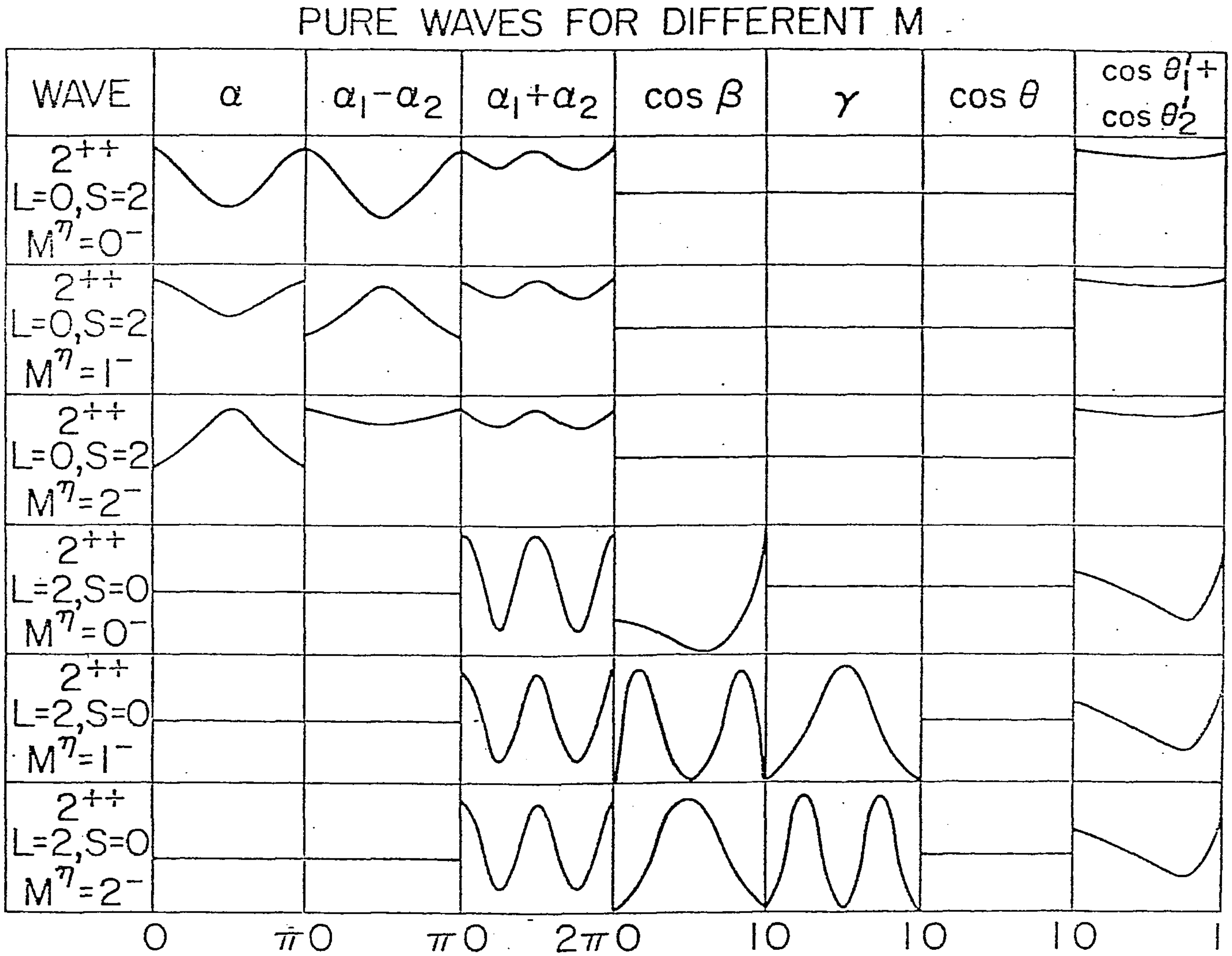

Fig. 5.1d Angular distributions expected for decay of individual spin states.

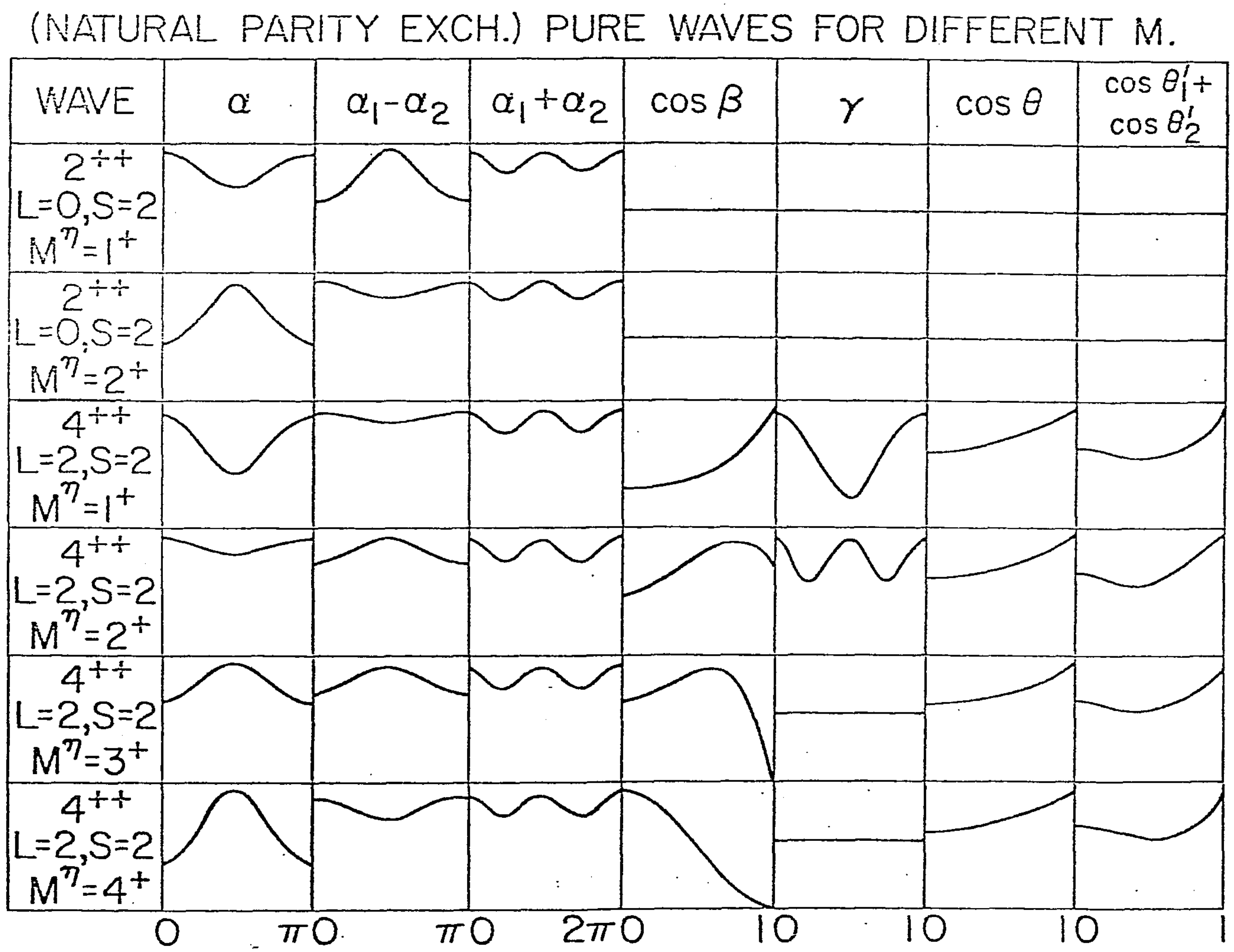

Fig. 5.1e Angular distributions expected for decay of individual spin states.

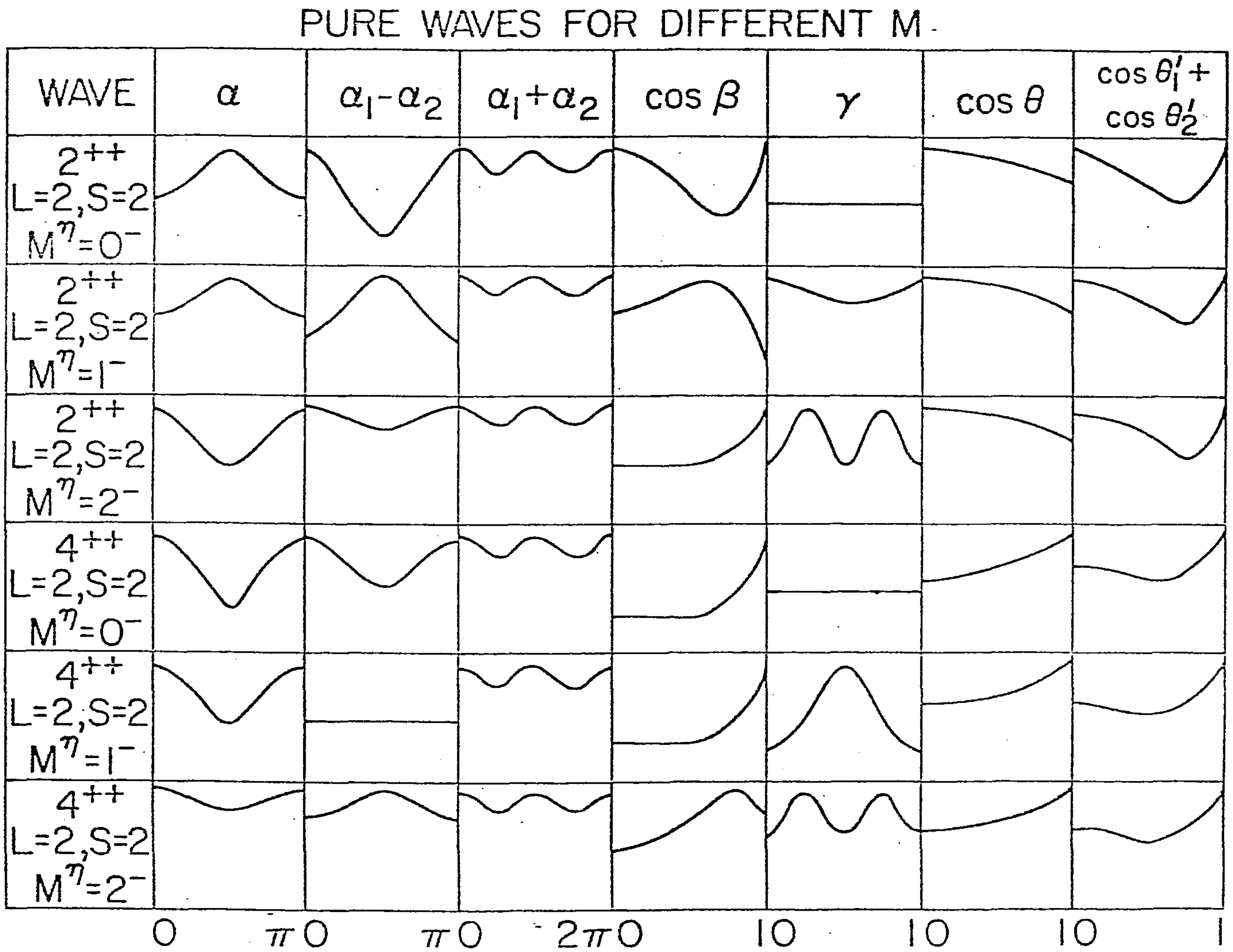

Fig. 5.12 Angular distributions expected for decay of individual spin states.

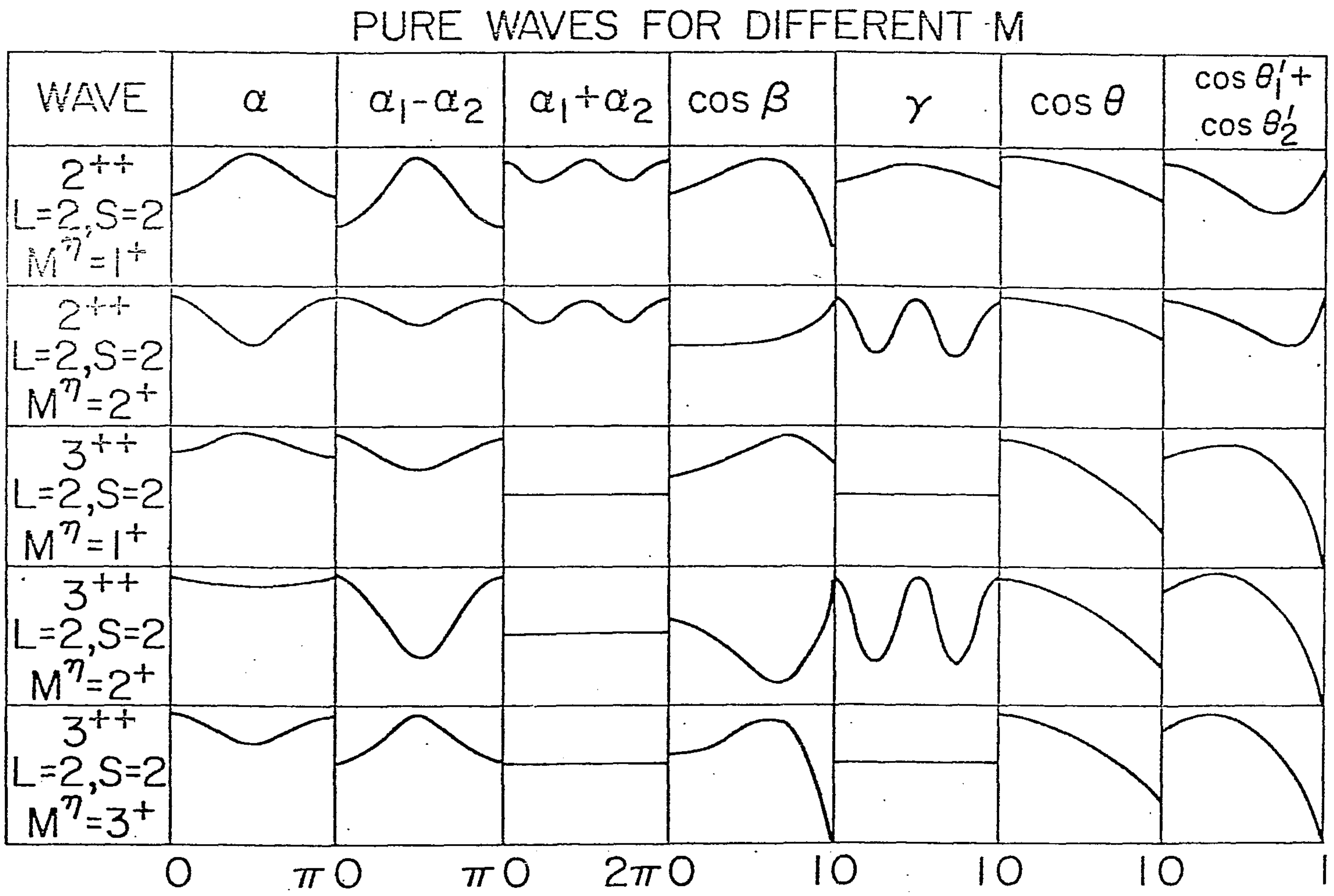

Fig. 5.1g Angular distributions expected for decay of individual spin states.

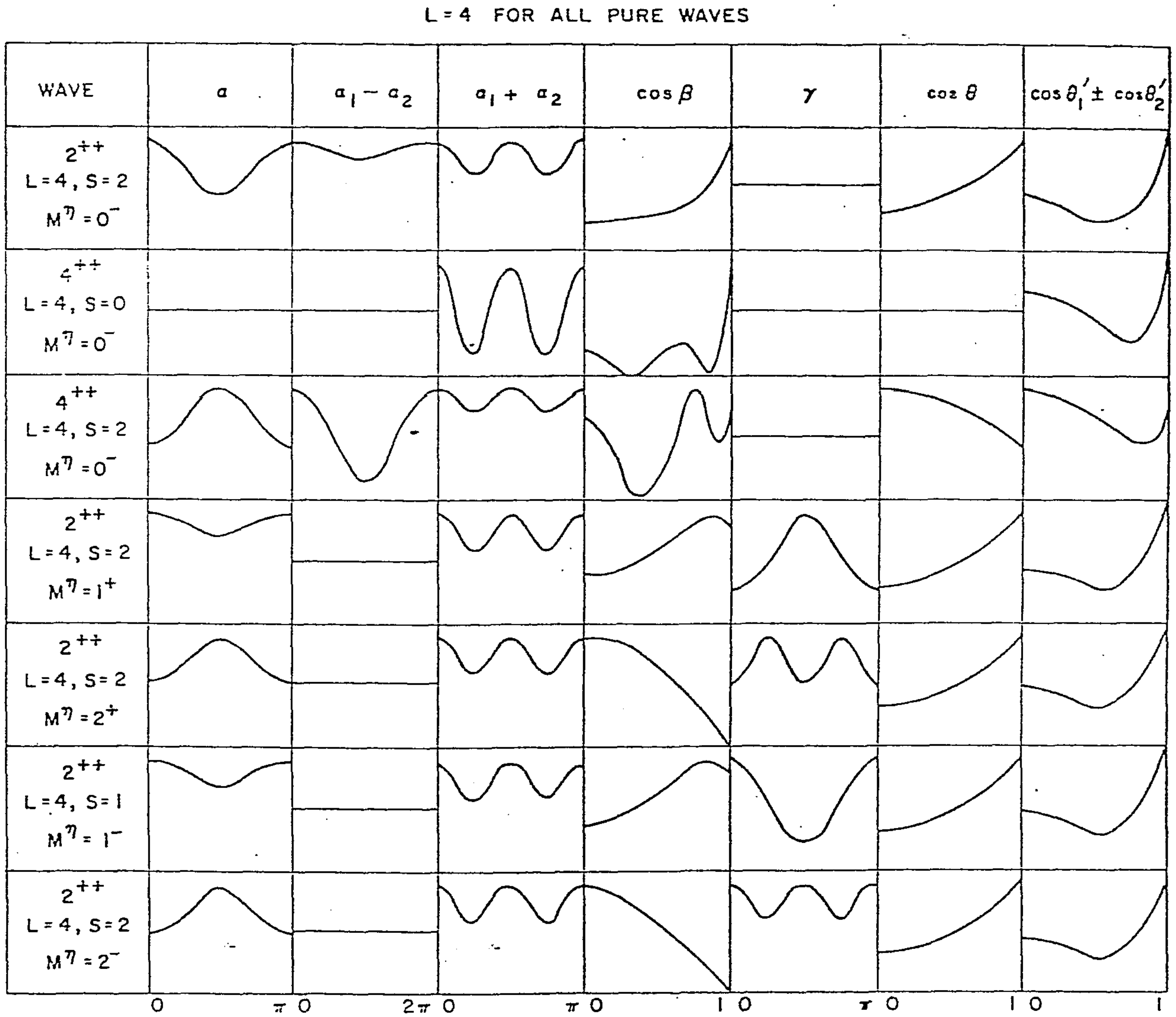

Fig. 5.1h Angular distributions expected for decay of individual spin states.

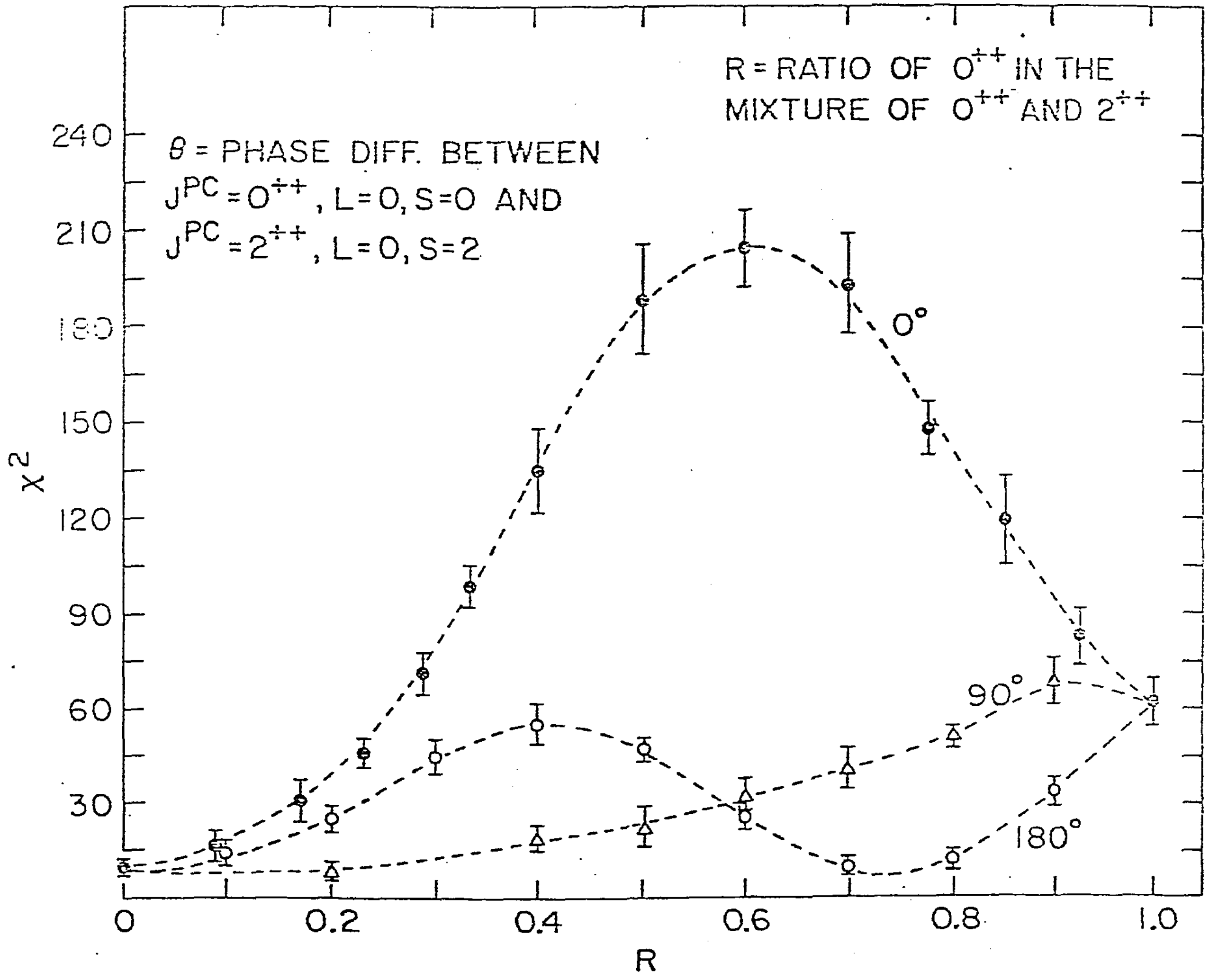

Fig. 5.2(a) χ^2 separation of 0^{++} from 2^{++} partial waves for α projection as a function of R at θ = 0°, 90° and 180° where R is the ratio of 0^{++} in the mixture of 0^{++} and 2^{++}, and θ is the phase difference between these two partial waves.

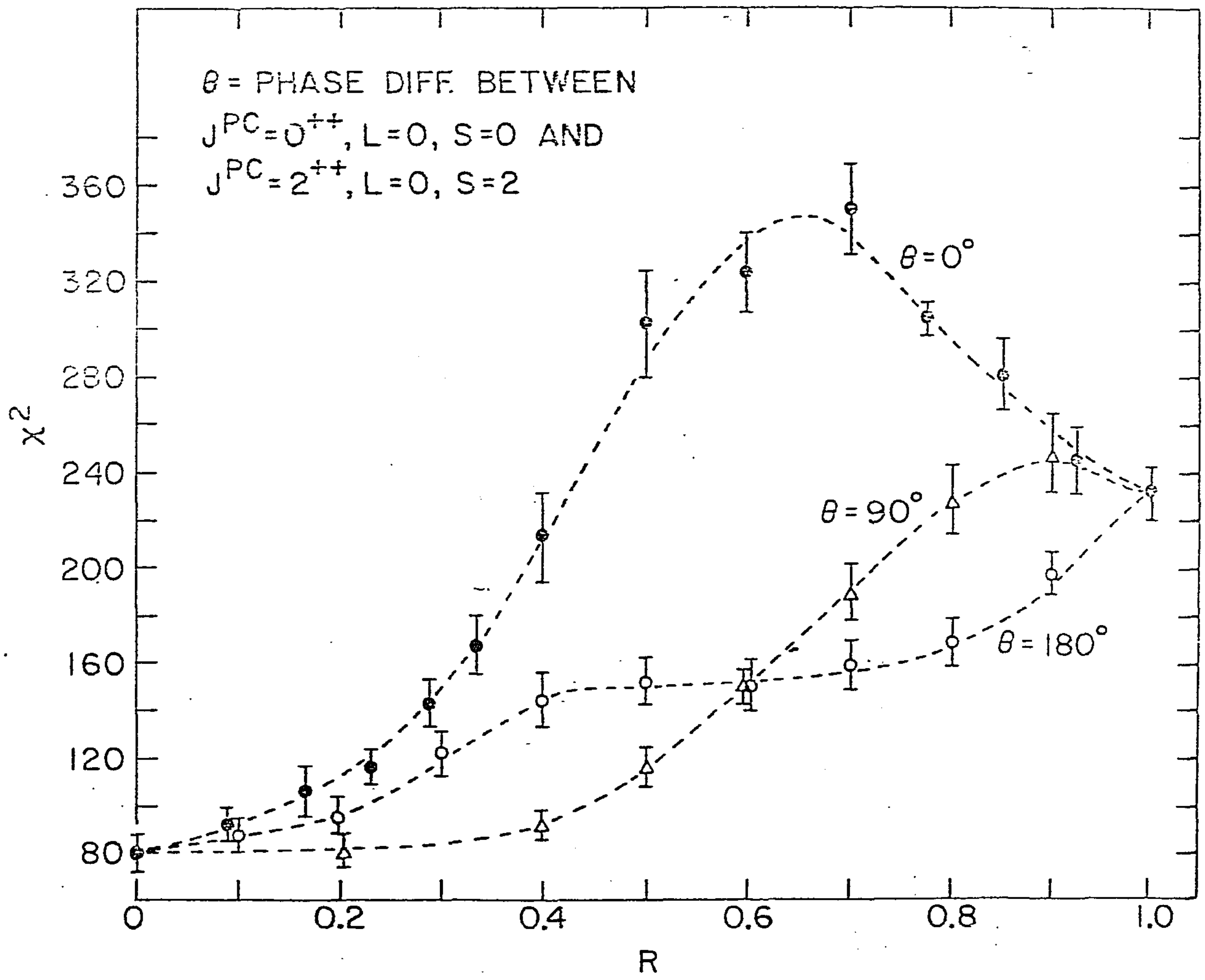

Fig. 5.2(b) χ^2 separation of 0^{++} and 2^{++} partial waves for eight projections (α, $\alpha_1 \pm \alpha_2$, cos β, α, cos θ, cos $\theta_1 \pm$ cos θ_2) as a function of R at $\theta = 0°$, 90° and 180° when R is the ratio of 0^{++} in the mixture of 0^{++} and 2^{++}, and θ is the phase difference between these two partial waves.

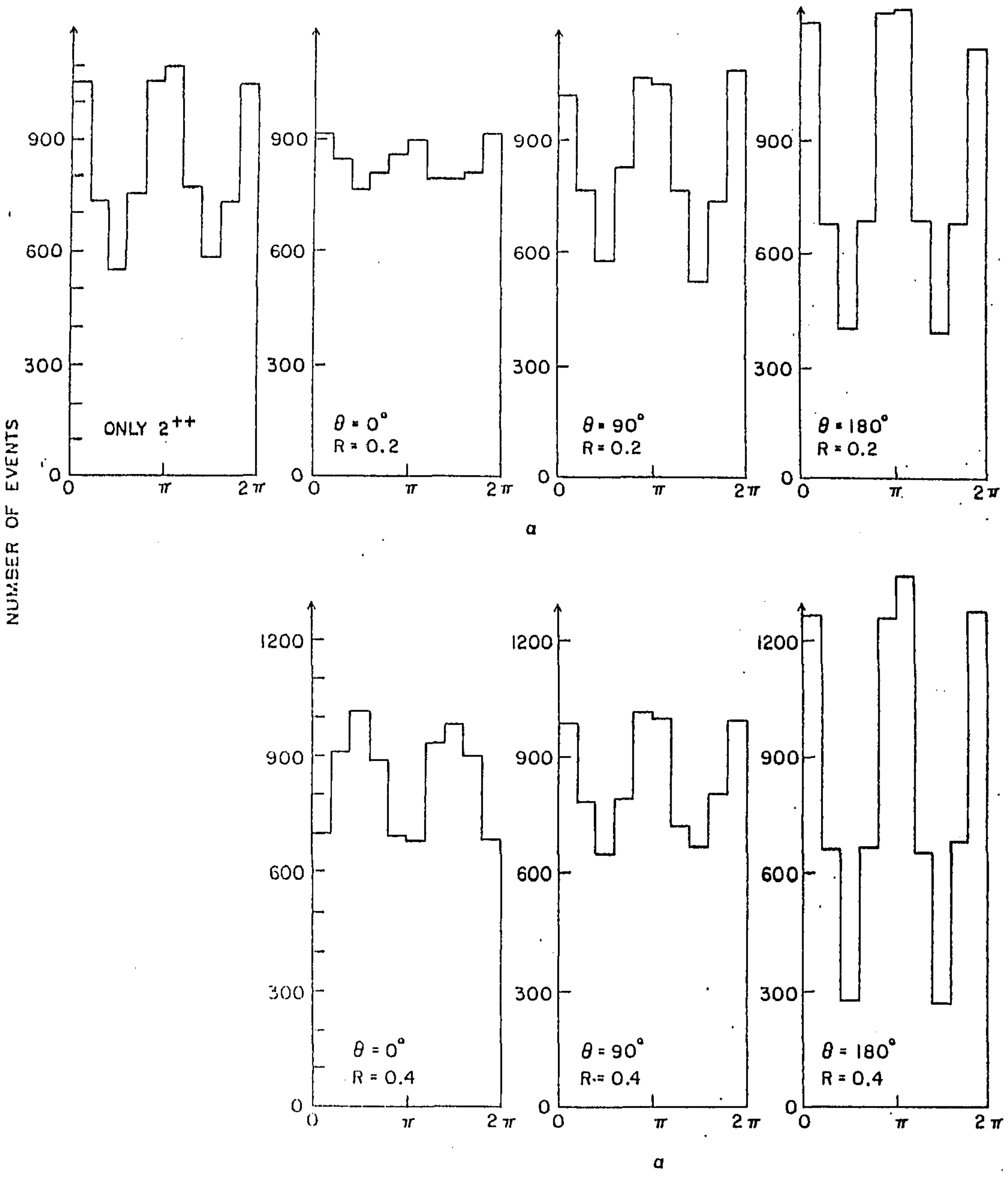

Fig. 5.2(c) Monte Carlo study of α distribution for $\theta = 0°$, 90° and 180° at two fixed values of R.

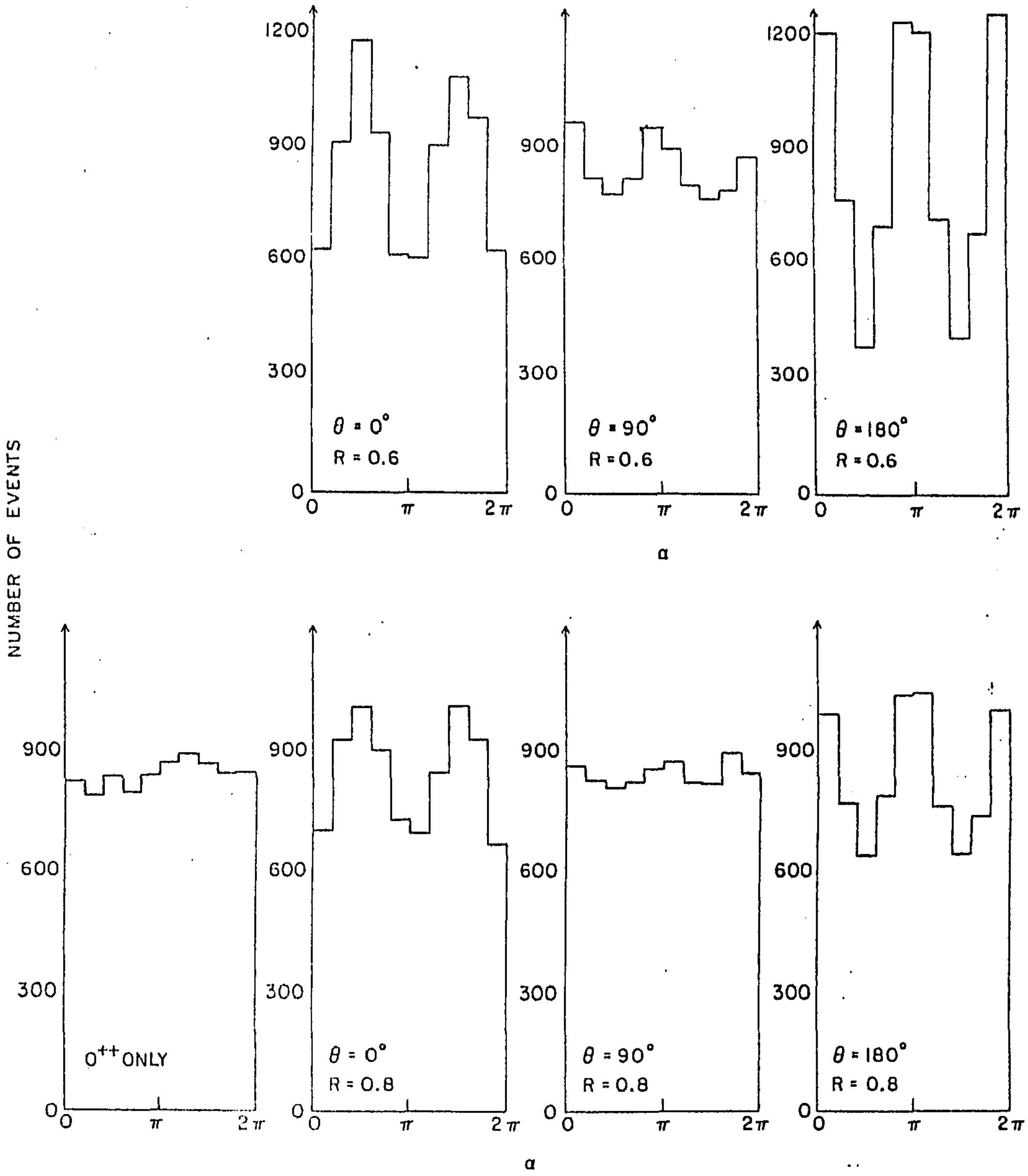

Fig. 5.2(d) Monte Carlo study of α distribution for θ = 0°, 90° and 180° at two fixed values of R. R= 0.6 and 0.8.

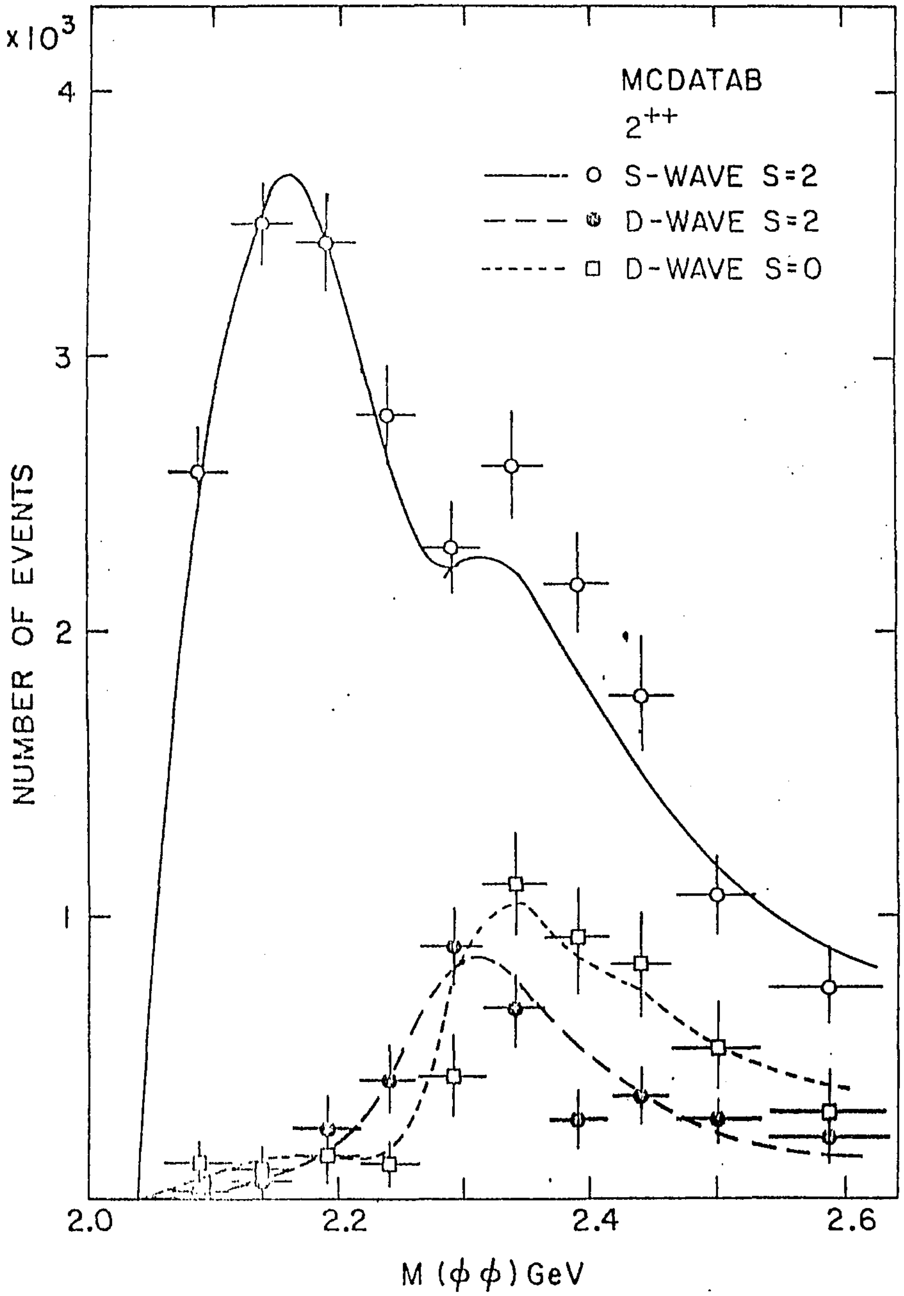

Fig. 5.3(a) A two-pole K-matrix fit (smooth curves) of the searched solution compared to the Monte Carlo generated $\phi\phi$ solution (file MCDATAB). The generated solution has background put in whereas the K-matrix fit did not consider the background contribution.

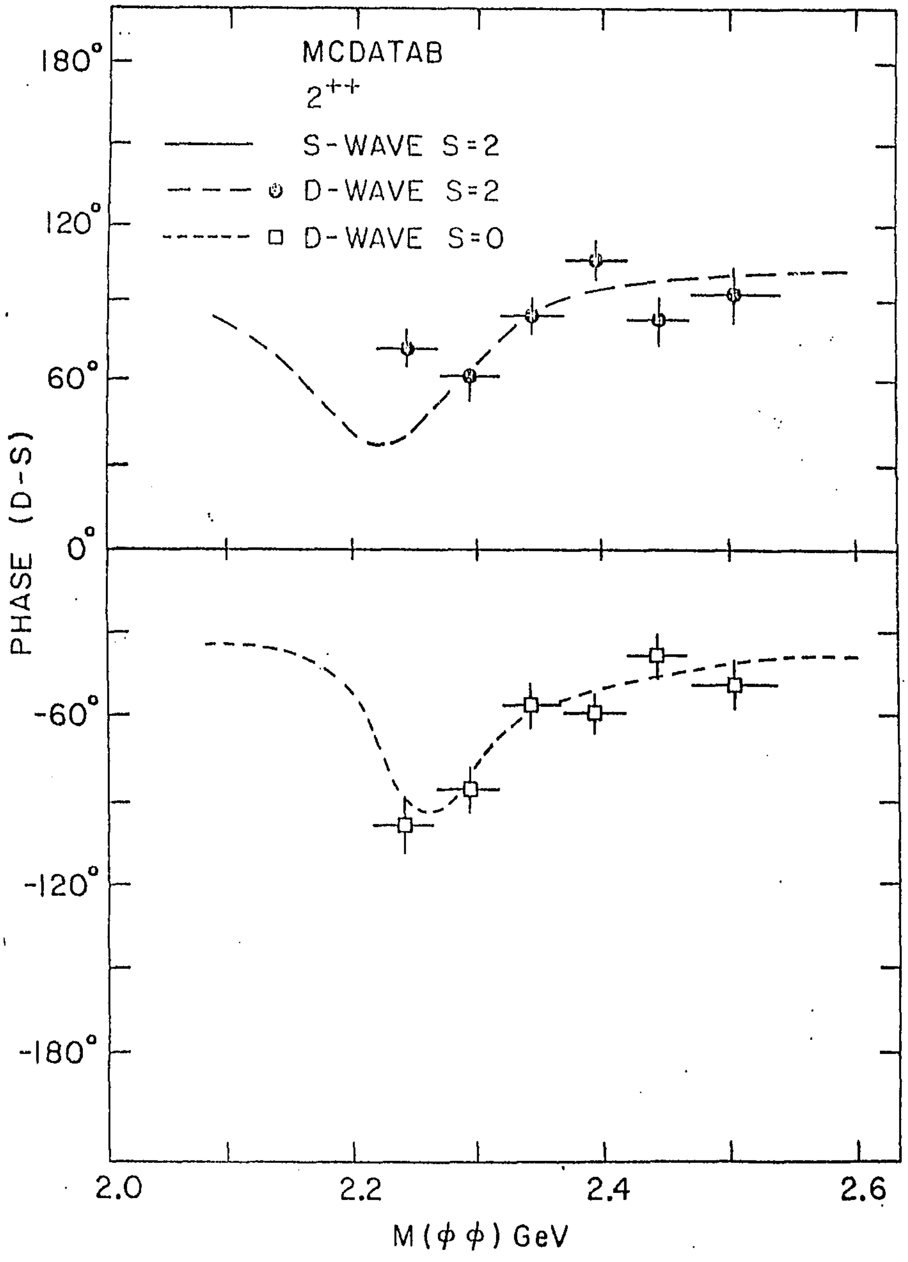

Fig. 5.3(b) A K-matrix fit of the phase difference (obtained from the searched solution) compared to the generated φφ solution (file MCDATAB). The generated solution has background put in whereas the K-matrix fit did not consider this.

CHAPTER 6: DATA FITTING AND RESULTS

6.1 Introduction

The phase II of Multiparticle Spectrometer was successfully completed in the spring of 1982 which was then quickly utilized to study the $\pi^- p \rightarrow \phi\phi n$ reaction.[29b] A collection of ≈ 1200 $\phi\phi n$ events were recorded for analysis purpose after satisfying certain selection requirements as well as some appropriate cuts as described in Chapter 4. These statistics were raised to ≈ 4000 $\phi\phi n$ events in the following year (1983) which represented the highest $\phi\phi n$ statistics so far achieved in this exclusive channel.

6.2 Mass Spectrum

Except for the momentum threshold set in the Cerenkov counter, the spectrometer was operated under practically the same experimental conditions for both runs so that events recorded in both runs could be combined without fears of equipmented bias. The Cerenkov counter threshold was modified from 3.2 GeV/c (1982) to 2.8 GeV/c (1983), primarily for the cleaner kaon samples which also resulted in a slight increase in acceptance. A glance of the effective mass spectrum of the $\phi\phi$ system shown in Figs. 6.1 and 6.2 clearly demonstrates that within the limits of the statistical fluctuations each individual behavior and structure of these two sets of data representing the 1982 and 1983 runs are generally consistent over the entire spectrum. One should realize that a momentum cut of 3.2 GeV/c was applied to both data sets. However, near 2.44 GeV/c^2 the old (1982) $\phi\phi$ spectrum shows an abrupt change whereas the corresponding new (1983) spectrum shows a much more gradual variation. This, however, is consistent with a statistical fluctuation. The final spectrum obtained from the superposition of these two spectra is shown in Fig. 6.3.

In Fig. 6.3, one can easily see the characteristic threshold enhancement which peaks around 2.2 GeV/c^2, then followed by a rapid fall and becomes vanishingly small above 2.7 GeV/c^2. Also shown in Fig. 6.4 is the Monte Carlo determined acceptance of the apparatus for our final partial wave analysis solution. The result obtained for the acceptance is close to what one would expect from the phase space consideration.

Due to the rapid falling acceptance and production at high mass and the competing statistics required in order to get a meaningful partial wave analysis, those $\phi\phi$ events that have effective masses beyond 2.64 GeV/c^2 were removed from analysis. Furthermore, after imposing other cuts such as the ambiguous assignment of K^+K^- pairs to double ϕ's, a total of 3652 events were available for final analysis. This quantity of data samples was divided into ten mass bins between 2.04 and 2.64 GeV/c^2 of the $\phi\phi$ mass region. Each bin was 50 MeV/c^2 wide except near the ends where the bin widths were made wider to compensate for the low acceptance. Table 6.1 lists the bin widths and the number of events contained therein.

6.3 Data Folding and Symmetry

We had found that some characteristic structures for the $\phi\phi$ partial waves could be exhibited in a number of selected projections (α, $\alpha_1 \pm \alpha_2$, $\cos\beta$, γ, $\cos\theta$, $\cos\theta_1 \pm \cos\theta_2$) which were formed from the six independent decay angles (α_1, α_2, β, γ, θ_1, θ_2). In Chapter 5 we have explicitly demonstrated in the histogram plots that for a given partial wave described by a set of permitted $\phi\phi$ quantum numbers, these projections always show one or more characteristics unique to that particular wave and rejected by any other waves. This mutually exclusive property for any pairs of partial waves makes the $\phi\phi$ data very selective among a variety of possibilities, in sorting the waves which correctly represent the $\phi\phi$ states.

Table 6.1

Ranges and the corresponding sizes of data in ten mass bins

Mass Range (GeV)	Width (MeV)	Events
2.040 - 2.115	75	423
2.115 - 2.165	50	471
2.165 - 2.215	50	528
2.215 - 2.265	50	476
2.265 - 2.315	50	418
2.315 - 2.365	50	381
2.365 - 2.415	50	340
2.415 - 2.465	50	215
2.465 - 2.540	75	215
2.540 - 2.640	100	185
	TOTAL	3652

In the following we shall discuss how to present these projections in order to satisfy the symmetry requirements.

6.3.1 Double entries for α and $\cos\theta$

In presenting our data we wish to point out that since each event has two ϕ's, so these gave twice as many entries in α and $\cos\theta$ distributions as the number of events available.

6.3.2 Discussion of symmetry

It has been described in Section 1.6 that the $\phi\phi$ system has two fundamental symmetries associated with it, i.e., Bose symmetry and Charge symmetry. These symmetries simply state that the amplitudes for the $\phi\phi$ remain the same upon:

(a) exchange the labels of the two ϕ's. (Bose symmetry)

(b) exchange frames of reference for K^+ and K^-. (Charge symmetry)

Of course, the $\phi\phi$ data must be presented in a form in accordance with these exchange processes. To this end, these procedures were implemented by some simple transformations for the six decay angles (α_1, α_2, θ_1, θ_2, β, γ):

(a') To satisfy (a), interchange ϕ_1 and ϕ_2 in Gottfried-Jackson frame (Fig. 2.2):

$$\alpha_1 \to \alpha_2, \qquad \alpha_2 \to \alpha_1 \tag{6.1}$$

$$\theta_1 \to \theta_2, \qquad \theta_2 \to \theta_1 \tag{6.2}$$

$$\beta \to \pi - \beta, \qquad \gamma \to \pi + \gamma \tag{6.3}$$

(b') To satisfy (b), interchange K^+ and K^- in ϕ's rest frame (Fig. 2.3):

$$\alpha_1 \to \pi + \alpha_1, \qquad \alpha_2 \to \pi + \alpha_2 \tag{6.4}$$

$$\theta_1 \to \pi - \theta_1, \qquad \theta_2 \to \pi - \theta_2 \tag{6.5}$$

It follows that the symmetrization of $\phi\phi$ data becomes the procedures of folding the angular distributions according to the transformations (6.1) through (6.5) for the eight projections obtained from the six decay angles.

6.3.3 Reduced Ranges and Data Folding

An immediate effect of folding is the reduction in range by mapping. We shall discuss each projection in turn to see how the $\phi\phi$ events are mapped and binned.

(a) γ and $\cos\beta$

It is obvious from Fig. 2.2 and Eq. 6.3 that the distribution for γ is periodic in π but $\cos\beta$ has left-right symmetry.

(b) $\text{Cos}\theta$, $\cos\theta_1 \pm \cos\theta_2$

First we note that in order to equalize the phase space in each histogram bin we used instead of $\cos\theta_1 \pm \cos\theta_2$ the transformed quantities

$$\cos\theta_1' \pm \cos\theta_2' = (\cos\theta_1 \pm \cos\theta_2)\ (1 - \frac{|\cos\theta_1 \pm \cos\theta_2|}{4}) \qquad (6.6)$$

and the limits for these parameters also changed accordingly from $-2 \leq \cos\theta_1 \pm \cos\theta_2 \leq 2$ to $-1 \leq \cos\theta_1' \pm \cos\theta_2' \leq 1$.

Then Eqs. 6.2 and 6.5 show that these three projections $\cos\theta$, $\cos\theta_1' \pm \cos\theta_2'$ all indicate left-right symmetry.

(c) α

An examination of the scatter plot for α_1 versus α_2 (Fig. 6.5) clearly indicates that exchanging the labels of ϕ_1 and ϕ_2 results in point A (α_1, α_2) having a mirror point A' (α_2, α_1) with respect to the diagonal MN. Then Eq. 6.4 maps A and A' to the points B $(\alpha_1 + \pi, \alpha_2 + \pi)$ and B' $(\alpha_2 + \pi, \alpha_1 + \pi)$. Therefore α-distribution is periodic in π.

The pattern of the observed α-distribution can be expressed, to the first approximation, as a linear combination of constant, $\cos\alpha$ and $\cos 2\alpha$, i.e. $F(\alpha) = A + B\cos\alpha + C\cos 2\alpha$, where A, B, C are constants. However, the linear term such as $\cos\alpha$-like or $\sin\alpha$-like should not enter the $\phi\phi$ system because of the spin 1 nature of ϕ and the inherent symmetry connected with the double ϕ system. This can be seen as follows:

At the amplitude level α appears only in the exponent weighed by three different values of helicity, $e^{i\mu\alpha_1}$ or $e^{i\lambda\alpha_2}$ where helicities $\mu, \lambda = 1, 0, -1$. The exchange naturality of each wave is identified by the respective real and imaginary parts of this complex function:

waves with unnatural parity exchange ~ $\mathrm{Re}(e^{i\nu\alpha}) = \cos\nu\alpha$

waves with natural parity exchange ~ $\mathrm{Im}(e^{i\nu\alpha}) = \sin\nu\alpha$

where ν stands for either μ or λ, α stands for either α_1 or α_2. Since waves with opposite exchange naturalities can never interfere so the cross section deduced from either naturality is represented by, upon integrating over all other kinematic variables, either

$$\sigma_{\mathrm{unnatural}} \propto \left|A' + C'\cos\alpha\right|^2 = A + B\cos\alpha + C\cos2\alpha$$

or

$$\sigma_{\mathrm{natural}} \propto \left|E' + F'\sin\alpha\right|^2 = E + F\sin\alpha + G\cos2\alpha$$

Putting in the effect of charge conjugation, $K^+ \to K^-$, with the associated transformation $\alpha \to \pi + \alpha$, we get immediately

$$\cos(\alpha + \pi) = -\cos\alpha \tag{6.7a}$$

$$\sin(\alpha + \pi) = -\sin\alpha \tag{6.7b}$$

Eqs. 6.7 imply the violation of charge symmetry, thus it is anticipated that all coefficients for linear terms such as $\cos\alpha$ and $\sin\alpha$ must vanish in order to conserve charge symmetry:

$$B = F = 0.$$

The appearance of the first or any odd harmonics in α-distribution would be attributed to the charge symmetry which can be understood if the interference phenomenon takes place between the $\phi\phi$-allowed partial waves which necessarily preserve charge symmetry and the non-$\phi\phi$ background waves which can violate this symmetry. The subsequent result of this effect will enhance one peak but reduce the other peak in the α projection. The final observation is the production of the $\cos\alpha$

structure as shown in Fig. 6.20. We shall return to this discussion when we consider the coherent background in Section 6.6.

Thus we anticipate on physical grounds that because the $\phi\phi$ system has to be symmetric and the absence of odd harmonics, it has a natural range of $\pi/2$ for α. Its precise variation is expected to be periodic and symmetrical like the curves drawn in Fig. 5.1. On the other hand, the manifestation of the charge asymmetry can be fully displayed with a π range [Fig. 6.20].

(d) $\alpha_1 + \alpha_2$ ($= \chi$), $\alpha_1 - \alpha_2$

It should be emphasized that the binnings of the $\alpha_1 - \alpha_2$ and χ entries are along the directions parallel to the diagonals SR and MN (Fig. 6.7). In this manner, those events which are mapped into the parallelograms MRSW and MRVN for binning are populated with equal phase space.

If we follow the full procedures for mapping α, including the final folding to obtain charge symmetry as described in the preceding section, we acquire a configuration as shown in Fig. 6.7 with all the points mapped by A (α_1, α_2) explicitly marked. It is clear from this figure that both χ and $\alpha_1 - \alpha_2$ have the same range $0 \rightarrow \pi$.

However, if only the periodic nature of α is assumed plus the characteristics of the pure waves (Fig. 5.1) and our knowledge of the spin of ϕ, the same range ($0 \rightarrow \pi/2$) for χ and $\alpha_1 - \alpha_2$ are again obtainable. This can be deduced in the following steps:

(d.1) The Eq. 6.1 gives double entries for χ but reverses the sign for $\alpha_1 - \alpha_2$.

(d.2) Applying Eq. 6.4 results in each point of χ and $\alpha_1 - \alpha_2$ having the repetitive occurrences after each 2π.

(d.3) The combination of the reflection symmetry with respect to the origin and the repetition period of 2π for $\alpha_1 - \alpha_2$ implies that the period of $\alpha_1 - \alpha_2$ can be further reduced to π.

(d.4) To satisfy both the reflection symmetry and the π periodicity for $\alpha_1 - \alpha_2$ it is quite safe to discard the $\sin 2(\alpha_1 - \alpha_2)$ and $\sin(\alpha_1 - \alpha_2)$ type distributions because they are anti-symmetric ω.r.t. the origin. This leaves the symmetric cosine function to be the only possibility and the final range used to show the $\alpha_1 - \alpha_2$ distribution is reduced to $0 \rightarrow \pi/2$. This range necessarily excludes the possibility of $\cos(\alpha_1 - \alpha_2)$ type structure.

(d.5) Turning to χ, it is not surprising that $\cos\chi$ may not vanish identically because χ is periodic in 2π but not necessary to be symmetric between 0 and π. The 2π period can be shown to follow from the charge symmetry, since

$$\alpha_1 \rightarrow \alpha_1 + \pi \text{ and } \alpha_2 \rightarrow \alpha_2 + \pi$$

hence

$$\chi = \alpha_1 + \alpha_2 \rightarrow \chi + 2\pi \tag{6.8}$$

One would expect from Eq. 6.8 that the basic range for χ is $0 \rightarrow \pi$.

To understand more about χ-distribution we consider the basis vector $G^j(\gamma,\beta,\alpha_1,\alpha_2,\theta_1,\theta_2)$ defined by Eq. 2.1 which is connected with χ only when helicities $\mu = \lambda = \pm 1$. To simplify our discussions we only display the α's and θ's dependence for G^j:

$$G^{J^PLSM^\eta}(\gamma,\beta,\alpha_1,\alpha_2,\theta_1,\theta_2) = \sum_{\mu,\lambda} C_{\mu,\lambda}^{J^PLSM^\eta}(\gamma,\beta) \cdot g_{\mu\lambda}(\alpha_1,\alpha_2,\theta_1,\theta_2) \tag{6.9}$$

where

$$g_{\mu\lambda}(\alpha_1,\alpha_2,\theta_1,\theta_2) = e^{i\mu\alpha_1} e^{i\lambda\alpha_2} d^1_{\mu,0}(\theta_1) d^1_{\lambda,0}(\theta_2) \tag{6.10}$$

and the Clebsch-Gordon coefficients are absorbed in $C_{\mu,\lambda}^{J^PLSM^\eta}$.

For

$$\mu = \lambda = \pm 1 \qquad g_{\mu\lambda} \sim e^{\pm i\chi} \sin\theta_1 \sin\theta_2 \qquad (6.11)$$

$$\mu = \lambda = 0 \qquad g_{\mu\lambda} \sim \cos\theta_1 \cos\theta_2 \qquad (6.12)$$

$$\mu = 0,\ \lambda = \pm 1 \qquad g_{\mu\lambda} \sim e^{\pm i\alpha_1} \cos\theta_1 \sin\theta_2 \qquad (6.13)$$

$$\lambda = 0,\ \mu = \pm 1 \qquad g_{\mu\lambda} \sim e^{\pm i\alpha_1} \sin\theta_1 \cos\theta_2 \qquad (6.14)$$

$$\begin{aligned} \lambda &= 1,\ \mu = -1 \\ \lambda &= -1,\ \mu = 1 \end{aligned} \qquad g_{\mu\lambda} \sim e^{\pm i(\alpha_1-\alpha_2)} \sin\theta_1 \sin\theta_2 \qquad (6.15)$$

Eqs. 6.11 through 6.15 are obtained by direct substitutions of $d^1_{1,0}(\theta) = - d^1_{-1,0}(\theta) = -\sin\theta/\sqrt{2}$ and $d^1_{0,0}(\theta) = \cos\theta$ into Eq. 6.10.

To get the cross section for a particular set of quantum numbers, it is necessary to sum over all helicity indices μ, λ shown in Eq. 6.9 and then squared. After expansion, cross terms involving χ can be obtained by the appropriate products of Eq. 6.9 through Eq. 6.15. It is readily seen that among the possible products formed from these expressions there are only two combinations which can provide with the desired χ-dependence but independent of other α's, other combinations show the α-dependence in the forms like $e^{\pm i\alpha_k}$, $e^{\pm 2i\alpha_k}$ or $e^{\pm i(\alpha_1-\alpha_2)}$ ($k = 1,2$). These two products are obtained by combining Eqs. 6.11 and 6.12 as well as Eqs. 6.13 and 6.14, both of them are represented by the same expression

$$F(\chi,\theta_1,\theta_2) = e^{\pm i\chi} \sin 2\theta_1 \sin 2\theta_2 \qquad (6.16)$$

with real and imaginary parts given by

$$\mathrm{Re}\, F = \sin 2\theta_1 \sin 2\theta_2 \cos\chi \qquad (6.17a)$$

$$\mathrm{Im}\, F = \sin 2\theta_1 \sin 2\theta_2 \sin\chi \qquad (6.17b)$$

With reference to Fig. 6.6 it is clear that $\sin 2\theta_1 \cdot \sin 2\theta_2$ changes sign upon shifting a point by $\pi/2$ from one quadrant to the adjacent one (A → B). Performing such an operation just once is equivalent to interchange K^+ and K^- for one ϕ. A double shifts (A → B → C) which preserve charge symmetry will restore the sign as before. An integration of $\sin 2\theta_1 \sin 2\theta_2 e^{\pm i\chi}$ over $0 \rightarrow \pi$ for both θ's will make this term vanishes. So we do not expect to observe $\sin\chi$- or $\cos\chi$-type distributions if charge symmetry is preserved.

We thus conclude that if charge symmetry is satisfied, the $\cos 2\chi$ is the only possible structure contributing to the χ-distribution with a natural range of $\pi/2$. However, a $\cos\chi$ term can be generated from the charge symmetric $\phi\phi$ amplitudes by selectively binning. Gathering events corresponding to K^+ [first and third quadrants of Fig. 6.6] and K^- [second and fourth quadrants]. Typical χ-distributions in $0 \rightarrow 2\pi$ range were shown separately for K^+ [Fig. 6.7(b)] and K^- [Fig. 6.7(c)]. It is obvious from these two figures that each of these two oppositely charged particles shows its own characteristic structure. The $\cos\chi$-type distribution could be demonstrated by folding events into $0 \rightarrow \pi$ range and taking into account the signs of deviations ΔN due to K^+ (K^-) resulted in addition (subtraction) to the average in each bin considered. In actual histogram plots this charge effect was considered by employing the following relation:

$$N^b = \frac{N_+^b + N_-^b + N_+^{b+\pi} + N_-^{b+\pi}}{2} + (N_+^b - N_-^b) \tag{6.18}$$

where N^b = Number of events in bin b of final histogram,

$N_+^b(N_-^b)$ = Number of events contributed to N^b due to positive (negative) charge,

$N_+^{b+\pi}(N_-^{b+\pi})$ = Number of events contributed to $N^{b+\pi}$ due to positive (negative) charge.

It is easy to see that the last term ($N_+^b - N_-^b$) of Eq. 6.18 enhances (reduces) the positive (negative) charge contribution from the average [Fig. 6.7(d)].

In Table 6.2 we summarize our discussions of folding for all the parameters used in our analysis. We emphasize once again that the reduced ranges and the data points mapped therein can fully represent the original data, the latter generally extended to wider intervals.

6.3.4 Unnatural Parity Exchange

If Ω stands for either χ or $\alpha_1 - \alpha_2$ then it is clear that with reference to Figs. 5.1(a) through 5.1(h) all the pure waves for Ω distributions show the cosine square-type structure for the unnatural parity exchange (η = −) while the natural parity exchange (η = +) shows the sin square-type structure over the same range. The fact that the patterns of the Ω projections for the $\phi\phi$ data can be recognized as the cosine square-type structure has already suggested that η = − is the correct parity exchange for reaction A.1. This is consistent with the final results which indicate that the three dominant waves identified in the $\phi\phi$ system all have η = −.

6.4 t-Dependence and Peripheral Production

Attempts to understand the production mechanism of the reaction $\pi^- p \rightarrow \phi\phi n$ is made by examining the t'-distribution. Among the possible exchange modes the gross feature of the slope at low t' [$|t'| < 0.3$ (GeV/c^2] as determined from the logarithmic dn/dt' vs t' plot, indeed shows that the production is preferentially peripheral.

6.4.1 Exchange Mechanism

Consider the process $\pi^- p \rightarrow \phi\phi n$ as via an intermediate state

$$\pi^- p \rightarrow Gn \rightarrow \phi\phi n \tag{6.19}$$

Table 6.2(a)

Foldings of the Eight Angular Distributions which Preserve the Bose and Charge Symmetries

Projection	Full Range	Nature of Symmetry	Reduced Range
α	$0 \to 2\pi$	periodic symmetric	$0 \to \pi/2$
$\chi = \alpha_1 + \alpha_2$	$0 \to 4\pi$	periodic symmetric	$0 \to \pi/2$
$\alpha_1 - \alpha_2$	$-2\pi \to 2\pi$	periodic symmetric	$0 \to \pi/2$
$\cos\beta$	$-1 \to 1$	symmetric	$0 \to 1$
γ	$0 \to 2\pi$	periodic	$0 \to \pi$
$\cos\theta$	$-1 \to 1$	symmetric	$0 \to 1$
$\cos\theta_1' + \cos\theta_2'$	$-1 \to 1$	symmetric	$0 \to 1$
$\cos\theta_1' - \cos\theta_2'$	$-1 \to 1$	symmetric	$0 \to 1$

Table 6.2(b)

Folding of an Angular Distribution which Violates the Charge Symmetry

Projection	Full Range	Nature of Symmetry	Reduced Range
α	$0 \to 2\pi$	periodic	$0 \to \pi$

Table 6.2(c)

Special binning with cuts on $\cos\theta_1$ and $\cos\theta_2$.

Projection	Full Range	Nature of Symmetry	Reduced Range
χ	$0 \to 4\pi$	periodic	$0 \to \pi$

where G denotes the intermediate state which can be identified by the glueballs. Fig. 6.9 shows the process $\pi^- p \rightarrow Gn$ in the center-of-mass frame where θ_s is the s-channel scattering angle. The 4-momentum transfer squared $t = (P_\pi - P_G)^2$ is related to the scattering angle by $t = -P^2(1 - \cos\theta_s) \cdot P_\pi$. P_G are 4-momentum vectors and $\vec{P}$ is the three momentum of the π^- in the center-of-mass.

It is readily seen that the charge exchange between the incident π^- and the target p as shown in Fig. 6.8 as well as the definite necessity for conserving the G-parity at the production vertex yield the exchange particle must have the quantum numbers I = 1 and negative G-parity. Candidates with these quantum numbers which are likely to play the significant roles in the exchange processes could be narrowed down to the π, A_1 and A_2. The quantum numbers, the naturalities of the allowed exchange particles (π, A_1, A_2), and the corresponding J^{PC} of the $\phi\phi$ states are given in Table 6.3.

Table 6.3

The Quantum Numbers and the Naturalities of the Allowed Exchange Particles for $\pi^- p \rightarrow \phi\phi n$ Along with the J^{PC} Values of the Associated $\phi\phi$ States. M = 0 for all Exchanges.

Exchange Mode	$I^G J^P$ (M=0)	Naturality	J^{PC} of the $\phi\phi$ States
π	$1^- 0^-$	Unnatural	$0^{++}, 2^{++}, 4^{++}$
A_1	$1^- 1^+$	Unnatural	$0^{++}, 1^{-+}, 2^{++}, 3^{-+}, 4^{++}$
A_2	$1^- 2^+$	Natural	$1^{++}, 3^{++}, 0^{-+}, 2^{-+}$

6.4.2 t'-Plot and Peripheral Production

To sort out the dominant exchanges underneath the $\phi\phi n$ events a plot of dn/dt' in logarithmic scale against t' is displayed in Fig. 6.10. Events are binned in t'-intervals of 0.02 $(\mathrm{GeV}/c)^2$. Within the statistical errors, the gross feature of the t'-plot indeed can be described by an exponential function $e^{bt'}$ with two different slopes b. The points appeared at low t' ($|t'| < 0.3\ (\mathrm{GeV}/c)^2$) are characterized by a linear fit which shows a trend of rapid fall-off with increasing t' at a rate faster than those appeared at high t' ($|t'| > 0.3\ (\mathrm{GeV}/c)^2$).

In the following we list the best values of the slope b in these two distinct t'-intervals which were derived from the least squares method:

(a) For $|t'| < 0.3\ (\mathrm{GeV}/c)^2$, $b = 9.4 \pm 0.7$.

(b) For $|t'| > 0.3\ (\mathrm{GeV}/c)^2$, $b = 7.0$.

A large statistical error is connected with the high t'-region which is related to the lack of statistics in this region. Because of this limited statistics we had not imposed any t'-cut to remove the $\phi\phi$ events from the high t'. However, we had examined the various angle projections of our data with a cut at $t' = 0.3\ (\mathrm{GeV}/c)^2$ and compared to the corresponding projections of the overall integrated samples without this cut. The result of this comparison showed no noticeable deviations from each other. It is thus justifiable in present work to include both low- and high-t' events in our analysis.

The slope obtained in (a) above is compatible with the value expected from the π-exchange and undoubtedly rules out the possibilities of A_1 or A_2 as important exchanges. Guided by this result we are thus led to the important conclusion that the π-exchange dominates the production mechanism for Reaction A.1. The subsequent process can be effectively expressed by

$$\pi\pi \rightarrow \phi\phi \tag{6.20}$$

In order to determine the t-dependence in the production amplitudes we would have to accumulate high enough statistics in future runs.

6.4.3 A_1 and A_2 Exchanges

Fig. 6.10 shows two linear fits with different slopes b. To deduce quantitatively the relative amount of samples enclosed in the area bounded by the fit with b = 7.0 we have constructed a linear combination of these two exponential functions given by

$$N(t') = Ae^{-9.4t'} + Be^{-7t'} \equiv N_1'(t') + N_2'(t') \tag{6.21}$$

and integrated over the t'-variable

$$N_1 = \int_0^{0.3} N_1'(t')dt' + \int_{0.3}^{0.6} N_2'(t')dt' \tag{6.22a}$$

$$N_2 = \int_0^{0.6} N_2'(t')dt' \tag{6.22b}$$

where N_1 = number of events bounded by both fits, and

N_2 = number of events bounded by linear fit with b = 7.0.

The ratio $R = N_2/N_1 \sim 15\%$ as determined from the last two integrals (Eqs. 6.22) is an estimate of the exchange modes for Reaction A.1 not induced by π-exchange. The discussion of the allowed exchanges mentioned in Section 6.4.1 suggests that the A_1 and A_2 exchanges are most likely responsible for this part.

The above estimated contaminations of A_1 and A_2 exchange modes can be used to compare with the results obtained from the CERN-Munich Collaboration.[45] This group had studied the reaction $\pi^-p \rightarrow \pi^+\pi^-n$ at 17.2 GeV/c using polarized proton target and found the presence of strong polarization-dependent moments which indicated the s-channel nucleon spin-non-flip amplitudes for unnatural parity exchange. These amplitudes were interpreted as corresponding to A_1 exchange. At low-t ($.005 < |t| < 0.2$ GeV^2/c^2) the ratio of A_1 to π exchanges was measured in this channel to be ~ 4%. In order to compare with our results this ratio R was extrapolated from 17.2 GeV/c to 22.6 GeV/c incident pion momentum using the following simple relations:

$$\sigma_{A_1}(\text{cross section for } A_1) \propto 1/(P_{lab})^{3/2} \tag{6.23}$$

$$\sigma_{\pi}(\text{cross section for } \pi) \propto 1/(P_{lab})^{2} \tag{6.24}$$

where P_{lab} is the incident beam momentum in the laboratory frame. Combining Eqs. 6.23 and 6.24, the ratio of A_1 to π exchanges extrapolated to 22.6 Gev/c is found to be

$$R(P_{lab} = 22.6 \text{ GeV/c}) = \left(\frac{22.2}{17.2}\right)^2 \cdot \left(\frac{17.2}{22.2}\right)^{3/2} \cdot 4\% \sim 4.5\% \tag{6.25}$$

The amount of natural parity exchange (A_2) was similarly determined in the $\pi^+\pi^-$ channel, its magnitude was found to be approximately the same as A_1 exchange at 17.2 GeV/c. It follows that the overall A_1 and A_2 exchanges as measured in te $\pi^-p \to \pi^+\pi^-n$ reaction (~ 9%) is compatible with our results (~ 15%) keeping in mind that large statistical fluctuations are connected with our low statistics in the determination of the abundances responsible for A_1 and A_2 exchanges.

6.4.4 One-Pion-Exchange in Relation to Glueballs

The finding of the peripheral production mechanism in the last section provides an independent way of justifying the simple quark structure diagram (Fig. 1.8) in which one particle exchange appears to be necessary. This quark diagram, if incorporated with the QCD according to which the gluons mediate the non-Abelian gauge field, may be viewed as a pion radiating some gluons during its exchange process. It is not surprising that the subsequent self-interactions of the radiated gluons in sweeping through a variable mass range could eventually end up with the formation of the glueballs in a form of resonance if some glueball states are available within that range.

From the phenomenological point of view, the intervention of the glueballs is the cause of the observed breakdown of the OZI rule already discussed in Chapter 1. Following this argument one can say that the glueballs play the role to bridge the gap between the two disconnected parts of the quark line diagram [Fig. 1.8].

6.5 Fitting Procedure

The primary function of the MPS SUMMARY program was to make the final $\phi\phi n$ event selections. For those events survived after running the SUMMARY program the five-vectors for each particle involved in the reaction (π^-, p, n, K_1^+, K_1^-, K_2^+, K_2^-) were calculated in the laboratory frame. The complete set of five-vector for a particle is defined as the momentum-energy (P, E) four-vector together with the rest mass (M) of that particle and consistently expressed in this order (P_x, P_y, P_z. E, M). All these five-vectors for our $\phi\phi$ data were stored in the computer for active use and also on tape for backup on event-by-event basis. At this stage our data were in a state ready for PWA.

In order to proceed with the fitting procedure we need to employ two more programs originally developed by SLAC-Berkeley Collaboration. The first program TRIA2[35] fully utilized the isobar model formulation as described in Chapter 2 to calculate the various partial wave basis vectors of decay amplitudes $G^{J^PLSM^\eta}(\gamma,\beta,\alpha_1,\alpha_2,\theta_1,\theta_2)$ as well as the acceptance normalization integrals M_{jk} for our data. These two physical quantities are defined in Eqs. 2.1 and 2.3 respectively. The second one OPTIME[46] is a fitting program which applied the previous results of the decay amplitudes and the acceptance normalization integrals to give a quantitative measure of the loglikelihood function for each partial wave or the combinations of them.

For completeness we state here that the complete set of the $\phi\phi$-allowed partial waves considered in present analysis had to be specified for both TRIA2 and OPTIME. Table 6.4 shows the 52 partial waves considered with $J = 0,1,2,3,4$; $L = 0,1,2,3$; $S = 0,1,2$; $-J \leq M \leq J$; $P = \pm$; $\eta = \pm$.

6.5.1 Preparations of Decay Amplitudes and Acceptance Normalization Integrals

The standard isobar PWA program was used, however it should be noted that due to the narrowness of the ϕ this PWA is independent of the isobar model and, for that matter, any modelistic assumptions. The isobar model enables us to obtain the basis vector $G^j (j = J^P LSM^\eta)$ of the decay amplitudes following the results of five-vector supplied by SUMMARY program. For a given allowable combination of j, G^j can be expressed in general as a sum of nine triple d-functions weighed appropriately by a product of two Clebsch-Gordon coefficients. These basis vectors were calculated corresponding to the complete set of partial waves (Table 6.4) for each event. To improve the computational efficiency we used a quick version of TRIA2, the essential idea was to tabulate the numerical values of the pre-calculated C-G coefficients in an easily accessible way so that basis vectors can be efficiently calculated upon calling this table. A similar Table was made for the D-functions on an event-by-event basis.

The matrix element M_{jk} of the acceptance normalization integral was obtained by randomly generating a number of $\phi\phi n$ events in the

Table 6.4

List of partial waves tried in the PWA

Order of labels (JPLSMη): (Spin, Parity, Relative Orbital Angular Momentum, Total Intrinsic Spin, Z-Component of Spin, Exchange Naturality)

I(Isospin) = 0 for all partial waves

0+S00-
2+S20-
2+S21-
2+S22-
2+S21+
2+S22+
0-P10+
1-P10-
1-P11-
1-P11+
2-P10+
2-P11+
2-P12+
2-P11-
2-P12-
0+D20-
1+D20+
1+D21+
1+D21-
2+D00-
2+D01-
2+D02-
2+D01+
2+D02+
2+D20-
2+D21-
2+D22-
2+D21+
2+D22+
3+D20+
3+D21+
3+D22+
3+D23+
3+D21-
3+D22-
3+D23-
4+D20-
4+D21-
4+D22-
4+D23-
4+D24-
4+D21+
4+D22+
4+D23+
4+D24+
3-F10-
3-F11-
3-F12-
3-F13-
3-F11+
3-F12+
3-F13+

S,P,D,F, are usual spectroscopic notation for L = 0,1,2,3 center-of-mass of the $\phi\phi$ system according to a phase space distribution at some specified $\phi\phi$ mass range. The size of the generated samples, after acceptance correction, was roughly a factor ten larger than the actual data samples. For each event generated the same isobar model was used to calculate the basis vectors corresponding to the 52 partial waves, results of these calculations were stored on tape. To estimate the acceptance effect, the entire generated samples were detected in the Monte Carlo simulation of our MPS apparatus. Loss of events due to the geometrical acceptance of the spectrometer and triggering devices, difficulties in pattern recognition, deficiency of triggering devices, random noise generated within the electronics, decay and interactions of the final state particles, were all considered in acceptance corrections. These acceptances were again stored on tape.

We have prepared three sets of acceptance normalization integral. The first two sets were primarily set for preliminary wide bin searches which covered the mass ranges from 2.1 to 2.3 GeV, 2.19 to 2.39 GeV and 2.39 to 2.59 GeV. The last set was prepared for narrow bin final fitting which contained ten separate acceptance integrals covering the entire $\phi\phi$ mass spectrum studied (2.04 - 2.64 GeV) with each of the ten bin widths identical to the corresponding intervals divided for the real events.

6.5.2 Fitting with OPTIME

The loglikelihood function log L is defined in Eq. 2.4 in terms of the cross section $I(\Omega)$, acceptance normalization integral M_{jk} and production amplitudes represented by the complex fitting parameters A^j where $j,k = J^PLSM^\eta$. It was assumed that within each of the mass bins studied these A^j were constant throughout that interval. Fitting with OPTIME in any of these bins involved the iteration technique to determine these complex constants A^j in the loglikelihood maximizing procedure and thus determined the relative amounts of each partial wave present in that particular bin.

Following this idea, OPTIME fitting package essentially looked for sets A that corresponded to maxima of log L(A). To this end the program started from some random values of A then followed by the search of maxima in a succession of steps. At each step during iteration OPTIME determined the next step by calculating a function Φ, its first derivative vector and second derivative matrix through a modified form of the Newton-Raphson method. The change in A, ΔA, at each step was used to estimate the new A by a negative product of the variance matrix and the first derivative vector at the last step. The Newton-Raphson method recalculated the variance matrix afresh at each step. The modified version calculated a negative-definite approximation to the local second derivative matrix. This approximation was such that if the events were distributed nearly as the model predicted for a vector A then the approximation matrix was nearly equal to the local second-derivative matrix at A. Thus provided the loglikelihood function log L(A) was maximized the summation over all the quantum numbers j,k for each of the matrix elements $A_j M_{jk} A_k$ would equal to the total number of events used in the maximization of the loglikelihood function.

To improve the iteration technique a variable metric method[56] was used. The method enabled us to calculate the second derivative Φ_1'', using only the function ϕ_1, and its first derivative ϕ_1' at the present point together with the first and second derivative ϕ_0', ϕ_0'' at the previous point.

6.6 Backgrounds

One of the prominent features of the $\phi\phi$ channel was that very low backgrounds contaminated our data. We shall soon see that the estimated experimental background was ~ 13% in the region where PWA was carried out. The resolution of our apparatus is larger than the ϕ width, thus the true physical background in this absence is only a fraction of our observation. This quantity is small compared to the typical backgrounds encountered in most hadronic reactions in this mass range. Thus the almost absence-of-background makes the PWA analysis much simpler and more reliable. This is to a large extent due to the operation of OZI rule according to which the production of two ϕ mesons in non-strange hadronic interactions is inhibited in the absence of glueballs.

It is interesting to note that in addition to the ordinary incoherent background inherently buried in the $\phi\phi$ region, our analysis revealed a coherent background with C = − which interfered with the dominant $\phi\phi$ partial waves ($J^{PC} = 2^{++}$).

6.6.1 Determination of the Backgrounds by Extrapolation

In order to extract backgrounds mixed with the real $\phi\phi$ events it was speculated that the best channels to look for were among the OZI allowed processes which could also produce four-kaon ($K^+K^-K^+K^-$) final state. Motivated by the high intensity extended along the single-ϕ bands in the K^+K^- pair effective mass scatter plot shown in Fig. 1.6 which represented the ϕK^+K^- production, the backgrounds were measured by the reaction

$$\pi^- p \to \phi K^+ K^- n \qquad (6.26)$$

Backgrounds could also be contributed by the production of four independent kaons via another allowed process,

$$\pi^- p \rightarrow K^+K^-K^+K^- n \qquad (6.27)$$

but with significant lower production rate than the previous process.

Both the ϕK^+K^- and $K^+K^-K^+K^-$ events were present in the ϕ mass bands and indistinguishable from the $\phi\phi$ events in the overlap region where the two ϕ bands crossed each other. Thus it was sufficient to consider the reaction 6.26 for background determination.

Direct measurements were made in each of the ten mass bins used (Table 6.1) by an extrapolation procedure from the events lay in the ϕ band near the $\phi\phi$ overlap region of Fig. 1.6. This was done by selecting the ϕK^+K^- events enclosed in a portion of the ϕ band shown in the K^+K^- scatter plot. Effects due to the tail of the ϕ resonance and the falling acceptance at K^+K^- high mass were minimized by pertinent mass cuts to K^+K^-. Of course these cuts also had to be compromised with the desired statistics. Considering all these factors the ϕK^+K^- events selected for background extrapolation were finally taken from those with constituent K^+K^- effective mass satisfying the following condition:

$$1.048 \text{ GeV} < M_{KK} < 1.104 \text{ GeV} \qquad (6.28)$$

This interval was twice the width of the ϕ band (0.028 GeV) and 0.014 GeV away from the $\phi\phi$ region (Fig. 6.11).

6.6.2 Incoherent Background

A study of the measured background described in the preceding section, is consistent with the absence of any observable structures. We anticipated on physical grounds that this background is in principle mostly incoherent in nature. However, as we shall see in the next section, a relatively small amount representing the real part of a coherent background could interfere with the $\phi\phi$ system but the imaginary part would have no effect at all and therefore was combined with the incoherent background in the fitting process. The interfering background was small compared to the incoherent background. The presence of the incoherent background in the $\phi\phi$ data merely gave rise to the flat distributions in each of the projections (γ, $\cos\beta$, α, $\alpha_1 \pm \alpha_2$, $\cos\theta$, $\cos\theta_1 \pm \cos\theta_2$). This non-interfering part was represented by a special partial wave in our subsequent fitting procedure.

6.6.3 Coherent Background

A $\cos\alpha$-type structure (~ 20%) was found in the α-distribution. The systematics were carefully checked and they did not cause this. The partial wave analysis revealed some interference between the dominant $J^{PC} = 2^{++}$ $\phi\phi$ state (i.e., the S-wave, S = 2) and the coherent ϕK^+K^- background with C = −. A simple calculation shows that even the presence of a small coherent background (~ 1-2%) is sufficient to interfere with the 2^{++} S-wave (~ 70%) to generate the observed $\cos\alpha$-structure. The calculation proceeds as follows:

$$\text{interference term} = 2 \cdot A_{2^{++}} \cdot A_{CB} \qquad (6.32)$$

where $A_{2^{++}}$ and A_{CB} are the amplitudes for the 2^{++} partial wave and the coherent background respectively. Substituting the appropriate numbers into Eq. 6.32 we get

$$2 \cdot (0.7)^{1/2} \cdot A_{CB} = 0.2$$

or

$$|A_{CB}|^2 \sim 1\text{-}2\%. \qquad (6.33)$$

This does not represent a significant amount in the overall background but is detectable by interference.

(a) Analysis of Background

As an initial step we prepared a set of partial waves (Table 6.5) corresponding to the ϕK^+K^- system. Since the constituent kaons were isospin doublet, the total isopin of these waves had two possible values, 0 and 1. On the other hand, only the s and p waves were considered in the subsequent analysis. The complete set of notations for each ϕK^+K^- partial wave was represented by IJ^PLSM^η, every symbol except I (isospin) was the same as for $\phi\phi$ representations.

In order to determine the significant partial waves associated with the ϕK^+K^- background a quantitative analysis was made through the OPTIME fitting program. Events were taken from the ϕK^+K^- band with the effective mass ($M_{\phi KK}$) between 2.1 and 2.3 GeV and simultaneously satisfied the condition 6.28. Fitting was performed with only two waves at a time which represented the incoherent background and one of the ϕK^+K^- partial waves listed in Table 6.5. Results of these two-wave fits are also found in Table 6.5.

According to this table, the wave with quantum numbers j' ($=IJ^PLSM^\eta$) = 11^-S10^- has the highest loglikelihood (4750). An independent study had shown that a difference of 4.3 (see Appendix C) in loglikelihood value was equivalent to one standard deviation, i.e. $\Delta\log L$ = 4.3 implies a 1σ effect. Viewing this conversion number as a guidance, j' = 11^-S10^- partial wave is about 2.5σ better than the wave with the second highest loglikelihood (4739) with j' = 02^+S20^- or 5σ better than the next highest (4728) with j' = 12^+P10^-. Therefore the importance of this wave (j' = 11^-S10^-) is well justified. Note that this wave is not allowed by the $\phi\phi$ system and has negative charge conjugation.

(b) If we denote α_1 as the azimuthal angle of K^+ in the ϕK^+K^- background and α_2 as the corresponding angle for another K^+ due to the decay of ϕ, then a glance of the α_1 and α_2 distributions [Fig. 6.14(d) and

Table 6.5

Loglikelihood values calculated by OPTIME fitting program for each combination of incoherent background plus one ϕK^+K^- partial wave. Complete wave notation is represented by IJ^PLSM^η.

Waves with natural parity exchange		Waves with unnatural parity exchange	
Partial wave (IJ^PLSM^η)	Loglikelihood value for two-wave fit (incoherent background plus the partial wave on the left)	Partial wave (IJ^PLSM^η)	Loglikelihood value for two-wave fit (incoherent background plus the partial wave on the left)
02^+S21^+	4718	00^+S00^-	4722
02^+S22^+	4718	02^+S20^-	4739
00^-P10^+	4718	02^+S21^-	4719
01^-P11^+	4718	02^+S22^-	4718
02^-P10^+	4718	01^-P10^-	4718
02^-P11^+	4718	01^-P11^-	4718
02^-P12^+	4719	02^-P11^-	4718
11^-S11^+	4718	02^-P12^-	4718
11^+P10^+	4718	11^-S10^-	4750
11^+P11^+	4726	11^-S11^-	4718
12^+P11^+	4722	10^+P10^-	4718
12^+P12^+	4718	11^+P11^-	4725
		12^+P10^-	4728
		12^+P11^-	4719
		12^+P12^-	4718

(e)] clearly demonstrates that each plot has its own characteristics. One can easily identify from these plots that α_2 shows pure $\cos 2\alpha$ structure whereas α_1 shows both $\cos\alpha$ and $\cos 2\alpha$ structures. Thus we conclude the partial wave 11^-S10^- ($J^{PC} = 1^{--}$) is present in the background and its interference with the dominant 02^+S20^- wave ($J^{PC} = 2^{++}$) explains the $\cos\alpha$ term. The pure $\cos 2\alpha$ structure can be understood as a natural consequence of $\phi\phi$ characteristics. However, the situation is different for the interference between the scalar system K^+K^- and the vector meson ϕ since scalar particles have no α dependence ($\mu = \lambda = 0$ for spinless particles) and should give flat α-distribution. Moreover, since the ϕK^+K^- system ($C = -$) is not required to preserve charge symmetry thus in changing from K^+ to K^- with the transformation $\alpha \to \alpha + \pi$, the subsequent interference will be either constructive at $\alpha = 0$ (or π) or destructive at $\alpha = \pi$ (or 0) depending on the sign of the interference term. Therefore, this explains the α_1-distribution as seen in Fig. 6.14(d). Similar effects are not observed in the $\cos\theta_1$ and $\cos\theta_2$ plots [Figs. 6.14(f) and (g)].

(c) Attempts to fit three-wave or four-wave with OPTIME were also tried, results of the loglikelihood values indicated that only the combination of incoherent background, 11^-S10^- and 02^+S20^- waves were significant in the ϕK^+K^- background spectrum.

After the preliminary wide bin search we then moved to the narrow bins. However, because of the limited quantity of the available background events (~ 800) we found it statistically meaningful only to group them into four mass bins each of 100 MeV wide. To determine the actual amounts of the three significant waves in each of these bins, a three-wave fit was done by OPTIME. Results of these fits together with the fitted curves made to each curve are given in Fig. 6.12. It is clear that the 02^+S20^- was not important as compared to the other two and was considered as part of the incoherent background. Therefore, we have primarily incoherent background, with a small amount of coherent ($j' = 11^-S10^-$) background.

6.6.4 Determinations of Coherent and Incoherent Backgrounds

Both the coherent and incoherent backgrounds were determined by the probability trials. This made use of the fits shown in Fig. 6.12 which enabled us to find the relative weights of these two backgrounds in each of the ten bins (Table 6.1). These weights were regarded as the probabilities to test a collection of events so that the amounts of coherent and incoherent backgrounds could be determined for these bins (Fig. 6.13). The method proceeded as follows:

Once the effective mass of an extrapolated event was calculated this same event underwent probability tests repeated ten times by random generation of numbers between 0 and 1. These numbers were compared to the weight corresponding to this mass. Depending on the magnitudes of the generated numbers background events were either coherent or incoherent. This procedure minimizes the statistical fluctuations. Results obtained by this method and the smoothed values obtained by fitting were also provided in Table 6.6(a). Note that the smoothed curves always satisfied the following constraint:

$$\left|CB_{EXT}\right|^2 + \left|IB_{EXT}\right|^2 = \left|CB_{SMO}\right|^2 + \left|IB_{SMO}\right|^2 \qquad (6.34)$$

where $CB_{EXT(SMO)}$ = amplitude for the extrapolated (smoothed) coherent background

$IB_{EXT(SMO)}$ = amplitude for the extrapolated (smoothed) incoherent background.

It is interesting to note that the ratio of coherent to incoherent backgrounds shown in Table 6.6(a) is in general a factor of 2 larger than the corresponding ratio measured from the two background curves shown in Fig. 6.12 according to which the values listed in Table 6.6(a) were derived. At first sight this result seems confusing, however a second thought would show that this inconsistency can be explained by a combination of the Bose-Einstein interference and the Watson final state interaction for the following reason:

The amplitude for the ϕK^+K^- events in a single ϕ band is either $A_{\phi_1 K_2^+ K_2^-}$ or $A_{\phi_2 K_1^+ K_1^-}$. Since each K^+K^- pair appears twice in the K^+K^- effective mass scatter plot, these two ϕ bands are in fact equal in average, i.e.

$$\left|\overline{A_{\phi_1 K_2^+ K_2^-}}\right|^2 = \left|\overline{A_{\phi_2 K_1^+ K_1^-}}\right|^2 = |A|^2 \tag{6.35}$$

In this case the ϕK^+K^- background contaminations in the $\phi\phi$ overlap region as measured by the extrapolation of each single ϕ band is simply

$$\left|\overline{A_{\phi_1 K_2^+ K_2^-}}\right|^2 + \left|\overline{A_{\phi_2 K_1^+ K_1^-}}\right|^2 = 2|A|^2 \tag{6.36}$$

In addition, as we moved away from the $\phi\phi$ overlap region along a single ϕ band, lets say ϕ_1, then the ϕ_2 system becomes massive and strongly suppressed by the Watson factor $W_f(= \frac{e^{i\delta_2}\sin\delta_2}{q^{\ell} + 1})$.

In this situation only one of the two amplitudes $A_{\phi_1 K_2^+ K_2^-}$ is non-vanishing. The full amplitude of the ϕK^+K^- events from which the backgrounds are extrapolated would have an identical form as expressed by Eq. 6.35. This means our extrapolation background is also equal to $2|A|^2$ (Eq. 6.36).

On the other hand, from the symmetry point of view the resultant amplitude arising from the amplitudes of two ϕ bands extrapolated to the $\phi\phi$ overlap region should be totally symmetric and contributed equally in average by each of them. In this picture, the amplitude is expressed by

$$A_{B.E.} = \overline{A_{\phi_1 K_2^+ K_2^-}} + \overline{A_{\phi_2 K_1^+ K_1^-}} \tag{6.37}$$

or

$$\left|A_{B.E.}\right|^2 = \left|\overline{A_{\phi_1 K_2^+ K_2^-}}\right|^2 + 2 \cdot \overline{A_{\phi_1 K_2^+ K_2^-}} \cdot \overline{A_{\phi_2 K_1^+ K_1^-}} + \left|\overline{A_{\phi_2 K_1^+ K_1^-}}\right|^2 = 4\left|A\right|^2 \tag{6.38}$$

By combining Eqs. 6.36 and 6.38, the factor 2 comes out naturally.

6.6.5 Real and Imaginary Parts of Coherent Background ($J^{PC} = 1^{--}$)

We want to determine the overall importance of the 1^{--} background. The individual loglikelihood value for each of the ten $\phi\phi$ bins was calculated by putting in coherent ($J^{PC} = 1^{--}$) and incoherent backgrounds as well as three dominant 2^{++} $\phi\phi$ waves (one S-wave with S = 2, two-D waves with S = 0 and S = 2). Two sets of loglikelihood values were obtained and listed in Table 6.7. The first set corresponded to the interference between the Re1^{--} and the 2^{++} S-wave (180° out of phase) while the Im1^{--} was combined with the incoherent background in the process of fitting. The second set corresponded to a fit without a 1^{--} wave. A difference of loglikehood Δlog L = 64, equivalent to 15σ effect, was found between these two sets of calculations. The loglikelihood increase for adding an imaginary part to the 1^{--} was essentially zero, thus the imaginary part did not enter into this activity.

Summing up our discussions, the backgrounds were finally divided up into two distinct interfering and non-interfering parts as given in Table 6.6(b). The interfering background corresponded to the real part of the coherent 1^{--} wave, the imaginary part of the 1^{--} was put together with the incoherent background to form the non-interfering part.

Table 6.6(a)

Incoherent and total coherent ($J^{PC} = 1^{--}$) backgrounds determined by the same momentum extrapolation method and also the smoothed values.

Bin No.	MASS RANGE (GeV)	EXTRAPOLATED (No. of events)		SMOOTHED (No. of events)	
		Incoherent background	Coherent background	Incoherent background	Coherent background
1*	2.040 - 2.115	16.2	21.3	14	19
2	2.115 - 2.165	39.0	44.1	40	42
3	2.165 - 2.215	48.5	44.9	46	43
4	2.215 - 2.265	49.8	39.2	45	36
5	2.265 - 2.315	41.1	27.7	41	28
6	2.315 - 2.365	31.9	17.5	34	20
7	2.365 - 2.415	23.3	12.3	27	14
8	2.415 - 2.465	19.4	9.9	22	10
9*	2.465 - 2.540	19.8	6.8	12	8
10*	2.540 - 2.640	11.9	3.8	9	5

Table 6.6(b)

Interfering background ($Re1^{--}$) and the non-interfering background (incoherent background + $Im1^{--}$) determined from the smoothed values.

Bin No.	Incoherent Background	Coherent BG($J^{PC}=1^{--}$)	$Re1^{--}$	$Im1^{--}$	Interfering BG (= $Re1^{--}$)	Non-interfering BG (Incoherent BG + $Im1^{--}$)
1*	14	19	4	15	4	29
2	40	42	9	33	9	73
3	46	43	8	35	8	81
4	45	36	4	32	4	77
5	41	28	13	15	13	56
6	34	20	1	19	1	53
7	27	14	6	8	6	35
8	22	10	7	3	7	25
9*	12	8	5	3	5	15
10*	9	5	4	1	4	10

* Corrected for bin width.

Table 6.7

Comparison of loglikelihood values between the 2^{++} S-wave of the $\phi\phi$ data which interferes with only the real part of the 1^{--} and without 1^{--}. In the former case the imaginary part of 1^{--} is combined with the incoherent background.

BIN NO.	Loglikelihood values of 2^{++} S-wave interferes with	
	$\mathrm{Re}1^{--}$	Without 1^{--}
1	2904	2898
2	3168	3159
3	3612	3601
4	3165	3161
5	2778	2764
6	2514	2513
7	2242	2237
8	1360	1353
9	1376	1368
10	1159	1157
Totals	24275	24211

Before closing this section, we present a simple description of the coherent background by a charge exchange Deck mechanism. The quark line diagram for $\pi^-p \rightarrow \phi K^+K^-n$ is shown in Fig. 1.5(a) in which ϕ lies between the two K's. The peripheral production of this diagram implies that ϕ is isotropic but K^- is moving preferentially with higher momentum than the corresponding K^+. This results in different kaon momentum distributions with the subsequent observation of charge asymmetry which is then transmitted to the α-distribution.

6.7 Wave fitting

The completion of the preparatory work described in the previous sections has paved the way for searching the solutions for our $\phi\phi$ data. This includes the availabilities of the decay amplitudes, acceptance normalization integrals, interfering and non-interfering backgrounds along with a set of $\phi\phi$ partial waves among which the solutions were looked for.

The full searching procedure progressed in a series of stages. The preliminary fits were conducted in wide bins (200 MeV) which started from fitting only one wave at a time and concluded in a four-wave fit. Fitting usually terminated at the stage where loglikelihood values failed to improve significantly by adding more waves to them. Both interfering and non-interfering backgrounds were treated as the special waves in the fitting program. However, during the initial wide bin searches, background waves were not tried except for one-wave fits since the fitting program was not equipped with capabilities to handle the automatic setting of the background event levels. Background subtractions were accomplished by guessing an input amplitude for the background wave which was allowed to vary freely during fitting. This normally needed a couple of trials before the background event level was correct. For two-, three- or four-wave fits the number of combinations emerging out of 52 partial waves would be enormous. To manually adjust the input parameters to correctly get the background event levels for all these combinations was impractical. In view of this, backgrounds were put in only in the final stage of the narrow bin fitting after a substantial number of partial waves and combinations had been screened from the more competing solutions. Skipping the background substractions in the initial wide bin search did not reduce the effective selectivity of the final solution, since this was selected in much finer bins (i.e. 50 MeV).

In practice this first wide bin skip merely acted as a filter to select all possible solutions of reasonable possibility which saved a tremendous amount of effort.

In the following we present the results of the significant waves found in the procedure of the wave fitting by the loglikelihood method.

6.7.1 Preliminary fits

Chronologically, fitting with only one $\phi\phi$ partial wave plus background was first made on 1982 data in the mass spectrum from 2.1 to 2.3 GeV. At the time of fitting only a collection of 338 events were available. Even with these limited samples the importance of the most significant wave found in this range, represented by the quantum numbers $J^PLSM^\eta = 2^+S20^-$, over the other 51 partial waves was unambiguously demonstrated. This finding was later reaffirmed by two- and three-wave fits performed in wider mass spectrum (2.19-2.59 GeV) with much higher statistics (2418 events). Loglikelihood values corresponding to the combination of background and one-wave fits for the complete set of 52 $\phi\phi$ partial waves were calculated. Results of these calculations are arranged in table 6.8(a) in the order of the waves taken up by the fitting program. The superiority of $J^{PC} = 2^{++}$, L = 0, S = 2 wave to other waves in terms of loglikelihood value was clearly unmatched.

A two-wave fit with background subtraction was also made in this bin for the 2^+S20^- and in turn each of the other 51 waves. The only significant contribution came from the 2^+S20^- and 2^+D20^- waves. Because of the importance of the 2^+S20^- wave it had been used throughout the entire study of the two-wave and three-wave fits. Table 6.8(b) shows the results of the loglikelihood calculations for the combinations of these waves with the dominant 2^+S20^-.

Results of the two-wave fit were further carried over to the three-wave fit. In this case, the two dominant waves 2^+S20^- and 2^+D20^- had been kept throughout the study. One can immediately identify from the loglikelihood values [Table 6.8(c)] that no meaningful progress was made by adding an extra wave to the two dominant waves found in the two-wave fit [Table 6.8(b)].

After this preliminary wave search in one bin, the 1982 data (≈ 1200 $\phi\phi n$) was fitted with a combination of these two waves in the five mass bins.[29] The fit was very good and it was also shown that this was the only possible two-wave fit to the data.

6.7.2 Fitting with Two-wave Without Background Subtraction

With the accumulation of the three-fold increased statistics an exhaustive two-wave fit cycling through all waves in two wide bins was carried out.

Because of the increased statistics, the $\phi\phi$ mass spectrum region to be cycled through by the set of partial waves was extended to two 200-MeV-wide bins along with two sets of acceptance normalization integrals (2.19-2.39 GeV, 2.39-2.59 GeV) prepared for the fitting program. Except near threshold, this range covered a substantial part of the $\phi\phi$ spectrum. Searching conducted in this range made it very unlikely that any important waves or combinations of waves would not show up with competitive loglikelihood values at this stage.

Each possible pair of waves formed out of the 52 partial waves was used in this two-wave fit. A total of $\frac{52 \cdot 51}{2} \cdot 2 = 2652$ two-wave fits were actually tried, a factor 2 was included to account for the two separate bins. In this way the interference effect due to coherent waves (same exchange parity) and non-interference effect due to incoherent waves (opposite exchange parity) were all considered. Loglikelihood values were calculated for each of the 200 MeV bins with its own particular acceptance normalization integrals. In order that a solution can satisfy the requirement of continuity the overall loglikelihood value for any pair of

Table 6.8(a)

Loglikelihood values for one partial wave and background fits in the mass range $M_{\phi\phi} = 2.20 \pm 0.10$ GeV.
Number of events used = 338

UNNATURAL PARITY EXCHANGE					
WAVE NO.	QUANTUM NO.				LOGLIKELIHOOD VALUE
	J^P	L	S	M^η	
1	0^+	S	0	0^-	2091
2	2^+	S	2	0^-	2144
3	2^+	S	2	1^-	2087
4	2^+	S	2	2^-	2087
5	1^-	P	1	0^-	2089
6	1^-	P	1	1^-	2087
7	2^-	P	1	1^-	2087
8	2^-	P	1	2^-	2091
9	0^+	D	2	0^-	2087
10	1^+	D	2	1^-	2087
11	2^+	D	0	0^-	2087
12	2^+	D	0	1^-	2087
13	2^+	D	0	2^-	2089
14	2^+	D	2	0^-	2091
15	2^+	D	2	1^-	2087
16	2^+	D	2	2^-	2096
17	3^+	D	2	1^-	2088
18	3^+	D	2	2^-	2096
19	3^+	D	2	3^-	2087
20	4^+	D	2	0^-	2089
21	4^+	D	2	1^-	2092
22	4^+	D	2	2^-	2087
23	4^+	D	2	3^-	2087
24	4^+	D	2	4^-	2087
25	3^-	F	1	0^-	2087
26	3^-	F	1	1^-	2087
27	3^-	F	1	2^-	2087
28	3^-	F	1	3^-	2087

NATURAL PARITY EXCHANGE					
WAVE NO.	QUANTUM NO.				LOGLIKELIHOOD VALUE
	J^P	L	S	M^η	
1	2^+	S	2	1^+	2087
2	2^+	S	2	2^+	2088
3	0^-	P	1	0^+	2091
4	1^-	P	1	1^+	2088
5	2^-	P	1	0^+	2086
6	2^-	P	1	1^+	2086
7	2^-	P	1	2^+	2089
8	1^+	D	2	0^+	2088
9	1^+	D	2	1^+	2089
10	2^+	D	0	1^+	2088
11	2^+	D	0	2^+	2092
12	2^+	D	2	1^+	2086
13	2^+	D	2	2^+	2090
14	3^+	D	2	0^+	2089
15	3^+	D	2	1^+	2089
16	3^+	D	2	2^+	2100
17	3^+	D	2	3^+	2087
18	4^+	D	2	1^+	2090
19	4^+	D	2	2^+	2089
20	4^+	D	2	3^+	2086
21	4^+	D	2	4^+	2087
22	3^-	F	1	1^+	2088
23	3^-	F	1	2^+	2086
24	3^-	F	1	3^+	2087

Table 6.8(b)

Loglikelihood values for two-wave fits (2^+S20^+ background + one selected partial wave) in the mass range = 2.20 ± 0.10 GeV.
Number of events used = 338

UNNATURAL PARITY EXCHANGE		
WAVE NO.	QUANTUM NO. J^P L S M^η	LOGLIKELIHOOD FOR 2^+S20^- PLUS ONE WAVE
1	2^+ D 2 0^-	2169
2	2^+ D 2 2^-	2148
3	1^- P 1 0^-	2147
4	2^- P 1 2^-	2146
5	0^+ S 0 0^-	2145
6	3^+ D 2 2^-	2145
7	2^+ D 0 2^-	2144
8	4^+ D 2 0^-	2144
9	4^+ D 2 1^-	2144

NATURAL PARITY EXCHANGE		
WAVE NO.	QUANTUM NO. J^P L S M^η	LOGLIKELIHOOD FOR 2^+S20^- PLUS ONE WAVE
1	0^- P 1 0^+	2148
2	2^+ D 0 2^+	2146
3	3^+ D 2 2^+	2146
4	2^- P 1 2^+	2144
5	2^+ D 0 1^+	2144
6	2^+ D 2 2^+	2144
7	4^+ D 2 1^+	2144
8	1^+ D 2 1^+	2141

Table 6.8(c)

Loglikelihood values for three-wave fits (2^+S20^- and 2^+D20^- + background + one selected partial wave) in the mass range = 2.20 ± 0.10 GeV.
Number of events used = 338

UNNATURAL PARITY EXCHANGE		
WAVE NO.	QUANTUM NO. J^P L S M^η	LOGLIKELIHOOD FOR 2^+S20^- AND 2^+D20^- PLUS ONE WAVE
1	2^- P 1 2^-	2175
2	1^- P 1 0^-	2174
3	2^+ D 2 2^-	2174
4	4^+ D 2 0^-	2173
5	4^+ D 2 1^-	2171
6	0^+ S 0 0^-	2170
7	2^+ D 2 1^-	2170
8	3^+ D 2 2^-	2170
9	2^+ D 0 2^-	2169

NATURAL PARITY EXCHANGE		
WAVE NO.	QUANTUM NO. J^P L S M^η	LOGLIKELIHOOD FOR 2^+S20^- AND 2^+D20^- PLUS ONE WAVE
1	0^- P 1 0^+	2171
2	1^+ D 2 1^+	2171
3	2^+ D 0 1^+	2170
4	2^+ D 0 2^+	2169
5	2^+ D 2 1^+	2169
6	2^+ D 2 2^+	2169
7	3^+ D 2 2^+	2169
8	4^+ D 2 1^+	2169
9	2^- P 1 2^+	2166

coupled waves representing the 400 MeV bin were obtained by adding the individual loglikelihood values for the two constituent bins.

The Monte Carlo simulation program was also improved, thus providing more accurate means to calculate the acceptance integrals. This was accomplished by putting in more realistic geometrical and kinematical effects such as space charge, random noise and limitations of track reconstruction capability, etc.. In order to recover these losses, the complete process began with the random generation of 50,000 $\phi\phi$ events according to the specific $\phi\phi$ phase space extending throughout the entire mass spectrum (2.04-2.64 GeV) and measured in the simulated MPS detector. Those events which survived were further tested by the pattern recognition program. Loss of events due to difficulties in event reconstruction in relation to the space charge and random noise effects could be incorporated in this way.

Following these lines a full two-wave fit with 2652 trials was finally completed. The loglikelihood of a continuous fit representing the 400 MeV interval (2.19-2.59 GeV) was obtained by simple addition as mentioned before. The set of two coupled waves corresponding to the top ten loglikelihood values of the two-wave fit performed in the range 2.19-2.59 GeV is given in Table 6.9.

The figures shown in Table 6.9 are clear and self-explanatory. According to these, the importance of the wave with the quantum numbers $j(= J^{P}LSM^{\eta}) = 2^{+}S20^{-}$ dominating the $\phi\phi$ spectrum is almost certain. This is unambiguously demonstrated both in two individual fits (200 MeV bins) and in a single continuous fit (400 MeV bin). In addition, the two-wave solution with $j = 2^{+}S20^{-}$ and $2^{+}D20^{-}$ is clearly selected. In comparison with the next most likely pair these two coupled waves show a much improved loglikelihood, ΔlogL = 100, corresponding to ≈ 22σ effect. This likely solution is consistent with our previous results using only the 1982 data.

6.7.3 Fitting with Three-wave Without Background Subtraction

A complete cycling procedure with all possible three-wave fits made out of the 52 waves would be practically impossible in terms of the amount of effort and the computer budget. Since a total of $\frac{52 \cdot 51 \cdot 50}{3\,!} \cdot 2 = 44200$ fits are necessary in order to finish the whole process. It is clear that the results we get from the previous two-wave fits have established that the $J^{PC} = 2^{++}$, L = 0 and S = 2 wave must be persistently included in participation of any wave fitting regardless of the number of waves involved in that fit. Without loss of generality, the persistent inclusion of this wave greatly reduces the number of combinations in an attempt to exhaust all necessary three-wave fits. It follows from this inherent property that the actual number of three-wave fits genuinely needed to be tried is only $\frac{51 \cdot 50}{2\,!} \cdot 2 = 2550$.

Finally, by keeping this dominant wave throughout our three-wave fit, a total of 2550 trials had cycled through the two 200 MeV bins which contained 1721 and 697 events respectively. The fitting procedure was analogous to a two-wave fit and no background subtraction was made. From this crude first fitting step it is clear that we again require the two waves 2^+S20^- and 2^+D20^- found in the 1982 data. In order to find the actual solution, we then included the background and used ten mass bins in our fits.

Table 6.9
List of the top ten coupled two-waves with the highest loglikelihood values in 400 MeV bins.
No background subtractions were put in.

NO.	Coupled Waves J^P L S M^η	Loglikelihood Values (Mass = 2.19-2.39 GeV, Events = 1721)	Loglikelihood Values (Mass = 2.39-2.59 GeV, Events = 697)	Loglikelihood Values (Mass = 2.19-2.59 GeV, Events = 2418)
1	2^+ S 2 0^- 2^+ D 2 0^-	13610	5091	18701
2	2^+ S 2 0^- 0^+ S 0 0^-	13510	5091	18601
3	2^+ S 2 0^- 2^+ S 2 1^-	13450	5108	18558
4	2^+ S 2 0^- 3^+ D 2 3^-	13450	5088	18538
5	2^+ S 2 0^- 2^+ S 2 1^+	13470	5062	18532
6	2^+ S 2 0^- 2^+ D 0 0^-	13440	5091	18531
7	2^+ S 2 0^- 3^+ D 2 1^-	13470	5055	18525
8	2^+ S 2 0^- 3^+ D 2 3^+	13450	5048	18498
9	2^+ S 2 0^- 0^- P 1 0^+	13440	5040	18480
10	2^+ S 2 0^- 2^+ S 2 2^+	13440	5040	18480

An analysis of the sets of the three coupled waves indicated by the loglikelihood values has noted the following points of interest:

Among the best 28 three-wave fits, there are 27 combinations which contain, in addition to the 2^+S20^-, the 2^+D20^- partial wave. Thus it is almost certain that another wave with quantum numbers j = 2^+D20^- (J^{PC} = 2^{++}, L = 2, S = 2, M = 0) is also an important wave next to the S-wave with S = 2 found by two-wave fits.

Most of the competitive three-wave solutions involve the natural waves with non-zero magnetic quantum numbers ($M \neq 0$). However, we have seen in Chapter 3 that generation of high statistics (100,000 events) pure waves all exhibit characteristic Y structures corresponding to different M values except L = 0. In this connection, the failure to observe any structure in our data for the Υ-distribution rules out the solutions found by the two bin wave fitting which have $M \neq 0$.

The best few calculated loglikelihood values for the three-wave fit in two 200-MeV-wide bins are comparable so that a definitive conclusion of three-wave solution cannot be achieved. In this case the use of the two wide bins would be insufficient to determine conclusively which set of coupled waves should represent the real solution. To account more fully for the variation with mass effects, further study should break up the entire $\phi\phi$ mass spectrum into the number of fine bins which are allowed by the statistics. In the next section we shall describe a detailed study of wave fitting as how to identify the best solution.

6.7.4 Detailed Fitting in Narrow Bins with Backgrounds

The result of the crude fitting procedure provides a set of competitive three-wave solutions which are found to be very useful for the purpose of detailed fitting. Guided by the logliklihood values therein as well as the physics revealed in the $\phi\phi$ data, such as the observations of the Υ projection, a sum of twenty-seven sets of three coupled waves were determined to be a more than adequate sample for detailed fitting.

A detailed fitting procedure was tried on each set of these coupled waves in all the mass bins (Table 6.1) which made up the whole $\phi\phi$ mass spectrum (2.04-2.64 GeV). The coherent and incoherent backgrounds were treated as two additional waves to the input of the OPTIME fitting program, fitting with coherent and incoherent backgrounds put together and without any background were both tried.

It was found that the most time consuming part in this detailed study was related to the correct choice of the input parameters for both the coherent and incoherent backgrounds. After an initial random guess one needed to wait for the return of the estimated background event levels before an improved guess could be made. Generally speaking, a few trials would normally suffice to restore the background levels to within 1.5% accuracy of the pre-determined values. Results of these fittings expressed in order of decreasing loglikelihood values obtained from background subtractions are given in Table 6.10. Note that in this Table each set of waves fitted in any particular mass bins has two loglikelihood values which correspond to the situations with (upper) and without (lower) background considerations.

With reference to Table 6.10 the following points are noted:

(a) It should be noted that since an accepted solution must satisfy the requirement of continuity, therefore in our comparison of different three-wave solutions we consider only the summation of the loglikelihood values in all ten mass bins. It is obvious that the loglikelihood values for the three-wave fit (2^+S20^-, 2^+D20^-, and 2^+D00^-) with and without the background considerations are both shown to be the best among all the three-wave fits. This shows that our solution is essentially dependent upon the size of the samples in use but independent of the background, despite the fact that a general improvement in loglikelihood is seen as a result of adding background waves. In terms of the loglikelihood difference (Δlog L) such an increment in the whole mass spectrum varies between 150 and 300, corresponding to 25σ and 50σ effects.

(b) The loglikelihood results of this detailed study show that the only acceptable solution corresponds to three coupled $J^{PC} = 2^{++}$ waves with L = 0, S = 2; L = 2, S = 2 and L = 2, S = 0. It is better than the next best solution by $\approx 9\sigma$ (Δlog L = 56). Thus in addition to the two dominant 2^{++} waves (L = 0, S = 2; L = 2, S = 2) found as before using only 1982 data, a third 2^{++} wave (L = 2, S = 0) has also emerged.

(c) The following sets of coupled waves represent the most competitive solutions with highest loglikelihood values obtained in three-wave fits:

$J^P LSM^\eta$	Solution	Loglikelihood
2^+D00^- 2^+D20^- 2^+S20^-	A	24287
0^+S00^- 2^+D20^- 2^+S20^-	B	24222
4^+D20^- 2^+D20^- 2^+S20^-	C	24174

It becomes noticeable that all the constituent waves for solutions A, B and C are purely unnatural (η = −) with vanishing magnetic quantum number (M = 0). The significance of the coupled waves with non-interfering mixed naturalities accomplished before, in the absence of background, is substantially lowered when background is included. The fact that only waves with unnatural parity exchange are selected overwhelmingly is related to the independent result of t'-dependence which implies that the π-exchange is the dominant exchange mode in our exclusive channel. The M = 0 is also expected on the grounds that this is consistent with the absence of any observable Υ-structure exhibited in the data.

(d) Even the loglikelihood value of the three 2^{++} (solution A) partial waves represents a set of best continuous solution in the whole mass spectrum, a local behaviour in some individual fine mass bins is also hinted. The values recorded in Table 6.10 indicates that if some structure indeed exists it should be most likely to appear in the threshold region. This feature can be seen by keeping the two basic partial waves 2^+S20^- and 2^+D20^- in solution A but replacing the third wave 2^+D00^- by either 0^+S00^- or 4^+D20^-. Such replacments lead to the next two best solutions B and C. Table 6.10 then immediately shows that the loglikelihood values of the first few threshold bins for solutions B and C are consistently higher than the corresponding values for solution A. Expressed in terms of Δlog L solutions B and C are better than solution A in the threshold bins by 15 (first three bins) and 25 (first four bins) respectively corresponding to 2-3σ and 4σ effects. It would be premature to draw any conclusion based on these marginal differences, however certain possibilities are suggested:

(d.1) The 2^+D00^- wave is very weak in the low mass region which is what we have observed.

(d.2) Some other phenomena are also present in this region.

(d.3) Purely statistical fluctuation.

6.7.5 Final Solution

Results obtained from three-wave fit have encouraged us to take further study of greater number of coupled waves. In fact, an ambitious four-wave fit has been tried for all M = 0 waves. This was done by retaining the two dominant 2^+S20^- and 2^+D20^- waves throughout the fitting procedure and cycling through all other possible combinations of two M = 0 waves. In particular, an attempt was made to understand any possible structure near the threshold region. In any event, the result of the four-wave fit shows that the loglikelihood values are unable to single out a set of four coupled waves which uniquely identified as the most representative solution.

Table 6.10

Loglikelihood values for twenty-seven sets of three-wave fit calculated in each of the ten mass bins with (upper) and without (lower) backgrounds. Backgrounds include both interfering and non-interfering parts.

THREE-WAVE FIT LOGLIKELIHOOD WITH AND WITHOUT BACKGROUNDS
(WAVE NOTATION: J^PLSM^η)

	A	B	C	D	E	F	G	H	I
Mass Range(Gev)	2^+D00^- 2^+D20^- 2^+S20^-	0^+S00^- 2^+D20^- 2^+S20^-	4^+D20^- 2^+D20^- 2^+S20^-	2^+S21^+ 2^+D20^- 2^+S20^-	2^+D22^+ 2^+D20^- 2^+S20^-	0^+S00^- 0^+D20^- 2^+S20^-	3^+D21^+ 2^+D20^- 2^+S20^-	2^+D21^+ 2^+D20^+ 2^+S20^-	3^+D23^+ 2^+D20^- 2^+S20^-
2.040-	2904	2914	2910	2904	2902	2914	2901	2903	2906
2.115	2875	2898	2882	2888	2883	2890	2878	2887	2887
2.115-	3176	3180	3176	3181	3175	3178	3174	3172	3171
2.165	3133	3145	3140	3163	3145	3141	3142	3142	3133
2.165-	3615	3616	3623	3608	3609	3608	3608	3605	3606
2.215	3587	3597	3604	3595	3587	3574	3589	3579	3580
2.215-	3163	3159	3174	3161	3174	3145	3162	3156	3159
2.265	3132	3120	3147	3147	3164	3120	3142	3131	3138
2.265-	2777	2758	2761	2762	2760	2720	2765	2758	2760
2.315	2749	2724	2724	2741	2735	2691	2742	2735	2737
2.315-	2514	2490	2485	2493	2488	2493	2488	2490	2488
2.365	2496	2468	2457	2483	2476	2478	2475	2480	2476
2.365-	2243	2234	2213	2217	2208	2229	2216	2228	2214
2.415	2221	2197	2175	2196	2183	2212	2195	2215	2192
2.415-	1360	1354	1338	1338	1341	1349	1335	1337	1336
2.465	1338	1332	1316	1323	1329	1327	1312	1323	1316
2.465-	1376	1365	1350	1352	1356	1364	1355	1354	1353
2.540	1361	1348	1335	1340	1344	1354	1346	1346	1344
2.540-	1159	1152	1144	1153	1146	1152	1147	1147	1149
2.640	1151	1141	1133	1149	1138	1147	1140	1141	1144
Totals	24287	24222	24174	24169	24159	24152	24151	24150	24142
	24043	23970	23913	24025	23984	23934	23961	23979	23947
Improved L.L. due to backgrounds	244	252	261	144	175	218	190	171	195

Table 6.10 continued

THREE-WAVE FIT LOGLIKELIHOOD WITH AND WITHOUT BACKGROUNDS
(WAVE NOTATION: $J^{P}LSM^{n}$)

	J	K	L	M	N	O	P	Q	R
Mass	$3^{+}D20^{+}$	$2^{+}D02^{+}$	$4^{+}D23^{+}$	$4^{+}D22^{-}$	$4^{+}D23^{-}$	$4^{+}D21-$	$4^{+}D21^{+}$	$4^{+}D22^{+}$	$2^{+}D01^{+}$
Range(Gev)	$2^{+}D20^{-}$	$2^{+}D20^{-}$	$2^{+}D20^{-}$	$2^{+}D20^{-}$	$2^{+}D20^{-}$	$2^{+}D20^{-}$	$2^{+}D20^{-}$	$2^{+}D20^{-}$	$2^{+}D20^{-}$
	$2^{+}S20^{-}$	$2^{+}S20^{-}$	$2^{+}S20^{-}$	$2^{+}S20^{-}$	$2^{+}S20^{-}$	$2^{+}S20^{-}$	$2^{+}S20^{-}$	$2^{+}S20^{-}$	$2^{+}S20^{-}$
2.040-	2905	2904	2904	2905	2906	2901	2900	2906	2905
2.115	2892	2877	2887	2867	2875	2868	2872	2891	2883
2.115-	3170	3168	3170	3173	3174	3171	3175	3170	3169
2.165	3138	3122	3133	3121	3120	3120	3144	3135	3129
2.165-	3608	3605	3605	3609	3606	3613	3606	3608	3608
2.215	3590	3572	3575	3586	3574	3581	3583	3590	3585
2.215-	3160	3156	3157	3156	3160	3157	3161	3156	3159
2.265	3140	3128	3133	3122	3125	3125	3139	3128	3132
2.265-	2759	2758	2759	2761	2758	2757	2759	2758	2759
2.315	2737	2730	2735	2724	2724	2723	2734	2730	2733
2.315-	2487	2489	2487	2484	2483	2484	2487	2484	2485
2.365	2475	2468	2474	2458	2458	2459	2472	2466	2463
2.365-	2212	2219	2220	2210	2211	2212	2204	2210	2205
2.415	2190	2199	2200	2169	2169	2170	2174	2184	2172
2.415-	1337	1335	1335	1335	1341	1337	1336	1338	1335
2.465	1325	1311	1315	1309	1327	1317	1315	1325	1316
2.465-	1352	1354	1353	1349	1352	1355	1352	1350	1350
2.540	1342	1344	1345	1335	1340	1340	1399	1337	1336
2.540-	1149	1148	1146	1144	1143	1143	1149	1144	1146
2.640	1144	1139	1140	1134	1133	1134	1143	1138	1137
Totals	24139	24136	24136	24134	24134	24130	24129	24124	24121
	23975	23890	23937	23825	23845	23837	23975	23924	23886
Improved L.L. due to backgrounds	164	246	199	309	289	293	154	200	235

Table 6.10 continued

THREE-WAVE FIT LOGLIKELIHOOD WITH AND WITHOUT BACKGROUNDS
(WAVE NOTATION: $J^{P}LSM^{\eta}$)

	S	T	U	V	W	X	Y	Z	ZZ
Mass	2^+S22^+	4^+D24^-	3^+D22^+	4^+D24^+	0^-P10^+	2^+S21^+	$2\text{-}P11^+$	2^+S22^+	2^+S21^+
Range(Gev)	2^+D20^-	2^+D20^-	2^+D20^-	2^+D20^-	2^+D00^-	2^+D00^-	2^+D00^-	2^+D00^-	2^+S21^-
	2^+S20^-	2^+S20^-	2^+S20^-	2^+S20^-	2^+S20^-	2^+S20^-	2^+S20^-	2^+S20^-	2^+S20^-
2.040-	2906	2905	2900	2901	2899	2901	2899	2902	2905
2.115	2885	2870	2868	2872	2878	2881	2875	2881	2894
2.115-	3170	3168	3169	3168	3169	3174	3163	3164	3175
2.165	3129	3121	3124	3123	3146	3155	3126	3124	3164
2.165-	3605	3607	3606	3605	3605	3603	3602	3601	3602
2.215	3577	3573	3579	3571	3592	3588	3581	3572	3595
2.215-	3156	3157	3156	3156	3142	3136	3131	3129	3138
2.265	3131	3120	3124	3125	3126	3115	3105	3099	3129
2.265-	2758	2758	2760	2758	2725	2703	2702	2704	2691
2.315	2730	2722	2732	2729	2708	2676	2673	2674	2672
2.315-	2486	2484	2488	2483	2477	2476	2479	2478	2462
2.365	2471	2459	2469	2463	2463	2462	2467	2466	2453
2.365-	2208	2204	2204	2205	2218	2215	2216	2217	2211
2.415	2183	2171	2173	2175	2203	2198	2201	2203	2204
2.415-	1335	1334	1335	1335	1349	1346	1352	1349	1332
2.465	1319	1309	1314	1316	1335	1328	1334	1334	1323
2.465-	1349	1349	1349	1349	1356	1349	1353	1351	1346
2.540	1336	1335	1335	1337	1340	1331	1337	1337	1339
2.540-	1143	1146	1143	1143	1141	1139	1133	1135	1134
2.640	1133	1136	1135	1135	1133	1131	1117	1122	1129
Totals	24116	24112	24110	24103	24081	24042	24030	24030	23996
	23894	23816	23853	23846	23924	23865	23816	23812	23902
Improved L.L. due to backgrounds	222	296	257	257	157	177	214	218	94

It is finally concluded that at the present level of statistics our best solution to the $\phi\phi$ data which satisfies continuity is a set of three coupled 2^{++} waves ($2^{+}S20^{-}$, $2^{+}D20^{-}$ and $2^{+}D00^{-}$), and there is no statistically significant evidence for a fourth wave.

6.8 K-matrix Fit

In the present analysis, the basic reaction $\pi^{-}p \rightarrow \phi\phi n$ which is described by isobar model has assumed that the process takes place through the intermediate resonant states. An immediate point of interest in doing the partial wave analysis is to find these resonant states and obtain their characteristic parameters. Here we try to apply the constraint of unitarity, i.e. the K-matrix fits, to isobar-model generated amplitudes so that a smooth description of the data can be obtained and as a result of this fit the K-matrix poles can determine the relevant resonance parameters.

6.8.1 Production Amplitudes for Final Solution

The results presented in Section 6.7 finally concluded that in our present wave searching the only accepted solution for our $\phi\phi$ data is a set of three coupled 2^{++} unnatural waves with $M = 0$. These three partial waves together with the corresponding incoherent background when fitted by OPTIME fitting program have produced a set of production amplitudes which can be used by K-matrix for fitting purposes.

At each energy all the inelastic amplitudes are well determined with respect to each other by the isobar model but have the intrinsic difficulty in the arbitrariness of an overall phase. In our case this overall phase uncertainty of the inelastic amplitudes is overcome by assuming that S-wave is purely real (phase = 0°) in each mass bin and the two D-waves were then measured relative to the S-wave. Hence the amplitudes for the D-waves are in general complex whereas the S-wave is consistently represented by real part only.

Since there were ten masses available (Table 6.1) we had prepared ten sets of production amplitudes in parallel which followed the same fitting procedure as before. These amplitudes corresponding to each partial wave of our solution for all ten bins are provided in Table 6.11.

6.8.2 K-Matrix Parameterization

All the formulae used in our K-matrix fit can be found in Chapter 2. To facilitate the necessary parameterization for the fitting program we reproduce here the explicit forms of the partial widths Γ_{ja} associated with each of the three channels:

$$\Gamma_{j(S_2)} = q_{\phi\phi}\, \gamma^2_{j(S_2)}$$

$$\Gamma_{j(D_2)} = q_{\phi\phi}\, B_2(q^2_{\phi\phi})\, \gamma^2_{j(D_2)}$$

$$\Gamma_{j(D_0)} = q_{\phi\phi}\, B_2(q^2_{\phi\phi})\, \gamma^2_{j(D_0)}$$

where S_2 = S-wave with S = 2;

D_2 = D-wave with S = 2; and,

D_0 = D-wave with S = 0.

The factor $B_2(q^2_{\phi\phi})$ is the D-wave Blatt-Weiskopf because the factor using one Fermi length of interaction (1 Fermi = 5 GeV^{-1} implies r = 5 GeV^{-1}) which is given by

$$B_2(q^2_{\phi\phi}) = \frac{(rq_{\phi\phi})^4}{(rq_{\phi\phi})^4 + 3(rq_{\phi\phi})^2 + 9}$$

In the last expression $q_{\phi\phi}$ is the center-of-mass momentum of ϕ which can be expressed in terms of CMS energy of the $\phi\phi m$ system ($E_{\phi\phi}$) and the mass of ϕ (M_ϕ):

$$q^2_{\phi\phi} = 1/4\ (E^2_{\phi\phi} - 4M^2_\phi)$$

TABLE 6.11(a)

Amplitudes for three dominant partial waves and two backgrounds calculated for production by isobar model. Each production amplitude was determined by mass independent fit.

(Phase for 2^{++} S-wave = 0°; phase for 1^{--} S-wave = 180°. Numbers in brackets represent errors.)

Mass Range (GeV)	$J^{PC} = 2^{++}$ S-wave; S=2	$J^{PC} = 2^{++}$ D-wave; S=2			$J^{PC} = 2^{++}$ D-wave; S=0			$J^{PC} = 1^{--}$ S-wave; S=1	Incoherent B.G.
	ReA	ReA	ImA	Phase (deg)	ReA	ImA	Phase (deg)	ReA	ReA
2.040-	37.4	4.0	-6.0	-56.1	0.4	-8.5	-87.1	-6.2	21.8
2.115	(1.4)	(1.6)	(4.9)	(25.0)	(1.7)	(3.5)	(11.3)	(0.6)	(1.0)
2.115-	34.8	6.2	-7.0	-48.6	0.3	-10.5	-88.3	-5.5	16.9
2.165	(1.2)	(1.4)	(2.8)	(13.1)	(1.6)	(2.0)	(8.6)	(0.6)	(1.0)
2.165-	36.8	6.5	-1.1	-9.2	0.7	-13.7	-87.2	-4.6	16.1
2.215	(1.1)	(1.2)	(2.9)	(24.5)	(1.5)	(1.8)	(6.1)	(0.6)	(1.0)
2.215-	33.0	8.4	14.7	60.3	-4.8	-6.6	-125.6	-6.11	14.3
2.265	(1.2)	(1.5)	(2.0)	(6.2)	(1.4)	(2.1)	(12.11)	(0.6)	(1.0)
2.265-	27.3	11.5	17.2	56.2	-3.0	-13.0	-102.9	-8.6	11.2
2.315	(1.2)	(1.7)	(1.9)	(5.9)	(1.7)	(1.8)	(7.8)	(0.6)	(1.0)
2.315-	28.0	4.9	16.5	73.5	7.4	-16.8	-66.1	-3.2	12.6
2.365	(1.3)	(1.8)	(1.7)	(6.5)	(2.0)	(2.0)	(6.4)	(0.6)	(1.0)
2.365-	27.0	5.2	14.9	70.8	-14.8	-15.2	-45.7	-5.2	10.5
2.415	(1.4)	(2.0)	(1.8)	(7.8)	(2.2)	(2.3)	(6.6)	(0.6)	(1.0)
2.415-	22.2	6.0	11.9	63.1	14.6	2.0	7.8	-3.8	9.8
2.465	(1.5)	(2.0)	(2.0)	(10.2)	(2.2)	(2.8)	(11.3)	(0.6)	(1.0)
2.465-	20.5	5.5	16.1	71.2	16.1	-6.6	-22.4	-5.8	10.3
2.540	(1.7)	(2.4)	(2.0)	(8.9)	(2.2)	(3.0)	(10.1)	(0.6)	(1.0)
2.540-	18.8	-1.1	21.3	92.8	14.8	-3.4	-12.8	-3.5	12.2
2.640	(2.1)	(3.2)	(1.7)	(8.4)	(2.6)	(2.9)	(11.2)	(0.6)	(1.0)

TABLE 6.11(b)

Amplitudes for three dominant partial waves and two backgrounds calculated for production by isobar model. The productions for the first three bins were determined from a high mass extrapolation procedure which maximized the loglikelihood for three-pole K-matrix. (Phase for 2^{++} S-wave = 0°; phase for 1^{--} S-wave = 180°. Numbers in brackets represent errors.)

Mass Range (GeV)	$J^{PC} = 2^{++}$ S-wave;S=2	$J^{PC} = 2^{++}$ D-wave;S=2			$J^{PC} = 2^{++}$ D-wave;S=0			$J^{PC} = 1^{--}$ S-wave;S=1	Incoherent B.G.
	ReA	ReA	ImA	Phase (deg)	ReA	ImA	Phase (deg)	ReA	ReA
2.040-	49.4	4.0	-10.4	61.0	-1.0	-10.4	-95.7	-9.3	14.3
2.115	(1.4)	(1.7)	(0.0)	(9.9)	(1.7)	(0.0)	(9.4)	(2.2)	(1.0)
2.115-	43.8	6.6	6.5	44.2	-0.5	-10.9	-92.5	-9.8	16.3
2.165	(1.3)	(1.6)	(0.0)	(6.9)	(1.8)	(0.0)	(9.3)	(1.9)	(1.0)
2.165-	44.8	6.9	8.1	49.5	0.3	-14.8	-88.7	-9.4	17.1
2.215	(1.4)	(1.6)	(0.0)	(6.5)	(1.7)	(2.2)	(6.7)	(2.0)	(1.0)
2.215-	39.7	10.7	15.9	56.1	-5.9	-8.9	-123.5	-6.8	16.6
2.265	(1.4)	(1.8)	(2.8)	(7.4)	(1.8)	(2.8)	(12.2)	(2.1)	(1.0)
2.265-	32.4	14.7	19.3	52.6	-4.1	-15.6	-104.8	-12.3	14.5
2.315	(1.5)	(2.2)	(2.6)	(6.8)	(2.2)	(2.5)	(8.4)	(2.1)	(1.0)
2.315-	33.6	6.3	19.7	72.3	9.0	-20.4	-66.3	-3.9	14.6
2.365	(1.6)	(2.3)	(2.3)	(6.9)	(2.5)	(2.6)	(6.8)	(2.2)	(1.0)
2.365-	32.4	6.8	17.4	68.7	18.0	-18.9	-46.3	-8.7	12.3
2.415	(1.7)	(2.5)	(2.5)	(8.5)	(2.8)	(3.1)	(7.1)	(2.1)	(1.0)
2.415-	26.6	7.7	13.8	60.8	18.0	2.1	6.6	-9.5	10.7
2.465	(1.8)	(2.5)	(2.6)	(10.9)	(2.7)	(3.7)	(12.1)	(2.2)	(1.0)
2.465-	24.8	6.7	19.5	71.1	19.7	-8.2	-22.7	-10.8	11.0
2.540	(2.0)	(3.0)	(2.5)	(9.2)	(2.8)	(3.8)	(10.4)	(2.6)	(1.0)
2.540-	22.7	-1.1	26.4	92.3	18.5	-4.3	-13.1	-8.7	11.2
2.640	(2.4)	(3.8)	(2.0)	(8.3)	(3.1)	(3.5)	(10.9)	(3.0)	(1.0)

We understand from the previous analysis that π is the dominant exchange mode responsible for $\phi\phi$ production, subsequently the $\phi\phi$ amplitudes obtained in the last section are essentially π-exchange amplitudes. In this connection, the K-matrix pole has coupled to the $\pi\pi$ channel. In fact, these poles should also have couplings to many other channels along with the $\pi\pi$ mode. However, in reality these channels are difficult to observe because of the lack of an effective operation of the OZI filter which strongly suppresses their productions. In order that these channels be properly considered in the parameterization of the fitting procedure, their implicit effects are also included to further constrain the problem. The constraints imposed by these channels have the followig properties:

(a) since they couple to $\phi\phi$ resonant states their partial widths are part of the total width;

(b) they can mix the K-matrix poles by cross coupling among themselves.

It is contemplated that the most logical way to describe these effects is to introduce two extra channels into the K-matrix formalism. Asymptotically all channel kinematics is equal to the mass of the $\phi\phi$ system. These extra channels are represented by the following expressions:

$$\Gamma_{j(\mathrm{EXT1})} = m_{\phi\phi}\ \gamma^2_{j(\mathrm{EXT1})}$$
$$\Gamma_{j(\mathrm{EXT2})} = m_{\phi\phi}\ \gamma^2_{j(\mathrm{EXT2})}$$

Thus for three-pole K-matrix fit, the total width Γ_j ($j = 1, 2, 3$) is given by

$$\Gamma_j = \Gamma_{j(S_2)} + \Gamma_{j(D_2)} + \Gamma_{j(S_0)} + \Gamma_{j(\mathrm{EXT1})} + \Gamma_{j(\mathrm{EXT2})}$$

To see how these two channels come about we note that there are altogether six extra numbers associated with three resonant states. In 3-pole K-matrix fit the resonance parameters are connected with a set of six variable (D_1, D_2, D_3, D_{12}, D_{13}, D_{23}) defined by Eqs. 2.14 and 2.15. Each of these variables can be expressed as a sum of linear products of U_{ja} which in turn is related to $\Gamma_{ja}^{1/2}$:

$$D_{jk} = \sum_a U_{ja} U_{ka}$$
$$U_{ja}^2 = \Gamma_{ja} \quad .$$

Each D_j or D_{jk} is thus made up by $\phi\phi$ amplitudes plus some other contributions which have not been measured in $\phi\phi$ channels. For each of these D_j and D_{jk} those terms which are outside the $\phi\phi$ origins are replaced by a single parameter to be determined by fitting. This means six additional parameters are necessary to fully describe these variables (D_j or D_{jk}). The introduction of six extra partial widths into the existing formalism can certainly serve to meet this need.

During the fitting process one of the results of parameterizing γ_{ja} is the determination of the coupling signs for various channels. These signs are useful to check with the theoretical prediction even though a theory which describes decay of glueball into $\phi\phi$ channel is still not available. From Eqs. 2.11 and 2.12 it is clear that the partial width Γ_{ja} with inherent mixing is determined by a product of kinematics and the coupling squared γ_{ja}^2. The pole location of each resonance is obtained from the real part of the propagator D_j as shown in Eq. 2.14, its imaginary part determines the total width Γ_j associated with that pole. This total width is the sum of a set of relevant partial widths, $\Gamma_j = \sum_a \Gamma_{ja}$ (Eq. 2.13).

The number of parameters involved in this three-pole K-matrix fit can be classified as follows:

(a) The complex quantities C_j which represent the production strength of the poles have 5 parameters consisting of three real and two imaginary amplitudes.

(b) The partial widths have 15 parameters which represent a set of 5 channels ($\Gamma_{j(S_2)}$, $\Gamma_{j(D_2)}$, $\Gamma_{j(D_0)}$, $\Gamma_{j(EXT1)}$, $\Gamma_{j(EXT2)}$) associated with 3 poles ($j = 1, 2, 3$).

(c) The pole locations m_j have 3 parameters which represent the three resonance masses.

With the above parameterization, we fitted the set of three amplitudes (S-wave and two D-waves) in the ten different mass bins. The fits were done by a least-square technique using the program MINUIT[47] to minimize χ^2.

One of the observations revealed in Table 6.11(a) was related to the abrupt change in phase of the D_2-wave in the lowest three bins. A plausible explanation for this effect was attributed to the smallness of the amplitudes associated with the two D-waves in this range and the resulting ratios of their imaginary and real parts were then unreliably measured. In fact, the interference between the S-wave and the D-waves at low mass causes a strong correlation between the phase (θ_D) and the D-wave amplitude (T_D). This correlation can be readily demonstrated using the following expansion:

$$\left|T_S + T_D\right|^2 = \left|T_S\right|^2 + 2\left|T_S\right| \left|T_D\right| \cos\theta_D + \left|T_D\right|^2$$

where D refers to both D-waves with different spin. In the last expression, $\left|T_D\right|^2$ can be neglected in comparison with the other two terms. However, the significance of the interference term makes the phase θ_D very dependent on the magnitude of $\left|T_D\right|$. It is conceivable that a change in $\left|T_D\right|$ can be counteracted by a change in $\cos\theta_D$. This means the phase is highly correlated from the magnitude of the D-wave which is not well determined because of its smallness.

In order to get a more reliable measurement of the relative phase θ_D in the threshold region, two independent K-matrix approaches have been tried.

In one approach, a three-pole K-matrix fit (same as our solution) has been tried. The phases of the lowest three bins were determined by the high mass extrapolation. The result of the fit showed that the extrapolated phases for the respective D_2-wave and D_0-wave tended to move away from each other with decreasing mass with the S-wave centered along the 0°-axis. In addition, the D_2 phases were located on the positive side whereas the corresponding D_0 phases were on the negative side. As a result of this fit, the threshold phase behavior showed no cross-over of the 0°-axis by either D_2 or D_0.

In another approach, a four-pole K-matrix fit was tried for all ten mass bins. The result of the fit indicated that for a satisfactory description of the sharp phase change behavior with a cross-over of 0°-axis by D_2-wave, the additional pole must be a very narrow resonance ($\Gamma_4 \sim 9$ MeV) and a strong coupling between the D_2 and S_2 partial waves.

In an attempt to decide which was the better approach to be followed in the subsequent analysis we were confronted with two contradicting threshold phase behaviors. In one fit the D_2 phase (upward) and D_0 phase (downward) were moving apart; in another fit the additional pole has caused the D_2 phase to cross the 0°-axis from the positive to the negative and approaching the D_0 phase. To compromise these two incompatible situations we found that the loglikelihood function for the three pole K-matrix fit could be maximized if the D_2 phase remained positive and parallel to the D_0 phase which was negative. This means by adapting the three-pole fit with the constraint that D_2 and D_0 phases being parallel in the lowest three bins, the loglikelihood difference (Δlog L) between these two K-matrix fits was minimized. In this case, the three-pole fit was off from the four-pole fit in these three bins given by Δlog L = 15 or 3.5σ.

Statistically speaking, our data are unable to justify such a narrow resonance ($\Gamma_4 \sim 9$ MeV) and moreover, an improvement of 3.5σ is not an overwhelming evidence to demonstrate its existence. Under these circumstances, we are more inclined to take a conservative attitude towards the second approach using the result of the three-pole K-matrix fit.

The above discussion can be summarized by referring to Fig. 6.16 in which the phases of the seven high mass bins are obtained from Table 6.11(b) while the phases of the three threshold bins are extrapolated from the high mass. The corresponding error bars for the low mass bins are taken from the diagonal elements of the error matrix. The curves drawn in the figure are the results of a three-pole K-matrix fit.

Taking all this into consideration, we finally concluded that in order to achieve a good fit ($\sim 3\sigma$) we needed to have at least three K-matrix poles. Our fit with two K-matrix poles was 16σ away from an ideal fit. The number of standard deviations for four-pole, three-pole and two-pole K-matrix fits could be determined as follows:

Productions for S_2-, D_2-, and D_0-waves
to be fitted in ten mass bins = 30

Phases for D_2- and D_0-waves to be fitted
in 9 mass bins (last bin not used) = 18

The above production and phase numbers were fixed quantities used throughout the K-matrix fit with different numbers of poles. To simplify our notation we use the subscripts in the following to denote the number of poles. It follows that the number of parameters (N.P.) in each case is

$$NP_4 = 7 + 5 \cdot 4 + 4 = 31$$

$$NP_3 = 5 + 5 \cdot 3 + 3 = 23$$

$$NP_2 = 3 + 5 \cdot 2 + 2 = 15$$

In the last expressions, the first term stands for the complex parameters, C_j, the second term for the number of partial widths, Γ_{ja}, and the last term for the number of poles, m_j.

The degree of freedom (D.F.) can be readily obtained by subtracting the number of parameters from the number of data points used:

$$(D.F.)_4 = 48 - 31 = 17$$

$$(D.F.)_3 = 48 - 23 = 25$$

$$(D.F.)_2 = 48 - 15 = 33$$

Hence the $\Delta\chi^2$ values corresponding to 1 standard deviation (SD) effect

$$SD_4 = [2(D.F.)_4]^{1/2} = (2.17)^{1/2} = 6$$

$$SD_3 = (2 \cdot 25)^{1/2} = 7$$

$$SD_2 = (2 \cdot 33)^{1/2} = 8$$

Finally the number of standard deviations (σ) for each K-matrix fit is derived from the measured $\Delta\chi^2$ (= χ^2 - D.F.):

$$\sigma_4 = \frac{(\Delta\chi^2)_4}{SD_4} = \frac{25}{6} = 4 \text{ SD}$$

$$\sigma_3 = \frac{(\Delta\chi^2)_3}{SD_3} = \frac{22}{7} = 3 \text{ SD}$$

$$\sigma_2 = \frac{(\Delta\chi^2)_2}{SD_2} = \frac{131}{8} = 16 \text{ SD}$$

Even though the three-pole fit and four-pole fit have comparable errors, however, it is more likely that an extra pole added to the three-pole fit only accounts for the systematic error or statistical fluctuation. This is connected with the few degrees of freedom used to determine σ (= $\frac{\chi^2 - \mathrm{D.F.}}{(2\mathrm{D.F.})^{1/2}}$) as a result of introducing more parameters. From the mathematical point-of-view, once a good fit is achieved to a set of prescribed data points with the minimum number of parameters, any further attempts to fit the detailed structure with additional parameters is nothing more than describing the inherent statistical errors rather than displaying new physics phenomena. Therefore we believe at the present level of statistics the three-pole solution is more realistic than the four-pole.

Figure 6.17 shows the three-pole fit to the three dominant waves along with the isobar model measurement of these waves in each mass bin.

6.8.3 Resonance Parameters and Argand Plot

In this section we give the results of the three-pole K-matrix fit. The Breit-Wigner resonance parameters of this fit are given in Table 6.12. The two lower mass resonance mainly decay through S = 2 amplitudes and the high mass resonance mainly decays through an S = 0 amplitude. The relative branching ratio of each channel and the signs of coupling are also given in Table 6.12. Since the K-matrix poles have the same quantum numbers, there is considerable mixing between the three waves and this leads to the sizeable error estimates shown.

In addition, a smoothed Argand plot is also provided (Fig. 6.18). The Argand amplitudes obtained from the solution are mass-independent. This means that they are defined at descrete energies and lack continuity from one energy to another. In the present K-matrix formalism the parameterization for the partial wave amplitudes can express them as smooth complex function of the total energy.

Table 6.12

Resonance parameters of the three-pole K-matrix fit

$M_1 = 2.050^{+.090}_{-.050}$ $\Gamma_1 = .200^{+.160}_{-.050}$ $\approx 50\%^{+10\%}_{-10\%}$ data

S-wave, S = 2 $\approx 98\%^{+02\%}_{-70\%}$ coupling sign (+) defined

D-wave, S = 2 $\approx$ 0% + 50% coupling sign (-)

D-wave, S = 0 $\approx 2\%^{+25\%}_{-02\%}$ coupling sign (-)

$M_2 = 2.300^{+.020}_{-.100}$ $\Gamma_2 = .200^{+.060}_{-.050}$ $\approx 20\%^{+20\%}_{-10\%}$ data

S-wave, S = 2 $\approx 30\%^{+20\%}_{-20\%}$ coupling sign (+)

D-wave, S = 2 $\approx 50\%^{+20\%}_{-10\%}$ coupling sign (+)

D-wave, S = 0 $\approx 20\%^{+20\%}_{-20\%}$ coupling sign (+)

$M_3 = 2.350^{+.020}_{-.030}$ $\Gamma_3 = .270^{+.090}_{-.130}$ $30\%^{+10\%}_{-20\%}$ data

S-wave, S = 2 $\approx 40\%^{+10\%}_{-20\%}$ coupling sign (+)

D-wave, S = 2 $\approx 05\%^{+15\%}_{-05\%}$ coupling sign (-)

D-wave, S = 0 $\approx 55\%^{+20\%}_{-15\%}$ coupling sign (+)

6.9 χ^2-Calculation

In this section we try to compare the various mass independent amplitudes of the real data with the corresponding predictions made by the K-matrix solution. Results of such comparison were expressed in terms of the well-defined quantity χ^2. From the knowledge of the number of parameters used in our specific solution of three-pole fit plus the measured χ^2 value we were able to determine the $\Delta\chi^2$ and the corresponding number of standard deviations (σ).

6.9.1 Monte Carlo Simulation of Acceptance

The K-matrix solution was generated by a program TRIA2 according to the production amplitudes obtained for each of the solution waves and backgrounds. For a high enough statistics we have generated 400,000 $\phi\phi$ events between 2.04 and 2.64 GeV. A crude estimate has shown that after acceptance loss the remainder of the samples was about ten times the size of the available data. A file SHORT TAPE was created to store these generated events.

The next step was to consider the acceptance effect due to the geometrical limitation of the detector and the triggering devices as well as some kinematic effects. This was completed in a program called MC747. At the end of the test, a set of coordinates was generated which represented the positions of hits made by each constituent track of a survived event.

While the geometric and kinematic acceptances were considered in MC747, the other subtle phenomena inherently associated with the real events such as the space charge close to the beam line, random noise, chamber deficiency, etc., which have introduced various degrees of uncertainty in track reconstruction were not considered here. These additional complications have made the acceptance determination time consuming. The best approach to these effects was to use the off-line processing package which analyzed the Monte Carlo events in the same way the real events were made. However, in order to facilitate the off-line analysis all the track information as well as the simulated noises and space charges must be supplied to the program via an array COORS. To this end, a separate routine MCPACK was used to play the role of interface between the programs MC747 and the off-line analysis program. Its purpose was to generate the noises and space charge effect while filling the array COORS.

During off-line processing the information stored in COORS was picked up by a routine used for pattern recognition. The latter then used the relevant hits to perform a sophisticated track reconstruction. Those events having all their constituent tracks successfully reconstructed by pattern recognition were finally binned and folded in a SUMMARY program.

The Monte Carlo events analyzed according to the above succession of steps have given us a reasonably good estimate of our acceptance from both the statistics and reliability points of view. As a summary, we present a flowchart of the program units involved in acceptance study in sequential order as follows:

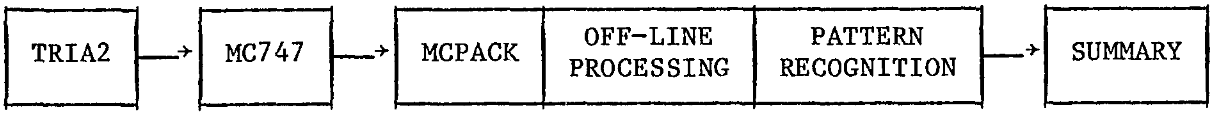

6.9.2 Comparison Between Monte Carlo Solution and Data

Even though the present K-matrix fit is considered as a legitimate approach to describe the production amplitudes of the data in a multidimensional space, however it is essential to compare the observed events and the generated K-matrix solution. This provides an independent check of the solution. In fact, the calculated χ^2 gives support to the correctness of the approach.

Table 6.13 shows the calculated χ^2 values by comparing the smoothed three-pole K-matrix solution with the data obtained from our experiment. Note that in this table, in addition to the usual eight parameters (α, $\alpha_1 \pm \alpha_2$, γ, $\cos\beta$, $\cos\theta$, $\cos\theta_1' \pm \cos\theta_2'$), we have also included the parameter $\alpha_1 + \alpha_2$ ($= \chi$) with special binning to reveal any possible $\cos\chi$ term, thus this has a natural range of π. The other eight parameters have been properly folded in accordance with symmetry requirements of the $\phi\phi$ system. The individual natural range associated with each parameter has been shown in Table 6.2(a). Also note that each χ^2 value listed in the table is a result of ten fine bins contained in a specified mass range. A glance at Table 6.13 shows that except perhaps for a few $\cos\beta$ and $\alpha_1 + \alpha_2$ bins most of the χ^2 values are reasonable from the standard theory of experimental error point-of-view. A closer look of the calculations shows that those bins with substantial χ^2 values are related to the very large statistical fluctuation which takes place in a small number of fine bins.

For an overall view of the χ^2 values contained in Table 6.13 it should be pointed out that each parameter is connected with 100 fine bins which made up the whole $\phi\phi$ mass spectrum. This means the overall χ^2 ($= 883$) is obtained on the basis of 900 fine bins. To acquire the number of degrees of freedom, the following parameters should be subtracted from the set of 900 bins:

(a) there are three empty bins without any entries;

Table 6.13

χ^2 values for nine projected angular distributions obtained by comparing the three-pole K-matrix solution and the observed events. Each displayed χ^2 value corresponds to a sum of χ^2 due to ten fine bins.

MASS RANGE (GeV)	α	$\alpha_1+\alpha_2$ (= χ)	$\alpha_1-\alpha_2$	$\alpha_1+\underset{\sim}{\alpha_2}$ (= $\underset{\sim}{\chi}$)	$\cos\beta$	γ	$\cos\theta$	$\cos\theta_1'+\cos\theta_2'$	$\cos\theta_1'-\cos\theta_2'$	SUBTOTAL
2.040-2.115	4.9	8.2	11.6	8.7	16.8	9.6	11.9	6.2	19.3	97.4
2.115-2.165	6.3	9.0	5.2	16.8	13.7	6.2	8.6	8.7	5.5	79.9
2.165-2.215	12.9	4.0	7.2	7.7	12.7	8.6	9.7	4.0	5.1	71.9
2.215-2.265	15.1	6.6	13.8	15.2	42.9	5.9	6.3	8.6	3.5	117.9
2.265-2.315	18.6	4.7	14.3	8.7	14.1	10.2	9.8	6.7	4.2	91.2
2.315-2.365	6.4	7.5	6.7	5.6	5.4	2.4	9.2	4.6	5.5	53.2
2.365-2.415	5.4	15.7	20.4	26.3	20.3	7.1	4.6	1.7	7.4	109.0
2.415-2.465	12.4	12.1	2.6	18.9	9.8*	14.1	3.6	10.7	6.4	90.6
2.465-2.540	7.0	14.9	8.0	17.1	9.7*	7.7	8.4	12.0	1.0	85.7
2.540-2.640	6.7	9.9	9.2	6.6	12.6*	14.1	7.7	4.2	15.7	86.7
SUBTOTAL	95.7	92.6	99.0	131.6	158.0	85.9	79.8	67.4	73.6	

TOTAL χ^2 = 883.4

* χ^2 value for the first nine fine bins only. The last bin has no entry.

(b) the three-pole K-matrix fit is parameterized by 23 parameters;

(c) the polynomials for coherent and incoherent backgrounds contain 8 fitting parameters.

As a result of these, the D.F. can be simply calculated as follows:

$$\text{D.F.} = 900 - 3 - 23 - 8 = 866$$

Hence, the overall χ^2 per degree of freedom is given by:

$$\chi^2/\text{D.F.} = 883/866 = 1.02$$

or alternatively

$$\text{Number of standard deviations} = \frac{\chi^2 - \text{D.F.}}{(2\text{D.F.})^{1/2}} = \frac{883 - 866}{(2 \cdot 866)^{1/2}} = \frac{17}{42} = 0.4\sigma.$$

From the results obtained above we immediately come to the conclusion that our K-matrix solution is in good agreement with the observation.

While the results of the χ^2 calculation are reassuring, it is also worthwhile to pursue a descriptive comparison. The various angular distributions of the data and the acceptance-corrected Monte-Carlo prediction for our K-matrix fit can be directly compared by superimposing the predicted distributions on the observed ones. Figs. 6.19(a) through 6.19(i) show such detailed comparison in which the smooth curves represent the normalized K-matrix fit. In addition to comparison, these plots also show the energy-dependence of each projection. Qualitatively, the solution waves found in the previous analysis can also be identified with the aid of the characteristics of the individual pure waves and the energy-dependence of the projection.

With reference to Figs. 6.19(a) through 6.19(i), the following points are noteworthy:

(a) Both the fit and the data show flat distributions [Fig. 6.19(f)] which are consistent with the solution for $M = 0$.

(b) A good fit to the $\cos\beta$ distribution [Fig. 6.19(e)] is seen in almost all ten bins. It is clearly demonstrated that with the increasing $\phi\phi$ effective mass the observed decay of the $\phi\phi$ system is preferentially in the azimuthal plane ($\beta = \pi/2$) of the Gottfried-Jackson frame. Poor acceptance at high mass is primarily related to this decay angle (β). Acceptance effect in other projections are not observed.

It is interesting to note that the characteristics of the two dominant D-waves, D_2 and D_0, which are important only at relatively high mass also show a broad peak centered around $\cos\beta = 0$ and $\cos\beta \rightarrow 1$ where the latter is affected by the acceptance.

(c) A pronounced peak at $\alpha = 0$ of α-distribution near the threshold [Fig. 6.19(a)] is compatible with the presence of an exclusive S_2-wave found in that region. The gradually diminished α peak from the low mass to medium mass is a signature of $S_2 - D_2$ destructive interference in this mass range since their α-dependences are completely opposite in phase. The return of the α peak at high mass can be attributed to the $S_2 - D_0$ interference.

(d) A small variation between 0 and $\pi/2$ in $\alpha_1 + \alpha_2$ ($= \chi$) [Fig. 6.19(b)] at low mass is also anticipated from the characteristics of the S_2 pure wave. However, a pronounced central peak can only be observed around 2.34 GeV which is consistent with the prominent $\alpha_1 + \alpha_2$ structure of D_0-wave found at that mass.

(e) The persistent $\alpha_1 - \alpha_2$ structure [Fig. 6.19(c)] with outstanding peak and dip at 0 and $\pi/2$ observed in all ten mass bins again strongly favor the S2- and D2-waves.

(f) Even though $\cos\theta$, $\cos\theta_1' \pm \cos\theta_2'$ [Figs. 6.19 (g)-(i)] are less definitive they are well reproduced and show systematic change as mass is increased.

One last point we shall compare is the charge asymmetry effect. This phenomenon is well-demonstrated in Fig. 6.20 in which the α-distribution is plotted between 0 and π. For a good enough statistics our data samples are divided into three wide bins (175 MeV, 150 MeV and 275 MeV). It is obvious that the inclusion of the $J^{PC} = 1^{--}$ partial wave in the K-matrix fit shows good agreement with the observed α-distribution at low and high mass bins. But the fit to the middle bin is less impressive even though the charge asymmetry effect is not well developed in this region. However, by referring to the three constituent bins each 50 MeV wide [Fig. 6.19(a)] it is noticeable that the fit in these bins (2.215 - 2.365 GeV) has a general tendency to be too low near $\alpha = 0$ and too high near $\alpha = \pi/2$. The accumulation of this statistical fluctuation thus gives rise to the observed discrepancy. Of course, one should realize that the plots drawn in Fig. 6.19(a) have been folded to half the range ($\pi/2$) than that used by Fig. 6.20.

Summing up the above discussions, we finally conclude that both the quantitative (χ^2) and qualitative (diagrammatic) comparisons remarkably support the K-matrix solution.

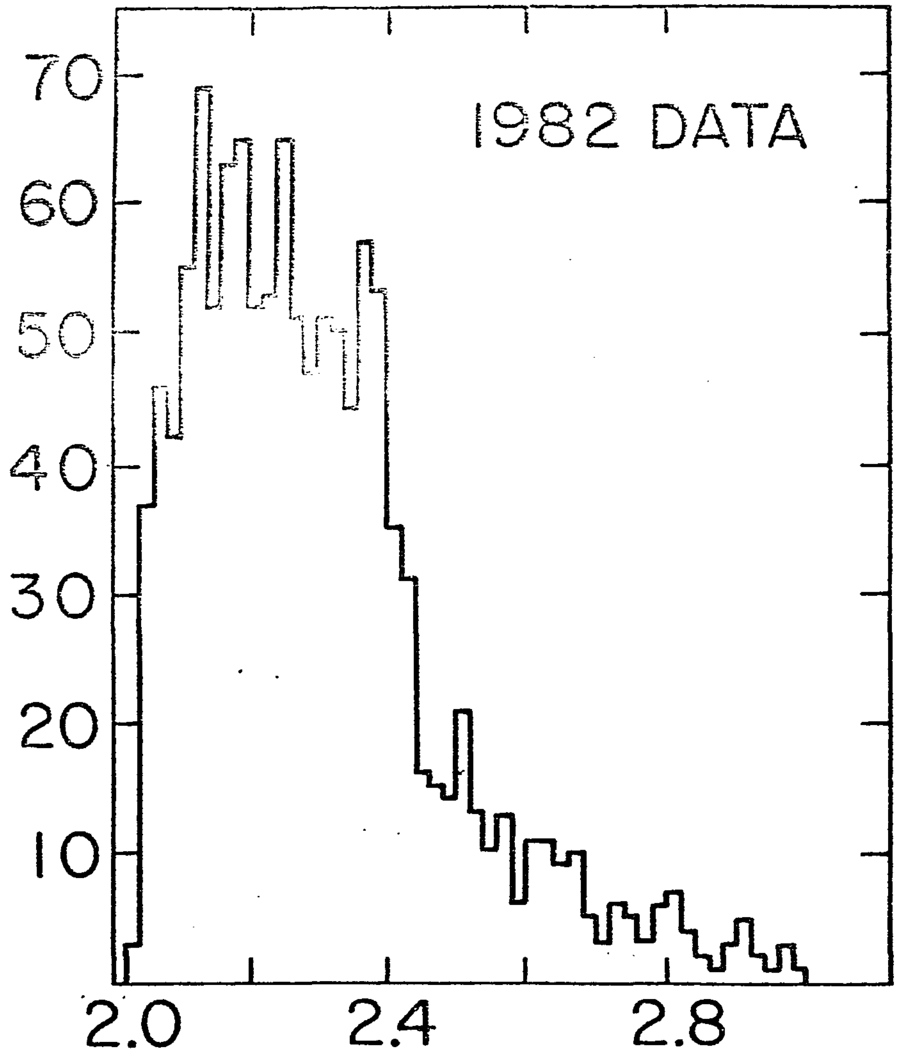

Fig. 6.1 The observed ØØ effective mass spectrum (1982 data).

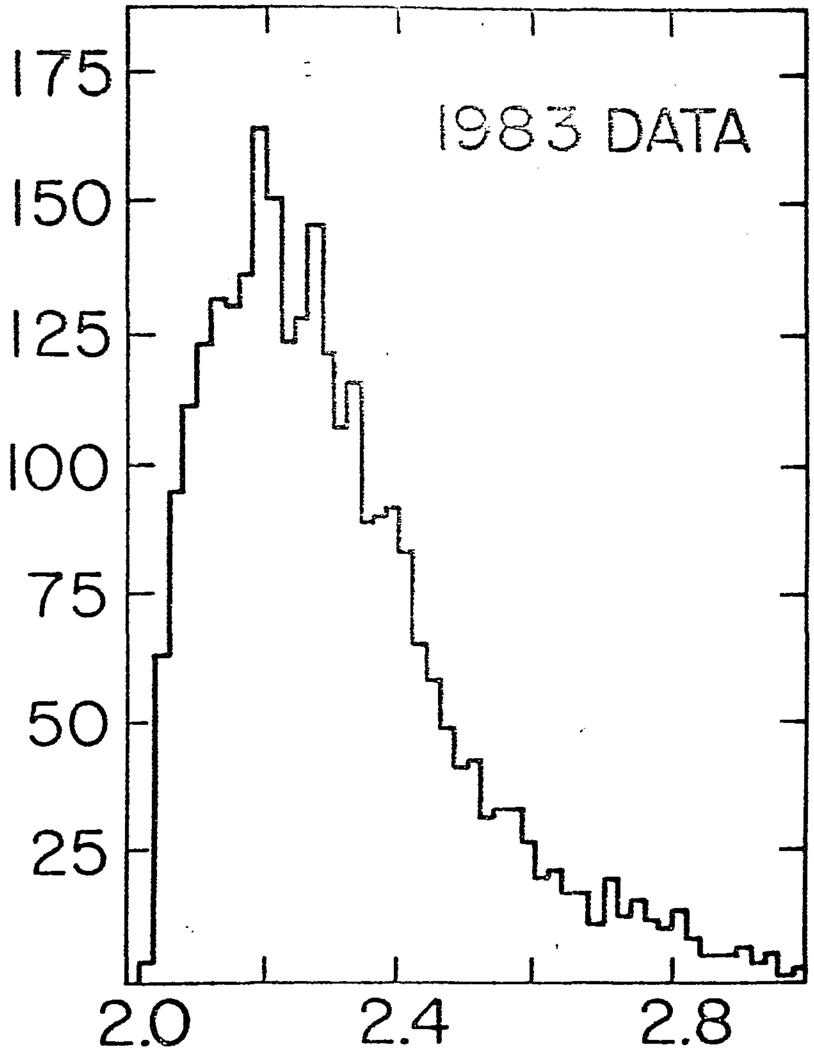

Fig. 6.2 The observed ØØ effective mass spectrum (1983 data).

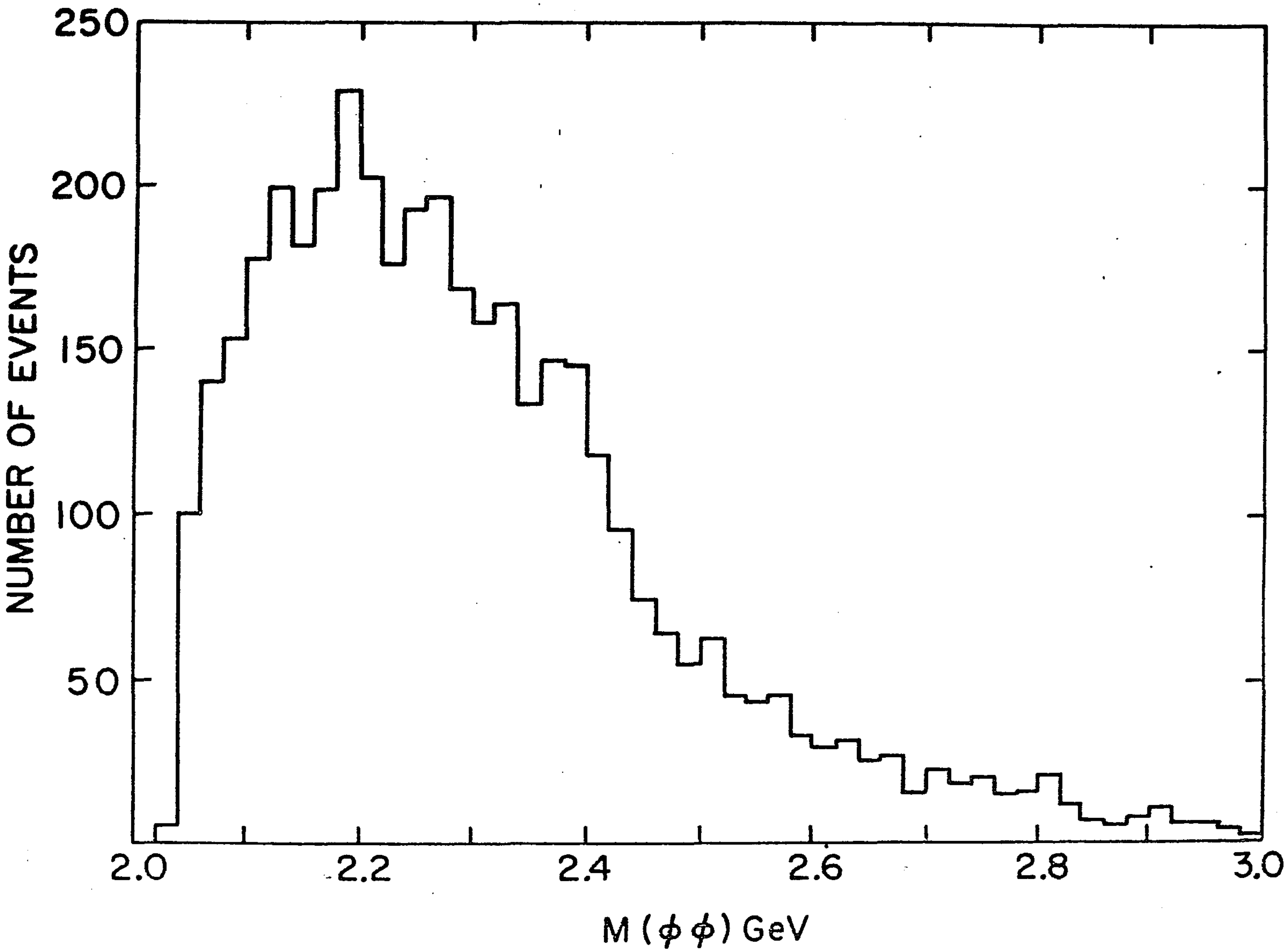

Fig. 6.3 The observed ϕϕ effective mass spectrum for a combined 1982 and 1983 data.

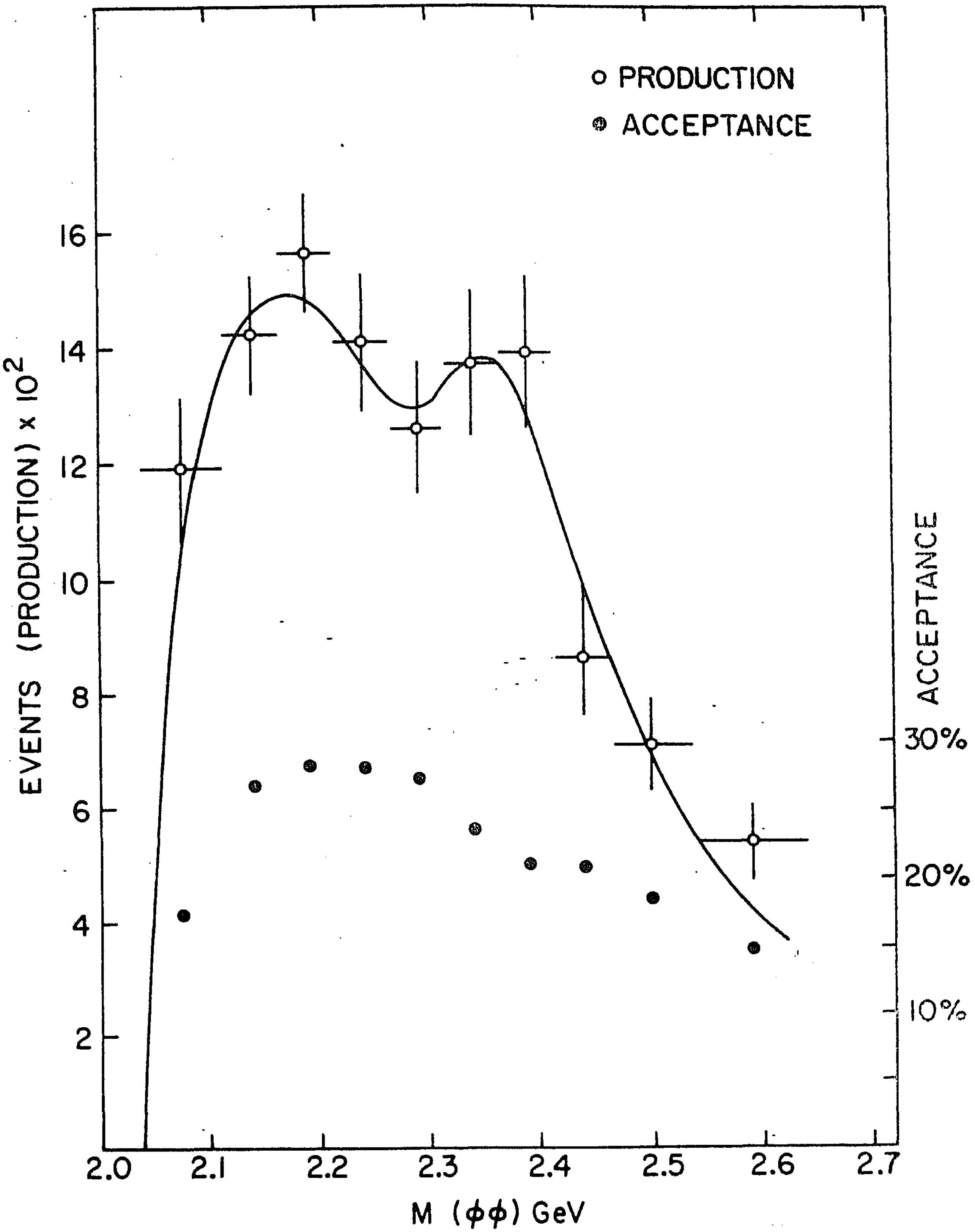

Fig. 6.4 The $\phi\phi$ mass spectrum corrected for acceptance. The solid line is the fit to the data with the three resonant states to be described later. The points at the bottom of the diagram are the acceptance for each mass bin to be read with the scale at the right.

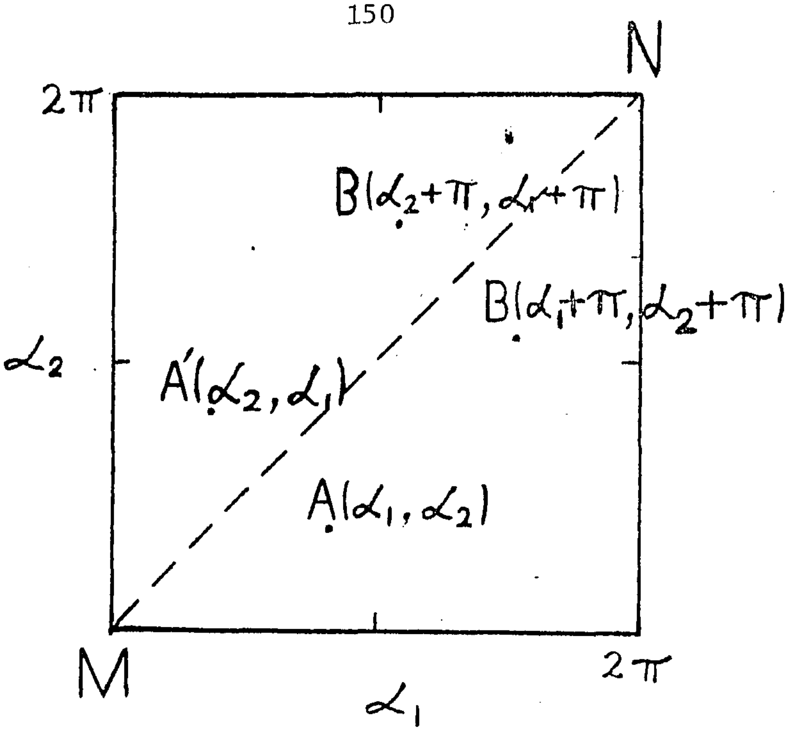

Fig. 6.5 The diagram to illustrate the mapping of a point A in α_1 vs α_2 scatter plot which satisfies charge symmetry, $A(\alpha_1,\alpha_2) \rightarrow B(\alpha_1+\pi,\alpha_2+\pi)$, and Bose symmetry, $A(\alpha_1,\alpha_2) \rightarrow A'(\alpha_2,\alpha_1)$ and $B(\alpha_1+\pi,\alpha_2+\pi) \rightarrow B'(\alpha_2+\pi,\alpha_1+\pi)$.

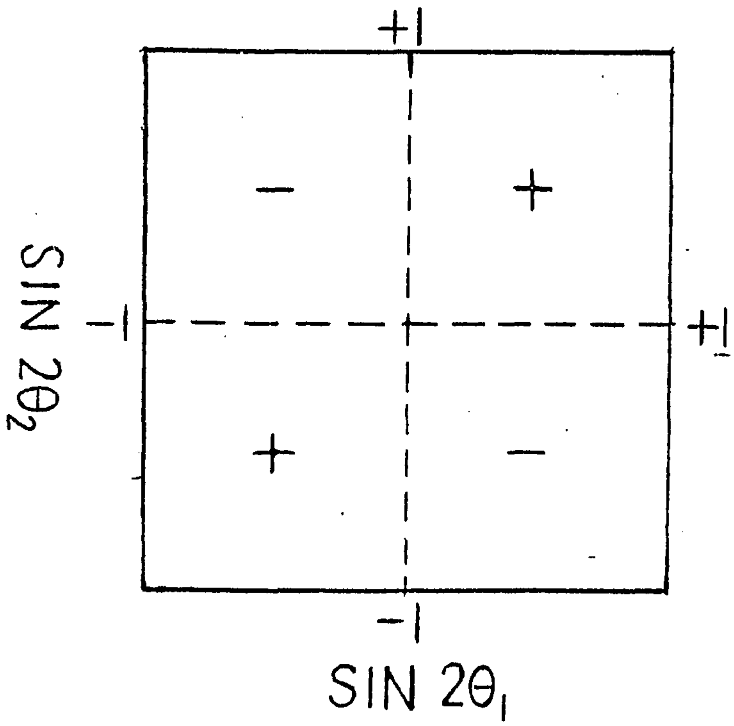

Fig. 6.6 The signs associated with cosχ or sinχ term ($\chi=\alpha_1+\alpha_2$) for different values of $\theta_1(0\rightarrow\pi)$ and $\theta_2(0\rightarrow\pi)$.

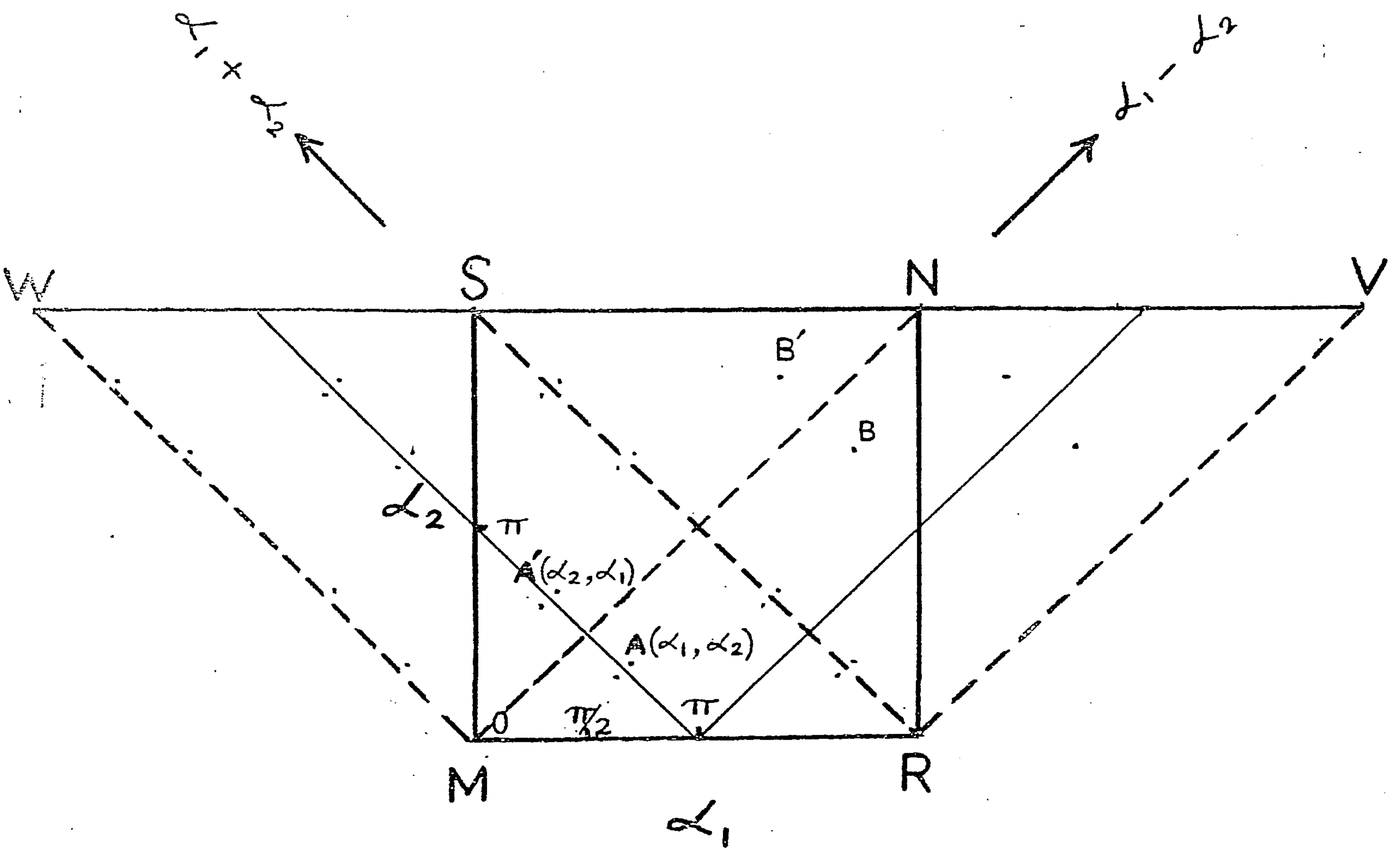

Fig. 6.7 Mappings of the $\alpha_1-\alpha_2$ and $\alpha_1+\alpha_2$ projections in α_1 vs α_2 scatter plot which satisfy both Bose symmetry and Charge symmetry. The natural ranges for both projections are reduced to $\pi/2$.

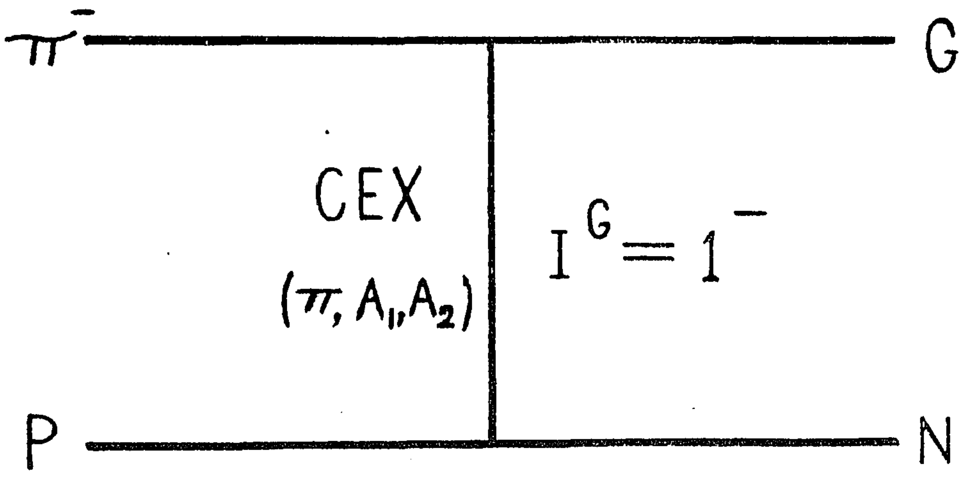

Fig. 6.8 Diagram for the charge exchange (CEX) process $\pi^- p \rightarrow Gn$ where G represents an intermediate state (glueball) for $\pi^- p \rightarrow \phi\phi n$.

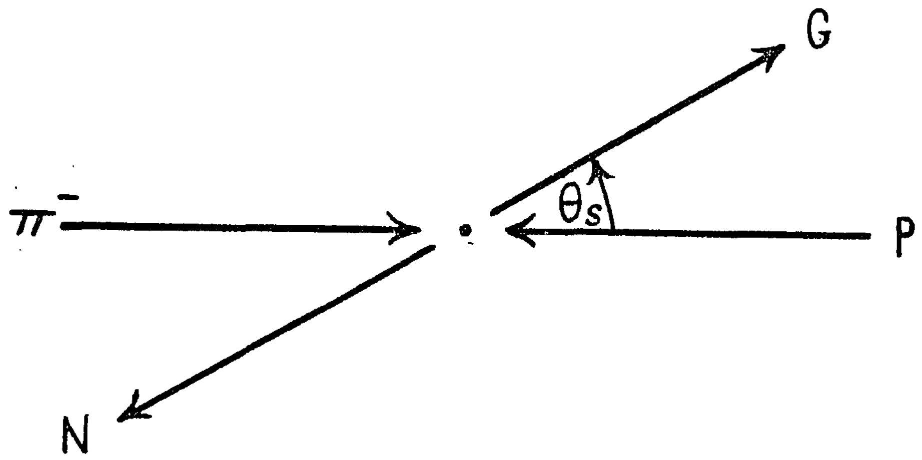

Fig. 6.9 The process $\pi^- p \rightarrow Gn$ in the center of mass frame. θ_s is the S-channel scattering angle.

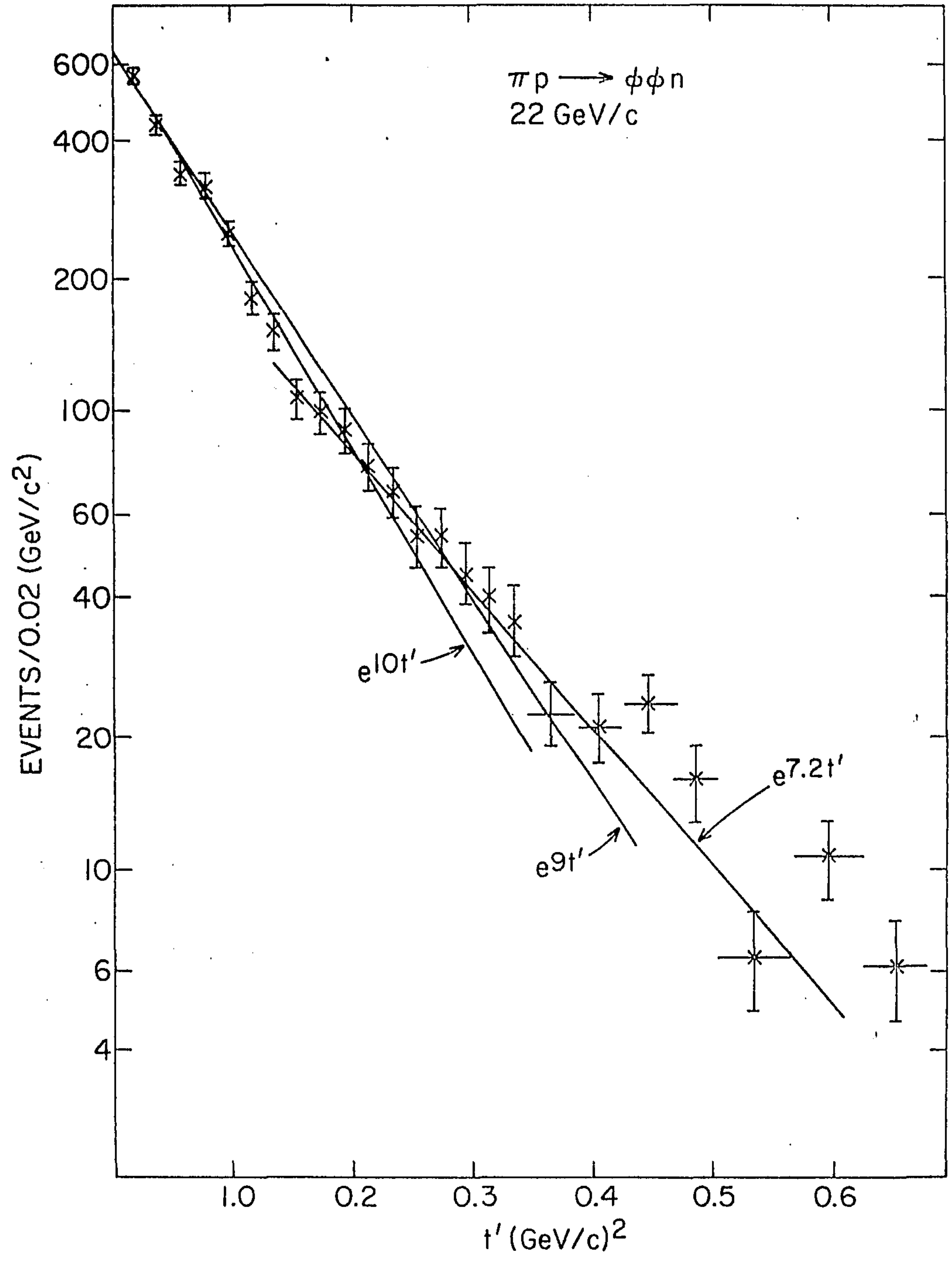

Fig. 6.10 Four momentum transfer squared distribution of the φφ system.

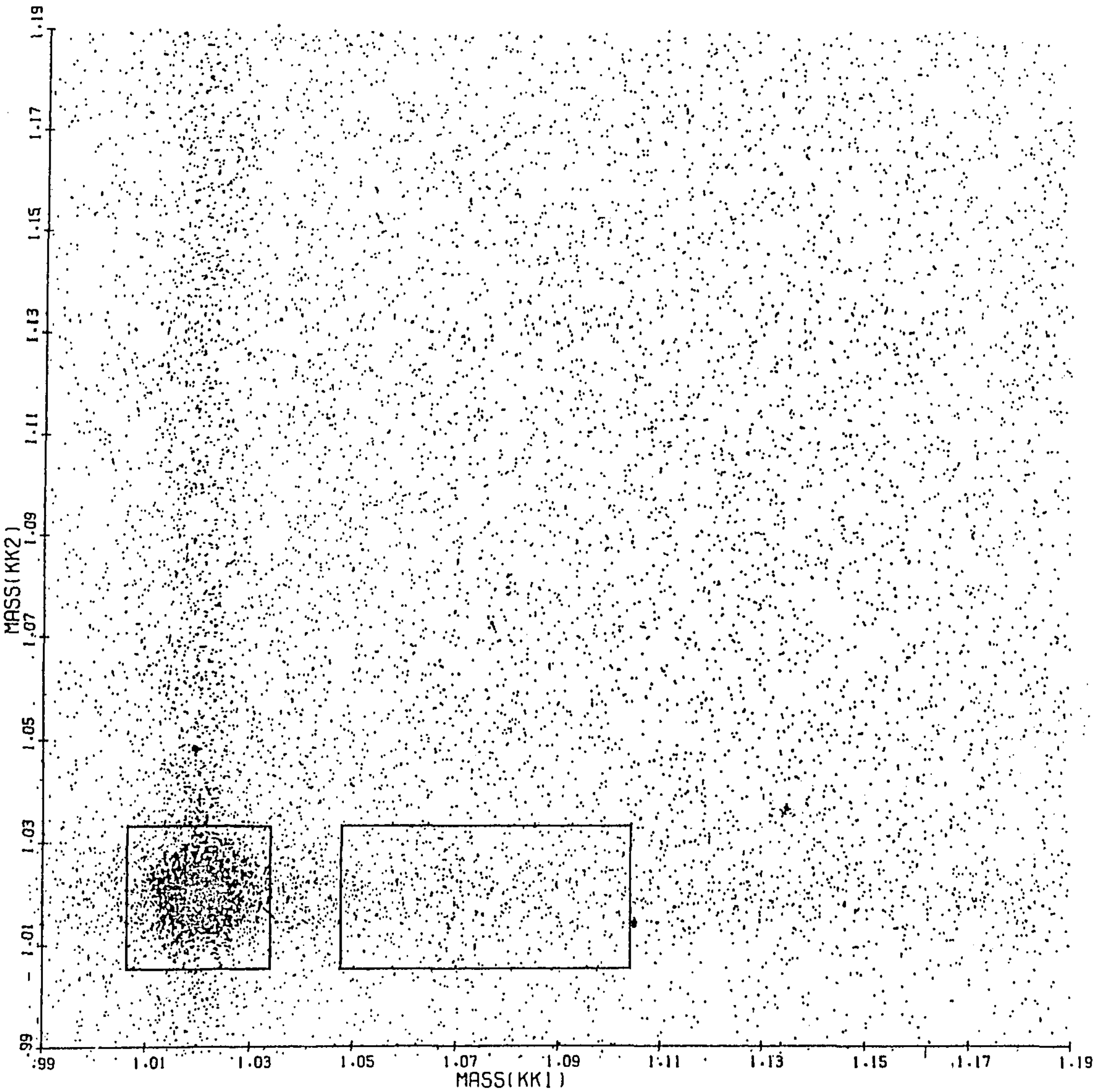

Fig. 6.11 The extraction of the $\emptyset K^+K^-$ background events (rectangular block) from the K^+K^- effective mass scatter plot.

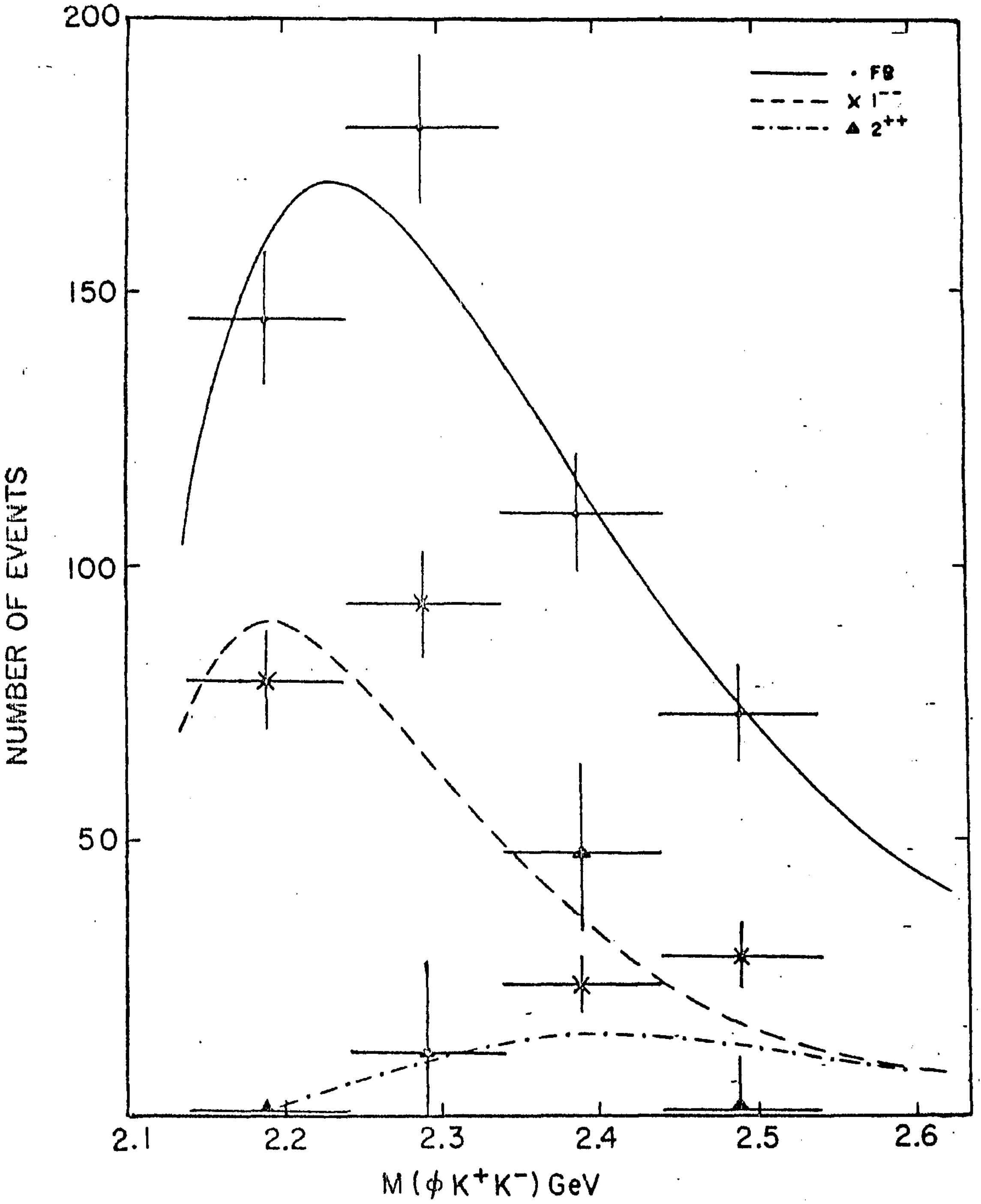

Fig. 6.13 Fitting the three ØK^+K^- backgrounds (1^{--},2^{++} S-wave and flat background) in four 100-MeV-wide bins.

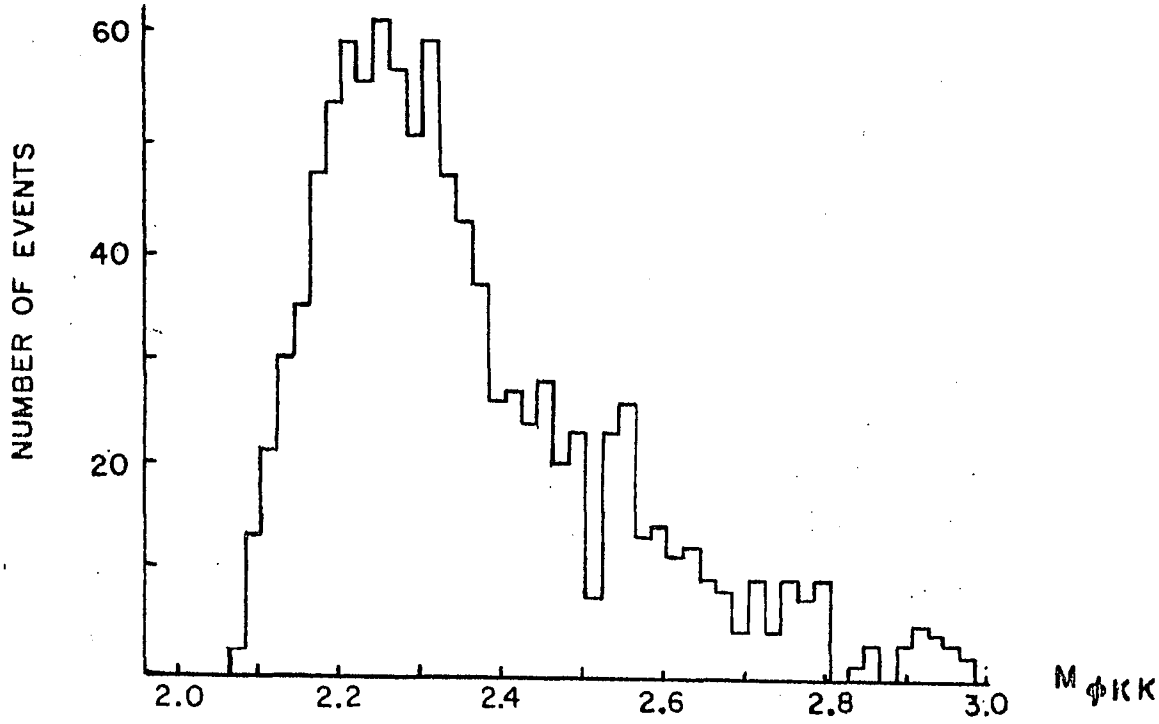

Fig. 6.14(a) The effective mass spectrum for the ϕK^+K^- background (1004 events).

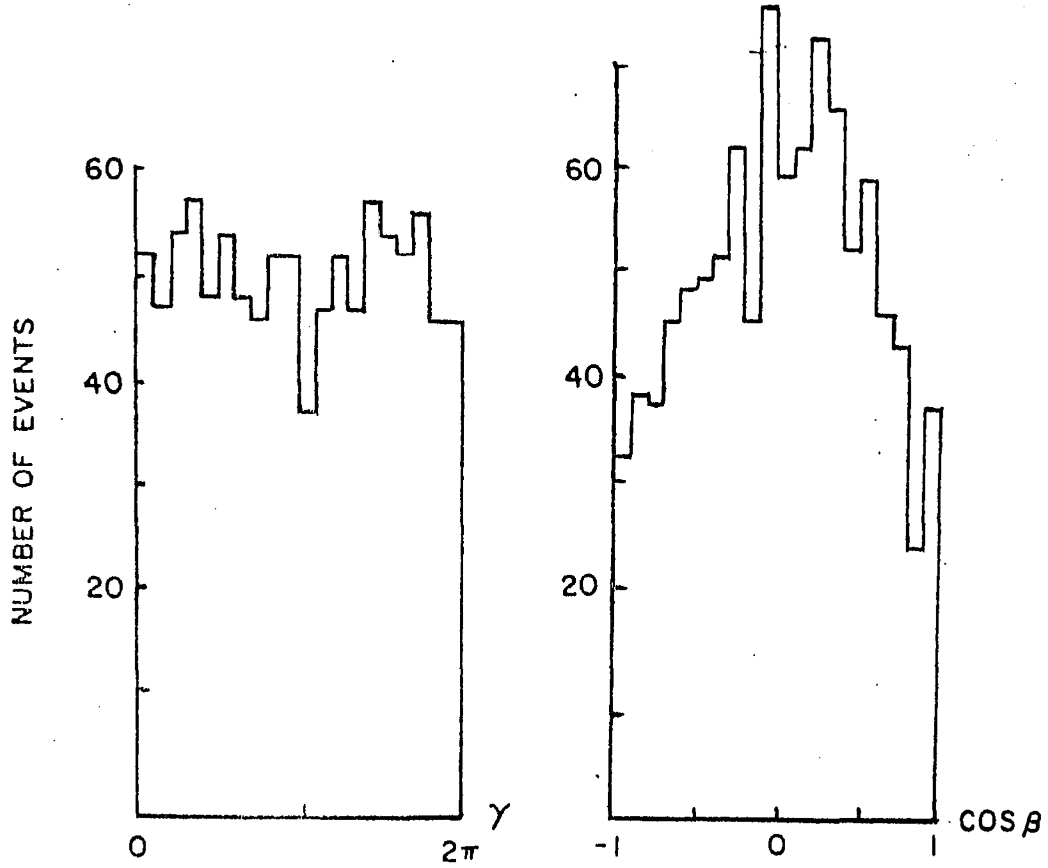

Fig. 6.14(b) The γ-distribution for the ϕK^+K^- background.

Fig. 6.14(c) The cos β-distribution for the ϕK^+K^- background.

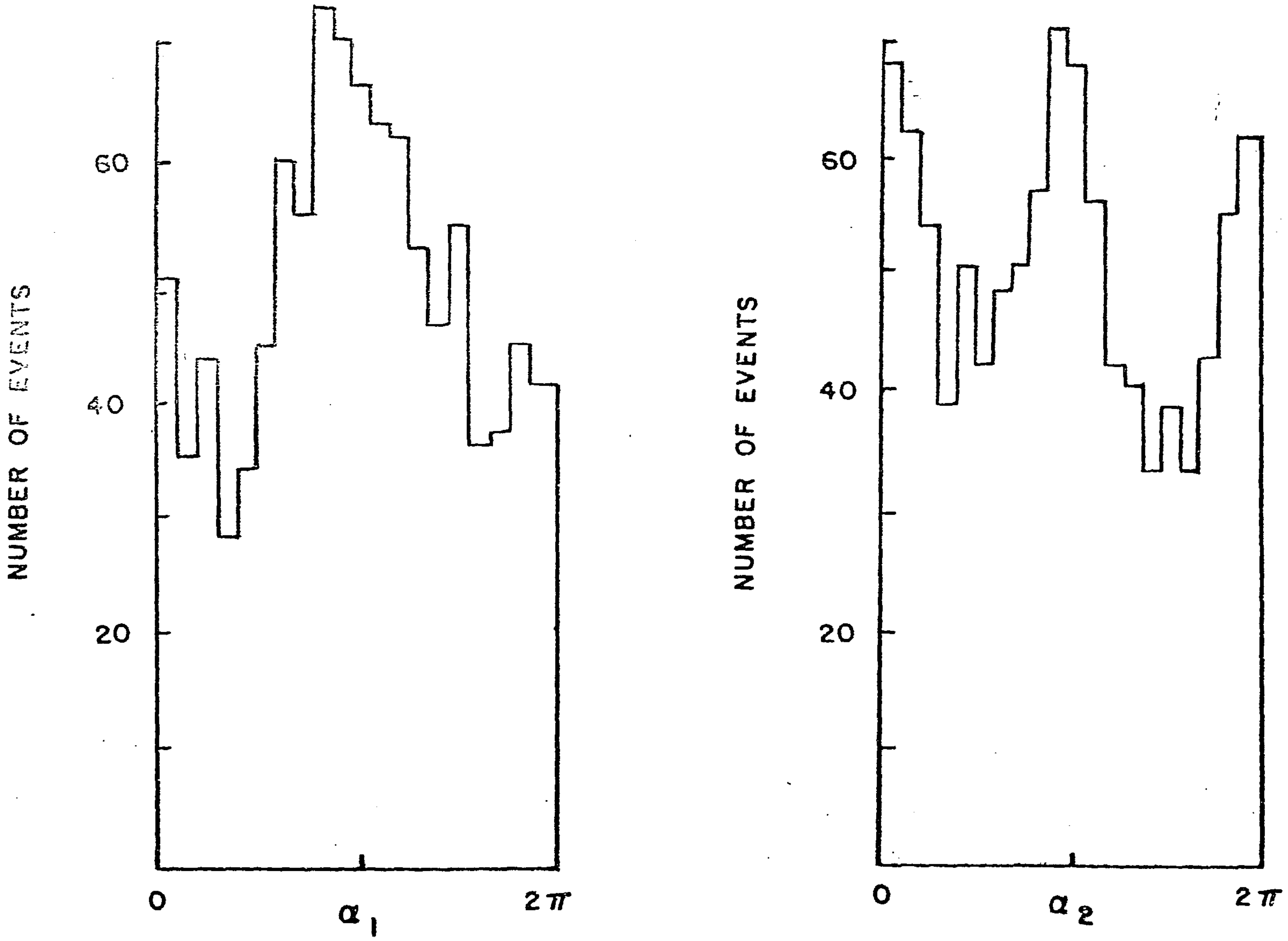

Fig. 6.14(d),(e) The α-distribution for α_1 and α_2 of the ϕK^+K^- background where α_1 is the azimuthal angle of K^+ in the CMS frame and α_2 is the corresponding angle due to the decay of ϕ.

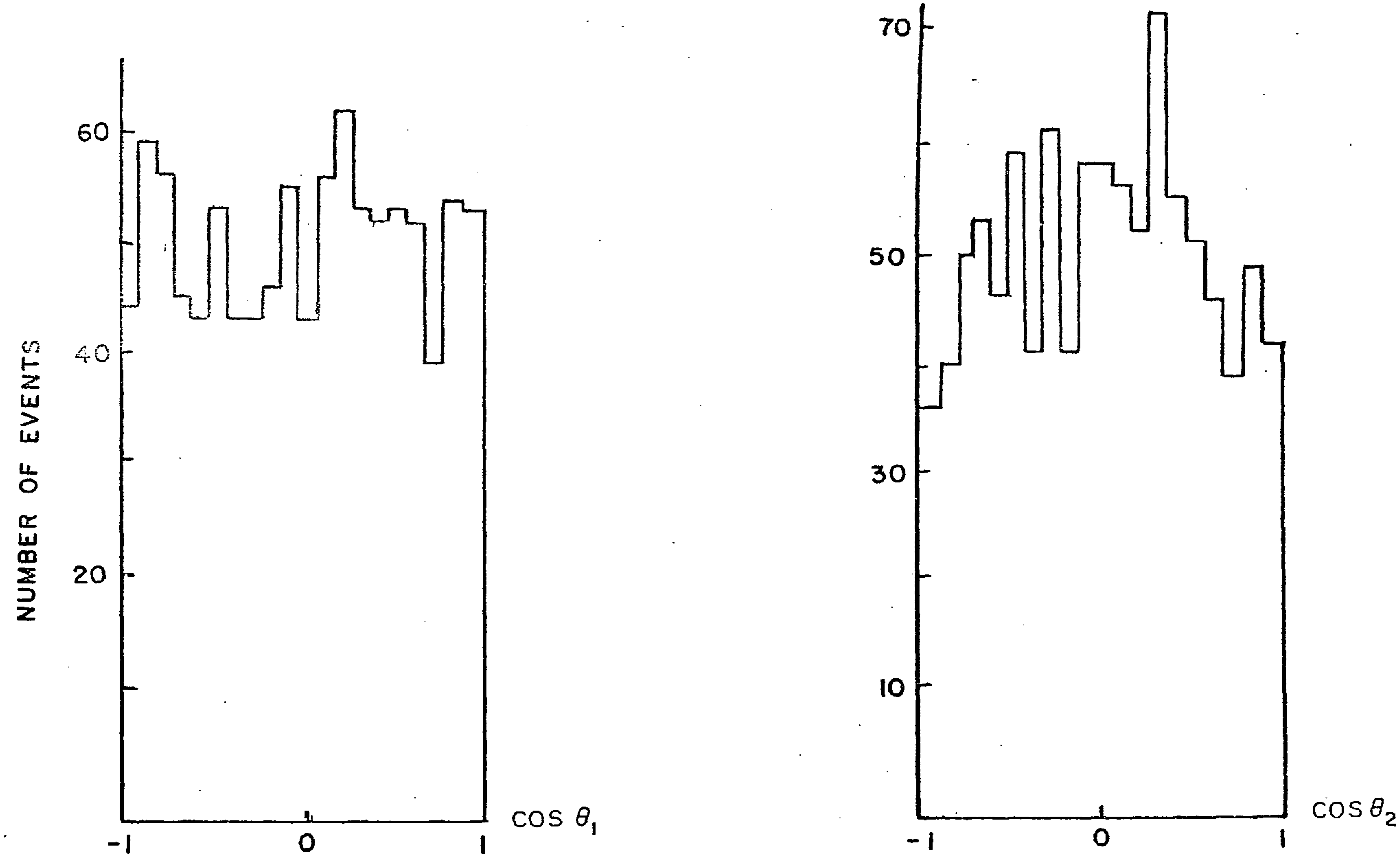

Fig. 6.14(f),(g) The cos θ-distributions for cos θ_1 and cos θ_2 of the ϕK^+K^- background where θ_1 is the polar angle of K^+ in CMS frame and θ_2 is the corresponding angle due to the decay of ϕ.

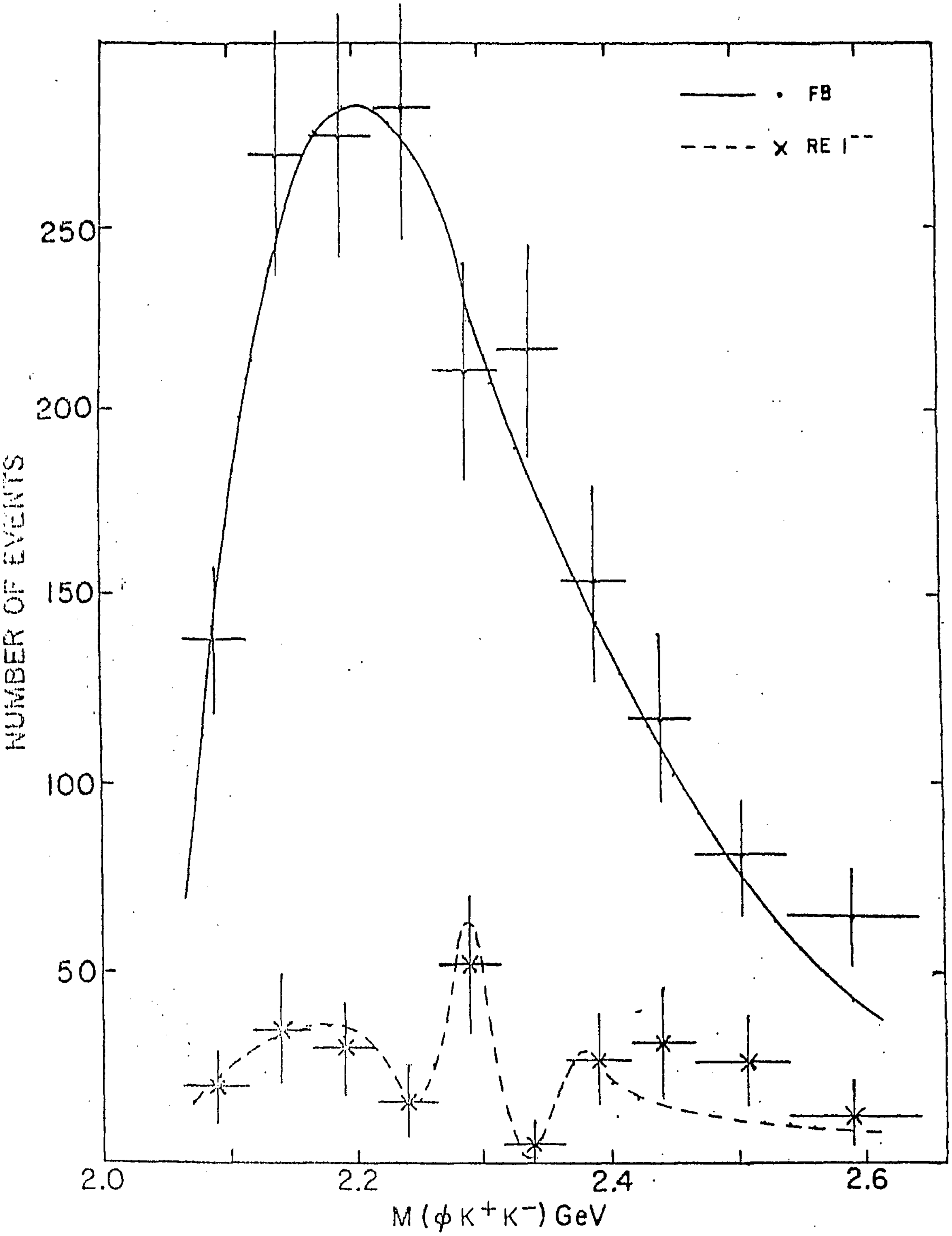

Fig. 6.15 Fitting the real part of 1^{--}(interfering) background and non-interfering background. The non-interfering consists of the incoherent background and imaginary part of 1^{--}.

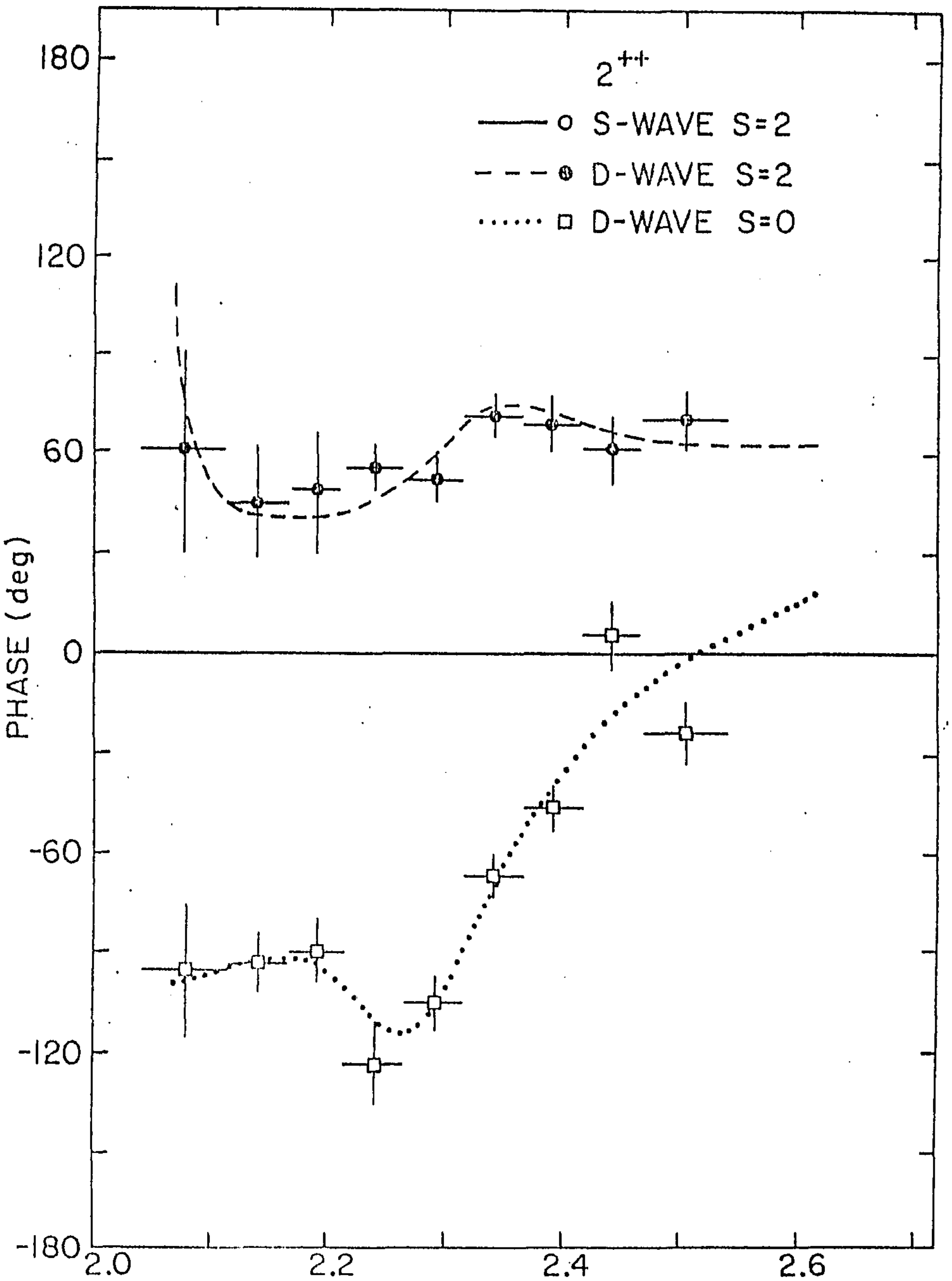

Fig. 6.16 D-S phase difference from the partial wave analysis vs. $\phi\phi$ mass. The smooth curves are derived from a K-matrix fit.

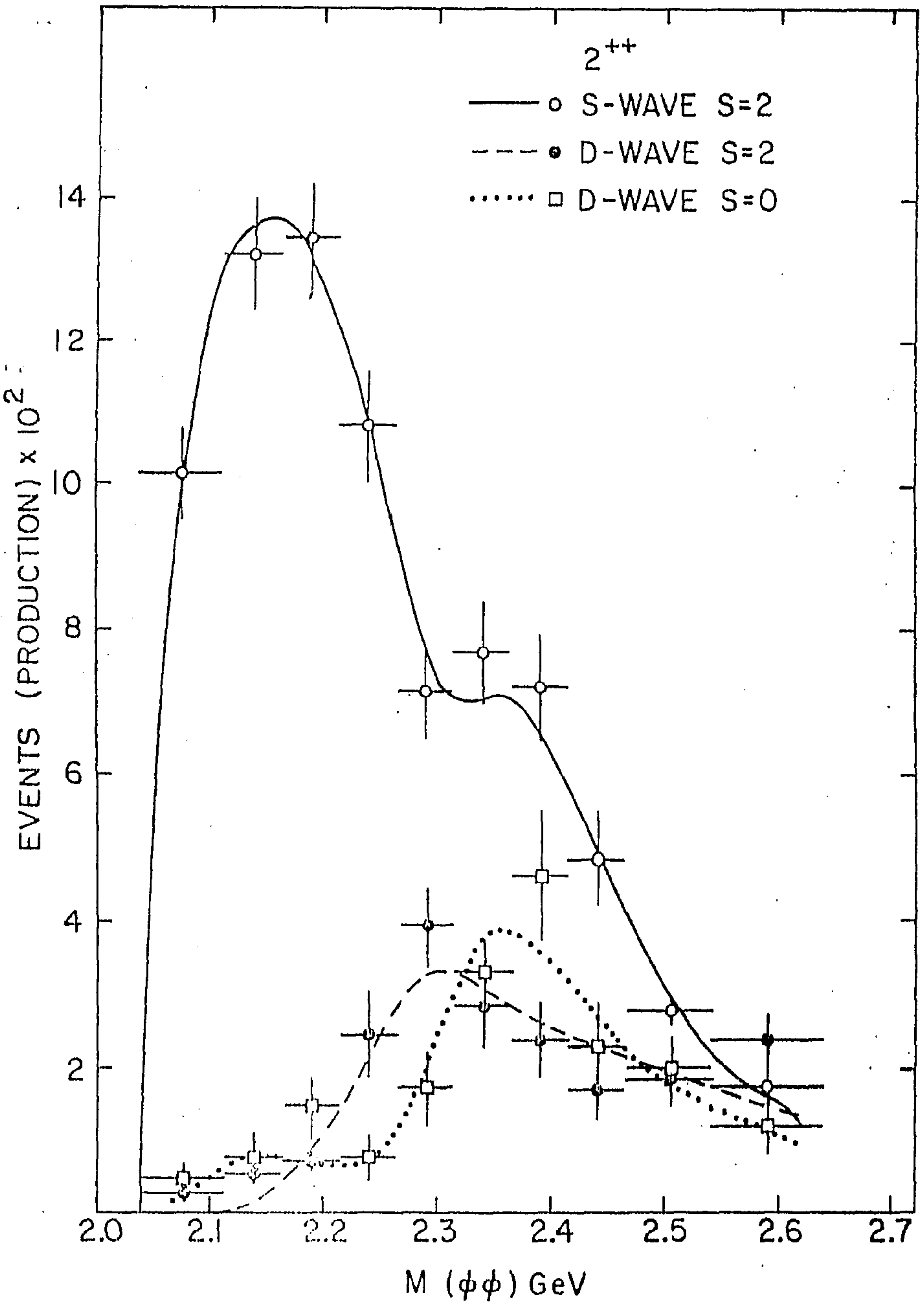

Fig. 6.17 The three φφ, $J^{PC} = 2^{++}$ partial waves at production in 50 MeV mass bins (except ends). The smooth curves are derived from a K-matrix fit.

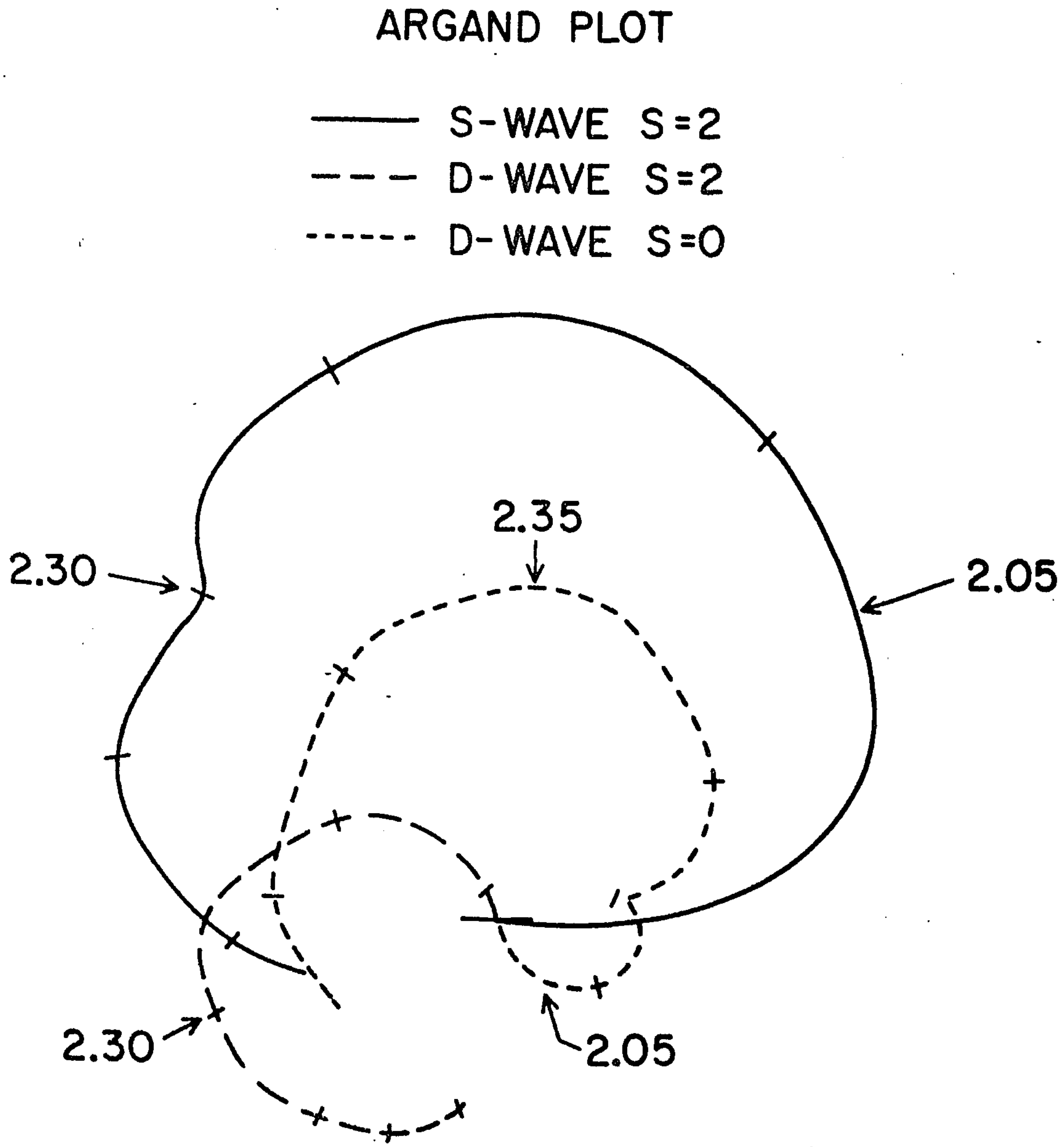

Fig. 6.18 Argand plot from K-matrix.

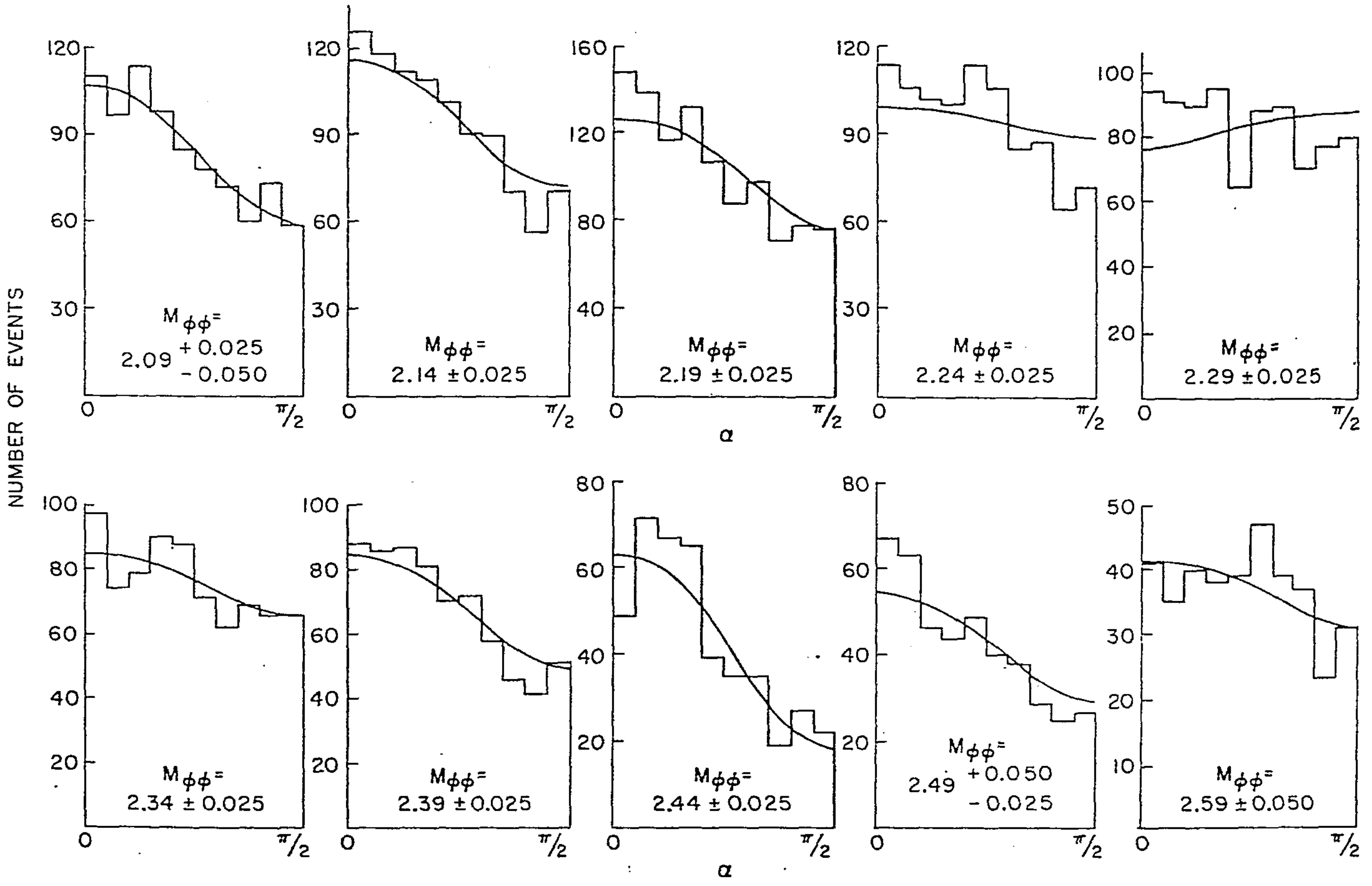

Fig. 6.19a Comparison of Monte Carlo generated events to the observed angular variable α

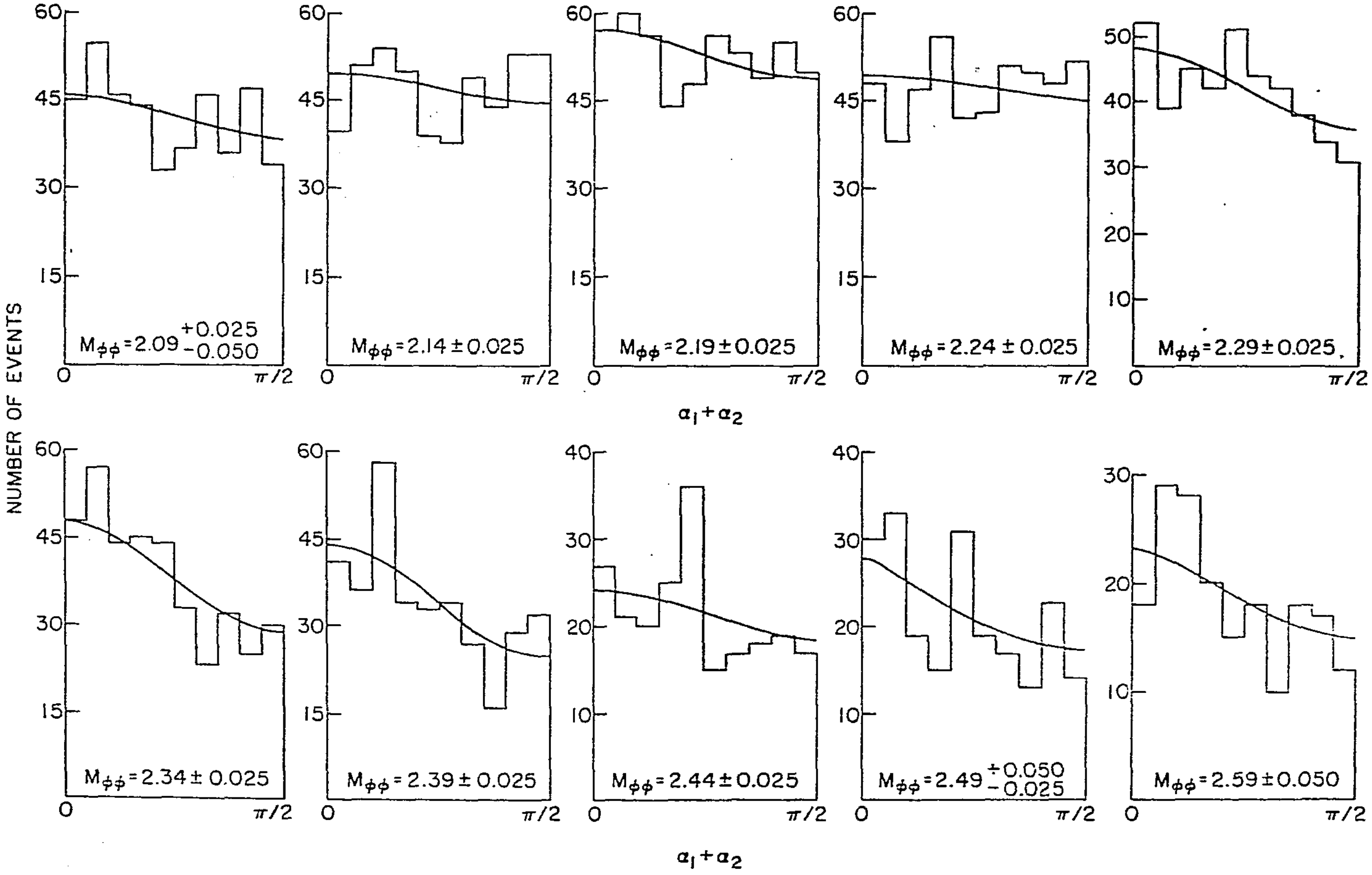

Fig. 6.19b Comparison of Monte Carlo generated events to the observed angular variable $\alpha_1+\alpha_2$

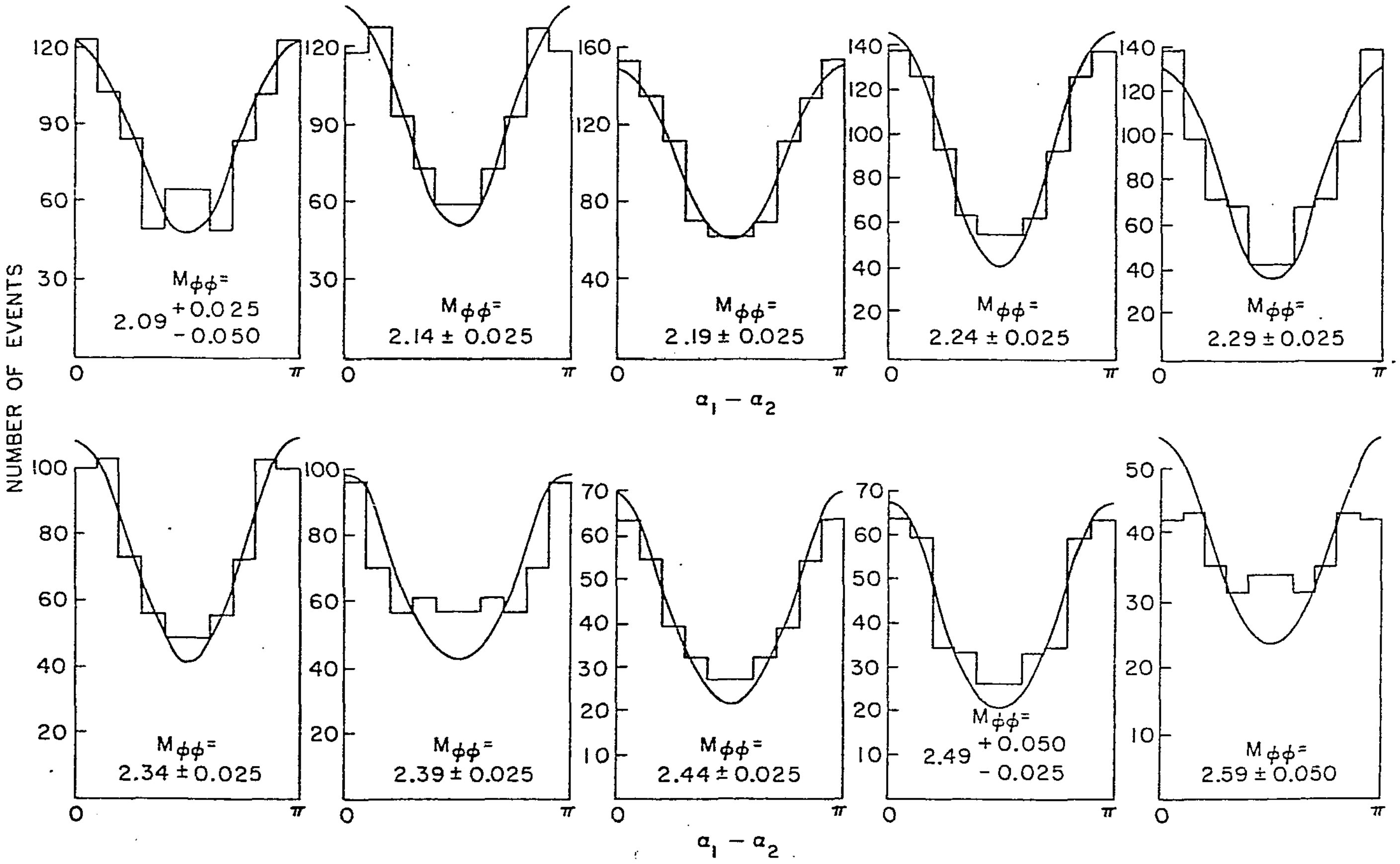

Fig. 6.19c Comparison of Monte Carlo generated events to the observed angular variable α_1-α_2

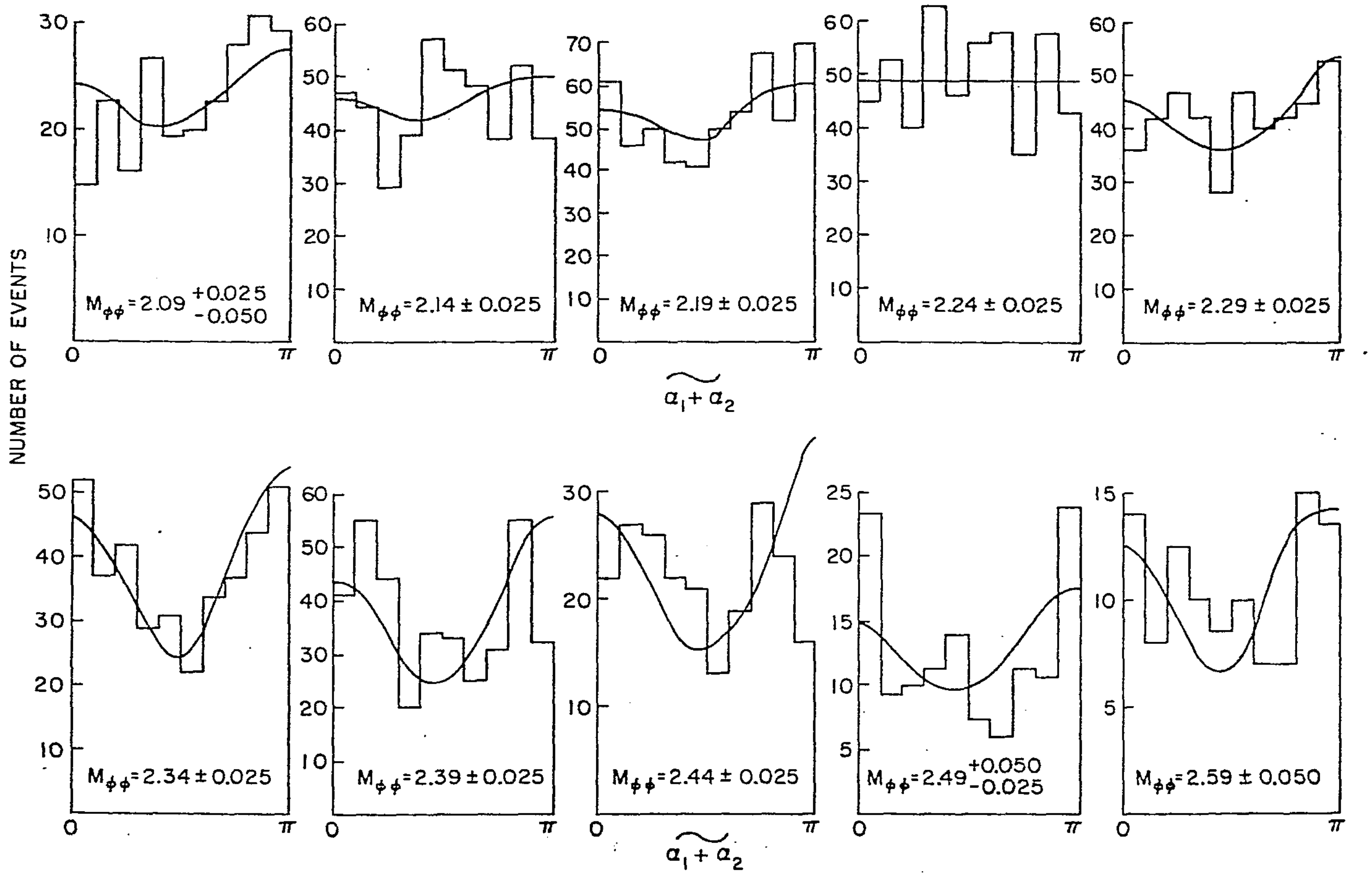

Fig. 6.19d Comparison of Monte Carlo generated events to the observed angular variable $\widetilde{\alpha_1+\alpha_2}$

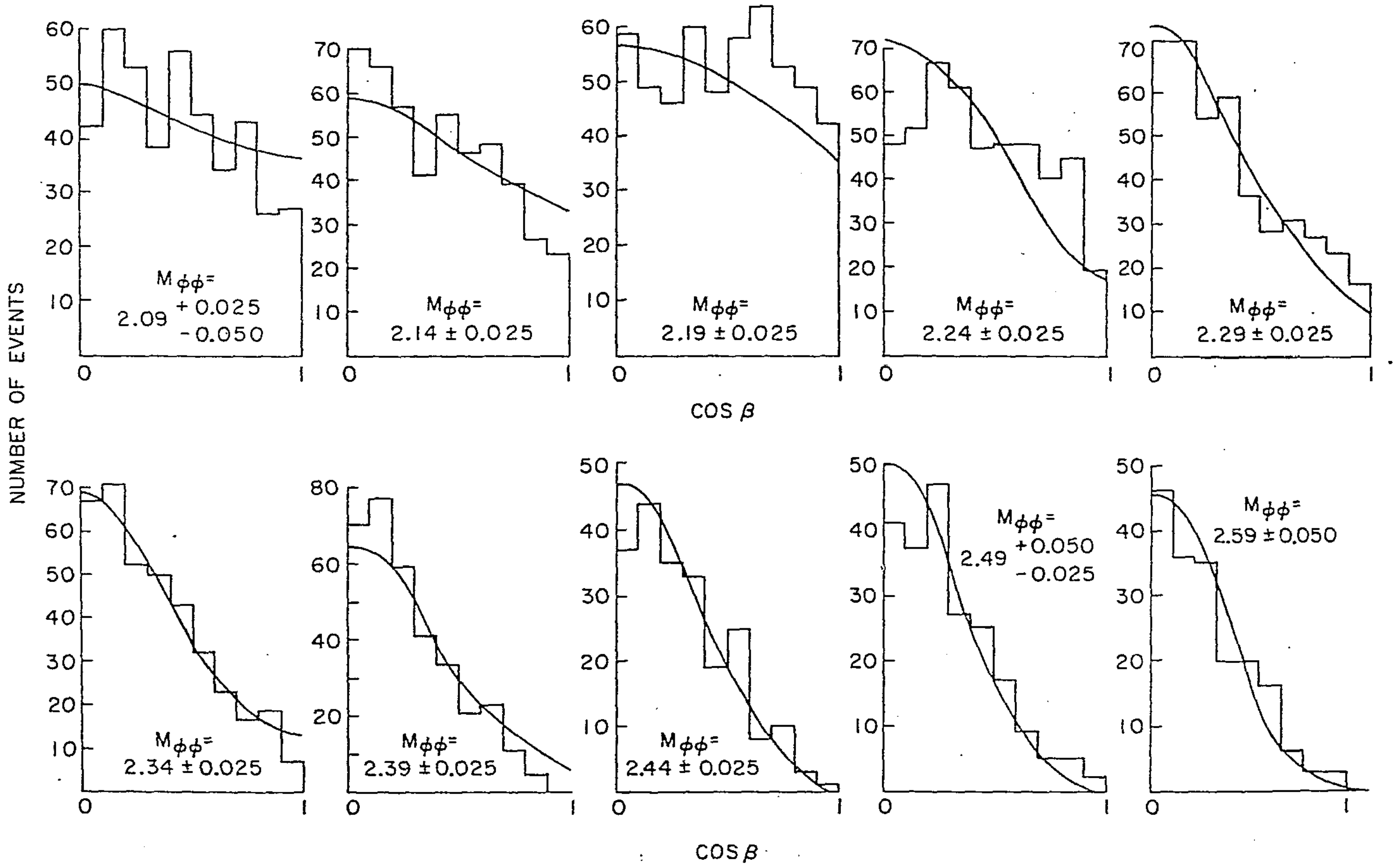

Fig. 6.19e Comparison of Monte Carlo generated events to the observed angular variable cosβ

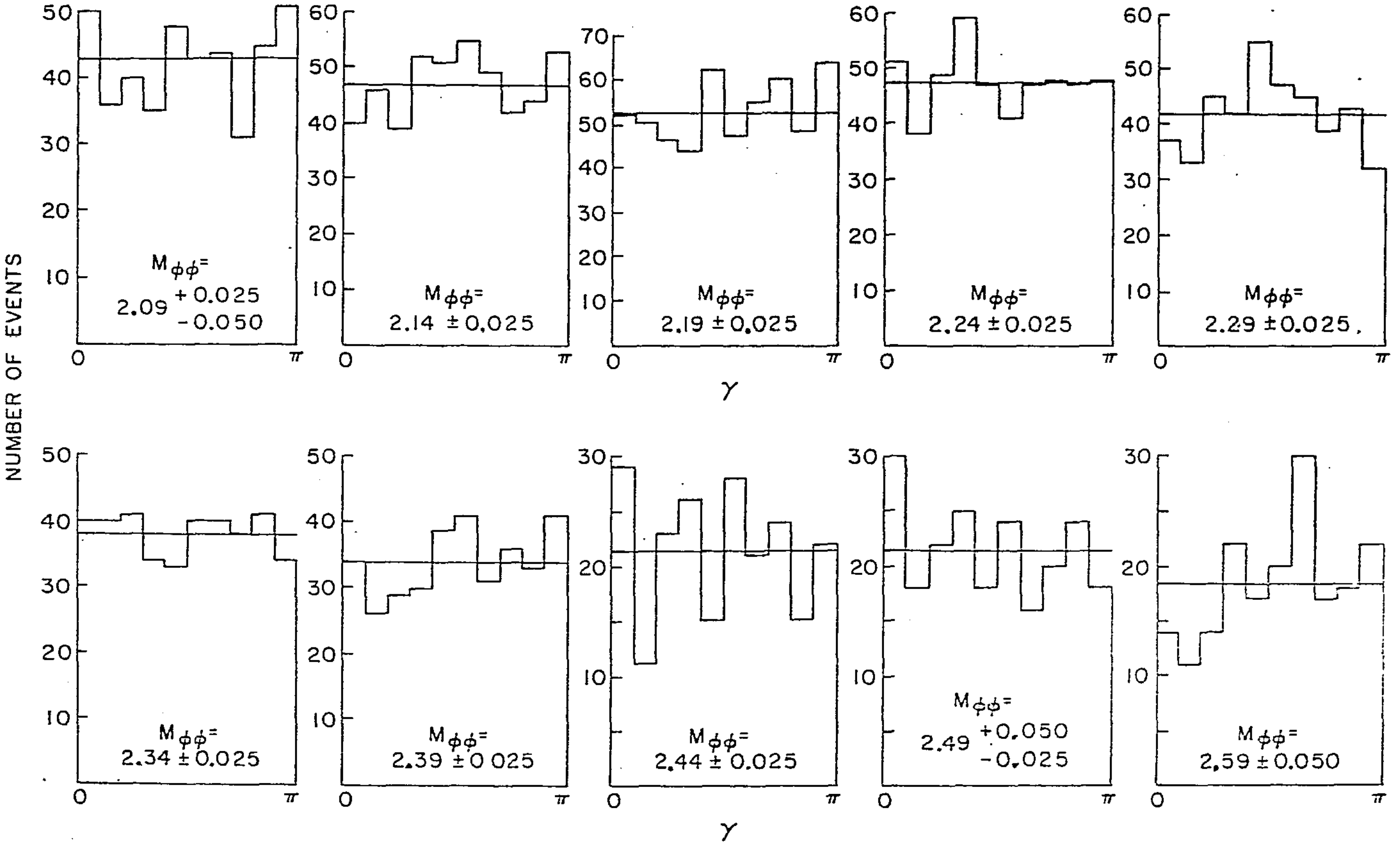

Fig. 6.19f Comparison of Monte Carlo generated events to the observed angular variable γ

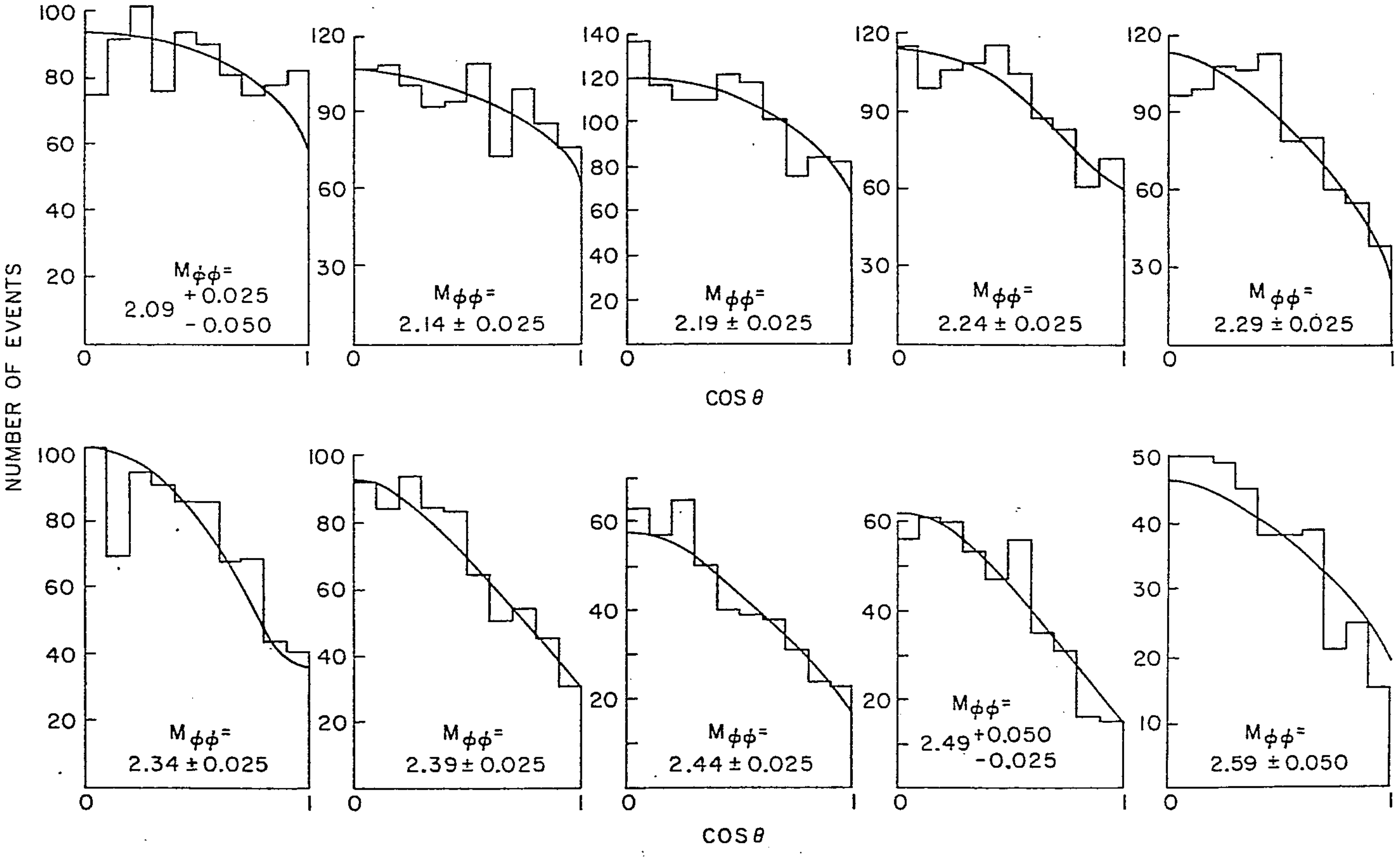

Fig. 6.19g Comparison of Monte Carlo generated events to the observed angular variable cosθ

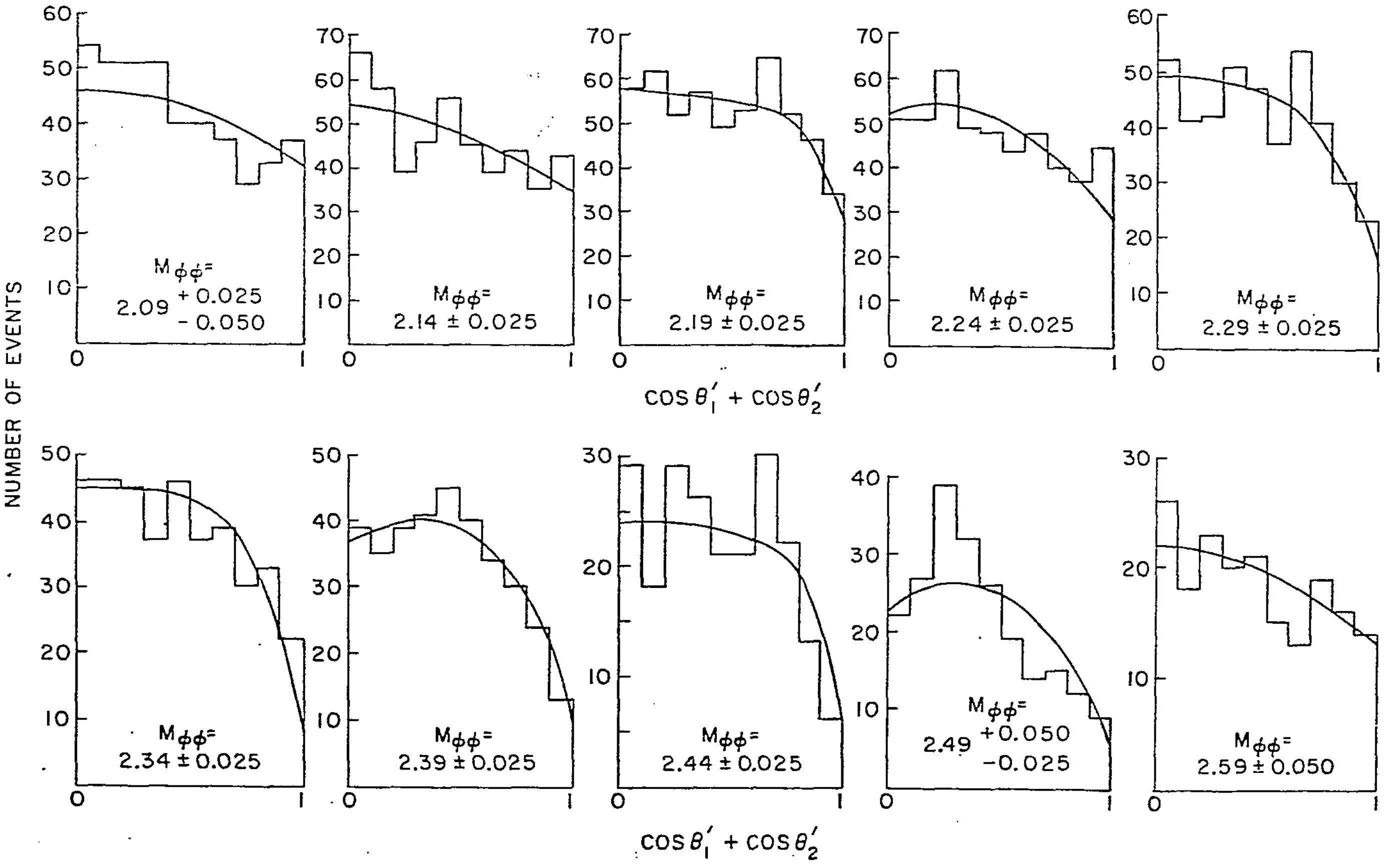

Fig. 6.19h Comparison of Monte Carlo generated events to the observed angular variable $\cos\theta_1' + \cos\theta_2'$

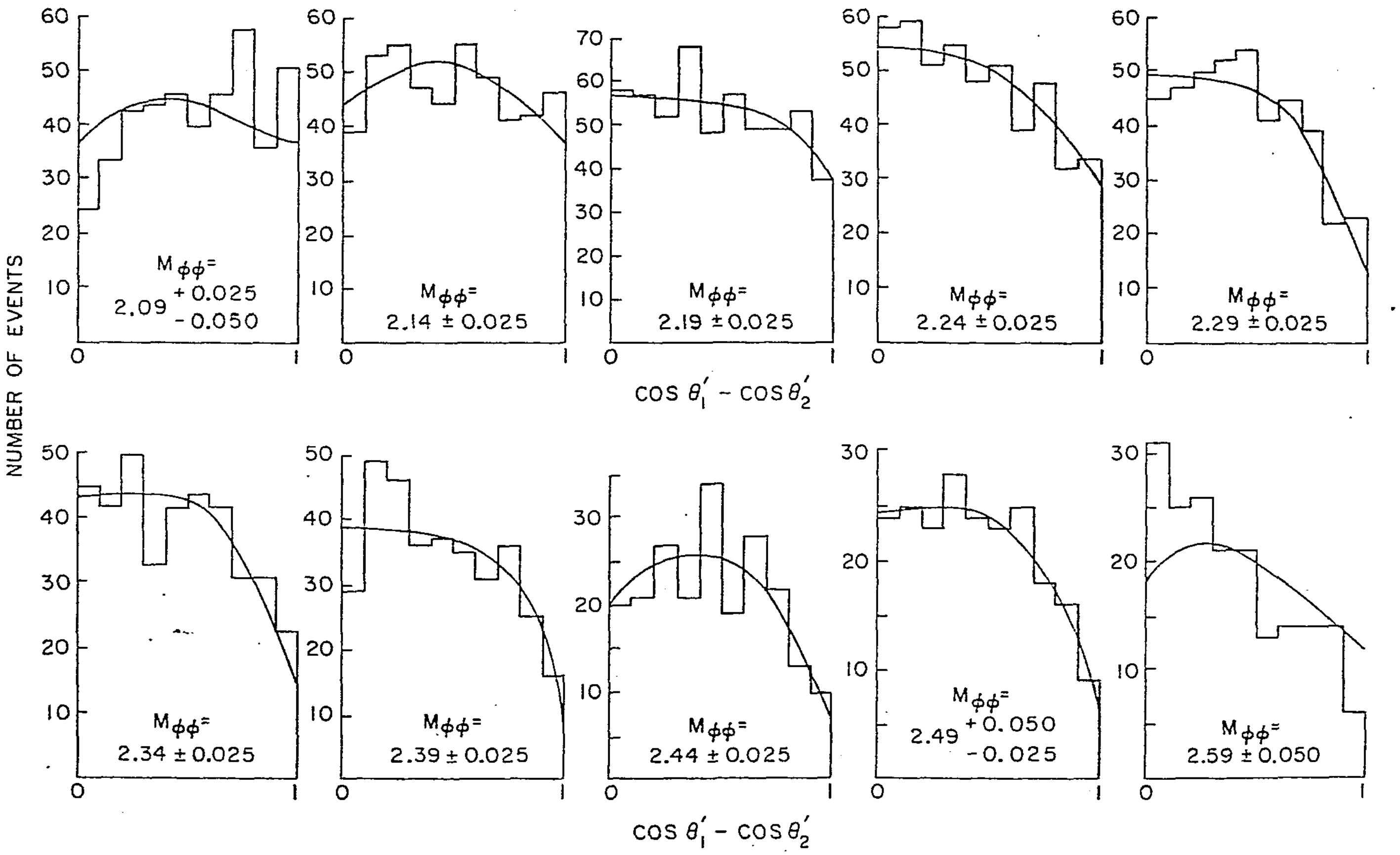

Fig. 6.19i Comparison of Monte Carlo generated events to the observed angular variable $\cos\theta_1' - \cos\theta_2'$.

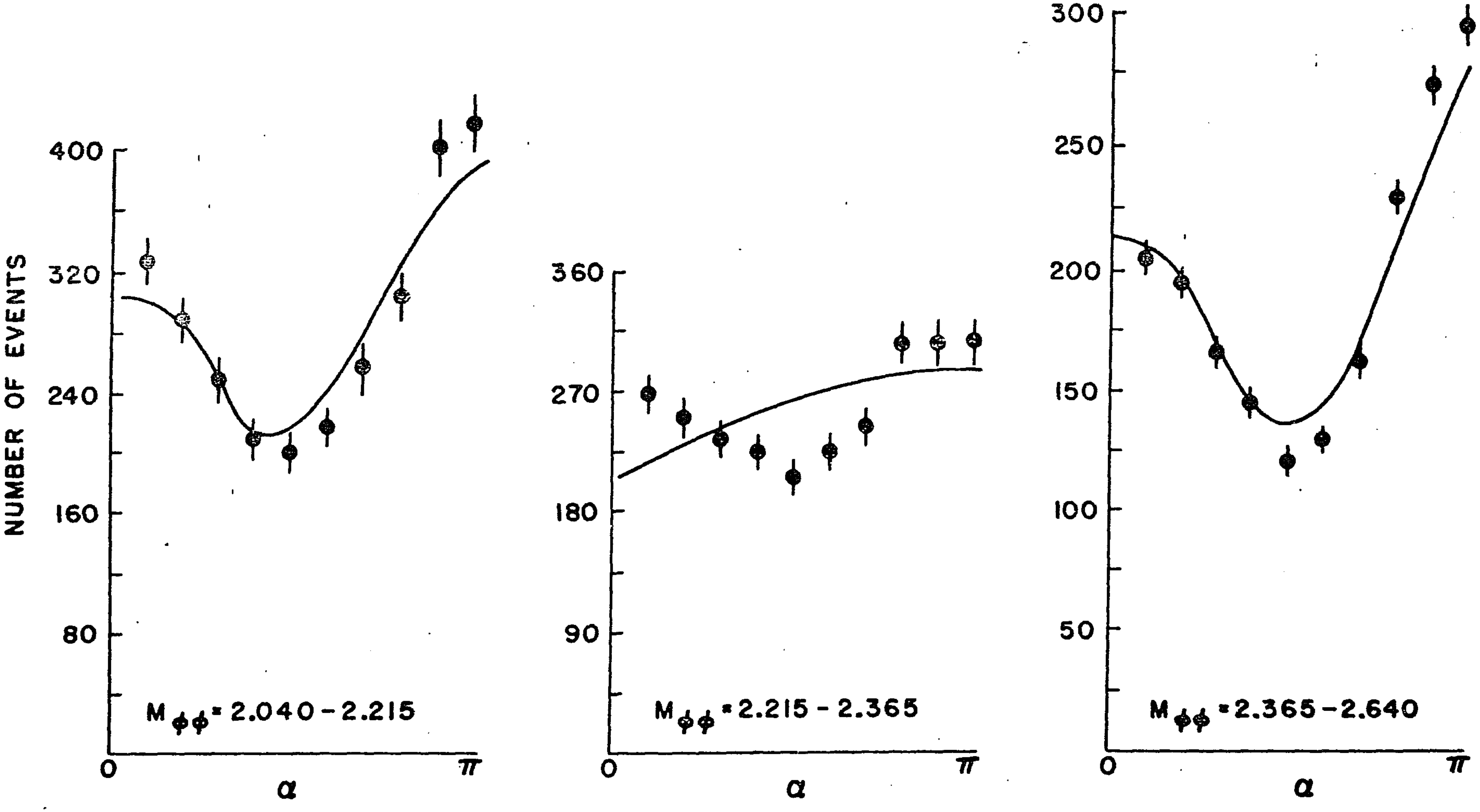

Fig. 6.20 Comparison of the generated K-matrix fit with $J^{PC} = 1^{--}$ partial wave and the data for the α projection in $0 \to \pi$ range. The asymmetrical structure for α distribution in low and high mass bins are clearly shown.

CHAPTER 7: DISCUSSION OF RESULTS

7.1 Summary of Results

The results of the present analysis obtained in the preceeding chapters can be summarized as follows:

(a) There is a complete absence of the substantial suppression expected for the OZI forbidden process $\pi^- p \rightarrow \phi\phi n$. This demonstrates the breakdown of the OZI rule in this channel.

(b) The t'-distribution is consistent with the peripheral production and thus the reaction can be effectively described by $\pi\pi \rightarrow \phi\phi$.

(c) The application of the isobar model formalism in a PWA together with the maximum likelihood method has selected three $\phi\phi$ partial waves ($I^G = 0^+$) all with quantum numbers $J^{PC} = 2^{++}$, which give a good fit to the data.

(d) The results of the PWA for the relative phase motion and the three partial wave amplitudes agree well with a 3-pole K-matrix solution.

(e) The resonance parameters of these three resonant states are also determined from dhe K-matrix fit. These states are denoted by $g_T(2050)$, $g_{T'}(2300)$ and $g_{T''}(2350)$ where the numbers in the parentheses represent the resonance masses. Their widths are given by $\Gamma_{g_T} = 200^{+160}_{-\ 50}$ MeV, $\Gamma_{g_{T'}} = 200^{+60}_{-50}$ MeV and $\Gamma_{g_{T''}} = 270^{+\ 90}_{-130}$ MeV respectively.

In the following, we present a discussion which concludes that the results listed above find a natural glueball interpretation within the context of QCD. It should be noted that as Table 6.13 indicates, the mixing of waves is substantial in these three 2^{++} states and the exact content of each resonance or K-matrix pole is therefore sensitive to details and somewhat uncertain. However, from the glueball physics point-of-view we are at present mostly interested in the quantum numbers and the parameters of the resonant states and not very concerned about their wave content.

7.2 Axioms

Our glueball interpretation for the observed reaction is based upon two basic assumptions taken as input axioms:

(a) QCD is correct;

(b) The OZI rule is universal for weakly coupled glue in Zweig disconnected diagrams where the disconnections are due to the introduction of new flavors of quarks. Thus the states we observe which break down the OZI suppression must have strong gluon coupling corresponding to the resonating glue or glueballs.

These axioms agree with the experiments seen in the ϕ, J/ψ and Υ systems and merely represent modern QCD practice. Note that axiom (b) allows only resonating glue (glueballs) to break down the Zweig suppression and possibly mix with two quark states or other possible states. In addition, Zweig's diagrams are to be taken literally as one-setp processes, or otherwise the nature of the multigluon exchange is replaced by a series of OZI allowed single gluon exchanges, and this is inconsistent with experiments.

7.3 Results Compared with Theory

Our measured g_T, $g_{T'}$, and $g_{T''}$ quantum numbers, masses and widths can be compared with theory to see how well they agree.

(a) Mass

Theoretical predictions for the glueball spectrum are available from the MIT bag model and lattice gauge method. It should be noted that the calculated masses of the low-lying glueball states in any of these models at present give only a rough guide to glueball masses.

Parisi and Petranzio[19] introduced a phenomenological non-zero effective mass for the gluon of about 0.75 GeV due to confinement. The same mass was also estimated in constituent models by Carlson et al.[10] In this sense, the mass for a two-gluon S-wave system should be ~ 1.5 GeV. However, we expect from the hyperfine splitting (~ 0.5 GeV) that the $J^{PC} = 0^{++}$ and 2^{++} to be around 1.0 GeV and 2.0 GeV respectively. In the three-gluon system, the estimated 2^{++} glueball mass is expected to be ~ 2.25 GeV.

The recent bag model calculations[10] show that, depending upon the cavity mode, the mass of the 2^{++} glueball state ranged from 1.9 GeV [$(TE)^2$ mode] to 2.4 GeV [$(TM)^2$ mode]. These differ markedly from the earlier bag model estimates made by Donoghue et al.[15] who concluded that the masses of 0^{++} and 2^{++} states were degenerate, i.e., $m(0^{++}) \approx m(2^{++}) \approx 1$ GeV. By assuming iota(1440) to be a glueball, Chanowitz and Sharpe[11] calculated the $m(2^{++})$ value and found that it varied from 1.75 GeV to 2.59 GeV depending on the self energies of the TE and TM modes.

The approach followed by the lattice gauge theories generally expresses the estimated glueball spectra in multiples of $m(0^{++})$ values. In this way, the three representative multiplicative factors for the 2^{++} states were calculated to be 2.5,[16a] 2.3[17a] and 1.7[48] respectively. Clearly a major problem is the precise determination of $m(0^{++})$. If we take the value of this state to be 1 GeV as determined by Berg, Billoire and Rebbi, then the corresponding mass of 2^{++} state lie primarily in the 1.7-2.5 GeV range. On the other hand, Carlson estimated the $m(0^{++}) \sim 0.8$ GeV with the subsequent 2^{++} mass ranged between 1.36 GeV and 2.0 GeV.

In the recent report of Experimental Meson Spectroscopy Conference (1983), Meshkov[50] has reviewed he current status of glueball spectra and concluded that even with the lack of a precise determination of m(0^{++}), the 2-3 GeV range was very likely to be the prime region for 2^{++} glueballs. The lattice gauge calculations were certainly consistent with this possibility. In particular, he emphasized the point that the g_T resonances found by the BNL/CCNY collaboration fitted in this scheme nicely.

(b) Quantum numbers

In considering the quantum numbers, T.D. Lee[51] has analytically calculated the J = 2 glueballs in the strong coupling limit by analytical means. He obtains three glueball states which correspond to our three states. In order to try to adjust his strong coupling calculation to the real world of intermediate coupling we took the mass of the 0^{++} glueball as ~ 1 GeV and fit our three masses with the other parameters and found a good fit.

In Meshkov's glueball review,[50] he specifically considered the 2^{++} states and showed that theory predicted five 2^{++} low-lying glueballs, three from the two-gluon sector and two from the three-gluon sector. Their exact location and splitting depended on a detailed dynamical model. However, the quantum numbers for the three glueballs in the two-gluon sector were explicitly demonstrated to be identical with the three resonant states of the present analysis. It should be noted that at the time Meshkov prepared his review, only two g_T resonances were available for comparison. The third resonance was later found following an increased statistics run in 1983.

(c) Width

The width of a glueball is not a well-predicted quantity. By assuming that glueballs decay to quarkonium through their coupling of gluonic constituents to pure quark states, Carlson *et al.*[52] estimated that the typical glueball width should be ~ 30 MeV. This value is obtained by taking the geometric mean of typical hadronic width and OZI violating width, i.e.

$$\Gamma_G \sim \sqrt{\Gamma_{\text{ordinary}} \cdot \Gamma_{\text{OZI-violating}}}$$

This estimate is different from what we get. However, according to Lindenbaum,[56] in hadrons, the hadronization process consists of creation of one or more $q\bar{q}$ pairs. This must occur near the outer region of confinement involving strongly interacting soft glue, probably including collective interactions, if we are to have resonances decay with typical hadronic widths. A glueball is a resonating multigluon system. The glue-glue coupling is stronger than the quark-glue coupling and it would be expected, via gluon splittings before the final hadronization, to have a similar hadronization process to a $q\bar{q}$ hadron. Hence a glueball would be expected to have typical hadronic widths. This is certainly to be expected for ordinary (non-exotic) J^{PC} states. In the case of exotic J^{PC} states, this argument may not be relevant since no one yet knows what suppresses the observed exotic sector. Therefore Meshkov's oddballs[53] (exotic J^{PC}) may be narrow.

From the discussions presented above, we thus conclude that our measured glueball masses and quantum numbers are in reasonable agreement with theory. Our measured widths are consistent with the expectation that should be similar to typical hadronic widths.

7.4 Other Comments

(a) $\pi^-p \to \phi\phi n$ as a Crossed Pomeron Process

Lipkin[54] has argued that the reaction $\pi^-p \to \phi\phi n$ is either not an OZI suppressed process or has a much smaller suppression factor since it is related by crossing to $\phi + n \to \phi + \pi^- + p$. Thus it is adequately explained as a crossed Pomeron process in which ϕ is elastically scattered by a nucleon with an additional production of pion, and there is no reason to believe that this process is forbidden.

It was pointed out by Lindenbaum[55] that one of the consequences of crossing is the associated change of physical and kinematic regions as compared to the original reaction. In this connection, it is erroneous to compare two reactions simply related by crossing without considering important factors such as the analytic continuation, the singularities involved, etc. Unfortunately, Lipkin didn't consider these in his article. To see how much physical change has resulted in Lipkin's crossed reaction, we note that the cross section for $\pi^-p \to \phi\phi n$ is ~ 20 nb, whereas the corresponding cross section for the elastic scattering is ~ 10 mb, which is a factor 10^6 difference. It is thus concluded that the crossed Pomeron process proposed by Lipkin is not a valid argument.

(b) $\psi \to \gamma\phi\phi$

Recently, the new MK III has observed the $\phi\phi$ events due to the radiative decay of the ψ, i.e., $\psi \to \gamma\phi\phi$. However, only ~ 10 events are seen in the mass region of the $g_T(2050)$, $g_{T'}(2300)$ and $g_{T''}(2350)$, which can be explained as related to the low detection efficiency in this mass region. If appropriate correction is made for this efficiency, their final mass spectrum is not incompatible with the mass spectrum seen in the present experiment. Therefore, it is not surprising that the MK III can detect the high mass, narrow width $\phi\phi$ states due to the decay of the η_c but is unable to observe the relatively low mass $\phi\phi$ wide states due to the decay of g_T's.

7.5 Conclusion

The present investigation of the reaction $\pi^- p \rightarrow \phi\phi n$ at 22 GeV/c has led to an unexpected observation of the breakdown of the OZI rule. By assuming that the QCD is a correct strong interaction theory and OZI is universal for weakly coupled glue in disconnected Zweig diagrams where the disconnection is due to the creation or annihilation of new flavor(s) of quark(s), then the BNL/CCNY $g_T(2050)$, $g_{T'}(2300)$ and $g_{T''}(2350)$ are produced by 1-3 primary glueballs. One or two primary glueballs could in principle break down the OZI suppression and mix with one or two quark states which accidentally have the same quantum numbers and nearly the same mass. However the simplest explanation of the rather unusual characteristics of our data is that we have found a triplet of $J^{PC} = 2^{++}$ glueball states.

APPENDIX A: OBSERVED CROSS SECTION

The product of the total cross section and the branching ratio was calculated using he formula

$$\sigma \cdot Br = \frac{N}{\rho \cdot N_O \cdot L \cdot \varepsilon \cdot A^{-1} \cdot \text{Beam}}$$

where σ = total cross section,

Br = branching ratio for the exclusive channel studied,

N = observed events of $\pi^- p \to \phi\phi n$,

ρ = density of liquid hydrogen = 0.0708 gm/cm^3,

A = atomic weight of hydrogen = 1.01,

N_O = Avagadro's number = 6.022×10^{23} mole^{-1},

Beam = total effective π^- beam to produce N events,

L = length of the liquid hydrogen target = 60 cm,

ε = overall program and apparatus efficiency.

Our observed cross section for this particular channel is

$$\sigma_{\text{observed}} = \frac{N}{\rho \cdot N_O \cdot L \cdot A^{-1} \cdot \text{Beam}}$$

Our overall trigger rate was about 5×10^{-6} per pion yielding about 5 triggers each AGS cycle. During the two running periods we recorded ~ two million triggers and ~ 4000 $\phi\phi n$ events, hence

$$\text{Beam} = \frac{2 \times 10^6}{5 \times 10^{-6}} .$$

We observe

$$\sigma_{\text{observed}} = \frac{4000 \cdot 5 \cdot 10^{-6}}{(0.0708)\cdot(6.02)\cdot(10^{23})\cdot(1.01)\cdot(60)\cdot(2)\cdot(10^6)} \text{ cm}^2$$

$$= 4 \times 10^{-33} \text{ cm}^2 = 4 \text{ nb}.$$

APPENDIX B: The Relationship Between the Loglikelihood L and the $\Delta\chi^2$

The loglikelihood function $\mathcal{L}(\tau)$ for N events is defined by

$$\mathcal{L}(\tau) = \log L\ (\omega/\tau) = \sum_{i=1}^{N} \log \omega_i(\tau) \tag{B.1}$$

where i indexes the events, ω_i is the probability of the i^{th} event and $\omega_i(\tau)$ is the function ω for the value τ of the parameter.

Expand $\mathcal{L}(\tau)$ about a point τ_o and make a second order approximation, we get

$$\mathcal{L}(\tau) \approx \mathcal{L}(\tau_o) + (\tau - \tau_o) \sum_{i=1}^{N} \frac{\omega_i'}{\omega_i} + \frac{(\tau - \tau_o)^2}{2} \sum_{i=1}^{N} \frac{\omega_i \omega_i'' - (\omega_i')^2}{\omega_i^2} . \tag{B.2}$$

Note that the term $\sum \frac{(\omega_i')^2}{(\omega_i)^2}$ of Eqn. B.2 has all contributions of the same sign. On the other hand, since the overall probability for an event must be unity, thus

$$\int \omega(A,\tau)\ dA = 1 \tag{B.3}$$

then

$$\sum \frac{\omega_i \omega_i''}{\omega_i^2} \approx \int \frac{\omega^2(A,\tau)\ \omega''(A,\tau)}{\omega^2(A,\tau)}\ dA$$

$$= \int \omega''(A,\tau)\ dA = 0 \tag{B.4}$$

The last step follows because

$$\int \frac{\partial^2}{\partial\tau^2}\ \omega(A,\tau)\ dA = \frac{d^2}{d\tau^2} \int \omega(A,\tau)\ dA = 0 \tag{B.5}$$

Therefore

$$\mathcal{L}(\tau) = \mathcal{L}(\tau_o) + (\tau - \tau_o) \sum_{i=1}^{N} \frac{\omega_i'}{\omega_i} - \frac{(\tau - \tau_o)^2}{2} \sum_{i=1}^{N} \left(\frac{\omega_i'}{\omega_i}\right)^2 \tag{B.6}$$

At the maximum of (τ), i.e.

$$\left. \frac{\partial \mathcal{L}(\tau)}{\partial \tau} \right|_{\tau=\tau^*} = 0 \tag{B.7}$$

we have

$$(\tau^* - \tau_o) = \frac{\sum_{i=1}^{N} \frac{\omega_i'}{\omega_i}}{\sum_{i=1}^{N} \left(\frac{\omega_i'}{\omega_i}\right)^2} \tag{B.8}$$

Thus

$$\mathcal{L}(\tau) = \mathcal{L}(\tau_o) + [(\tau^* - \tau_o)(\tau - \tau_o) - \frac{(\tau - \tau_o)^2}{2}] \sum_{i=1}^{N} (\frac{\omega_i'}{\omega_i})^2 \qquad (B.9)$$

Define $$S = \int (\frac{\omega'}{\omega})^2 \omega dA \qquad (B.10)$$

then $$\sum_{i=1}^{N} (\frac{\omega_i'}{\omega_i})^2 = NS \qquad (B.11)$$

so that $$(\tau^* - \tau_o) = \frac{1}{NS} \sum_{i=1}^{N} (\frac{\omega_i'}{\omega_i}) \qquad (B.12)$$

and $$\mathcal{L}(\tau) = \mathcal{L}(\tau_o) + (\tau - \tau_o)\ (\tau^* - \frac{\tau + \tau_o}{2})\ NS \qquad (B.13)$$

$$(\tau^* - \tau_o) = \frac{1}{NS} \sum_{i=1}^{N} (\frac{\omega_i'}{\omega_i}) \qquad (B.14)$$

where the summation in B.14 represents the sum of random numbers about the average value, hence Eqn. B.14 becomes

$$(\tau^* - \tau_o) = \frac{\langle\frac{\omega_i'}{\omega_i}\rangle}{S} \qquad (B.15)$$

when $\langle\frac{\omega_i'}{\omega_i}\rangle = 0$, this gives $\tau^* = \tau_o$. (B.16)

In this case $$\mathcal{L}(\tau) = \mathcal{L}(\tau^*) - \frac{(\tau - \tau^*)^2}{2} NS \qquad (B.17)$$

or $$L(\tau^*/\tau) = L_{max}\ e^{-\frac{(\tau - \tau^*)^2}{2} \cdot NS} \qquad (B.18)$$

let $$\sigma(\tau) = 1/\sqrt{NS}, \text{ and } \Delta\chi^2 = (\tau - \tau^*)^2 \qquad (B.19)$$

then Eqn. B.18 becomes $$L = L_{max}\ e^{-\Delta\chi^2/2} \qquad (B.20)$$

where $\Delta\chi^2$ in Eqn. B.20 is equivalent to one σ effect.

APPENDIX C

Conversion Between the Loglikelihood Change and σ

In the course of our analysis, two distinctive standards have been adopted to estimate the deviation of a solution from a good fit. In one approach, the isobar model has used the maximum likelihood method to sort out the most representative combination of partial waves. This means the acceptance or rejection of a solution is primarily determined by the amount of change in loglikelihood value. However, the approach followed by the K-matrix formalism has made use of the more familiar quantity σ as a measure of the goodness of a fit. Thus it is very desirable to establish their equivalence so that a change in loglikelihood as a result of an improved solution can be readily equated to the corresponding change in σ. In the following we present a detailed description as how to equate these two quantities through a conversion factor.

In generating the K-matrix Monte Carlo solution we have included, in addition to three dominant waves, the coherent and incoherent backgrounds. Thus the set of data points taken for fitting purposes is given by:

$$\text{Number of mass independent amplitudes} = 48 + 10 + 10 = 68 \qquad \text{(C.1)}$$

where the first term represents the productions and phases for three 2^{++} waves already described in Section 6.8.2. The last two terms are introduced to account for the productions of coherent (phase = 180°) and incoherent backgrounds.

To identify how many parameters have been used in describing backgrounds we note that a satisfactory description of their behaviors can be accomplished by two high order polynomial functions with two sets of parameters, two for incoherent background and six for coherent background.

With suitable parameterization of these functions, background event levels could be well fitted (~ 1σ).

Putting these parameters together and recalling that the number of parameters used in a three-pole K-matrix fit is 23, we have

$$\text{Number of parameters} = 23 + 2 + 6 = 31 \tag{C.2}$$

consequently $$\text{D.F.} = 68 - 31 = 37 \tag{C.3}$$

or, 1σ is equivalent to

$$\Delta\chi^2 = (2\ \text{D.F.})^{1/2} = (2.37)^{1/2} = 8.6 \tag{C.4}$$

It can be shown that (see Appendix B) that the likelihood function is related to the $\Delta\chi^2$ by the following relation:

$$\mathcal{L} = \mathcal{L}_o\ e^{-\Delta\chi^2/2} \tag{C.5}$$

or alternatively $$\Delta\log \mathcal{L} = \log \mathcal{L}_o - \log \mathcal{L} = \frac{\Delta\chi^2}{2} \tag{C.6}$$

By substituting the $\Delta\chi^2$ of Eq. C.4 into Eq. C.6, we finally obtain that a change of 4.3 in loglikelihood value is equivalent to one standard deviation effect, or

$$\Delta\log \mathcal{L} = 4.3 \xrightarrow{\text{equivalent to}} 1\sigma. \tag{C.7}$$

REFERENCES

1. (a) M. Gell-Mann, Phys. Lett. 8, 214 (1964);

   (b) G. Zweig, CERN Reports Nos. TH-401 and TH-412, 1964 (unpublished); Proc. of the Intern. School of Physics, "Ettore Majorana", Erice, Italy, 1964, Editor, A. Zichichi (Academic Press, NY 1965), p. 192.

2. C.N. Yang and R.L. Mills, Phys. Rev. 96, 191 (1954).

3. H. Fritzsch and M. Gell-Mann, Proc. XVI Intern. Conf. on High Energy Physics, Chicago-Batavia, 1972, Vol. 2, p. 135.

4. (a) H. Fritzsch, M. Gell-Mann, and H. Lentwyler, Phys. Lett. 47B, 365 (1973);

   (b) S. Weinberg, Phys. Rev. Lett. 31, 494 (1973); Phys. Rev. D8, 4482 (1973);

   (c) D.J. Gross and F. Wilczck, Phys. Rev. D8, 3633 (1973).

5. For a review, see W. Marciano and H. Pagels, Phys. Report 36, 137 (1978).

6. For a review of recent results on confinement, see S. Mandelstam, Proc. of the 1979 Intern. Symposium on Lepton and Photon Interactions at High Energies, Editors, T.B.W. Kirk and H.D.I. Abarband, p. 513.

7. (a) K.G. Wilson, Phys. Rev. D10, 2445 (1974);

   (b) J.B. Kogut and L. Susskind, Phys. Rev. D11, 395 (1975).

8. (a) M. Creutz, Phys. Rev. D21, 2308 (1980); Phys. Rev. Lett. 45, 313 (1980).

   (b) G. Mack, Phys. Rev. Lett. 45, 1738 (1980);

   (c) G. Münster, Phys. Lett. 95B, 59 (1980).

REFERENCES (continued)

9. (a) D.J. Gross and F. Wilczck, Phys. Rev. Lett. 30, 1343 (1973);
   (b) H.D. Politzer, Phys. Rev. Lett. 30, 1346 (1973);
   (c) G't Hooft (unpublished); Phys. Reports 14C, 129 (1974).
10. C.E. Carlson, T.H. Hansson, and C. Peterson, Phys. Rev. D27, 1556 (1983); 28, 2895(E) (1983).
11. M. Chanowitz and S. Sharpe, Nucl. Phys. B222, 211 (1983).
12. J. Donoghue, Proc. of the Sixth Intern. Conf. on Experimental Meson Spectroscopy, April 25-26, 1980, Editors, S.U. Chung and S.J. Lindenbaum, AIP Conf. Proc. No. 67, p. 104.
13. J. Coyne, P. Fishbane, and S. Meshkov, Phys. Lett. 91B, 259 (1980).
14. C.E. Carlson, J. Coyne, P. Fishbane, D.J. Gross and S. Meshkov, Phys. Lett. 98B, 110 (1981).
15. J.F. Donoghue, K. Johnson, and B. Li, Phys. Lett. 99B, 416 (1981).
16. (a) B. Berg and A. Billoire, Phys. Lett. 113B, 65 (1982);
    (b) B. Berg and A. Billoire, Phys. Lett. 114B, 324 (1982);
    (c) B. Berg and A. Billoire, Nucl. Phys. B221, 109 (1983);
    (d) B. Berg and A. Billoire, Nucl. Phys. B226, 405 (1983).
17. (a) Ishikawa, M. Teper, and G. Scherholz, Phys. Lett. 116B, 429 (1982);
    (b) Ishikawa, M. Teper, and G. Scherholz, Z. Phys. C21, 167 (1983).
18. C. Rebbi, Proc. of the 21st Intern. Conf. on High Energy Physics, Paris, France, 26-31 July 1982, Journal De Physique 43, C3-C723 (1982).
19. G. Parisi and R. Petronzio, Phys. Lett. 94B, 51 (1980).

REFERENCES (continued)

20. D.L. Scharre et al., Proc. of the Sixth Intern. Conf. on Experimental Meson Spectroscopy, Brookhaven National Laboratory, April 25-26, 1980, Editors, S.U. Chung and S.J. Lindenbaum, AIP Conf. Proc. No. 67, p. 329; Phys. Lett. 97B, 329 (1980).

21. E. Bloom, Proc. XXI Intern. Conf. on High Energy Physics, Paris, France, July 26-31, 1982.

22. A. Etkin et al., Phys. Rev. D25, 2446 (1982).

23. S. Okubo, Phys. Lett. 5, 165 (1963).

24. G. Zweig, CERN Reports TH-401 and TH-412 (1964) (unpublished).

25. (a) J. Iizuba, Prog. Theor. Phys. Suppl. 37-38, 21 (1966); J. Iizuba, K. Okaba, and O. Shito, Prog. of Theor. Phys. 35, 1061 (1966);

    (b) S. Okubo, Phys. Rev. D16, 2336 (1977);

    (c) T. Applequist, K. Kane and M. Barnett, Ann. Rev. Nucl. Sci. 28, 387 (1978);

    (d) I.J. Muzinich and F.E. Paige, Phys. Rev. D21, 1151 (1980).

26. S. Okubo, A Survey of the Quark Line Rule U.R. 641 (Dept. of Physics and Astronomy, Rochester, New York, 1977).

27. P.L. Woodworth et al., Phys. Lett. 65B, 19 (1976).

28. S.J. Lindenbaum, Quark Line Diagrams, Rules and Some Recent Data, BNL 50812 (1977).

29. (a) A. Etkin et al., Phys. Rev. Lett. 41, 784 (1978);

    (b) A. Etkin et al., Phys. Rev. Lett. 49, 1620 (1982);

    (c) S.J. Lindenbaum, The Discovery of Glueballs, Surveys in High Energy Physics, Vol. 4, Editor, M. Charap (Harvard Academic Publishers, London, 1983), p. 69-126.

REFERENCES (continued)

29\. (continued)

(d) R.S. Longacre, Glueballs in the Reaction $\pi^- p \to \phi\phi n$ at 22 GeV/c, *Proc. of the Seventh Intern. Conf. on Experimental Meson Spectroscopy, Brookhaven National Laboratory, April 14-16, 1983*, Editor, S.J. Lindenbaum, AIP Conf. Proc. No. *113*, p. 51-77.

30\. S.J. Lindenbaum, Hadronic Physics of $q\bar{q}$ Light Quark Mesons, Quark Molecules and Glueballs, *Proc. of the XVIII Course: The High Energy Limit, The International School of Subnuclear Physics, 31 July-11 August 1980, "Ettore Majorana Center for Scientific Culture," Erice, Trapani, Italy*, Editor, A. Zichichi (Plenum Press, NY 1983), p. 509-562 (1983).

31\. (a) T.A. Armstrong *et al.*, Nucl. Phys. *B196*, 176 (1982);

(b) M. Baubillier *et al.*, Phys. Lett. *118B*, 450 (1982).

32\. D. Cohen *et al.*, Phys. Rev. Lett. *38*, 269 (1977).

33\. (a) S.J. Lindenbaum, Glueballs in the Reaction $\pi^- p \to \phi\phi n$. *Proc. Hadronic Session of the Eighteenth Rencontre De Moriond, La Plagne-Savoie-France, January 23-29, 1983*, Vol. I, Gluons and Heavy Flavours, J. Tran Thanh Van, Editor (Editions Frontieres, Gif sur Yvette, France), p. 441-468.

(b) S.J. Lindenbaum, Status of the Glueballs, Invited Lecture. *Proc. of the 21st Course of the International School of Subnuclear Physics on "How Far we are From the Electronuclear Interactions and the Other Gauge Forces", Erice, Trapani-Sicily, 3-14 August 1983*, to be published.

34\. For example, see D.J. Herndon *et al.*, Partial Wave Analysis of the Reaction $\pi N \to \pi\pi N$, Phys. Rev. D*11*, 3183 (1975).

REFERENCES (continued)

35. D.J. Herndon, P. Söding, and R.J. Cashmore, Generalized Isobar Model Formalism, Phys. Rev. D11, 3165 (1975).

36. (a) R.S. Longacre *et al.*, K-matrix Fits to $\pi N \rightarrow N\pi$ and $\pi N \rightarrow N\pi\pi$ in the Resonance Region $\sqrt{s} = 1.3$ to 2.0 GeV, LBL Preprint 2636, January 1977.
    (b) I.J.R. Aitchison, Nucl. Phys. A189, 417 (1972).

37. (a) S.J. Lindenbaum and R.M. Sternheimer, Phys. Rev. 123, 333 (1961);
    (b) S.J. Lindenbaum and R.M. Sternheimer, Phys. Rev. 105, 1874 (1957);
    (c) S.J. Lindenbaum and R.M. Sternheimer, Phys. Rev. 106, 1107 (1957);
    (d) S.J. Lindenbaum and R.M. Sternheimer, Phys. Rev. 109, 1723 (1958).

38. M. Jacob and G.C. Wick, Ann. Phys. (N.Y.) 7, 404 (1959).

39. L.R. Miller, Ph.D. Thesis, University of California, Berkeley, 1971.

40. R.T. Deck, Phys. Rev. Lett. 13, 169 (1964).

41. R.S. Longacre, Phys. Rev. D26, 82 (1982).

42. C.J. Goebel and K.W. McVoy, Phys. Rev. 164, 1932 (1967).

43. (a) E.D. Platner, The MPS II - A Tracking Detector System for Large High Rate Experiments, *Proc. Third LAMPF II Workshop, July 18-29, 1983, Los Alamos National Laboratory, Los Alamos, New Mexico,* LA-9933-C, Vol. II, pp. 649-654.
    (b) A. Etkin and M.A. Kramer, IEEE Transactions on Nuclear Science NS-27, p. 139-144 (1980).

44. E.D. Platner *et al.*, Nucl. Instrum. and Methods 140, 549 (1977).

45. H. Becker *et al.*, Nucl. Phys. B150, 301 (1979).

REFERENCES (continued)

46. P. Eberhard, Comput. Phys. Commun. 3, 296 (1972); 5, 163 (1973).

47. F. James and M. Roos, Comput. Phys. Commun. 10, 343 (1975).

48. R. Petronzio, Proc. XVIII Rencontre De Moriond, LaPlagne, Savoie, France, January 17-23, 1983.

49. B. Berg, A. Billoire, and C. Rebbi, BNL 30826 (Preprint, December 1981).

50. S. Meshkov, Proc. of the Seventh Intern. Conf. on Experimental Meson Spectroscopy, April 14-16, 1983, Brookhaven National Laboratory, S.J. Lindenbaum, Editor, AIP Conf. Proc. No. 113, p. 125.

51. T.D. Lee, Time as a Dynamical Variable, CU-TP-266; Talk at Shelter Island II Conf., June 2, 1983; also, Proc. of the 21st Course of the Intern. School of Subnuclear Physics on How Far We are From the Electronuclear Interactions and the Other Gauge Forces, Erice, Trapani, Sicily, 3-14 August 1983 (to be published).

52. C.E. Carlson, J.J. Coyne, P.M. Fishbane, F. Gross, and S. Meshkov, Phys. Lett. 99B, 353 (1981).

53. S. Meshkov, Proc. Hadronic Session of the Eighteenth Rencontre De Moriond, La Plagne-Savoie-France, January 23-29, 1983, Vol. I, Gluons and Heavy Flavours, Editor, J. Tran Thanh Van (Editions Frontieres, Gif sur Yvette, France), p. 427.

54. H.J. Lipkin, Phys. Lett. 124B, 509 (1983).

55. S.J. Lindenbaum, Phys. Lett. 131B, 221 (1983).

56. W.C. Davidon, ANL-5990 (1959).